ScuDo
Scuola di Dottorato ~ Doctoral School
WHAT YOU ARE, TAKES YOU FAR

Doctoral Dissertation
Doctoral Program in Mechanical Engineering (31^{th}cycle)

Development of a resonance-tunable Wave Energy Converter.

By

Sergej Antonello Sirigu

******

Supervisor(s):
Prof. Giuliana Mattiazzo, Supervisor

Doctoral Examination Committee:
Prof. Stefano Brizzolara , Referee, Virginia Tech (USA)
Prof. John Ringwood, Referee, Maynooth University (Ireland)
Prof. Ermina Begovic, Università degli Studi di Napoli Federico II (Italy)
Prof. Alessandro Fasana, Politecnico di Torino (Italy)
Prof. Stefano Mauro, Politecnico di Torino (Italy)

Politecnico di Torino
2019

Declaration

I hereby declare that, the contents and organization of this dissertation constitute my own original work and does not compromise in any way the rights of third parties, including those relating to the security of personal data.

Sergej Antonello Sirigu
2019

* This dissertation is presented in partial fulfillment of the requirements for **Ph.D. degree** in the Graduate School of Politecnico di Torino (ScuDo).

Al Cuore,
All'Amor che move il sole e l'altre stelle.

Acknowledgements

Non basterebbero le parole per ringraziare la mia relatrice Giuliana Mattiazzo, che in questi 4 anni mi ha dato innumerevoli occasioni di crescita professionale e personale, che spero di aver colto (almeno qualcuna). Soprattutto ringrazio l'entusiasmo trasmesso per un progetto che ho imparato ad amare e rendere mio. Una cosa non banale è sicuramente essere stato l'esser stato accettato per quello che sono, non aver mai avuto timore di dire ciò che pensavo e aver avuto la possibilità di tentare, sbagliare e provarci.
Un grande ringraziamento va anche a Giovanni Bracco, che mi ha trasmesso un po' di quell'ordine e metodo a cui non sono tanto avvezzo, e per avermi sempre dato una mano quando ne avevo più bisogno. Un doveroso ringraziamento va a tutti i colleghi del Poli, sia chi ha iniziato con me il mio percorso di dottorato, e quelli che mi stanno accompagnando tutt'ora. Ringrazio di far parte di un team di ricerca che ha voglia di innovazione, ma che sappia anche prendersi in giro e divertirsi.
Ringrazio tutti i ragazzi di W4E che in questi anni mi hanno aiutato ad uscire dai meandri dei modelli numerici, e farmi capire che alla fine le idee e i sogni si possono anche costruire realmente, con grande orgoglio. Un ringraziamento va anche al prof. Stefano Brizzolara che durante il miei periodi di soggiorno negli States mi ha permesso di cambiare punto di vista e imparare metodi nuovi ed efficaci per la mia ricerca, per avermi fatto sentire un po' a casa, anche a migliaia di km di distanza.
L'ultimo grazie va a tutte quelle persone a cui voglio un bene dell'anima, famiglia e amici, senza di loro non ci sarebbe nessun traguardo di cui giore.

Computational resources were provided by HPC@POLITO, a project of Academic Computing within the Department of Control and Computer Engineering at the Politecnico di Torino (http://hpc.polito.it)

Abstract

The purpose of this thesis work is the development of a novel technology for a more efficient wave energy harvesting. IOwec, Inertial Ocean wave energy converter (WEC), is a floating pitching WEC based on the ISWEC technology (Inertial Sea Wave Energy Converter) developed by the Renewable Energy group of Politecnico di Torino (Italy). The novelty consists on the the integration of the water sloshing tank (U-Tank) technology derived from the naval field. The variation of the dynamic properties of the U-Tank, allows the shifting of the resonance condition of the device with a consequent improvement of the energy harvesting from ocean waves.
The result is a novel device able to adapt itself in different wave-climates through the dynamic tuning of the U-Tank with the incoming sea-state. The adaptability and flexibility of this new technology is advantageous for the future industrialization, because able to work in various installation sites avoiding a site-dependant design.
A numerical model is developed in order to assess the dynamics and performance of the device, and a numerical design tool is implemented in Matlab to design and optimize the device. A sea-state based control is proposed for the tuning of the device with the incoming wave. The performances of the novel technology are evaluated in regular and irregular wave condition and complex measured sea states with promising results.
A multi-objective optimization algorithm is implemented in order to optimize the performance of the IOwec device in two chosen installation sites, one in Hamboldt Bay in California and the second one in Hawaii islands, at the Wave Energy Test Site (WETS). The optimization result show interesting techno-economic trends for the future design of the system and an improvement of the performance index of 20 % compared with the first draft of IOwec. Moreover, the preliminary results show an energy extraction improvement of 20 % due to the active control of the U-Tank. Nevertheless, the resulting device is optimal in both sites, demonstrating the adaptability of the technology for different wave-climates.

Contents

List of Figures

List of Tables

Chapter 1

Introduction

In the last decades the rise of energy demand and CO_2 emissions [11] has induced a major attention on renewable energy such as solar, wind and geothermal that have already reached commercial maturity. Another unexploited source of renewable energy, available worldwide, are ocean waves [1]. In the last decades several technology solutions have been studied and developed to harvest the ocean wave energy [12]. So far, wave energy is still a not mature technology and the cost of energy is not yet competitive with other renewable energy sources such as solar, wind and geothermal [13]. The main reason of the difficulty of the wave energy technologies commercialization is the harsh conditions that the devices must be face in marine environment: high corrosion due to salt water, high loads due to extreme events. Therefore, the survivability and reliability of the technology is one of the most challenging fields of wave energy.

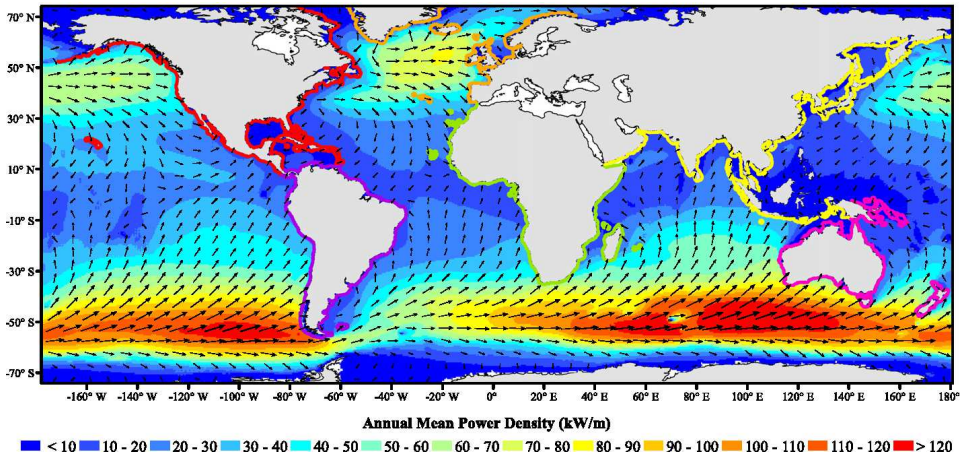

Figure 1.1 Wave energy resource potential [1]

.

Both Europe and United States are investing on the cost and time-to-market reduction of the technology in view of the carbon emission reduction policies and the economic and social benefits of ocean waves [14],[15]. One of the objectives is the test of full-scale devices in order to prove the reliability and performance of the technology, and from the lessons learned in real operation conditions improve the design and reduce the costs.

1.1 Wave Energy Technology

First appearance of technology able to harvest ocean wave energy is dated 1799 [16]. Modern research on wave energy technology started in the early 70s in conjunction with oil crisis. Unlike solar and wind, water waves technology has not reached maturity and convergence towards a unique technology solution. Several reviews have been published (see for example references [12], [17], [18]).

1.1.1 Classification of wave energy converters

Since the existence of different concepts of wave energy converters a classification is needed. First, WECs can be classified according to their installation location and

their distance from the shore and bathymetry. We can distinguish between shoreline, nearshore and offshore devices.

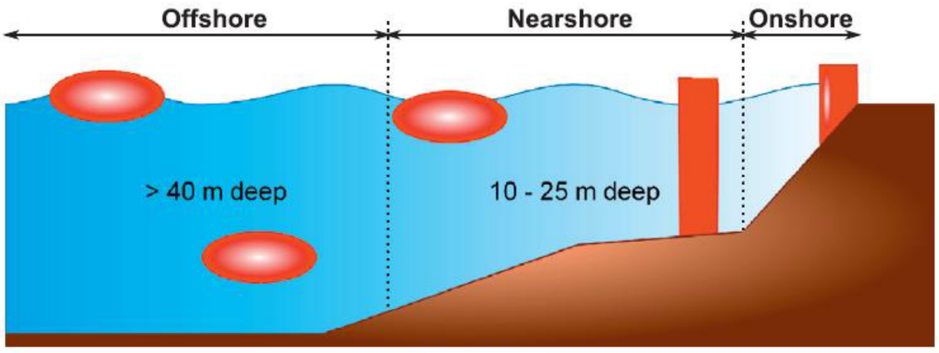

Figure 1.2 Classification of wave energy converters based on their location [2].

.

- Shoreline devices are typically fixed structures embedded with the shoreline or harbor infrastructures and breakwaters. A wide variety of shoreline devices are based on the oscillating water column technology (OWC). A shoreline OWC consisted mainly in a concrete structure where the water waves can oscillate and the air trapped in the chamber is induced to flow through a Wells turbine adopted to harvest the wave energy.

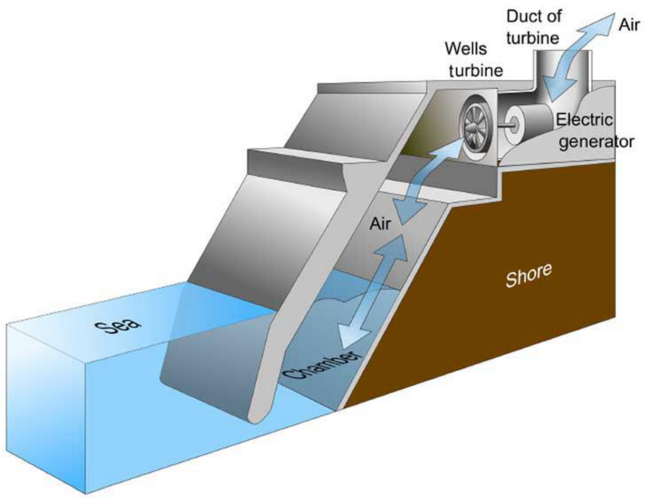

Figure 1.3 Sketch of a fixed-structure Oscillating Water Column (OWC) device [3].

Examples of OWC are the shoreline-integrated device installed in Pico (Azores, Portugal) and built in 1999 [19] and the breakwater-integrated OWC device installed in the harbor of Sakata (Japan) and built in 1990 [20]. The advantage of this technology is the proximity with the end-users and the reduction of maintenance costs compared to nearshore and offshore devices that required marine operations for maintenance. The drawbacks are the high costs of civil constructions required, the strong social and environmental impact due to the installation of the devices in the shoreline. Moreover, the energy resource in shallow water is less than offshore deep water impacting on the performance of this technology.

- Devices are considered nearshore if they are installed relatively close the shore (few hundreds of meters) and with a bathymetry in the range 10-25 m. Typically the proposed devices and concepts avoid the use of moorings and are fixed at the seabed. The advantage is a relatively proximity to the shore as in the case of shoreline devices and since they are installed in open sea the wave energy resource is higher. Mooring costs, in case of floating devices, are lower than offshore installation and in general electrical cable and installation costs. The main drawback is the environmental and social impact due to the presence of the WECs, usually installed in arrays, too close to the shore.

- WECs are considered offshore devices when installed in sites with a bathymetry higher than 40 m and far from the shore. Usually the technology solution is of floating or submerged structures moored at the sea bed. The energy resource in deep water sea is higher compared with previous cases, and the environmental and social impact is minor since the long distance from the coast. Offshore structure must be designed to withstand the harsh marine environment and high loads in extreme events with an increase of costs.

Wave energy converters can be also classified with respect to their size and working direction with reference to the dominant wave. Therefore, it is possible to distinguish between four main cases: attenuators, point absorbers, large absorbers, terminators.

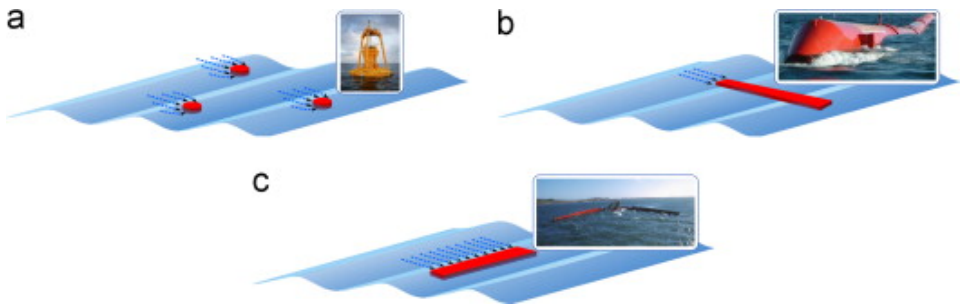

Figure 1.4 Classification of WECs based on their size and orientation a) Point Absorbers (OPT) b) Attenuator (Pelamis) c) Terminator (Wave Dragon) [2].

- Attenuators are typically multi-body structures slack-moored at the sea-bed with a total length longer than the incident wavelength. This type of devices are constitute of several floating section linked together by hinged joints and their relative motion is damped by hydraulic power take off to harvest the wave energy. During operation the multy-body structure is aligned with the direction of the dominant wave. A famous example of this technological solution is the Pelamis full-scale prototype (750 kW rated power) and it was the first offshore wave energy converter connected at the electrical grid [2].

- Terminators main dimension is along the perpendicular to the incoming dominant wave direction.The aforementioned fixed-structure OWCs are classified as attenuators. Other example are overtopping devices such as the Wave Dragon [12] and WECs that exploit wave energy damping the pitching motion of a

flapper hinged to the sea-bed, of which the best known is the Oyster WEC [12].

- Point absorbers shown dimensions that are relatively small compared to the incident wavelength. They are floating or submerged structures moored at the sea-bed and harvest wave energy damping the motion of the structure, typically heave. Because of their small dimensions, point absorbers are expected to be installed in arrays, with benefits in terms of economy of scale. Examples of point absorbers are the floating device Powerbuoy developed by Ocean Power Technology [21] and the fully-submerged buoy CETO developed by Carnegie [22].

1.1.2 Reaction-based WECs

Big disadvantage of devices that harness wave energy damping directly the motion of a floating or submerged buoy is the presence of relative motion of mechanical and structural parts constantly in contact with the harsh marine environment with high risk of corrosion and biofouling, with consequent reduction of reliability. In the past years different technology solutions seek to address this issue integrating tuned inertial dampers inside rocking or heaving structures. A tuned inertial damper is a system constitute of a mass spring and damper attached to a structure in order to reduce its dynamic motion. The idea is to harvest wave energy damping the floater motion through rotating or translating masses inside the hull. Mass dampers are widely used to damp vibrations, and a famous application is the tuned mass used to damp the oscillations induced by wind of the skyscraper Taipei 101 [23].

Within this category, concepts based on pendulum working principle are of big interest: the SEAREV device developed by Ecole Centrale de Nantes [24] and PEWEC developed by Politecnico di Torino in collaboration with ENEA [25]. Both concepts exploit wave energy damping the pitching motion of the floater and therefore they need a mooring system that allows the device to align with the dominant sea-state. An interesting pendulum-based device is WITT developed by WITT Limited [26] that can harvest the energy from four directions surge, pitch, sway and roll due to its particular technology solution [27]. Penguin (Wello [28]) device working principle is based on a rotational mass with vertical axis installed inside a sealed hull. Penguin

full-scale prototype was deployed in open-sea in EMEC test site in 2012 [29]. The device concept PS Frog MK 5 designed and developed by the University of Lancaster [30] is consists of a large floater and its pitching motion is damped by a sliding mass connected to a power take off. Gyroscope systems can be used as well in order to reduce the rocking motion of a floater and harvest wave energy: ISWEC (Inertial Sea Wave Energy Converter) developed by Politecnico di Torino is argument of this thesis and a section will be entirely dedicated. Another example of gyroscope-based WEC is the Oceantec device [31].

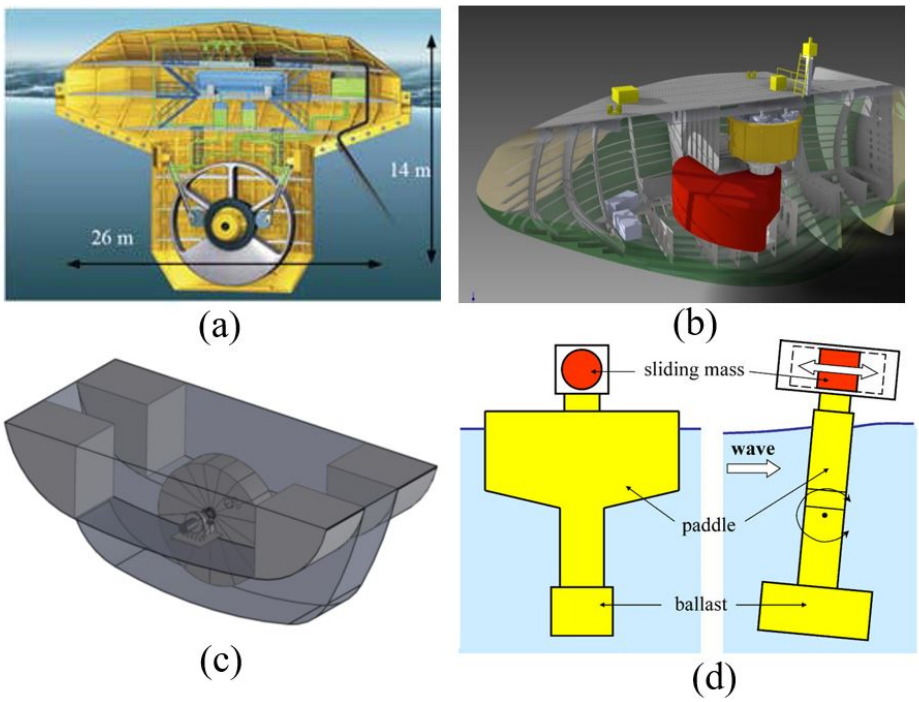

Figure 1.5 Examples of reaction-based WECs: a) SEAREV b) Penguin Wello c) Pewec d) PS Frog MK 5

Floating wave energy converters working principle is based typically in the frequency-resonance matching of the floating body dynamics with the incoming sea-state. [19]. Therefore, the device should be operate as near as possible to the resonance condition to maximize the power extraction. Floating structures of wave energy devices are characterized by their Response Amplitude Operator (RAO) that define the behavior of the floater in frequency domain. However, sea-states show high variability both in wave period and height and tuning of the dynamics characteristics

of the WEC are required to guarantee high performance in each sea-state condition. Despite the geometrical and inertial properties of the device can not be varied easily during operation due to technological limitations, the resonance-matching of the device dynamics can be achieved with a proper control logic of power take off system, in a limited range of action [32].
Since the performance of the device depend on the frequency response of the oscillating floater, the design and optimization of the WEC will be influenced by the specific deployment site. It follows that oscillating WECs suffer of low versatility that can affect the economy of scale of the technology. A technological solution to this problem an oscillating floating WEC embedded with a sloshing water ballast tank, which dynamic characteristics can be modified during operation through a proper control logic, in order to achieve the resonance-matching of the WEC for several sea state conditions.

1.2 Water sloshing tank technology

Water sloshing tank are a particular case of tuned mass dampers often called also Tuned Liquid Dampers (TLD). TLDs have been widely adopted to reduce the wind-induced oscillations in tall buildings [33] and to reduce the roll motion of ships [34]. Sir Philip Watts conducted a pioneering work on the application of free surface water tank to reduce the ship roll motion during operation [35, 36], based on the work of Froude [37]. He suggested the use of a rectangular-shape tank filled with water to be installed above the center of gravity of the ship. If well designed, the shifting liquid provide a roll moment out-of-phase with the wave excitation force, reducing consequently the roll amplitude. Moreover, changing the water depth in the tank a proper tuning of the anti-roll tank with different sea-state conditions can be achieved. As discussed by Moaleji [34] after the work of Watts the interest on free surface anti-roll tank declined without a clear reason. A modern implementation of this technology can be found *MV Searod Tamar* vessel [4]. The vessel suffered of high roll oscillations during operation and in 1998 a large passive water tank was integrated on the deck of the ship after experimental investigations in wave tank, demonstrating the effectiveness of the technology (see figure 1.6). Bass conducted sea trials of the effect of free-surface tanks on three sister vessels [38], highlighting the advantage in roll amplitude reduction.

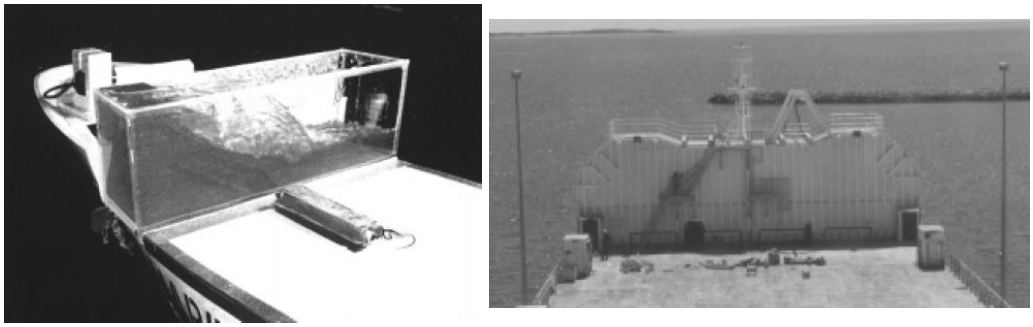

(a) (b)

Figure 1.6 (a) Experimental test of anti-roll water tank integrated on the 1:37 vessel model (b) The view of the *MV Searod Tamar* vessel with roll damping tank integrated [4].

A relevant disadvantage of free-surface tanks are the difficult controllability of the water sloshing freely inside the tank. An example of study about the active control of free-surface tanks was conducted by Birmingham [39] who proposed a butterfly valves mechatronic system and a control logic based on artificial intelligence. Another problem of free-surface tanks are the unpredictable and high impulsive loads due to the sloshing and breaking waves phenomena of the water inside the tank. U-shaped tanks, also known as U-Tube tanks, were proposed to overcome the main problems that affect free-surface tanks. U-Tube tanks were suggested by Frahm [40] is composed by two water filled reservoirs connected by a duct at the base. His design included also an air connection between the two reservoirs located at port and starboard provided with a throttling apparatus. It served to stop the water motion by closing the throttle valve and control the damping action of sloshing water by regulating the throttle valve. Frahm's tanks were installed and tested in two vessels, the *SS Ypiranga* and *Corcovado*, that presented bad rolling behavior. In his work Frahm discussed how good results were obtained integrating the U-Tanks in the ship reducing the roll motion during operational conditions.

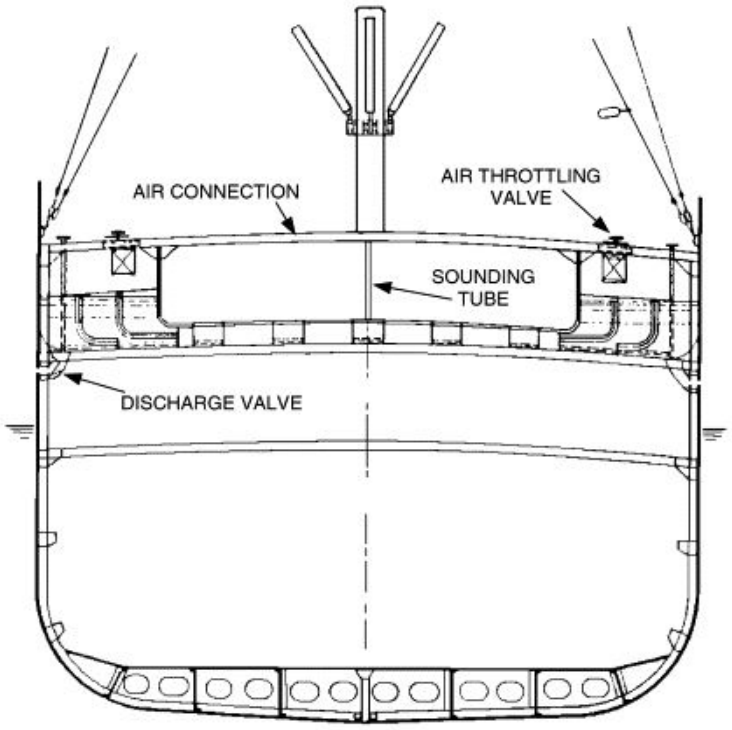

Figure 1.7 *SS Ypiranga* with integrated Frahm tank [5].

The easiest geometry and absence of strong sloshing and breaking wave phenomena of U-Tanks permitted the development of numerical models that can predict with high accuracy the dynamics behavior of the U-tank. Reliable numerical models allows the development of model-based control algorithms and a more accurate design of the system (it will be discussed more in detail in section 2.3.1). Goodrich [41] investigated theoretically and experimentally the influence of the design parameters of passive U-tanks on its dynamics properties such as natural frequency and damping, highlighting how the vessel equipped with the U-tank can be seen as a 2 Degree of Freedom dynamic system. If lightly damped such dynamic systems show two resonance and one anti-resonance frequency. Resonance at lower periods, with increase of roll motion, is un undesirable effect when designing anti-roll tanks. Gawad [6] also studied theoretically the effect of tank damping, water mass and tank location on the roll motion of the vessel for a wide range of encountered frequencies. Figure 1.8 show the effect of U-Tank on ship roll RAO for different tank damping values, showing the presence of two separate resonance peaks when the U-Tank is lightly damped.

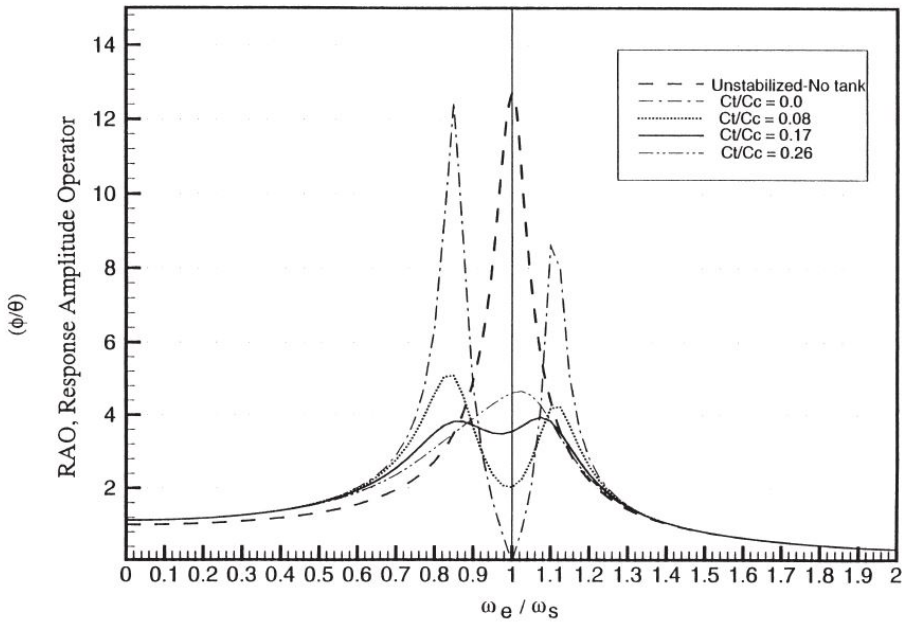

Figure 1.8 Effect of the U-Tank on the vessel dynamics for different values of tank damping [6].

Despite the presence of two roll resonance peaks due to the U-tank dynamics is harmful for ships, this peculiar characteristic can be exploited for wave energy conversion purposes.

1.2.1 U-tank integration in WECs

The idea of absorbing energy from the water motion inside U-tanks is not new. In a recent work [42], the energy absorption of anti-roll tank on ships is investigated; the authors analyse how the natural frequency and damping ratio of both ship and U-Tank influences the power absorbed by the tank. They also state that the maximisation of the power harvested by the tank is linked to the minimization of the roll kinetic energy and the natural frequency of the U-tank should be as close as possible to the natural frequency of ship roll motion. Tiao [43] carried out a preliminary assessment of a U-Tank integrated in a ship-form carrier and evaluated the power extraction efficiency with numerical model of the coupled vessel-plus-Utank system.
An interesting application of U-tank for wave energy harvesting was investigated by *Technical University of Lisbon* with the development of the Ugen concept (see figure 1.9) [44]. Ugen consists in a large asymmetric floater with an internal U-tank filled

with water. The two lateral reservoirs of the U-tank are connected by an air duct. The water motion pressurized the air in the reservoirs inducing an air flow, which energy is harvested by a Wells turbine that constitutes the PTO system. the water motion inside the U-Tank is mainly excited by the roll motion of the floater. Since roll motion is coupled with sway and heave motions the device can theoretically exploit energy from three modes of oscillation of the floater. The numerical model used for designing and assessing the performance of the device has been compared with scaled model experimental results with good agreement [45].

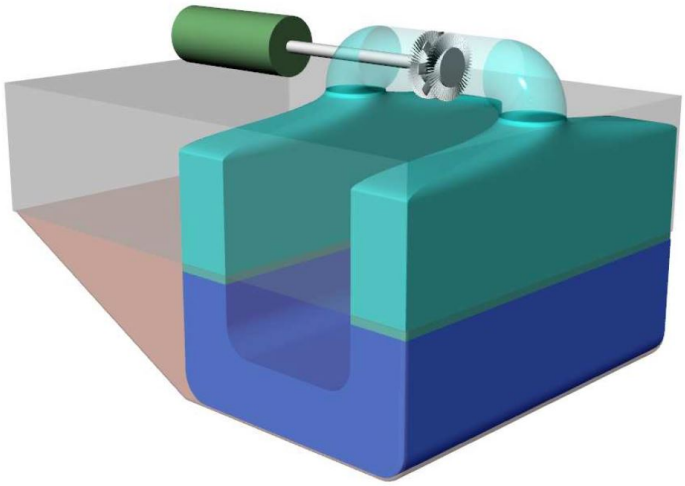

Figure 1.9 concept of the Ugen wave energy converter [7].

Crawley et al. [46] developed a wave energy converter, similar to the Ugen concept, based on previous theoretical studies on coupled multi-resonance absorbers [47]. The device consists in a pitching submerged cylinder moored at the sea bed with an internal annular tank filled with water. The sloshing motion of the water pressurized the air in the two reservoir branches that drives an air turbine.

Resonance-tuning of WECs through U-tank integration

Wave energy converters suffer of their resonance characteristic being sharply (and naturally) tuned to a specific incoming wave frequency, so that their efficiency rapidly decays for incident waves with a different frequency. The main negative consequence is the low adaptability of the device with different wave climate and

a site-dependent design. McCabe et al. [30] underline the need of a "slow-tuning" of the PS Frog to adapt the device for different wave conditions so that optimum performance can be reached for a broad frequency range. They proposed a solution based on pumping ballast water in chambers within the hull with the aim of changing the inertia and CoG of the device, therefore, its natural frequency. Another study on inertia adjustment applied on a pitching bottom-hinged type WEC was carried out by Flocard and Finnigan [48]. They investigated experimentally the effect of varying the water ballast of the WEC on the performance for a wide range of wave conditions both regular and irregular. The results shown that the power capture ratio was increased through inertia adjustment by 75% in regular waves and 15-40% compared to a reference fixed ballast configurations demonstrating the high impact of slow-tuning control on the device performance.
Besides the use of U-tank to harvest wave energy, this technology can be used to dynamically adjust the resonance frequency of rocking buoy wave energy converters. The resonance frequency of the coupled system floater-plus-Utank can be tuned through control of the sloshing dynamics of the water inside the tank. In this thesis ISWEC is adopted as case study to investigate the effect of U-tank on the power absorption performance.

1.3 ISWEC: State of the Art

The first concept of ISWEC (Inertial Sea Wave Energy Converter) was developed in 2005 by the renewable group of the Department of Mechanical and Aerospace (DIMEAS) of Politecnico di Torino (Italy). ISWEC is an offshore pitching floating device designed for the Mediterranean sea wave climate (see figure 1.10).

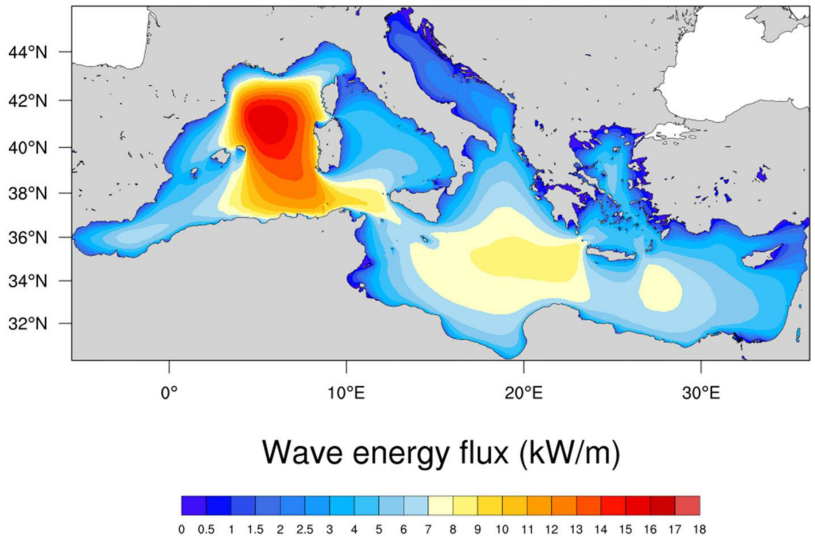

Figure 1.10 Wave energy resource potential in Mediterranean Sea [8]

.

The idea of the ISWEC device is to harvest exploiting the gyroscopic effect and thus it falls within the category of reaction-based WECs. The pitch motion of a sealed floater, induces the precession motion of a gyroscope housed within the hull and this mechanical energy is converter in electricity by an electrical Power Take Off (PTO). The device is moored at the sea-bed with a slack mooring system, designed to be multi-directional and thus the device can align itself with the incoming wave direction [49], [9] as shown in figure 1.11. The novel mooring system coupled with the floater was tested in a 1:20 scale model in the towing tank of Università degli studi Napoli Federico II to investigate the dynamics and loads in both operational and extreme sea-state condition and the weathervaning capability of the layout.

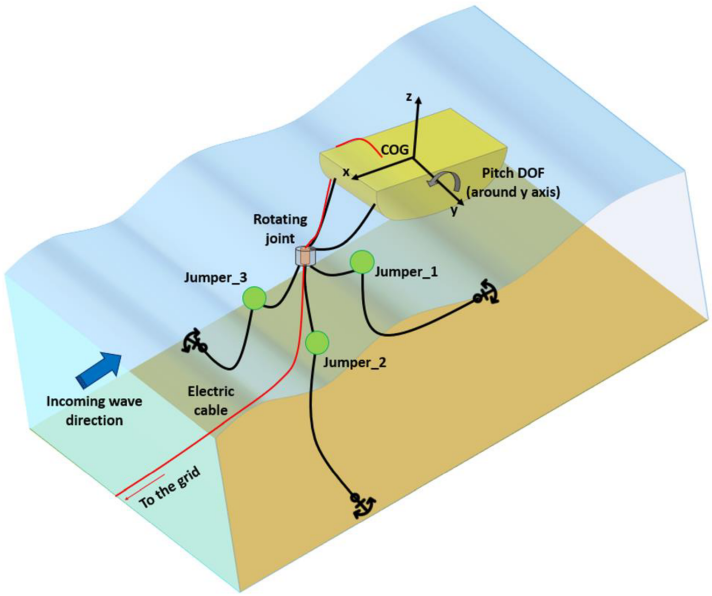

Figure 1.11 Mooring layout concept of ISWEC [9].

A significant advantage of this solution is the totally absence of moving parts involved in the energy transformation in contact with the harsh marine environment, with consequent improvement of the device durability and reliability. The performances power extraction can be improved with the tuning of the flywheel speed as a function of the incoming sea-state increasing and with the PTO control system. The gyroscope technology show high efficiency for high frequency waves, characteristic of sea states generated by limited fetch as the case of Mediterranean Sea.
The first proof of concept was demonstrated in 2007 in the wave tank of University of Edimburgh (Scotland) [50]. A numerical model for the performance assessment and an experimental campaign test was conducted on a 1:8 scaled model device in the wave tank INSEAN in Rome (Italy) in 2012 [51]. The first full-scale device of ISWEC was deployed off the coast of Pantelleria island (Island) from September 2015 to December 2015 in order to prove the technological solutions and the survivability of the device [52], [10].

Figure 1.12 ISWEC full-scale prototype during operation off the coast of Pantelleria island (Italy), 2015.

In 2016 Politecnico di Torino, the academic spin-off Wave-for-Energy started a synergistic collaboration with the multinational company Eni for the development of a scaled 1:2 prototype of an improved version of the ISWEC to be tested in open-sea environment for demonstration purposes. The scaled model has been successfully deployed off the coast of Ravenna (Italy) in Adriatic Sea [53]. In view of this important achievement, a non-binding agreement has been stipulated in April 2019 between the big italian financial and industrial companies Cassa Deposito e Prestiti (CDP), Eni, Terna and Fincantieri, that seeks to combine the expertise of the companies to lead the ISWEC pilot project towards the industrial scale for immediate application and use [54].

Figure 1.13 ISWEC 1:2 prototype deployed in Adriatic Sea off the coast of Ravenna (Italy), 2018.

After more than a decade of research and development the ISWEC project is reaching a pre-commercialization phase, with a tight collaboration between academia and industry, necessary when tacking an innovative and challenging technology such as wave energy. Much effort in future must be done to optimize the device and improve the reliability and reduce the costs, in view also of all the experienced gained with the new deployment of the demonstrative prototype in Adriatic Sea.

The future of the ISWEC project is not aimed to be constrained in the Mediterranean Sea, but an other market scenario is of interest: oceans. Wave power density in oceans is much higher compared to Mediterranean Sea (see figures 1.1 and 1.10). The wave-climate of oceans is more various and complex, with the contemporary presence of local wind waves and swells generated by distant storms. Therefore, the wave resource characteristics, expressed in terms of wave period and height, are spreader and can vary significantly as a function of the installation site compared with a closed sea such the Mediterranean Sea. The ISWEC device is a pitching floating device that works in resonance conditions within a specific range of wave frequencies. Hence the need to develop a new technology solution that allows the device to tune its resonance condition with the incoming wave, and have a broader frequency response. The objective is to design a new device that is wave-climate adaptable, through the tuning of its resonance conditions. The implication is the

possibility to realize a unique site-independent technology with the advantage of designing, engineering and industrializing different device solutions as a function of the installation site.
The work of this thesis is to tackle this challenges with the development of a novel resonance-tunable device named IOwec Inertial Ocean Wave Energy Converter.

1.4 IOwec Technology

The idea of developing the IOwec technology started in 2015, from a collaboration of the Renewable Energies Group of Politecnico di Torino and the MIT i-Ship Lab directed by prof. Stefano Brizzolara (now professor at Virginia Tech (USA)). The innovative project started with the participation at the Wave Energy Prize (WEP) competition funded by the Department of Energy (DOE) of United States and the team reached the phase two with the experimental tests of the first 1:20 IOwec prototype at Stevens Institute (USA) wave tank.
The aim of the IOwec project is to develop a novel pitching floating wave energy converter based on the ISWEC technology that can enhance the performance through an environmental adaptive control system. The integration of U-tank technology into ISWEC device permits the "slow-tuning" of the device with the incoming sea-state, broadening the performance bandwidth. The proposed U-Tank technology offers significant cost reductions and technological breakthrough with respect to the current state of the art. The U-Tank system, named Pitch Resonant Tuning Tank (PRTT), can be easily integrated into the ISWEC device and also in other rocking wave energy converters, and it is expected to achieve significant improvements on current state of the art and in particular on previous ISWEC technology [55].

The purpose of this thesis work is the development of the IOwec concept, and the demonstration of the performance improvements of the device due to the integration of the U-Tank. A preliminary numerical model of the whole system is implemented in Matlab in order to predict the dynamics of the system and assess the power absorption performance. The numerical model of the U-Tank is validated with high-fidelity CFD and experimental results of a scaled model. A Numerical Design Tool is developed for the design and optimization of the IOwec device characteristics. A sea-state based control is preliminary proposed for the tuning of the U-Tank: the

dynamics characteristics of the U-Tank are varied as a function of the discrete volume of air in the two reservoirs of the U-Tank, that can be modeled as an "air spring".
A first draft of the IOwec has been proposed and studied, designed with the experience matured during these years of PhD dedicated to the design of the ISWEC 1:2 scaled model deployed in Adriatic Sea. The dynamics and performance have been evaluated in regular and irregular waves.
The last part of the thesis focuses on the multi-objective optimization of the IOwec with reference to two different possible deployment sites, one in California and the other one in Hawaii islands.

Chapter 2

IOwec modelling

In this chapter, the theoretical background of the IOwec numerical model is discussed. The early design stage of a novel device or technology solution requires a model characterized by fast computational speed and good accuracy. In this work a linear state-space model of the IOwec device is developed in order to assess the perfomance of the system. Moreover, it allows the investigation of the influence of the design parameters on the dynamics and loads of the system. A linear wave-to-PTO model is developed and its assumptions and limitations discussed. The full model of the system can split in three parts:

- Floater Hydrodynamics model.
- model of the U-tank water sloshing dynamics.
- model of the gyroscope dynamics.

2.1 Hydrodynamic Model of the floater

The modelling of the hydrodynamic interaction between waves and floater represents a fundamental element to predict the dynamics of the wave energy converter. The motion of the floater is given, by the second law of Newton, when the balance of the forces and moments acting on the floating structure is known.

The hydrodynamic loads can be calculated integrating the pressure field of the fluid on the wet surface of the structure. structure. The pressure field can be

calculated solving the equation of continuity together with the equations of Navier-Stokes, which are the basis of the Computational Fluid Dynamics (CFD). Despite these methods allow a high-fidelity prediction of the motions of the floater, the numerical solution of the problem is computationally high-demanding. Therefore, simplified theories have been developed in order to estimate the hydrodynamic loads with reduced computational time.
Boundary Element Methods (BEM) solve the wave-structure interaction problems based on the potential flow theory assumptions (incompressible, inviscid fluid and irrotational flow).The flow potential theory at the basis of BEM algorithms is well known and described in detail by several textbooks [56, 57]. BEMs are widely used among the wave energy community for the design and assessment of wave energy converters [58–60]. Moreover, these methods allow the calculation of the hydrodynamics coefficients that can be integrated in a lumped parameter wave-to-PTO model of the device [51, 25, 61, 62]. In the following chapter the flow potential theory is briefly explained as well as the derivation of the hydrodynamic coefficients that will constitute IOwec lumped parameter model.

2.1.1 Flow Potential Theory

The motion of the floater can be described by its 6 spatial degree of freedom, three translations (surge, sway and heave) and three rotations around its main axis of inertia (roll, pitch, yaw):

$$X = \begin{Bmatrix} surge \\ sway \\ heave \\ roll \\ pitch \\ yaw \end{Bmatrix} = \begin{Bmatrix} x \\ y \\ z \\ rx \\ ry \\ rz \end{Bmatrix} \tag{2.1}$$

Figure 2.1 shows the fixed global reference axes $O(X,Y,Z)$,which constitutes a right handed axis system with the x-axis coincident with the mean free surface and the z-axis pointing upwards.
For the description of floater motions, it is more convenient to use a local reference axes $o(x,y,z)$, which constitutes a right handed axis system with the origin centered

on the center of gravity of the floater, the x-axis directed forward, and the z-axis pointing upwards.

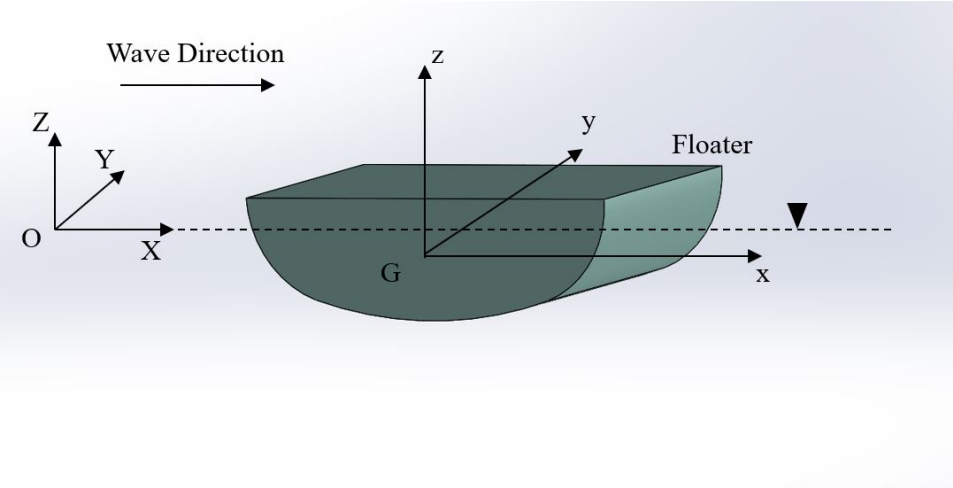

Figure 2.1 Geometrical and inertial reference system of the floater.

The flow potential theory is based on the following assumptions:

- the floating body is considered a rigid body.
- the fluid is assumed inviscid and incompressible.
- the fluid flow is assumed irrotational.
- The time-averaged speed of the body is zero.
- small steepness of the incident waves.
- small amplitude of the floater's motions .

Under these assumptions the velocity $\mathbf{v} = (u, v, w)$ field of the fluid may be expressed in terms of its *velocity potential* Φ:

$$\mathbf{v} = \left(\frac{\partial \Phi}{\partial x}, \frac{\partial \Phi}{\partial y}, \frac{\partial \Phi}{\partial z} \right) \tag{2.2}$$

Since the fluid is considered incompressible, then the fluid velocity field $\mathbf{v}$ in the domain will satisfy the *equation of continuity*:

$$\nabla\Phi = \frac{\partial u}{\partial t} + \frac{\partial v}{\partial t} + \frac{\partial w}{\partial t} = 0 \tag{2.3}$$

Substituting the velocity potential equation (2.2) in the continuity equation (Eq. (2.3) we obtain the well known *Laplace equation*:

$$\frac{\partial^2\Phi}{\partial x^2} + \frac{\partial^2\Phi}{\partial y^2} + \frac{\partial^2\Phi}{\partial z^2} = 0 \tag{2.4}$$

The Laplace equation fully described the velocity and motion of the fluid domain except for the boundaries. In order to solve the Laplace equation in the fluid domain boundary conditions must be defined (see section 2.1.1).

According the linear seakeeping theory [57, 63], the overall problem of a floating body moving in waves can be decomposed in three simpler problems:

$$\Phi = \Phi_I + \Phi_D + \Phi_R \tag{2.5}$$

in which:

- Φ_I is the velocity potential of the undisturbed incident wave.
- Φ_D is the velocity potential of the diffracted wave with restrained floater.
- Φ_R is the velocoty potential of the radiated wave of the oscillating floater in still water.

The incident wave, diffraction and radiation problems can be addressed separately. Only the solution of the incident wave problem can be solved analytically [64, 57]:

$$\Phi(x,y,z,t) = \frac{i\eta_0 g}{\omega}\frac{cosh(k(z+h))}{cosh(kh)}e^{-jk(xcos\theta+ycos\theta)}e^{-j\omega t} \tag{2.6}$$

in which:

- η_0 is the incident wave amplitude.
- i is the imaginary unit.
- ω is the incident wave frequency.

- h is the water depth.
- g is the gravity acceleration.
- k is the incident wave number.
- θ is the wave direction. If $\theta = 0$ the wave travels along the x-direction.

The other flow potentials are computed numerically through the Green's theorem which transform a volume integral into a surface integral, which is faster and much easier to handle. Besides the Laplace equation, the mathematical definition of the boundaries of the fluid domain is necessary to solve the potential flow problem.

Boundary conditions

Incident wave The analytical solutions of the incident wave potential is given in (3.1). For the sake of completeness, the boundary conditions of the incident wave potential problem are listed below:

- The **Sea bed boundary condition** involves the not permeability of the sea bed. Therefore, the vertical velocity w must be equal to zero at every instant of time t:

$$w = \frac{\partial \Phi}{\partial z} = 0, \qquad for: \ z = -h \tag{2.7}$$

- The **Free surface dynamic boundary condition** is derived assuming that the pressure p at the water free surface ($z = \eta$) is given by the Bernoulli equation and considering an arbitrary constant term can be written as:

$$p = -\rho \frac{\partial \Phi}{\partial t} - \frac{1}{2}\rho \left|\nabla \Phi\right|^2 - \rho g \eta + p_0 \tag{2.8}$$

  Where ρ is the density of the water fluid, g is the gravity acceleration and p_0 is the atmospheric pressure. In view of the assumption of small steepness the quadratic terms can be neglected and the boundary condition can be written as:

$$\frac{\partial \Phi}{\partial t} + g\eta = 0, \qquad for: \ z = 0 \tag{2.9}$$

]

- The **free surface kinematic boundary condition** involves the concept that the water waves are not braking and the water particle remains on the water surface for all the instants of time. Considering the equilibrium point $z = 0$ this boundary condition can be described by the equation:

$$\frac{\partial z}{\partial t} + \frac{\partial^2 \Phi}{\partial t^2} = 0, \qquad for: \ z = 0 \tag{2.10}$$

Diffracted wave The diffraction boundary condition can be imposed considering the wet hull surface restrained and imposing that the normal fluid velocity at every point must be equal to zero on the wet surface S_f:

$$\frac{\partial \Phi_I}{\partial n} + \frac{\partial \Phi_D}{\partial n} = 0, \qquad on: \ S_f \tag{2.11}$$

Where n is the outward normal versor of the floater surface. The wave potential due to the incident wave and the potential due to the scattered waves can be solved together and split from the radiation problem.

Radiation wave The radiation boundary conditions for the radiation problem are similar to the previous case, except for the absence of water waves. The velocity of fluid at a point of the wet surface of the hull must be equal to the velocity of the point in the hull itself. This statement can be translated mathematically in the following boundary condition valid on the wet surface S_f:

$$\frac{\partial \Phi_R}{\partial n} = v_n(x,y,z,t) = \sum_{j=1}^{6} v_j f_j(x,y,z), \qquad on: \ S_f \tag{2.12}$$

Where v_n is the normal velocity at a point of the hull surface, v_j is the oscillatory velocity of the body and f_j is the generalized direction cosine for the j-DOF.

Another boundary condition for the radiation problem states that for long distances R from the oscillating body the wave potential tends to zero:

$$\lim_{R \to \infty} \Phi_R = 0 \tag{2.13}$$

Pressures, Forces and Moments

The pressure field in the fluid domain can be determined by the *linearized Bernoulli equation* [57] and it can be generalized including the contribution of the different wave potential sources:

$$p = -\rho \frac{\partial \Phi}{\partial t} - \rho g \eta = -\rho \left(\frac{\partial \Phi_I}{\partial t} + \frac{\partial \Phi_D}{\partial t} + \frac{\partial \Phi_R}{\partial t} \right) - \rho g \eta \tag{2.14}$$

The forces $\vec{F}$ and the moments $\vec{M}$ acting on the floater can be calculated integrating the pressure p over the wetted surface S_f of the floater:

$$\vec{F} = \rho \iint_{S_f} \left(\frac{\partial \Phi_I}{\partial t} + \frac{\partial \Phi_D}{\partial t} + \frac{\partial \Phi_R}{\partial t} + g\eta \right) \vec{n} \, dS_f \tag{2.15}$$

$$\vec{M} = \rho \iint_{S_f} \left(\frac{\partial \Phi_I}{\partial t} + \frac{\partial \Phi_D}{\partial t} + \frac{\partial \Phi_R}{\partial t} + g\eta \right) (\vec{r} \times \vec{n}) \, dS_f \tag{2.16}$$

First order hydrodynamic loads

Firstly, the hydrodynamic loads due to the radiation wave field are discussed. The radiation potential Φ_R is given by the summation of Φ_j components due the harmonic oscillation of the j-th degree of freedom:

$$\Phi_R(x,y,z,t) = \sum_{j=1}^{6} \Phi_j(x,y,z,t) = \sum_{j=1}^{6} \phi_j(x,y,z) v_j(t) \tag{2.17}$$

Where the j-th radiation term $\Phi_j(x,y,z,t)$ is split in a spatial dependent component $\phi_j(x,y,z)$ and an oscillatory velocity $v_j(t)$. The boundary condition on the wet surface of the floater can be written as:

$$\frac{\partial \Phi_R}{\partial n} = \sum_{j=1}^{6} \frac{\partial \phi_j}{\partial n} v_j \tag{2.18}$$

The generalized direction cosines are given by:

$$f_j = \frac{\partial \phi_j}{\partial n} \tag{2.19}$$

The forces and moments acting on the floater are defined by a 1x6 vector of $\vec{X_{r_k}}$ components, where the index k identify the degree of freedom of the force/moment action:

$$\vec{X_{r_k}} = \rho \iint_{S_f} (\frac{\partial}{\partial t} \sum_{j=1}^{6} \phi_j v_j)\, f_k\, dS_f = \rho \iint_{S_f} (\frac{\partial}{\partial t} \sum_{j=1}^{6} \phi_j v_j)\, \frac{\partial \phi_k}{\partial n}\, dS_f \qquad for:\ k = 1,...6 \tag{2.20}$$

Since only the term v_j is time dependent, the expression can be written as:

$$X_{r_k} = \sum_{j=1}^{6} X_{r_{kj}} \qquad for:\ k = 1,...6 \tag{2.21}$$

Where $X_{r_{kj}}$ is given by:

$$X_{r_k} = \frac{dv_j}{dt} \rho \iint_{S_f} \phi_j \frac{\partial \phi_k}{\partial n} dS \tag{2.22}$$

The generic complex motion for the j-th degree of freedom may be defined:

$$s_j = s_{a_j} e^{-i\omega t} \tag{2.23}$$

Deriving this expression, the velocities and the accelerations can be obtained. The forces and moments may be split in two components: one component in phase with the acceleration and the other component in phase with the velocity:

$$\begin{aligned} X_{r_{kj}} = -M_{kj}\ddot{s_j} - B_{kj}\dot{s_j} &= (s_{a_j}\omega^2 M_{kj} + i s_{a_j}\omega B_{kj}) e^{-i\omega t} \\ &= (-s_{a_j}\omega^2 \rho \iint_{S_f} \phi_j \frac{\partial \phi_k}{\partial n} dS) e^{-i\omega t} \end{aligned} \tag{2.24}$$

The frequency dependent hydrodynamic added mass **A** and the radiation damping **B** matrices can be defined, and the generic kj component is given by:

$$A_{kj} = -\mathbb{R}e(\rho \iint_{S_f} \phi_j \frac{\partial \phi_k}{\partial n} dS) \tag{2.25}$$

$$B_{kj} = -\mathbb{I}m(\rho\omega \iint_{S_f} \phi_j \frac{\partial \phi_k}{\partial n} dS) \tag{2.26}$$

Since the IOwec device is symmetrical with respect to its longitudinal and transversal plane, some coefficients of the added mass and radiation damping matrices are zero:

$$\mathbf{A} = \begin{bmatrix} A_{11} & 0 & 0 & 0 & A_{15} & 0 \\ 0 & A_{22} & 0 & A_{24} & 0 & 0 \\ 0 & 0 & A_{33} & 0 & 0 & 0 \\ 0 & A_{42} & 0 & A_{44} & 0 & 0 \\ A_{51} & 0 & 0 & 0 & A_{55} & 0 \\ 0 & 0 & 0 & 0 & 0 & A_{66} \end{bmatrix} \tag{2.27}$$

$$\mathbf{B} = \begin{bmatrix} B_{11} & 0 & 0 & 0 & B_{15} & 0 \\ 0 & B_{22} & 0 & B_{24} & 0 & 0 \\ 0 & 0 & B_{33} & 0 & 0 & 0 \\ 0 & B_{42} & 0 & B_{44} & 0 & 0 \\ B_{51} & 0 & 0 & 0 & B_{55} & 0 \\ 0 & 0 & 0 & 0 & 0 & B_{66} \end{bmatrix} \tag{2.28}$$

Observing the structure of the added mass and radiation damping matrices, the motion of IOwec device can be solved independently for the longitudinal XZ-plane and for the transversal YZ-plane.
The wave and diffraction forces and moments, known also with the *Froude-Krylov and diffraction forces* can be calculated as:

$$\vec{F}_{exc} = \vec{F}_w + \vec{F}_d = \rho \iint_{S_f} (\frac{\partial \Phi_w}{\partial t}) + \frac{\partial \Phi_d}{\partial t})\vec{n}\, dS \tag{2.29}$$

$$\vec{M}_{exc} = \vec{F}_w + \vec{F}_d = \rho \iint_{S_f} (\frac{\partial \Phi_w}{\partial t}) + \frac{\partial \Phi_d}{\partial t})(\vec{r} \times \vec{n})\, dS \tag{2.30}$$

Solving the boundary element problem numerically with a 3D panel code like Nemoh [65] it is possible to compute the Froude-Krylov and diffraction complex coefficients for each degree of freedom. These coefficients represent the external wave excitation forces acting on the floater.

The buoyancy forces and moments can be calculated integrating the fluid static pressure over the wet surface:

$$\vec{F_s} = \rho g \iint_{S_f} z\vec{n}\, dS \tag{2.31}$$

$$\vec{M_s} = \rho g \iint_{S_f} z(\vec{r} \times \vec{n})\, dS \tag{2.32}$$

Solving the boundary element problem the 6x6 stiffness matrix **K** that multiplies can be defined:

$$\mathbf{K} = \begin{bmatrix} 0 & 0 & 0 & 0 & 0 & 0 \\ 0 & 0 & 0 & 0 & 0 & 0 \\ 0 & 0 & K_{33} & 0 & 0 & 0 \\ 0 & 0 & 0 & K_{44} & 0 & 0 \\ 0 & 0 & 0 & 0 & K_{55} & 0 \\ 0 & 0 & 0 & 0 & 0 & 0 \end{bmatrix} \tag{2.33}$$

All the hydrodynamic linear parameters of the floater are computed via boundary element method based software and in this thesis the open-source routine Nemoh has been used.

2.1.2 Frequency domain equation

The hydrodynamics of the floater is governed by the second Newton's law:

$$M\ddot{X} = F_{hydro} \tag{2.34}$$

Where **M** is the 6x6 inertial matrix of the floater, F_{hydro} the external hydrodynamic forces acting on the floater and X is the 6x1 floater degree of freedom variables. Since the IOwec floater is symmetrical both to the longitudinal xz-plane and the transversal yz-plane we have:

$$\mathbf{M} = \begin{bmatrix} \rho\nabla & 0 & 0 & 0 & 0 & 0 \\ 0 & \rho\nabla & 0 & 0 & 0 & 0 \\ 0 & 0 & \rho\nabla & 0 & 0 & 0 \\ 0 & 0 & 0 & I_{h_{xx}} & 0 & 0 \\ 0 & 0 & 0 & 0 & I_{h_{yy}} & 0 \\ 0 & 0 & 0 & 0 & 0 & I_{h_{zz}} \end{bmatrix} \tag{2.35}$$

Where ∇ is the volume displacement of the floater and $I_{h_{xx}}$, $I_{h_{yy}}$, $I_{h_{zz}}$ are respectively the moment of inertia in roll, pitch and yaw direction.
The hydrodynamic forces has been defined in the previous section and therefore Equation (2.41) can be written in case of incident planar wave with angular frequency ω and unitary wave amplitude η_0:

$$(M + A(\omega))\ddot{X} + B(\omega)\dot{X} + KX = f_{exc}\eta_0(\omega)sin(\omega t) \tag{2.36}$$

In complex form:

$$-\omega^2(M + A(\omega))X - jB(\omega)X + KX = f_{exc}(\omega)\eta_0 \tag{2.37}$$

Where f_{exc} is the 1x6 vector of complex Froude-Krylov and diffraction coefficients.

The transfer function of the motions, better known as *Response Amplitude Operator* (**RAO**) are defined as the ratio between the motion amplitudes X_0 and the wave amplitude η_0:

$$RAO = \frac{X_0}{\eta_0} = \frac{f_{exc}(\omega)}{-\omega^2(M + A(\omega)) + j\omega B(\omega) + K} \tag{2.38}$$

The RAO of describes the hydrodynamical behaviour of the floater in regular wave conditions.

2.1.3 Time domain equation

Under the assumptions of linear wave theory, small wave steepness and floater motion, the integro-differential time domain equation of the floater hydrodynamics was developed by Cummins [66]:

$$(M + A_\infty)\ddot{X}(t) + \int_0^t K_r(t-\tau)\dot{X}(t)d\tau + KX(t) = F_{exc}(t) \tag{2.39}$$

With:

- A_∞ is the added mass at infinite frequency. It represents the radiation force component in phase with floater accelerations.
- K_r is the 6x6 matrix of the *radiation impulse response functions* . The convolution of the radiation impulse with the floater velocities models the "memory effect" and the radiated wave energy due to the motion of hull. K_r is also called *Retardation Matrix*.
- $F_{exc}(t)$ is the time domain wave excitation forces acting on each degree of freedom of the hull.

Therefore, the computation of the radiation forces F_{rad} can be done solving the convolution term, with the knowledge of previous time steps:

$$F_{rad} = -A_\infty\ddot{X}(t) - \int_0^t K_r(t-\tau)\dot{X}(t)d\tau \tag{2.40}$$

The convolution term is not easy to compute numerically and in section 2.1.3 a method to substitute the convolution term with an equivalent state-space model to increse the computational speed will be discussed. Moreover, the state-space representation is well suited for numerical simulation and the development of control logics.

Relationship between time domain and frequency domain

Ogilvie [67] compared the time and frequency hydrodynamic equations to find the relations between them:

$$A(\omega) = A_\infty - \frac{1}{\omega}\int_0^\infty K(\tau)sin(\omega\tau)d\tau \tag{2.41}$$

$$B(\omega) = \frac{1}{\omega}\int_0^\infty K(\tau)cos(\omega\tau)d\tau \tag{2.42}$$

The retardation function matrix is given by:

$$K(\tau) = \frac{2}{\pi}\int_0^\infty B(\omega)cos(\omega\tau)d\omega \tag{2.43}$$

State-Space realization of the radiation convolution term

In the Cummins' time domain model the radiation forces are represented by a convolution term, which constitutes a limitation in terms of calculation time and a representation of the model for control and analysis purposes. Therefore, the convolution term may be approximated by a state-space representation:

$$F_r = \int_0^t K_r(t-\tau)\dot{X}d\tau \simeq \begin{cases} \dot{\zeta}_r = A_r\zeta_r + B_r\dot{X} \\ F_r = C_r\zeta_r + D_r\dot{X} \end{cases} \tag{2.44}$$

The state space matrices A_r, B_r, C_r and D_r can be identified in different ways in both time and frequency domain and several approaches have been proposed in the past [68–70]:

In this work, the method proposed by Fossen and Perez [71, 72] is adopted. This method uses a parametric identification of the state-space matrices in frequency domain.

2.1.4 Irregular waves and excitation forces

The linear wave theory [64] is based on the assumption of regular harmonic unidirectional waves. However, real gravity water waves generated or by local winds or by distant storms (also called *swells*), are irregular and short-crested.
According the linear wave theory [73, 74], the irregular water surface waves can be model as superposition of harmonic waves with different frequencies, phases and

directions. In this preliminary work, only unidirectional waves are considered and then all the harmonic wave components travel in the same direction:

$$\eta(x,t) = \sum_{n=1}^{N} \eta_{0,n} sin(\omega_n t - k_n x + \theta_n) \tag{2.45}$$

With:

- $\eta(x,t)$ is the planar irregular water wave profile.
- $\eta_{0,n}$ is the amplitude of the n-th harmonic wave component.
- N is the total number of harmonic wave components
- ω_n is the angular frequency of the n-th harmonic wave component.
- k_n is the wave number of the n-th harmonic wave component.
- θ_n is the phase of the n-th harmonic wave component.

The phases associated with each wave component are pseudo-random and in the range of $[0, 2\pi]$. In literature, different analytical Power Spectral Densities (PSD) functions were proposed in order to model the real measured wave spectra. In the offshore structures and wave energy converters field two wave spectra functions are widely used [57, 56]: the *JONSWAP* and *Bretshneider* functions [75–77].

The JONSWAP (Joint North Sea Wave Project) spectrum was developed using data from the North Sea for non developed wind seas. The spectral density function can be written as:

$$S\eta(\omega) = A\omega^{-5} e^{-B\omega^{-4}} \gamma^{\alpha} \tag{2.46}$$

Where γ^{α} is the peak enhancement factor. The γ value depends on the conditions of wind speed, fetch and time duration. Hasselman et al. (1973) [78] suggest:

- $A = \frac{4\pi H_s^2}{T_p^4}$
- $B = \frac{23\pi^3}{T_p^4}$

- $\alpha = e^{-\left(\frac{0.2049 T_p \omega - 1}{\sqrt{2}\sigma}\right)^2}$

where:

$$\begin{cases} 0.07 \; for \; \omega \leq \frac{4.88}{T_p} \\ 0.09 \; for \; \omega > \frac{4.88}{T_p} \end{cases} \tag{2.47}$$

The value of γ can be expressed as a function of H_s and T_p and thus as a function of the sea state conditions as discussed by Torsethaugen (2004) [79]. A common value of γ is 3.3.

The *Bretshneider* spectrum can be seen as a particular case of JONSWAP spectrum with $\gamma = 1$ and it is suggested [80] in case of no wave data available:

$$S_\eta(f) = \frac{5}{16} \frac{f_p^4}{f^5} H_s^2 e^{\frac{-5 f_p^4}{4 f^4}} \tag{2.48}$$

with:

- $S_\eta(f)$ is the Bretshneider power density spectrum (m^2/Hz).
- f is the wave frequency at which the spectrum is evaluated (Hz).
- f_p is the peak frequency of the spectrum (Hz).
- H_s is the significant wave height of the sea state (m).

The statistical parameters of the sea state can be calculated by means of the spectral moments. The general definition of spectral moments is:

$$m_n = \int_0^\infty f^n S_\eta(f) df \tag{2.49}$$

Where n defines the order of the moment. The most relevant statistical parameters of the sea state, used in this work, are:

- **Peak Period**, T_p: is the wave period with the highest energy and it can be calculated as the inverse of peak frequency f_p.

- **Energetic Period** T_e: represents the regular wave period with the equivalent energy of the sea state and it is useful in the calculation of the wave power density:

$$T_e = \frac{m_{-1}}{m_0} \tag{2.50}$$

- **Significant wave height** H_s: defined as the average of the highest one-third of the trough-to-crest heights of the wave profile:

$$H_s = 4\sqrt{m_0} \tag{2.51}$$

The *Wave Power Density* P_w can be calculated as:

$$P_w = \frac{\rho g^2}{64\pi} T_e H_s^2 \approx 0.49 T_e H_s^2 \tag{2.52}$$

Irregular wave excitation forces

According the seakeeping theory [57, 81], the wave excitation forces acting on a moored floating structure may be split into three parts:

- Mean wave drift forces.
- Low frequency drift forces.
- first-order excitation forces.

Mean and low-frequency drift forces are relevant when the station keeping of the floating moored structure is under study. Drift forces are very important when designing mooring systems but are generally neglected during the early design of a novel wave energy converter [56]. Moreover, the IOwec device will adopt the same mooring layout concept of ISWEC [9] and it is possible to assume that during operational conditions the mooring loads will not have a relevant effect on the performance of the device. The design of the mooring system requires the knowledge of the deployment site characteristics (i.e. the bathymetry) and the geometrical/inertial properties of the floater, therefore, it will be carried out in a later design stage. Since the focus of this thesis is the optimization of the IOwec device, the design of the mooring system will be done in a second design phase.

Given a wave spectra characterized by a significant wave height H_s and energetic period T_e, the pseudorandom wave $\eta(t)$ is given by the superposition of sinusoidal wave components:

$$\eta_n = \sqrt{2S_{\eta_n}\Delta\omega} \tag{2.53}$$

Where $\Delta\omega$ is the PSD frequency resolution, n is the total number of discretized spectrum frequencies, ω_i is a discrete spectrum frequency and S_{η_n} is the associated value of spectral energy density, θ_n is the associated pseudorandom phase in the range $[0, 2\pi]$, η_n is the amplitude of the sinusoidal n-th wave component. Therefore, the first order excitation forces can be calculated given the geometry of the floater and sea-state characteristics:

$$F_{exc_j}(t) = \sum_{n=1}^{N} \left| f_{FK_{j,n}} \right| \eta_n sin\left(\omega_n t + \theta_n + \angle f_{FK_{j,n}}\right) \tag{2.54}$$

Where $f_{FK_{j,n}}$ is the Froude-Krylov and diffraction coefficient associated to the j_{th} DOF and the n_{th} wave frequency.

2.2 Gyroscope Dynamics Model

The power absorption principle of IOwec is based on the gyroscopic technology of ISWEC device [49, 50]. The gyroscopic units are housed inside the hull. The dynamic coupling between the pitch motion and the spinning flywheel induces a precession motion of the gyroscope is induced. This mechanical energy can be converted in electrical energy through different Power Take Off technology. The ISWEC device extracts this mechanical energy through a mechanical gearbox and an electrical generator, but in the case of an oceanic device like IOwec, where the entities of the mechanical torques increase, the adoption of hydraulic-electrical PTO may be a more suitable solution.

2.2.1 Gyroscope Reference Frame and dynamic equations

Figure 2.2 shows the reference frames of the floater and gyroscopic system. The floater reference system $o(x,y,z)$ is coherent with the one one discussed in section 2.1.1. For the gyroscopic dynamic a new reference system $o_g(x_g,y_g,z_g)$, with the origin on the center of gravity of the flywheel is defined.

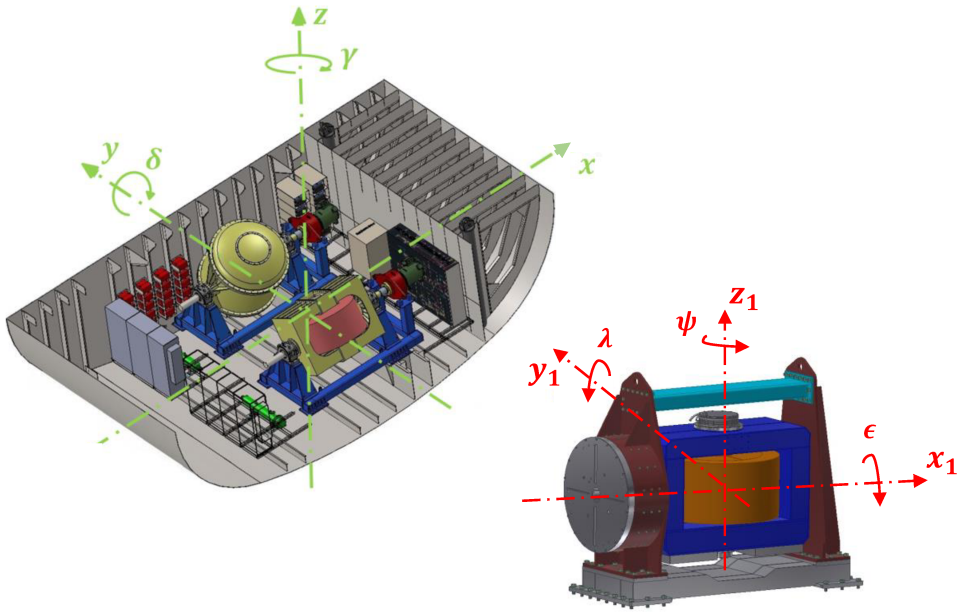

Figure 2.2 Floater and Gyroscope reference frames.

The flywheel is able to spin about its axis of symmetry ψ with a speed $\dot{\phi}$. The gyroscope system constitutes a one Degree of Freedom system, and it is restrained to oscillate only around its precession axis ε. 7 The inertia matrix of the flywheel I_{fw} and support frame I_s are:

$$I_{fw} = \begin{bmatrix} I_{fw_{xx}} & 0 & 0 \\ 0 & I_{fw_{yy}} & 0 \\ 0 & 0 & J \end{bmatrix} \tag{2.55}$$

$$I_s = \begin{bmatrix} I_{s_{xx}} & 0 & 0 \\ 0 & I_{s_{yy}} & 0 \\ 0 & 0 & I_{s_{zz}} \end{bmatrix} \tag{2.56}$$

Since the flywheel is axisymmetric about its spinning axis ψ then $I_{fw_{xx}} = I_{fw_{xx}} = I_{fw}$.

The gyroscope dynamics is governed by the Newton's law and the derivation of the simplified gyroscopic equation is out of the scope of this work and more details can be found in [82, 49]. The simplified gyroscopic torques acting on the three directions are:

$$T_\lambda = J\dot{\phi}\dot{\varepsilon} \tag{2.57}$$

$$T_\varepsilon = J\dot{\phi}\dot{\delta}cos\varepsilon \tag{2.58}$$

$$T_\psi = J\dot{\varepsilon}\dot{\delta}sin\varepsilon \tag{2.59}$$

The torques acting on the floater due to the gyroscopic dynamics can be split in the pitch δ and roll ρ components:

$$T_\delta = T_{ry} = T_\lambda cos\varepsilon \tag{2.60}$$

$$T_\rho = T_\lambda sin\varepsilon \tag{2.61}$$

The flywheel angular momentum $L = J\dot{\phi}$ determines the entity of the coupling torques T_ε and T_δ between the floater and the gyroscope. Therefore, the parameter L is fundamental during the design of the system, and it can be regulated in operational condition varying the flywheel speed $\dot{\phi}$ to be optimal to the current sea-state ("slow control strategy"). The gyroscopic torque T_ρ can induce the roll motion of the floater and degrade the performance of the device. To overcome this problem, the gyroscopic units may be suited in the floater in even numbers with opposite flywheel speed direction to cancel the roll gyroscopic torque.

Gyroscopic eccentric mass

The gyroscope dynamics has an equilibrium position for $\varepsilon = 90°$, and the torque T_ε becomes null. A stiffness component will avoid the gyroscope to remain in its equilibrium status. In the ISWEC technology this stiffness term was provided by the electrical PTO through the control torque [49]. The main advantage of this solution is the possibility to tune, through the stiffness term, the dynamics of the gyroscope with the current sea-state.This method improves the power absorption, however, it add a control parameter that complicate the control logic of the device. A drawback of such technological solution is the presence of reactive power due to the stiffness term. A passive mechanical solution is proposed to avoid this issue and simplify the PTO control logic. The stiffness component is then provided by an eccentric mass mounted on the support frame [83], as graphically explained in Figure 2.3.

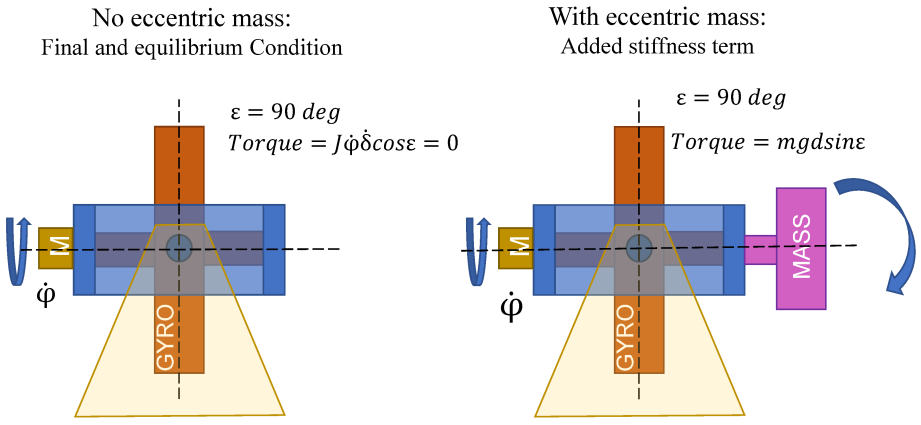

Figure 2.3 Gyroscopic stiffness term provided by an eccentric mass.

The torque due to the presence of the eccentric mass is:

$$T_{mass} = mgdsin\varepsilon \tag{2.62}$$

Where m is the eccentric mass mounted at a distance d from the gyroscope center of gravity. These parameters influence the dynamic response of the gyroscope and the power absorption and thus they will play an important role in the design phase.

Power Take Off Model

The power take off of the ISWEC device consists of a Permanent Magnet Synchronous Motor (PMSM) connected to the gyroscope frame by means of a 1:10 ratio gearbox [49]. This technological solution was well suited for low-medium energetic sea-states of the Mediterranean Sea. The aim of this thesis work is to design a device to be deployed in highest energetic sea-states and thus higher loads. Since commercial PMSMs show limitation in terms of nominal torque, the PTO technological solution may vary from that adopted for the ISWEC device. Another PTO technology for the IOwec device may be the hydraulic-electric system , where the high gyroscopic torques are managed by an hydraulic pump and circuit coupled with an electrical generator. Bonfanti et al. [84] made a preliminary numerical analysis on the control and performance of an hydraulic PTO adopting ISWEC as case study.
An advantage of the gyroscopic technology is the possibility of a modular layout and the consequent subdivision of loads among the gyroscopic units. The decision of which solution is more suitable for IOwec is not the sake of this work, and it will be evaluated after the optimization process, considering the entity of the loads involved.

The ISWEC PTO control logic [49] was based on the concept of *impedance matching* for the maximization of the power absorption, frequently used in wave energy applications [32]. The concept is to control the PTO torque to constitute a spring-damping system:

$$T_{PTO} = k\varepsilon + c\dot{\varepsilon} \tag{2.63}$$

Where k is the stiffness coefficient and c is the damping coefficient to be tuned with the current sea-state to maximize the power extraction. Since in the IOwec device the stiffness term is provided by the eccentric mass the control law of the PTO torque may be simplified:

$$T_{PTO} = c\dot{\varepsilon} \tag{2.64}$$

Bonfanti et al. [83] analysed numerically the ISWEC performance when providing the stiffness term by PTO control, and thus tuning it for each sea-state, or by a fixed

optimized eccentric mass for all the sea-state. The results show that the two solutions present the same annual productivity. The instantaneous absorbed gross power from the system P_{gross} is defined as:

$$P_{gross} = T_{PTO}\dot{\varepsilon} = c\dot{\varepsilon}^2 \tag{2.65}$$

The PTO damping coefficient c represents a control parameter that can be optimized for the considered sea-state in combination with the flywheel speed $\dot{\phi}$.

Linearization of gyroscope's dynamic equations

The frequency-domain model that describes the non-linear coupled-dynamics hull-plus-gyroscope is given below. For the sake of simplicity, only the hydrodynamic pitch DoF is considered:

$$(M_{55}+A_{55})\ddot{\delta} + A_{51}\ddot{x} + B_{55}\dot{\delta} + B_{51}\dot{x} + K\delta = F_{55_{exc}} + J\dot{\phi}\dot{\varepsilon}cos\varepsilon \tag{2.66}$$

$$I_g\ddot{\varepsilon} + c\dot{\varepsilon} + mgdsin\varepsilon = J\dot{\phi}\dot{\delta}cos\varepsilon \tag{2.67}$$

The non-linear gyroscopic and PTO model has been experimentally validated during the ISWEC full-scale testing (see Vissio 2017, [49]), and the coupled floater-plus-gyroscope non-linear model was validated with model-scale experimental tests in regular wave conditions [51] with good matching. A linear version of the system equations is necessary to build a faster model that will constitute the core of the IOwec design and optimization tool. The linearized equations of the coupled-model about the gyroscopic equilibrium position, $\varepsilon = 0$, are given below:

$$(M_{55}+A_{55})\ddot{\delta} + A_{51}\ddot{x} + B_{55}\dot{\delta} + B_{51}\dot{x} + K\delta = F_{55_{exc}} + J\dot{\phi}\dot{\varepsilon} \tag{2.68}$$

$$I_g\ddot{\varepsilon} + c\dot{\varepsilon} + mgd\varepsilon = J\dot{\phi}\dot{\delta} \tag{2.69}$$

2.2.2 Floater-plus-gyroscope 4-DoF time domain model

It has already been discussed in section 2.1.1, that the hydrodynamic problem for the IOwec device can be resolved separately respect to the *xz*-longitudinal plane and *yz*-transversal plane. Since the mooring system of the full scale device, will have a layout configuration similar to the ISWEC device, then the IOwec will align itself with the dominant sea state condition. Therefore, a 3DoF hydrodynamic model of the floater in the *xz* plane is adequate to estimate the performance of the device and it will be adopted in this thesis. The hydrodynamic 1x3 vector variables is:

$$X_h = [x,\ z,\ \delta]^T\ =\ [Surge,\ ,Heave,\ Pitch]^T \tag{2.70}$$

Including also the precession angle ε of the gyroscope we obtain a 4-DoFs model, and the vector of variables becomes:

$$X = [x,\ z,\ \delta,\ \varepsilon]^T \tag{2.71}$$

The dimension of the vector X is also named l in this work. The linear time domain model can be defined in matrix form:

$$\mathbf{M}\ddot{X}\ +\ \mathbf{B}\dot{\mathbf{X}}\ +\ \mathbf{K}X\ =\ \mathbf{F_{exc}}\ +\ \mathbf{F_r} \tag{2.72}$$

Where **M** is the 4x4 mass matrix, **B** is the 4x4 damping matrix and **K** is the 4x4 stiffness matrix:

$$\mathbf{M}\ =\ \begin{bmatrix} \rho\nabla + A_{\infty_{11}} & 0 & A_{\infty_{15}} & 0 \\ 0 & \rho\nabla + A_{\infty_{33}} & 0 & 0 \\ A_{\infty_{51}} & 0 & I_{h_{yy}} + A_{\infty_{55}} & 0 \\ 0 & 0 & 0 & I_g \end{bmatrix} \tag{2.73}$$

$$\mathbf{B}\ =\ \begin{bmatrix} 0 & 0 & 0 & 0 \\ 0 & 0 & 0 & 0 \\ 0 & 0 & 0 & -J\dot{\phi} \\ 0 & 0 & J\dot{\phi} & c \end{bmatrix} \tag{2.74}$$

$$\mathbf{K} = \begin{bmatrix} K_{h_{11}} & 0 & 0 & 0 \\ 0 & K_{h_{33}} & 0 & 0 \\ 0 & 0 & K_{h_{55}} & 0 \\ 0 & 0 & 0 & mgd \end{bmatrix} \tag{2.75}$$

$\mathbf{F_{exc}}$ are the hydrodynamic excitation forces acting on surge, heave and pitch DoF and $\mathbf{F_r}$ are the radiation forces calculated through the state-space approximation (see eq. (2.44)). In this work, the radiation state-space variables vector ζ_r is defined as:

$$\zeta_r = [\zeta 11_{n_1 \times 1}, \zeta 15_{n_3 \times 1}, \zeta 33_{n_4 \times 1}, \zeta 51_{n_5 \times 1}, \zeta 55_{n_6 \times 1}]^T \tag{2.76}$$

Where n_i is the order of the state-space model that best fits the convolution radiation term. The total dimension m of the ζ_r vector and of the is given by the sum of the single orders. The same can be said for the state-space matrices A_{ss} and B_{ss} and C_{ss}. Hence, the state-space model of the device can be derived. The state-space variable is defined as:

$$X_{sys} = [\dot{X},\ X,\ \ \zeta_r]^T \tag{2.77}$$

The dimension of the state-space vector X_{sys} is $2l + m$. The state-space matrices $A_{sys}, B_{sys}, C_{sys}$ are given by:

$$A_{sys} = \begin{bmatrix} [-M^{-1}K]_{(l,l)} & [-M^{-1}B]_{(l,l)} & [-M^{-1}C_r]_{(l,m)} \\ I_{(l,l)} & 0_{(l,l)} & 0_{(l,m)} \\ B_{r_{(m,l)}} & 0_{(m,l)} & A_{r_{(m,l)}} \end{bmatrix} \tag{2.78}$$

$$B_{sys} = \begin{bmatrix} [-M^{-1}I]_{(l,l)} \\ 0_{(l+m,l)} \end{bmatrix} \tag{2.79}$$

$$C_{sys} = I_{2l+m,2l+m} \tag{2.80}$$

Where the matrices that approximate the state forces A_r and B_r have dimension (m,l), with zero values for the *m-th* degree of freedom corresponding to the ε gyroscope precession angle. The feed-forward matrix D_{sys} is equal to zero. The input

matrix B_{sys} multiplies the excitation forces F_{exc} calculated for the three hydrodynamical degree of freedom. The linear lumped parameter model of floater and gyroscope can be written in state-space representation:

$$\begin{cases} \dot{X}_{sys} = A_{sys}X_{sys} + B_{sys}F_{exc} \\ Y_{sys} = C_{sys}X_{sys} \end{cases} \tag{2.81}$$

The response of the system and the performances of the device can be easily calculated numerically in Matlab environment.

2.3 U-Tank Dynamics Model

In this section the derivation of the U-Tank model and its coupling with the floater model is discussed. In literature different models have been proposed to describe the dynamics of the U-tank. Froude [37] initially considered the effect of water tanks by adding a stabilizing moment term in the roll dynamic equation of the vessel. But he did not develop a model to predict the motion of the water inside the tank. Stigter [85] developed a theory for U-tube passive tanks based on the integration of the Euler's equation. Moreover, he carried out experimental tests on a U-Tank model scale to validate the model with good matching between the results. In 1989 Lloyd [86] proposed a simplified linear version of the Stigter's model. These two U-Tank models have been widely used for the design and performance assessment of U-Tank both in naval field [6, 87] and wave energy applications [44, 42].
Non-linear models of U-tank dynamics have been proposed in the past years [34, 88, 89]. Holden et al. [89] developed a non-linear model of the U-Tank based on the Lagrangian approach. They conducted model experimental tests and compared the results with the non-linear model and its linearized version. The non-linear model show good agreement with the experimental results, even with large motion amplitudes.
In this work the Lloyd's linear model has been adopted to predict the U-Tank dynamics and its coupling with the floater hydrodynamic model to be integrated in the IOwec linear model. Therefore, the full-coupled model floater-Utank-gyroscope is linear with consequent high computational speed.

2.3.1 Reference system and dynamic equations

The reference system of the U-tank with the description of all the geometrical properties is shown in Figure 2.4.

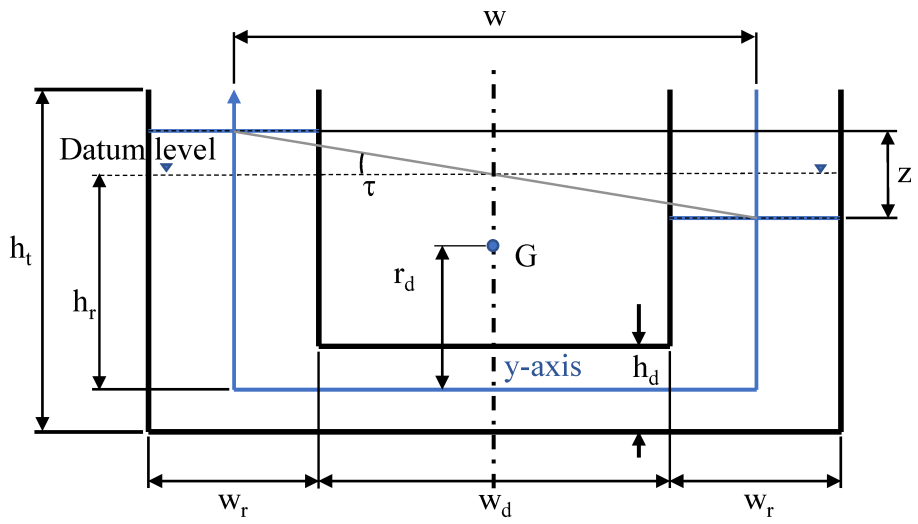

Figure 2.4 U-Tank reference system.

The tank is assumed to consist of two rectangular reservoirs connected by a central duct. The left reservoir is located on the bow of the device, and the right reservoir on the stern. The U-tank is considered to be an extrusion (in the port/starboard direction) with a breadth x_t.
The water flow inside the U-tank can be described by the Euler equation:

$$\frac{dv}{dt} = Y - \frac{1}{\rho}\frac{dP}{dy} \tag{2.82}$$

Where v and P are respectively the fluid velocity and pressure along the $y-axis$, and with Y are denoted all the external forces acting on the fluid. The main assumptions can be resumed as follows:

- The motion of the liquid inside the U-Tank is one-dimensional.
- only the coupling of the U-Tank with the pitch DoF of the floater is considered.

- The system response is linear.
- Absence of velocity gradient perpendicularly to the $y-axis$.

The velocity can be expressed as a function of the angle between the water level of the two reservoirs:

$$v = \frac{d}{dt}\left(\frac{z}{2}\right) = \frac{w}{2}\dot{\tau} \tag{2.83}$$

Where τ is considered to be small. Considering the continuity equation the velocity v at any point of the tank is given by the following equation:

$$v = \frac{w_r w}{2n}\dot{\tau} \tag{2.84}$$

Where n is the U-Tank width in the perpendicular direction of $y-axis$

The external forces per unit mass Y are due to different contributions:

- accelerations applied to the tank due to the floater motion
- gravity forces
- frictional forces due mainly to distributed and localized losses (change of geometry shape,tank corners,water free surface)

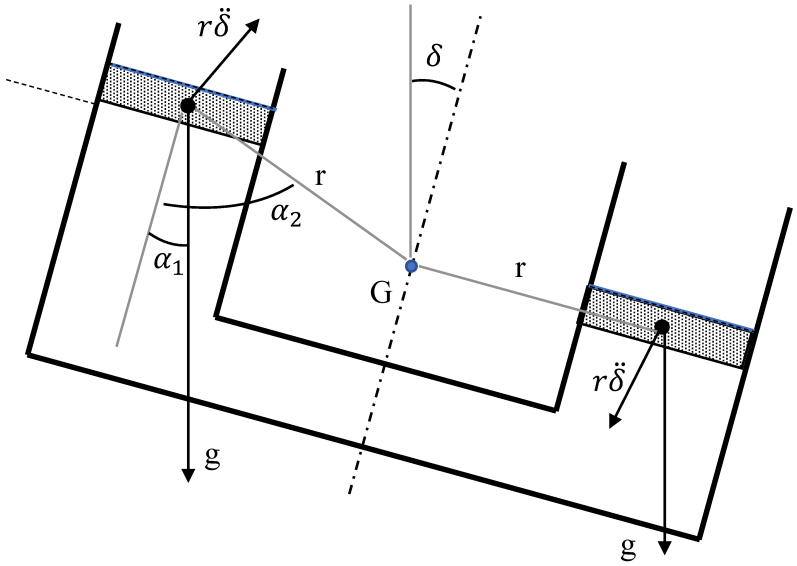

Figure 2.5 Acceleration forces acting on the U-tank.

With reference to Figure 2.5 the external force component per unit of mass due to the gravity acceleration is:

$$Y_g = -gcos\alpha_1 \tag{2.85}$$

and the force component due to flaoter's pitch acceleration $\ddot{\delta}$ is:

$$Y_\delta = -r\ddot{\delta}sin\alpha_2 \tag{2.86}$$

Despite the hydraulic losses are generally considered to be proportional to the square of local velocity, LLoyd [86] proposes a linear damping term to be used in his model:

$$Y_d = -\frac{qv}{n} \tag{2.87}$$

Where q is a coefficient of resistance to be evaluated experimentally or through a CFD analysis.

Equation (2.82) becomes:

$$\frac{w_r w\ddot{\tau}}{2n} + \frac{q w_r w\dot{\tau}}{2n^2} + gcos\alpha_1 + r\ddot{\delta}sin\alpha_2 = -\frac{1}{\rho}\frac{dP}{Dy} \tag{2.88}$$

Integrating Equation (2.82) along the y-axis between the datum level of the two reservoirs we obtain:

$$\frac{\rho w_r w I_1 \ddot{\tau}}{2} + \frac{\rho q w_r w I_2 \dot{\tau}}{2} + \rho g I_3 + \rho \ddot{\delta} I_4 = P_{stern} - P_{bow} \tag{2.89}$$

Where:

$$I_1 = \int_{tank} \frac{dy}{n} = \frac{w}{h_d} + \frac{2h_r}{w_r} \tag{2.90}$$

$$I_2 = \int_{tank} \frac{dy}{n^2} = \frac{w}{h_d^2} + \frac{2h_r}{w_r^2} \tag{2.91}$$

$$I_3 = \int_{tank} cos\alpha_1 dy = w\delta \tag{2.92}$$

$$I_4 = \int_{tank} rsin\alpha_2 dy = w(r_d + h_r) \tag{2.93}$$

The hydrostatic pressures difference between the two reservoirs is:

$$P_{stern} - P_{bow} = -\rho g w \tau \tag{2.94}$$

Combining all the derived equations above, equation (2.89) may be multiplied by the moment of the area of the two reservoirs M_r:

$$Q_r = \frac{w w_r x_t}{2} \tag{2.95}$$

to obtain the motion of the fluid as a function of the moment applied to the tank. Hence, equation (2.89) can be written in a more clear form:

$$a_{\tau\tau}\ddot{\tau} + b_{\tau\tau}\dot{\tau} + c_{\tau\tau}\tau = -[a_{\tau 5}\ddot{\delta} + c_{\tau 5}\delta] \tag{2.96}$$

With:

- $a_{\tau\tau} = Q_t w_r \left(\frac{w}{2h_d} + \frac{h_r}{w_r}\right)$
- $b_{\tau\tau} = Q_t q w_r \left(\frac{w}{2h_d^2} + \frac{h_r}{w_r^2}\right)$
- $c_{\tau\tau} = Q_t g$
- $a_{\tau 5} = Q_t \left(r_d + h_r\right)$
- $c_{\tau 5} = Q_t g$

Where:

$$Q_t = \frac{\rho w_r w^2 x_t}{2} \tag{2.97}$$

It represents a 1-DoF lumped parameter model of the second order, dynamically coupled with the pitch acceleration and oscillation of the floater. The torque due to the U-tank water motion acting on the floater pitch DoF is:

$$a_{5\tau}\ddot{\tau} + c_{5\tau}\tau \tag{2.98}$$

Where the dynamic coupling coefficients $a_{5\tau}$, $c_{5\tau}$ are respectively equal to $a_{\tau\delta}$ and $c_{\tau\delta}$.

The transfer function of the U-tank angle τ, with the input oscillation δ is given:

$$\frac{\tau(\omega)}{\delta(\omega)} = \frac{-a_{\tau 5}\omega^2 + c_{\tau 5}}{-a_{\tau\tau}\omega^2 + j\omega b_{\tau\tau} + c_{\tau\tau}} \tag{2.99}$$

For what concern the transfer function of the U-tank torque M_{U-tank}, we obtain:

$$\frac{M_{U-tank}(\omega)}{\delta(\omega)} = \frac{(-a_{\tau\delta}\omega^2 + c_{\tau\delta})^2}{-a_{\tau\tau}\omega^2 + j\omega b_{\tau\tau} + c_{\tau\tau}} \tag{2.100}$$

Both transfer functions present two coincident poles, and two coincident zeros. The resonance frequency of the water motion inside the U-tank is function of the geometrical properties:

$$\omega_{res} = \sqrt{\frac{c_{\tau\tau}}{a_{\tau\tau}}} = \sqrt{\frac{2gh_d}{w_r w + 2h_r h_d}} \tag{2.101}$$

The non dimensional tank linear damping ζ that can be estimated through free decay analysis, is given by:

$$\zeta = \frac{b_{\tau\tau}}{2\sqrt{c_{\tau\tau}a_{\tau\tau}}} \tag{2.102}$$

Proposed modifications of the U-Tank LLoyd's equation

In this section, two modification of the Lloyd's formulation are proposed in order to improve the linear model. The first one involves the integration (2.90) whose result becomes part of the mass term coefficient $a_{\tau\tau}$, that play an important role in the U-Tank dynamics. In fact, the integration is carried out only on the reservoirs line and central duct, neglecting any corner effect, that is relevant especially when in presence of high shape ratios between the reservoir and the central duct.

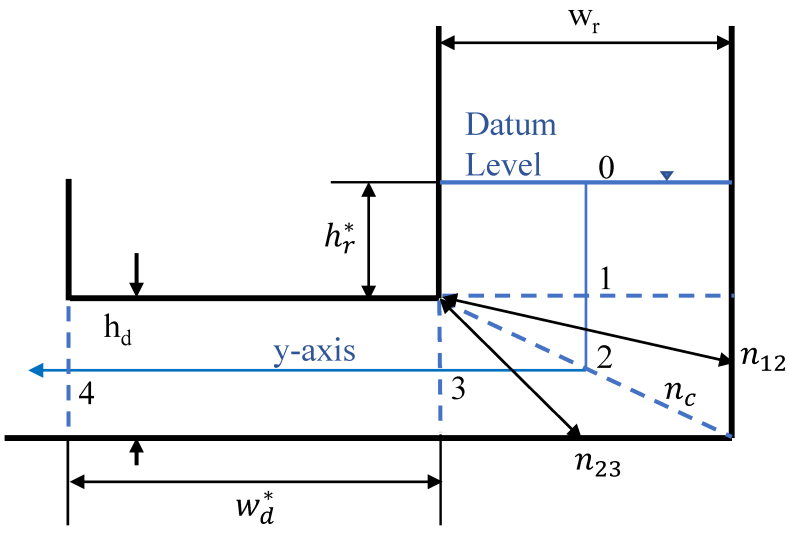

Figure 2.6 Scheme of the U-Tank with the integration intervals.

With reference to Figure 2.6 the integral I_1 of equation (2.96) becomes:

$$I_1 = \int_{tank} \frac{dy}{n} = 2\int_0^1 \frac{dy}{w_r} + 2\left(\int_1^2 \frac{dy}{n_{12}} + \int_2^3 \frac{dy}{n_{23}}\right) + \int_3^4 \frac{dy}{h_d} = \\ = \left(\frac{w_d^*}{h_d} + \frac{2h_r^*}{w_r}\right) + \left(\frac{h_d}{n_{12}} + \frac{w_r}{n_{23}}\right) \tag{2.103}$$

Where n_{12} is the average between the reservoir width w_r and the length n_c at the U-Tank corner, and n_{23} is the average between n_c and the central duct height h_d.

In this work, the expression of the damping coefficient $b_{\tau\tau}$ defined by Lloyd as a function of the geometry and a friction coefficient q will not be used. The evaluation of the damping coefficient will be done through a CFD free decay analysis and discussed in chapter 3. The damping torque T_{damp} is modeled with a linear and quadratic term, function of the U-Tank angle velocity $\dot{\tau}$:

$$T_{damp} = -b_L\dot{\tau} - b_{NL}\dot{\tau}|\dot{\tau}| \tag{2.104}$$

Where β_L is the linear damping coefficient and β_{NL} is the quadratic damping coefficient. The damping coefficients can be determined with free decay test conducted experimentally or through a CFD simulation.
The non linear damping term can be linearized to develop the linear state-space model of the U-Tank:

$$-b_L\dot{\tau} - b_{NL}\dot{\tau}|\dot{\tau}| \approx -b_{\tau\tau}\dot{\tau} \tag{2.105}$$

The quadratic term is linearized about an angle τ_0 (considered to be 5 deg in this thesis):

$$b_{\tau\tau} = b_L + b_{NL}\omega_{res}\tau_0 \tag{2.106}$$

2.3.2 IOwec Time Domain Model

In this section the model of the IOwec device, that consider the coupled dynamics of the three fundamental system floater, gyroscope and U-Tank is discussed. In section

2.2.2, the time domain model of the floater coupled with the gyroscope was derived. In order to include the U-Tank dynamics is necessary to augment the variables vector X with the inclusion of the U-tank water surface angle τ:

$$X = [x,\ z,\ \delta,\ \varepsilon,\ \tau]^T \tag{2.107}$$

Therefore, the dynamics of the IOwec device is described by five variables. For the sake of coherence, the dimension of the variables vector X is still named l and equation (2.72) is still valid. Moreover, the mass matrix **M**, the damping matrix **B** and the stiffness matrix **K** are augmented with dimension 5x5 and include the U-Tank dynamic equation presented in equation (2.96) and the coupling terms with the floater pitch dynamics:

$$\mathbf{M} = \begin{bmatrix} \rho\nabla + A_{\infty_{11}} & 0 & A_{\infty_{15}} & 0 & 0 \\ 0 & \rho\nabla + A_{\infty_{33}} & 0 & 0 & 0 \\ A_{\infty_{51}} & 0 & I_{h_{yy}} + A_{\infty_{55}} & 0 & -a_{5\tau} \\ 0 & 0 & 0 & I_g & 0 \\ 0 & 0 & a_{\tau 5} & 0 & a_{\tau\tau} \end{bmatrix} \tag{2.108}$$

$$\mathbf{B} = \begin{bmatrix} 0 & 0 & 0 & 0 & 0 \\ 0 & 0 & 0 & 0 & 0 \\ 0 & 0 & 0 & -J\dot{\phi} & 0 \\ 0 & 0 & J\dot{\phi} & c & 0 \\ 0 & 0 & 0 & 0 & b_{\tau\tau} \end{bmatrix} \tag{2.109}$$

$$\mathbf{K} = \begin{bmatrix} K_{h_{11}} & 0 & 0 & 0 & 0 \\ 0 & K_{h_{33}} & 0 & 0 & 0 \\ 0 & 0 & K_{h_{55}} & 0 & -c_{5\tau} \\ 0 & 0 & 0 & mgd & 0 \\ 0 & 0 & c_{\tau 5} & 0 & c_{\tau\tau} \end{bmatrix} \tag{2.110}$$

the state space representation of the IOwec device with the integration of the U-Tank system can be derived with the same procedure presented in section 2.2.2 (Equation (2.78)) where the dimension l is 5. The numerical implementation of the state space model of the device allows the assessment of the IOwec dynamics and performance, and it constitutes the core of the design tool of the system .

Chapter 3

Validation of the U-Tank lumped parameter model

In section 2.3.1 the derivation of the lumped parameter model of the water sloshing phenomena inside a U-shaped tank was presented and discussed. As stated before, the hydrodynamic model of the ISWEC device, the gyroscopic system were validated against scaled experimental results with good agreements also for the coupled system [51]. Therefore, the validation of the U-Tank model used in this workis necessary to investigate the fidelity and the limits of such linear model.
The sloshing phenomenon inside the U-Tank involves viscous effects and the existence of areas of stagnation where the fluid is not involved in the sloshing motion. A 3D unsteady RANSE (Reynolds-averaged Navier–Stokes equation) solver has been used in this work to perform a free decay test on the water sloshing dynamics of the U-Tank for a scale model in order to identify the linear and viscous damping coefficients. Successively, a regular test analysis is carried out and the results are compared with the analytical linear model of the U-Tank described by its transfer function (see Equation (2.99)). The dynamic response of U-Tank is also evaluated in irregular test analysis and the comparison between the linear and fully-non linear models has been discussed and presented. An experimental campaign test was carried out at Politecnico di Torino in order to validate the CFD model in regular wave. Once the CFD results are validated against the experimental results, the RANSE numerical tool can be used with high fidelity to evaluate the performance of full scale U-Tank models with different geometries, that is impossible to carry out through experimental investigations.

3.1 U-Tank scaled model description

In order to compare the experimental, CFD and linear model results is necessary to use the same parameters for all the simulations. Therefore, a U-Tank prototype was designed for small scale tests in order to conduct an experimental campaign in the laboratory of Politecnico di Torino and it will be described in detail later in this chapter.
The scaled prototype is consistent with the U-Tank linear model formulation except for the inner and external fillets on the U-Tank corners. In fact, in order to avoid as much as possible sources of non-linear viscous damping due to flow separation and minimize vortices and stagnation, which are not considered in Lloyd's numerical model, it is necessary to avoid right angles at duct elbows and strong variations in the geometry shape. Figure 3.1 shows the U-Tank prototype with all the geometrical parameters, and their values are listed in table 3.1.

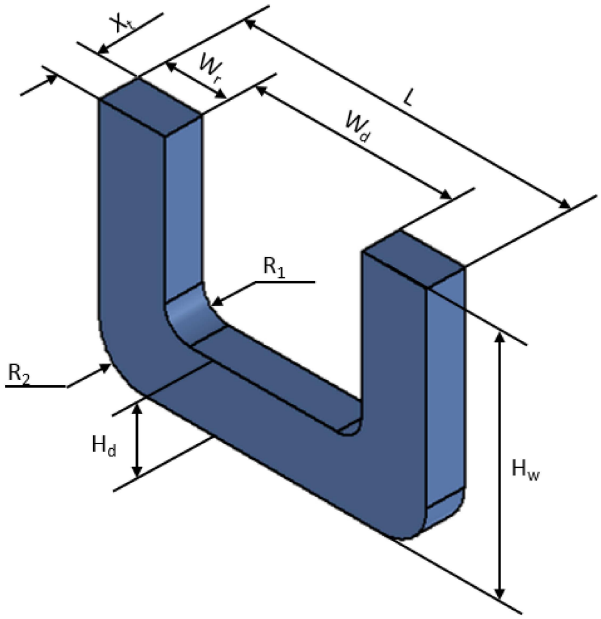

Figure 3.1 U-Tank scaled prototype.

Table 3.1 Geometrical properties of the U-Tank prototype.

Property	Symbol	Units	Value
U-Tank width	X_t	*mm*	100
Duct height	H_d	*mm*	170
Duct length	W_d	*mm*	514
Reservoir length	W_r	*mm*	170
Reservoir distance	W	*mm*	684
Total U-Tank height	H_t	*mm*	610
Total U-Tank length	L	*mm*	854
Mean water level from bottom	H_w	*mm*	320
Datum level (LLoyd Ref)	H_r	*mm*	235
COG distance from duct centerline	r_D	*mm*	63
Inner fillet radius	R_1	*mm*	65
External fillet radius	R_1	*mm*	115

3.2 Fully viscous CFD approach

With the increase of computational power more studies are carried out about the flow inside U-tube tank. Zhong et al. (1999) [90] performed CFD 2D simulation with Finite Element method in which the Navier Stokes equation are solved using Galerkin scheme. Van Daalen et al. (2000) [91] studied the performance of U-Tank by mean fully 3D CFD numerical simulations validated through experimental results . Taskar et al (2014) [92] proposed a method to estimate the damping coefficient from curve regression of a free decay test in 2D and 3D numerical simulation and stated that the damping is quadratic with the velocity and most of the head losses are due to the bends of U-tube. Moreover, in his work Taskar demonstrates that not all the mass of fluid is involved in the sloshing motion, and a correction of the mass term of the linear model is necessary.
Kerkvliet et al (2014) [93] tested and validated a new CFD code ReFRESCO with experimental results and demonstrate the effectiveness of CFD code to calculate the roll damping of a U shaped ART. Here the fluid motion inside the U-tube is investigated through 3D numerical simulation with Volume of Fluid method. First the model is validated with the experimental results with particular attention on resonance condition. The grid sensitivity and time resolution effect are investigated.

3.2.1 Numerical Model

The CFD solver used in this thesis is the commercial software STAR-CCM+. The CFD code can solve unsteady incompressible multi-phase flows described by the Reynolds Average Navier Stokes Equation (RANSE) which implements different turbulent models.
The fully viscous dynamics of the water sloshing inside the U-Tanks can be described in conservative form by the Navier Stokes equations that represent the conservation of mass and momentum here reported in their integral form:

$$\frac{\partial}{\partial t}\int_V \rho dV + \int_A \rho \mathbf{v} \cdot d\mathbf{a} = 0 \tag{3.1}$$

$$\frac{\partial}{\partial t}\int_V \rho \mathbf{v} dV + \int_A (\rho \mathbf{v} \otimes \mathbf{v}) \cdot d\mathbf{a} = -\int_A p\mathbf{I} \cdot d\mathbf{a} + \int_S \mathbf{T} \cdot d\mathbf{a} + \int_V \rho \mathbf{g} dV \tag{3.2}$$

With:

- $\mathbf{v}$ is the velocity field.
- p is the pressure field.
- ρ is the density of the fluid.
- $\mathbf{g}$ is the gravity field.
- $\mathbf{T}$ is the viscous stress tensor.

The U-Tank physical domain presents two phases: the water liquid inside the tank and the air in contact with the water in the two reservoirs, both assumed to be incompressible. The VOF (Volume of Fraction) method is used by STAR-CCM+ to manage the multi-phase problem. The VOF is a numerical method that allows the tracking and location of the free surface between the two phases that not requires re-meshing and it is numerically robust and it is commonly used in the resolution of multi-phase problems.

Volume of Fluid Method

The interface between the two phases is captured with an Interface capturing method developed by Muzaferija and Peric (1998) [94] that can be classified as an Eulerian Multiphase method, in which the shape of the interface is determined by the volume of fraction of the primary phase (water in this case). In each cell the volume of of fraction of all phases must be:

$$\sum_{i=1}^{N} \alpha_i = 1$$

Where N is the total number of phases. And:

- $\alpha_i = 0 \implies$ the cell is completely void of phase i.
- $\alpha_i = 1 \implies$ the cell is completely filled with phase i.
- $0 < \alpha_i < 1 \implies$ an interface between the two phases is present inside the cell.

And the material properties of the fluid contained in the cells are defined as:

$$\rho = \sum_{i=1}^{N} \rho_i \alpha_i \qquad \mu = \sum_{i=1}^{N} \mu_i \alpha_i \qquad C_p = \sum_{i=1}^{N} \frac{(C_p)_i \rho_i}{\rho} \alpha_i$$

Where ρ_i is the density, μ_i is the dynamic viscosity and $(C_p)_i$ is the specific heat. The transport equation for the phase i is:

$$\frac{\partial}{\partial t} \int_V \alpha_i dV + \int_A \alpha_i \mathbf{v} \cdot d\mathbf{a} = -\frac{\alpha_i}{\rho_i} \frac{\mathrm{D}\alpha_i}{\mathrm{D}t} \tag{3.3}$$

Muzafreija and Peric [94] developed an High Resolution Interface Capturing scheme (HRIC) to solve this equation and avoid a smeared interface or artificial mixing of the two fluids.

Turbulence Modelling

In nature most of the flow are turbulent, the fluid motion is chaotic and all properties of it change chaotically nevertheless a statistically mean flow could be found. There are various method to keep in account the turbulent motion:

- DNS (Direct Numerical Simulation).

- LES (Large Eddy Simulation).
- RANS (Reynolds Averaged Navier-Stokes).
- DES (Detached Eddy Simulation).

Currently the RANS models are the most used in industry application because of their low computational cost compared to other methods. RANS method is based upon the Reynolds decomposition: each instantaneous quantity of the fluid motion in its time averaged quantity and its fluctuating quantity:

$$\phi = \bar{\phi} + \phi'$$

Where $\bar{\phi}$ indicate the time averaged quantity. The two governing equation (3.1) and (3.2) become:

$$\frac{\partial}{\partial t}\int_V \rho dV + \int_A \rho \bar{\mathbf{v}} \cdot d\mathbf{da} = 0 \tag{3.4}$$

$$\frac{\partial}{\partial t}\int_V \rho \bar{\mathbf{v}} dV + \int_A (\rho \bar{\mathbf{v}} \otimes \bar{\mathbf{v}}) \cdot d\mathbf{a} = -\int_A \bar{p}\mathbf{I} \cdot d\mathbf{a} + \int_S \bar{\mathbf{T}} \cdot d\mathbf{a} + \int_V \rho \mathbf{g} dV \tag{3.5}$$

Where $\mathbf{T_{RANS}} = -\rho\overline{u_i' u_j'}$ is the Reynolds stress tensor that is momentum fluxes of the fluctuating velocities. According to how the Reynolds stress tensor is modeled various methods have been developed. Here the *Realizable k-ε* is used.

The closure of the set of equations is obtained by mean of the introdution of two integral quantities:

- k the turbulent kinetic energy.
- ε the turbulent dissition rate.

Two transport equation in differential form are introduced for each:

$$\frac{\partial(\rho k)}{\partial t} + \nabla \cdot (\rho k \mathbf{v}) = \nabla \cdot \left[\left(\mu + \frac{\mu_t}{\sigma_k}\right) \nabla k \right] + P_k - \rho(\varepsilon - \varepsilon_0) + S_k \tag{3.6}$$

$$\frac{\partial \varepsilon}{\partial t} + \frac{U_j \partial \varepsilon}{\partial j} = -\frac{\partial(\bar{u_j}\varepsilon)}{\partial j} + C_1 S\varepsilon - C2\frac{\varepsilon^2}{k + \sqrt{nu\varepsilon}} \tag{3.7}$$

For further details see the Star-CCM+ User Guide [95].

Wall treatment

A turbulent boundary layer is much different by a laminar boundary layer: the motion of the particles is chaotic and the total boundary layer thickness (δ) increase but the mean velocity can be still considered parallel to the wall. In the former one the wall shear stress τ_w is greater than in the latter one as shown in figure. The turbulent boundary layer can be described by mean of non dimensional parameter:

- $y^+ = \frac{yu_\tau}{\nu}$
- $u^+ = \frac{u}{u_\tau}$

Where:

- y is the distance from the wall.
- ν is the cinematic viscosity of the fluid.
- u is the velocity of the fluid particles inside the boundary layer.
- $u_\tau = \sqrt{\frac{\tau_w}{\rho}}$ is the friction velocity.
- ρ is the density of the fluid.
- τ_w is the wall shear stress at location $y = 0$ (at the wall).

It is possible to divide the entire boundary layer in two major zones:

- Outer Region (or Wake Region) y/δ >0.2 (δ here is the boundary layer thickness).
- Inner Region y/δ <0.2.

Within the Inner Region the relationship between u^+ and y^+ is defined by the *law of the wall*:

$$u^+ = f_w(y^+)$$

The inner region can be divided in three small regions:

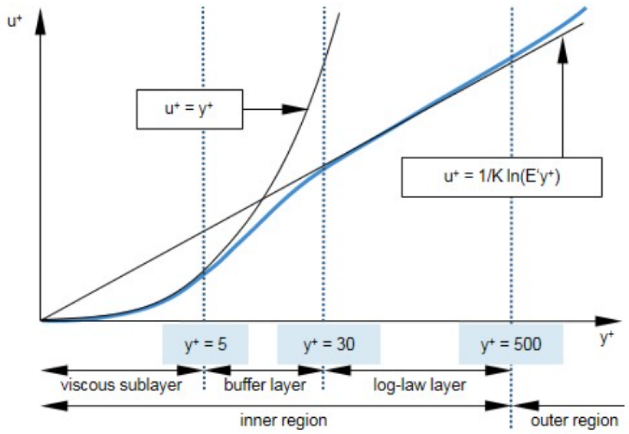

Figure 3.2 Near wall regions and wall law validity.

- Viscous sublayer ($y^+ < 5$): the viscous stress dominate above the Reynolds shear stress and the law of the wall is linear:

$$u^+ = y^+$$

- Logarithmic Layer ($30 < y^+ < 500$):the Reynolds shear stress dominate and the law of the wall is logarithmic, hence in literature is usually called the *log law* :

$$u^+ = \frac{1}{k} \ln y^+ + C$$

  Where $k = 0.41$ is the von Karman constant and $C = 5$.

- Buffer Layer ($5 < y^+ < 30$): it is a transition region between the viscous sublayer and the log law layer. Here the law of the wall is a blended function of the previous two. In figure 3.2 a schematic representation is shown.

Here the *All y+ wall treatment* is implemented in which the solver compute the exact distance between the wall and the nearest cell centre to decide which *law* has to be used.

Temporal discretization method

Consider the generic trasport equation of the quantity ϕ:

$$\frac{\partial \phi}{\partial t} = f(\phi)$$

Integrating both sides of the equation in time between time step n and time step $n+1$:

$$\phi^{n+1} - \phi^n = \int_{t_n}^{t_{n+1}} f(\phi)$$

To evaluate the integral on the right hand side some approximation are needed since it can not be usually solved analytically. If it is estimated using the value of the integrand at the initial point the explicit Euler method is obtained:

$$\phi^{n+1} = \phi^n + f(\phi^n) \cdot \Delta t$$

If the integral is estimated using the value of the integrand at final point then the implicit Euler method is obtained:

$$\phi^{n+1} = \phi^n + f(\phi^{n+1}) \cdot \Delta t$$

The implicit Euler method as described above is first order accuracy in time and needs nested iterations (inner and outer). The first order is numerical diffusive because of its first order truncation error. Here the time discretization of the variables is by mean of the implicit Euler 1° order. Following the best practice of Star-CCM+ User Guide [95] to avoid smeared interface due to numerical diffusion the time step is chosen such as:

- Average Courant number < 0.5.
- Maximum Courant number $=< 1$.

Spatial discretization method

According to the finite volumes approach, the entire domain is discretized in small volumes and the conservation of the mass and of the momentum are enforced on each cell.

The convective fluxes are discretized with a 2° order Upwind interpolation. The diffusive fluxes at the cell's face are evaluated by mean of linear interpolation of cells center values. Thus, the second order accuracy is achieved for both convective and diffusive fluxes.

3.2.2 CFD Setup

The same U-Tank geometry of the experimental setup has been replied in CFD environment with the same geometrical properties given in Table 3.1. Figure 3.3 shows the Volume of Fluid of the CFD model in rest conditions.

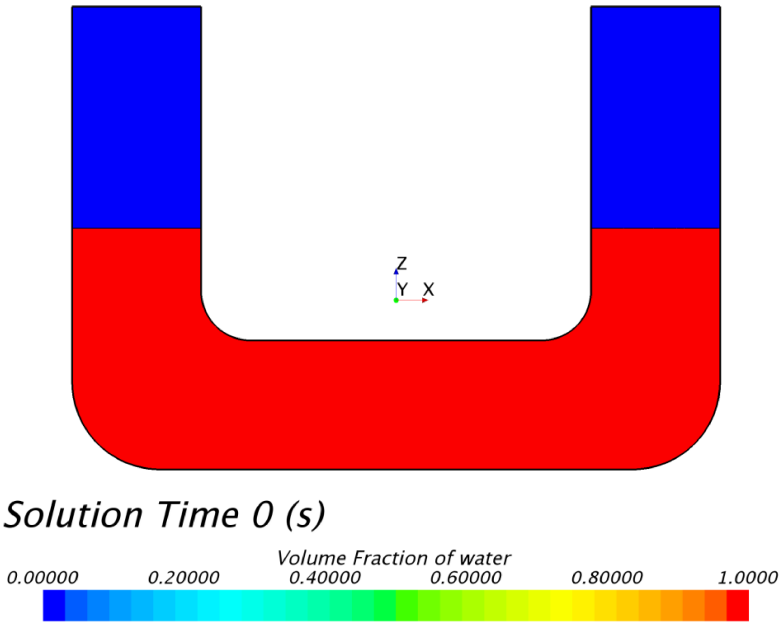

Figure 3.3 VOF of the U-Tank domain in rest conditions.

With reference to Figure 3.4 the boundary conditions are:

- Stagnation inlet at the top of each reservoir:
  - The static pressure is evaluated by mean of Bernoulli equation and the total pressure is set to $P_0 = 101325\ Pa$.
  - The velocity magnitude is extrapolated by the interior domain and the direction is normal to the boundary: $\mathbf{v} = |\mathbf{v}^{ext} \cdot \mathbf{n}|$ with $textbfn$ the inward-pointing normal vector to the surface.

- Symmetry plane on the U-Tank symmetrical plane $Z-X$:
  - No fluxes through the surface: $\frac{\partial}{\partial \mathbf{n}} = 0$ with $textbfn$ normal vector to the surface.
- No slip walls in correspondence to the physical walls of the U-Tank:
  - No relative velocity with respect to the wall: $\mathbf{V_B} = 0$.

The datum level of the water in the two reservoir is $H_w = 320\,mm$ calculated from the bottom wall of the tank, and it is set equal to the experimental setup value. With the symmetry condition only half of the prototype is simulated with the assumption that the flow is symmetric with respect the plane $Z-X$.

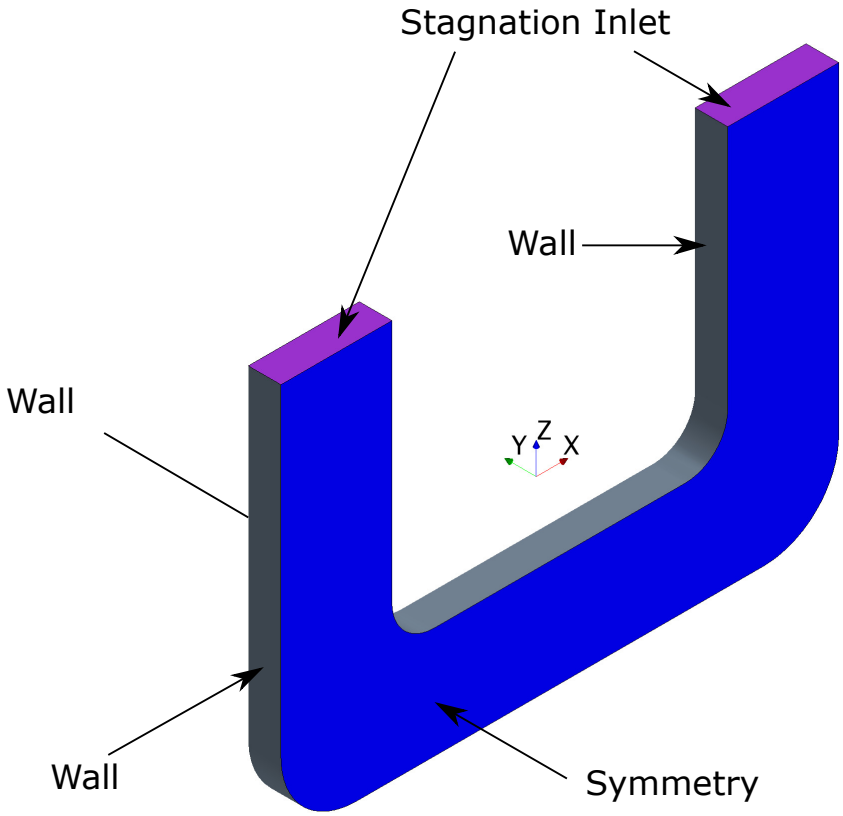

Figure 3.4 Boundaries of the U-Tank fluid domain.

The physical domain is discretized in hexahedral cells that are trimmed near the surface. The unstructured grid is refined in the two reservoirs to save computational

time and keep the accuracy of the model since the free surface need to be correctly captured. A good resolution of the mesh near the wall is required to well capture the friction losses, hence the first cell near the wall needs to be at least inside the log region to solve the boundary layer by mean of wall functions. To keep in account the vortices generate from the elbows and their transport a fine mesh resolution near the bends and along the path of the vortices is required. To avoid a high computational effort a good balance between it and CFD model accuracy is necessary. These considerations lead to the mesh settings reported in table 3.2 and shown in figure 3.5.

Table 3.2 Mesh Settings.

Default Controls		
Base Size	1	m
Target surface Size	1	%
Minimum Surface Size	0.25	%
Surface Curvature	72	pts/circle
Prism Layer Total Thickness	1.5	%
Number of prism layers	4	
Prism layer stretching factor	1.3	
Total number of cells	121051	
Custom Controls		
Refinment - surface size	0.5	%
Elbows sup - surface size	0.5	%
Elbows down - surface size	0.5	%
Block - surface size	0.5	%

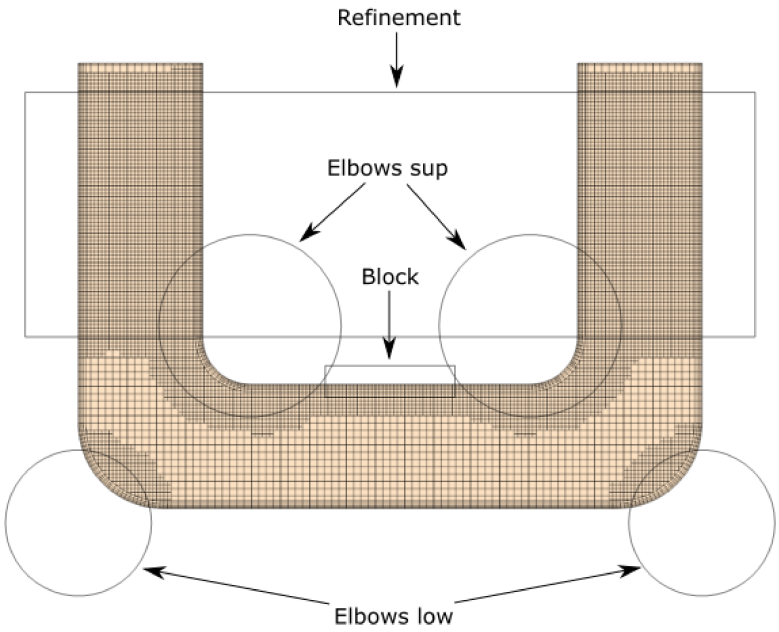

Figure 3.5 Mesh grid of the U-Tank for the CFD analysis.

The water elevation is extrapolated by averaging the free surface in the two reservoirs.

3.3 CFD free decay analysis

It is common practice to carry out free decay tests to identify damping coefficients to be used in lumped parameter models. A water level difference of 200 mm is imposed between the two reservoirs (corresponding to a U-Tank angle $\tau = 16.3\ deg$, according to the reference system shown in figure 2.4) shown in figures 3.6 and 3.7.

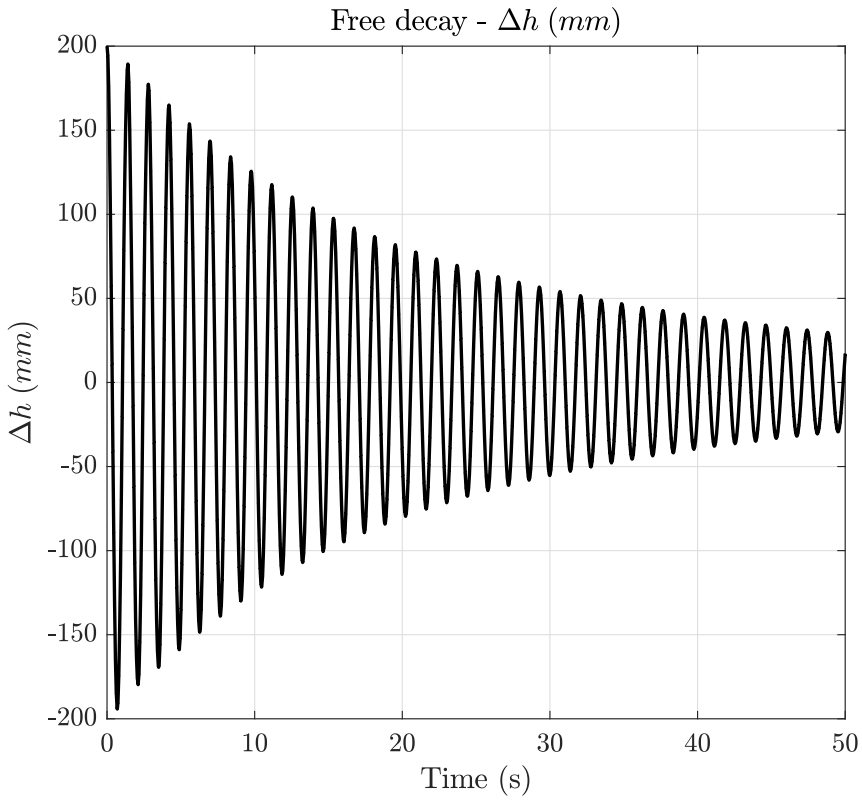

Figure 3.6 CFD free decay test. Δh is the water level distance between the two reservoirs.

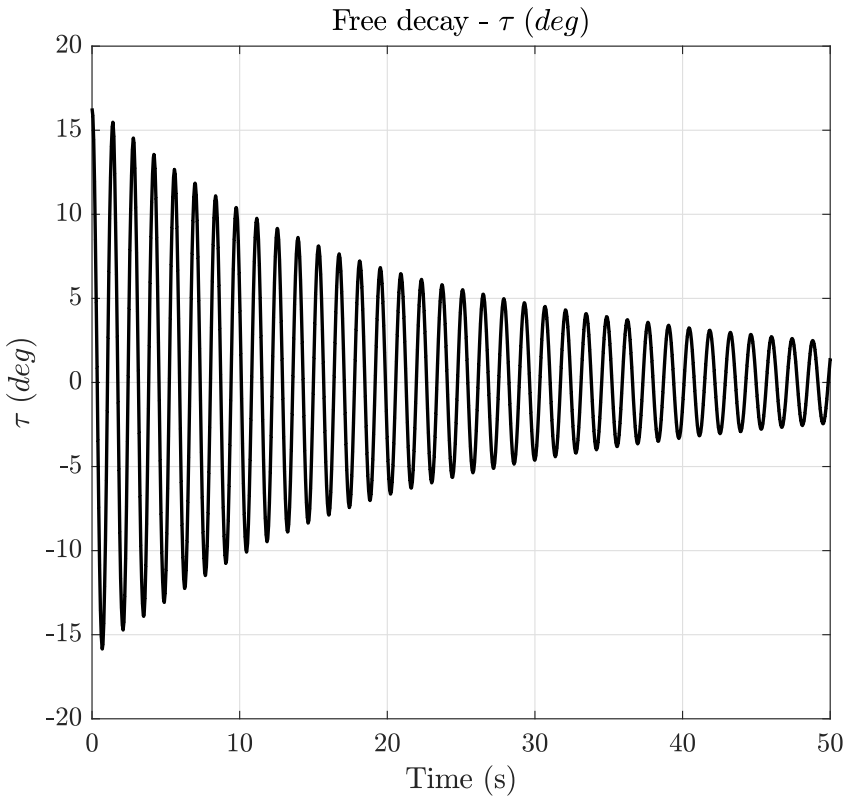

Figure 3.7 CFD free decay test. U-Tank angle τ.

3.3.1 Identification method of the damping coefficients

It is assumed that the damping component of the water motion inside the U-Tank can be modeled with a linear and quadratic term function of the U-Tank angle velocity $\dot{\tau}$ as anticipated in section 2.3.1. The method used in this work for the identification of the damping coefficients is derived from the naval field, for the evaluation of the roll damping of ships. This methodology is discussed by Chakrabarti (1987) [63] and an example of application can be find in the work of Begovic et Al. (2013) [96]. Equation (2.96) can be rewritten as:

$$\ddot{\tau} + 2\alpha\dot{\tau} + \beta\dot{\tau}|\dot{\tau}| + \omega_n^2\tau = 0 \tag{3.8}$$

Where:

- $\alpha = \frac{b_L}{2a_{\tau\tau}}$: linear extinction coefficient.

- $\beta = \frac{b_{NL}}{a_{\tau\tau}}$: quadratic extinction coefficient.
- $\omega_n = \sqrt{\frac{c_{\tau\tau}}{a_{\tau\tau}}}$: natural angular frequency.

It can be assumed that the oscillation is reasonably sinusoidal for each half cycle and therefore the Fourier series expansion can be applied to linearize the non-linear damping term:

$$\dot{\tau}|\dot{\tau}| \approx \frac{8}{3\pi}\omega_n \tau_i \tau \tag{3.9}$$

Where ω_τ is the angular frequency of the i-th oscillation cycle and τ_i is the corresponding angle amplitude.

Thus, it is possible to define the equivalent linear extinction coefficient as:

$$\alpha_{eq} = \alpha + \frac{4}{3\pi}\omega_\tau \tau_i \beta \tag{3.10}$$

Equation (3.8) can be rewrite in its linearized form:

$$\ddot{\tau} + 2\alpha_{eq}\dot{\tau} + \omega_\tau^2 \tau = 0 \tag{3.11}$$

The equation represent an under-damped second order linear equation, and the envelope curve of the free decay is given by the equation in the form:

$$\tau = \tau_0 e^{\alpha_{eq} t} \tag{3.12}$$

The logarithmic decay for two consecutive peaks i and $i+1$ is given by the equation:

$$\frac{\tau_i}{\tau_{i+1}} = e^{\alpha_{eq}(t_{i+1} - t_i)} \tag{3.13}$$

Thus, the equivalent linear extinction coefficient can be written as:

$$\alpha_{eq} = \frac{1}{t_{i+1} - t_i} \ln\left(\frac{|\tau_i|}{|\tau_{i+1}|}\right) \equiv \alpha + \frac{4}{3\pi}\omega_\tau \tau_{mean,i} \beta \tag{3.14}$$

where

$$\tau_{mean,i} = \frac{|\tau_i| + |\tau_{i+1}|}{2} \tag{3.15}$$

The angular frequency ω_n is given by:

$$\omega_n = \sqrt{\omega_\tau^2 + \alpha_{eq}^2} \tag{3.16}$$

A linear regression fitting is applied to the calculated points from the CFD free decay and the equation line parameters a and b can be obtained:

$$\alpha_{eq} = a\delta_{mean} + b \tag{3.17}$$

which allows to identify the linear and quadratic extinction coefficients:

$$\begin{aligned} \alpha &\equiv b \\ \beta &\equiv \frac{3\pi}{4\omega_\delta} a \end{aligned} \tag{3.18}$$

Figure 3.8 shows the results of the free decay analysis with the elaborated plotted data and the regression curve that best fits the data points.

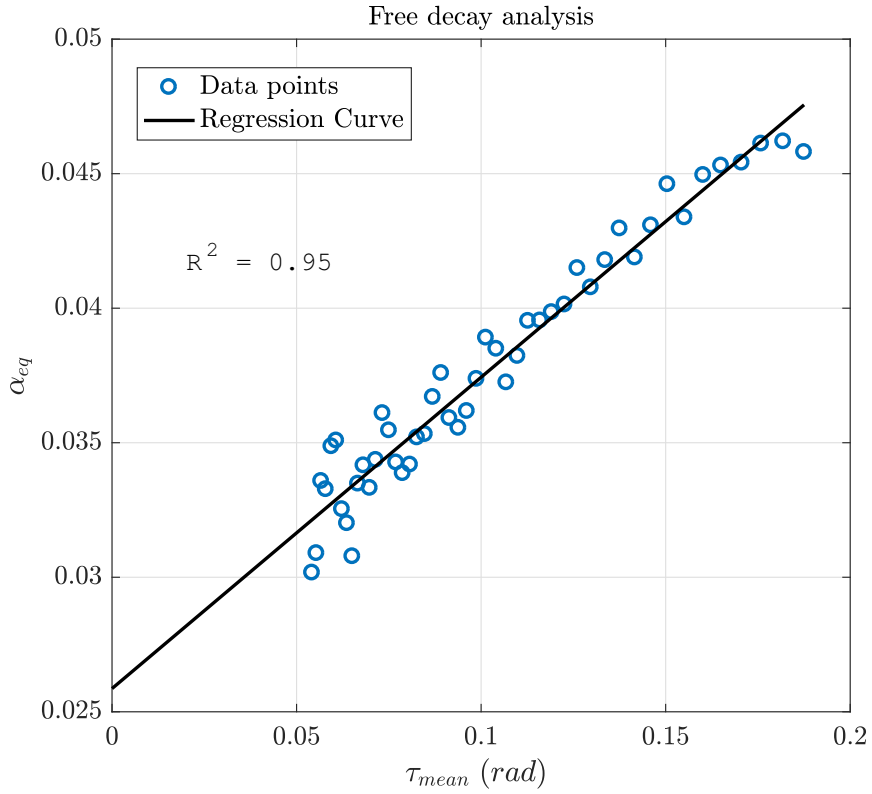

Figure 3.8 CFD free decay test. U-Tank angle τ.

The regression curve slope a is related to the quadratic extinction coefficient, while the intercept is related to the linear damping term. Table 3.3 resumes the relevant properties that can be extrapolated from the free decay analysis.

Table 3.3 Free decay analysis results.

Property	Units	Value
ω_τ	rad/s	4.51
a	rad/s	0.113
b	s^{-1}	0.026
α	s^{-1}	0.026
β	–	0.140
b_L	$(Nm\ s)/rad$	0.100
b_{NL}	$kg\ m^2$	0.114

With reference to equation (2.105) the linearization of the quadratic term and the derivation of a linear damping term to be used in the U-Tank linear model is given by:

$$b_{\tau\tau} = b_L + b_{NL}\omega_n\tau_0 = 0.15 \quad \left(\frac{Nms}{rad}\right) \tag{3.19}$$

Thus, the The U-Tank model coefficient $a_{\tau\tau}$ can be directly estimated from the free decay analysis data, from the calculation of the restoration coefficient $c_{\tau\tau}$:

$$a_{\tau\tau} = \frac{c_{\tau\tau}}{\omega_n^2} \tag{3.20}$$

Thus, the damping ratio ζ can be calculated as follows:

$$\zeta = \frac{b_{\tau\tau}}{2\omega_n a_{\tau\tau}} = 0.0087 \tag{3.21}$$

The U-Tank mass coefficient is also calculated considering the Lloyd's relations presented in section 2.3.1. With reference to equation (2.89) the integral I_1:

$$I_1 = \int_{tank} \frac{dy}{n} \tag{3.22}$$

is computed numerically along the $y-axis$ in order to take into account the geometrical variations at the U-Tank corners. It is worth remembering, that the Lloyd's equations are derived with the assumption of absence of velocity gradient in the direction perpendicular to the $y-axis$.

The LLoyd's model coefficients are given in table 3.4.

Table 3.4 Lloyd's model coefficients.

Property	Units	Value
$a_{\tau\tau}$	Nms^2/rad	1.92
$a_{\tau\tau_{Lloyd}}$	Nms^2/rad	1.99
$b_{\tau\tau}$	Nms/rad	0.15
$c_{\tau\tau}$	Nm/rad	39
$a_{\tau 5}$	Nms^2/rad	1.18
$c_{\tau 5}$	Nm/rad	39

The mass coefficient $a_{\tau\tau_{Lloyd}}$ calculated through the integration term I_1 (see equation (3.22)) is 4% greater than the estimated $a_{\tau\tau}$ with equation (3.20). This difference is probably due to the assumption of absence of velocity gradients along the direction perpendicular to $y-axis$.

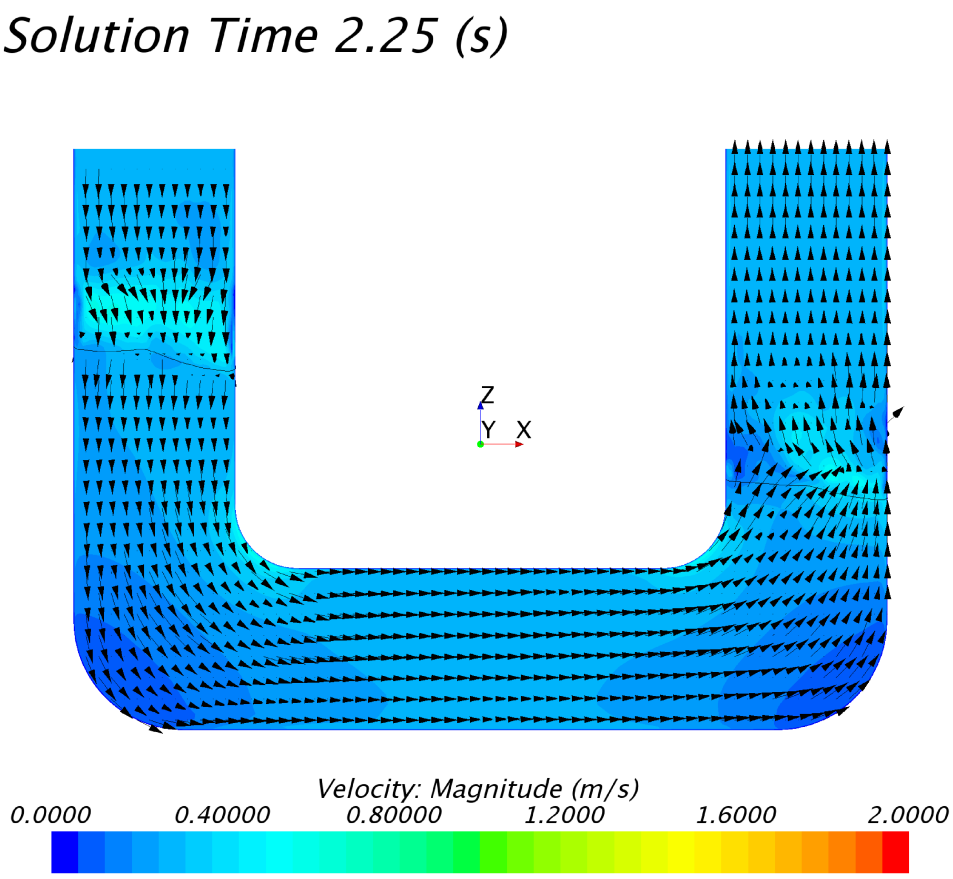

Figure 3.9 Magnitude velocity field of the fluid domain in the U-Tank for a specific time instant.

Figure 3.9 shows the magnitude velocity field of the fluid domain. It can be seen that, except for the boundary layer, the gradient of velocity is reasonable null in the central duct and in the upper part of the two reservoirs below the free surface.But in correspondence to the corners a gradient of velocity exists in the perpendicular direction of $y - axis$.

Comparison between CFD and lumped parameter model

The free decay evolution of the U-Tank angle τ is shown in figure 3.10 with a comparison between CFD results and the lumped parameter model, considering both the case of non-linear damping contributions and linearized damping. The lumped

parameter model show in both cases good match between the CFD and lumped parameter models.

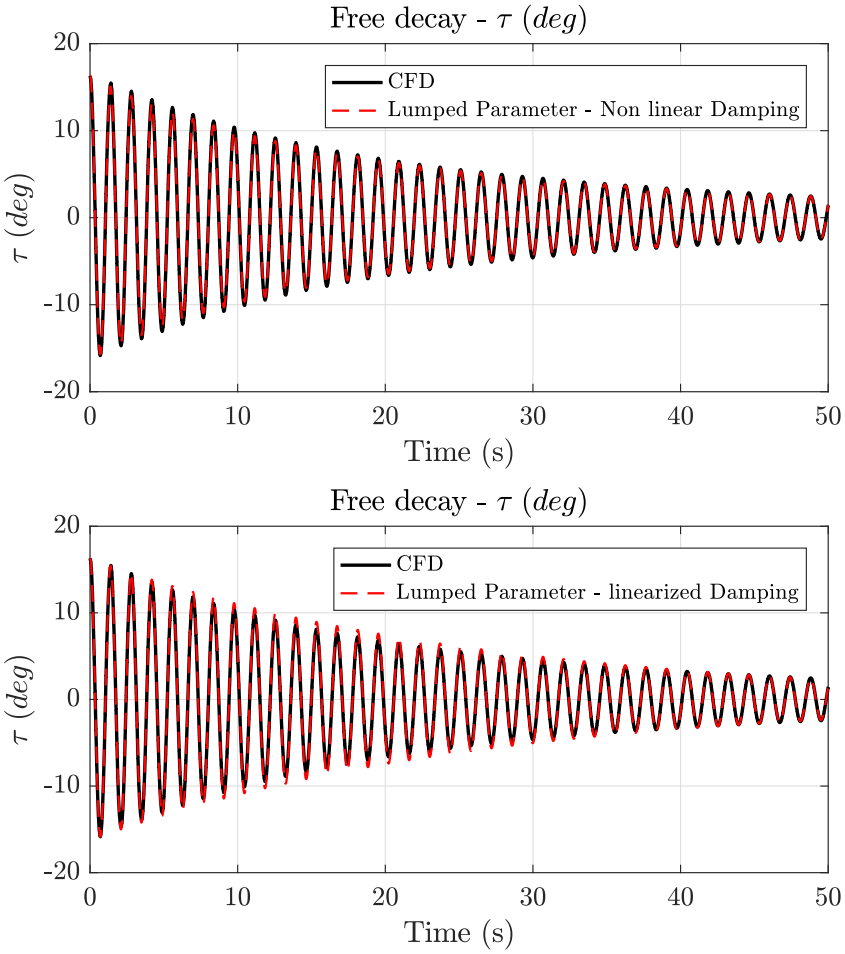

Figure 3.10 Comparison between CFD and lumped parameter model free decay evolution of the U-Tank angle.

3.4 CFD frequency response of U-Tank

In this section the dynamics of the frequency response of the U-Tank is investigated with CFD simulation and compared with the analytical model, and in the next section the validation against experimental results will be discussed. According to the

reference system shown in figure 2.5, the signal input δ that represents the pitch oscillation of the floater is modelled as a sinusoidal signal:

$$\delta(t) = \delta_0 sin(\omega t) \tag{3.23}$$

Where δ_0 is the input oscillation amplitude, ω is the angular frequency, and t is the time. FFT analysis is done on the output signal $\tau(t)$ when the stationary condition is reached in order to calculate the amplitude of the U-Tank angle response. The frequency response is calculated for three different amplitudes in order to investigate the non-linearities of the system.

In table 3.5 the results from the CFD results are given. Figure 3.12 show the time response of the $U-Tank$ oscillation angle τ for different input signal frequencies and for a fixed value of amplitude ($\delta_0 = 2\ (deg)$).

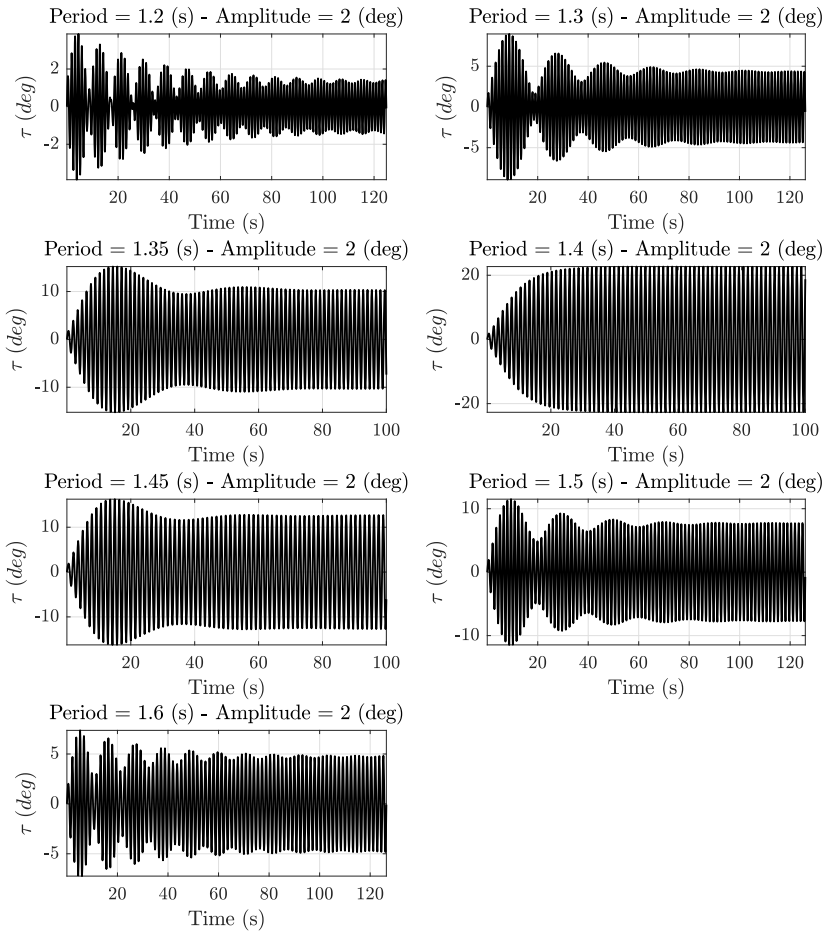

Figure 3.11 Kinematic response of the U-Tank with sinusoidal input for different frequencies and fixed amplitude.

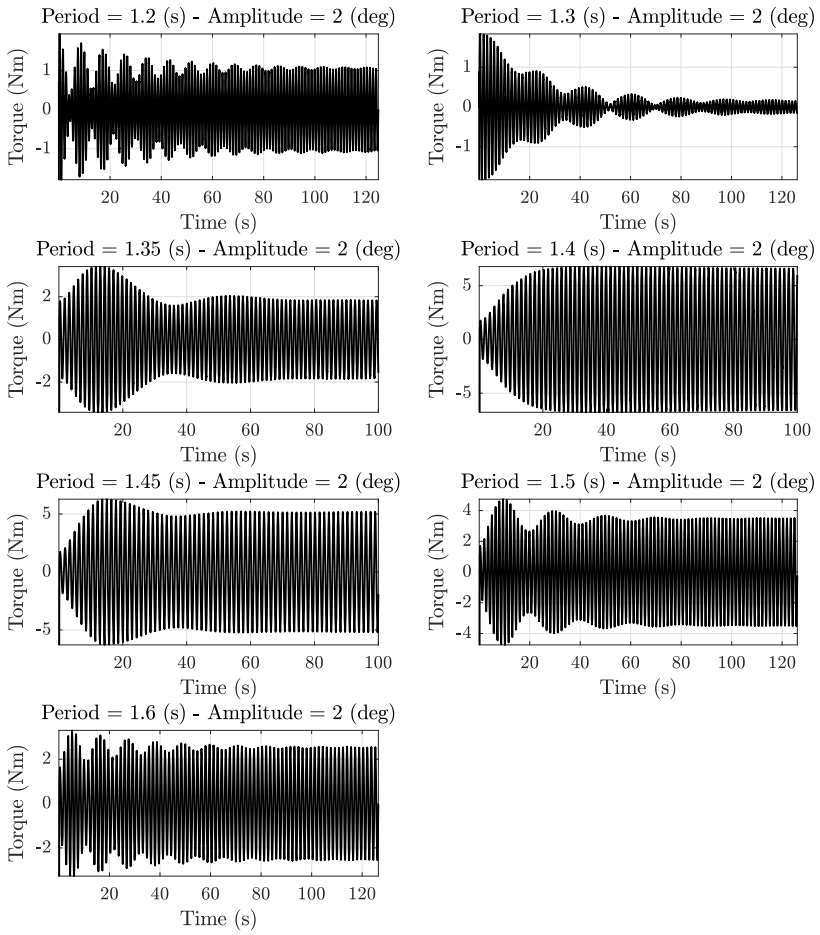

Figure 3.12 Torque response of the U-Tank with sinusolidal input for different frequencies and fixed amplitude.

The response amplitude operator (RAO) of the U-Tank can be calculated for both the angle τ and the coupled torque M_τ as:

$$RAO_\tau = \frac{\tau_0}{\delta_0} \ (\frac{deg}{deg}) \tag{3.24}$$

$$RAO_{M_\tau} = \frac{M_{\tau_0}}{\delta_0} \ (\frac{Nm}{deg}) \tag{3.25}$$

Table 3.5 CFD results in regular wave conditions.

(a) Amplitude δ_0 = 1 (deg)

Period (s)	τ_0 (deg)	$\angle\tau$ (deg)	M_{τ_0}(Nm)	$\angle M_\tau$ (deg)
1.2	0.68	168.42	0.52	2.49
1.3	2.25	172.83	0.06	60.73
1.35	6.57	165.04	2.52	156.96
1.4	15.7	80.64	4.85	72.31
1.45	6.53	11.87	2.52	9.71
1.5	3.76	2.95	1.69	2.52
1.6	2.38	0.20	1.26	0.20

(b) Amplitude δ_0 = 2 (deg)

Period (s)	τ_0 (deg)	$\angle\tau$ (deg)	M_{τ_0}(Nm)	$\angle M_\tau$ (deg)
1.2	1.35	169.29	1.04	2.85
1.3	4.38	171.14	0.16	66.46
1.35	10.39	161.65	1.89	150.88
1.4	23.05	98.77	7.00	88.89
1.45	12.64	15.47	4.98	11.50
1.5	7.72	5.66	3.46	4.30
1.6	4.76	0.76	2.52	0.99

(b) Amplitude δ_0 = 2.5 (deg)

Period (s)	τ_0 (deg)	$\angle\tau$ (deg)	M_{τ_0}(Nm)	$\angle M_\tau$ (deg)
1.2	1.67	171.06	1.31	3
1.3	5.46	170.89	0.22	66.63
1.35	12.33	160.69	2.15	148.48
1.4	25.24	109.85	7.43	99.63
1.45	15.95	18.65	6.29	11.83
1.5	9.61	6.456	4.33	4.80
1.6	6.00	1.73	3.17	1.33

Where τ_0 is the amplitude of the U-Tank oscillation in stationary conditions. Figure 3.13 shows the RAO of U-Tank oscillation τ. The CFD results are compared with the non-linear and linear lumped parameter model. In the non-linear model the viscous damping is modeled with a linear and quadratic term with the velocity (see eq. (2.104)) and the linear model adopt a linearized viscous damping term (see eq. (3.19)). Both linear and non-linaer model show good agreements with the CFD results. When the amplitude of the tank imposed motion δ_0 increases, the viscous non-linearities are highlight in correspondence of the resonance condition. The non-linear model is able to catch better than the linearized model the sloshing dynamics in resonance conditions.

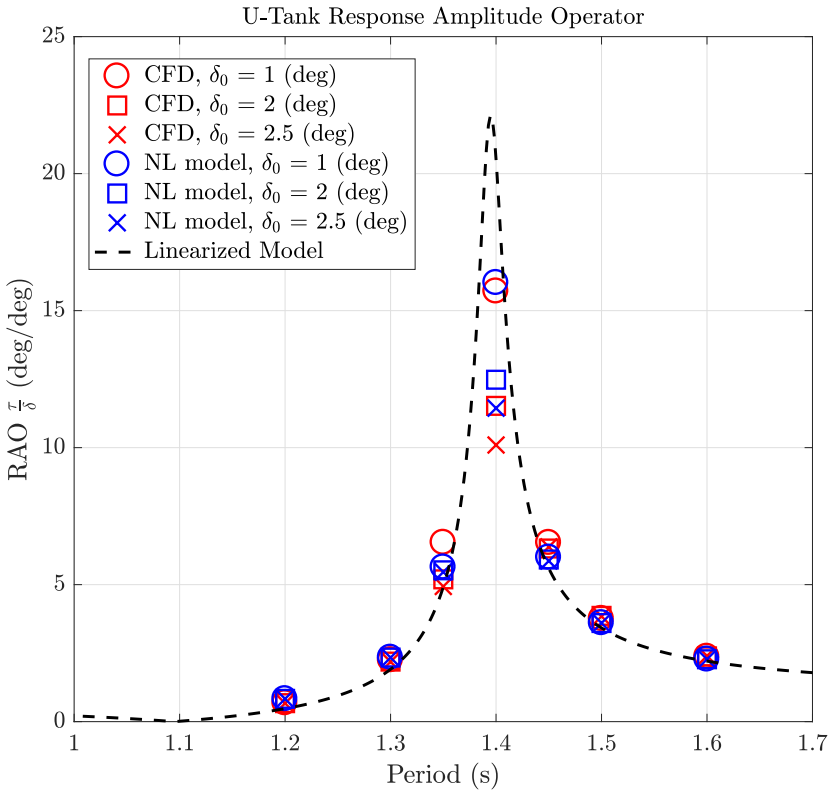

Figure 3.13 U-Tank Response Amplitude Operator. Oscillation angle τ.

Figure 3.14 shows the CFD torque due to the U-Tank dynamics compared with the non-linear and linearized model. Both linear and non-linear model show differences compared to the CFD results. The reason can be attributed to the approx-

imation in the calculation of the acceleration coupling coefficient $a_{\tau 5}$ and further investigations are necessary to better model the coupling torque.

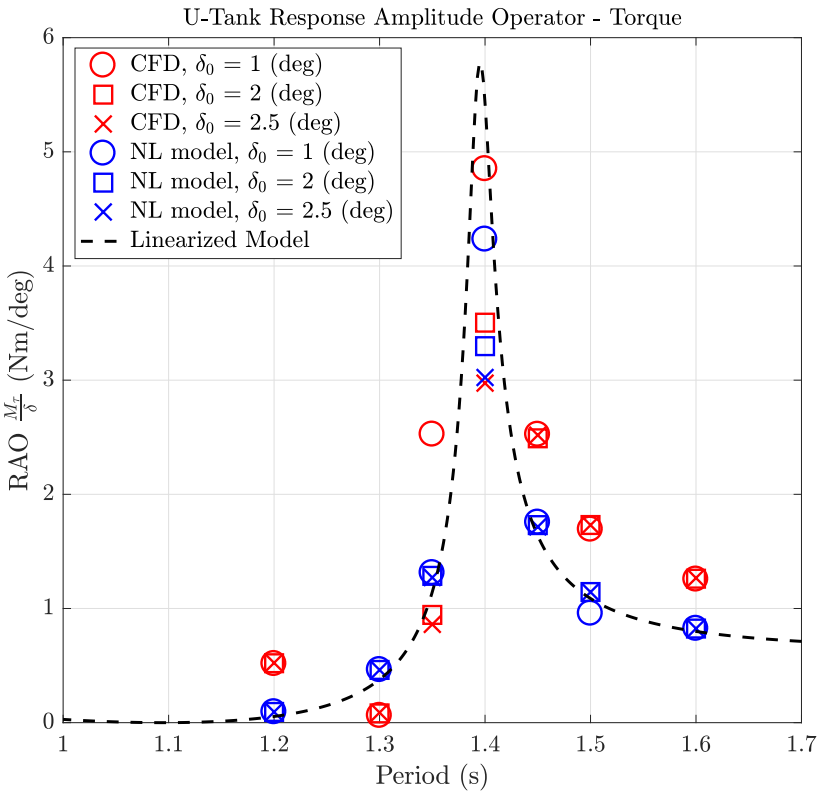

Figure 3.14 U-Tank Response Amplitude Operator. coupled torque M_τ.

An example of time domain response of the linearized model compared to the CFD simulation is given in figure 3.16.

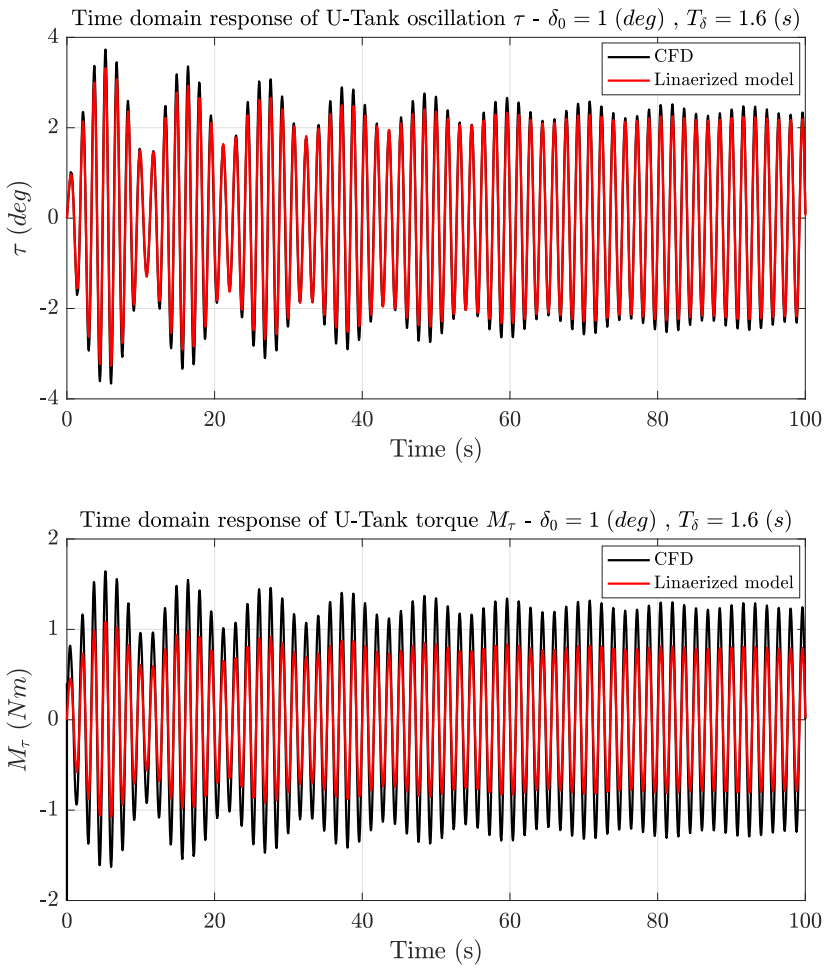

Figure 3.15 Comparison between CFD and linearized lumped parameters model in time domain.

3.5 CFD response of U-Tank in irregular conditions

The ocean environment is represented by irregular waves that can be described by analytical spectra, as discussed in section 2.1.4. Therefore, also the motion of the floater will be irregular and its response will depend on its hydrodynamic RAO (see eq. (2.38)). Since the U-Tank under analysis is not designed for a specific hull, the PSD of the pitch response of the floater is not available.Therefore, it is assumed to be equal to the wave spectrum S_η.

A peak period T_p of the spectrum equal to the natural period of the U-Tank T_{res} and a $\delta_{rms} = 1.5$ have been chosen:

- $f_p = \frac{1}{T_p} = 0.714\ (Hz)$
- $H_s = 4\sqrt{m_0} = 4\delta_{rms} = 0.105\ (rad)$
- $\gamma = 3.3$

A pseudo-random irregular record of the floater's pitch $\delta(t)$ has been generated considering the JONSWAP spectrum data defined above. A record length of 300 (s) was chosen and Figure shows the generated irregular pitch motion $\delta(t)$.

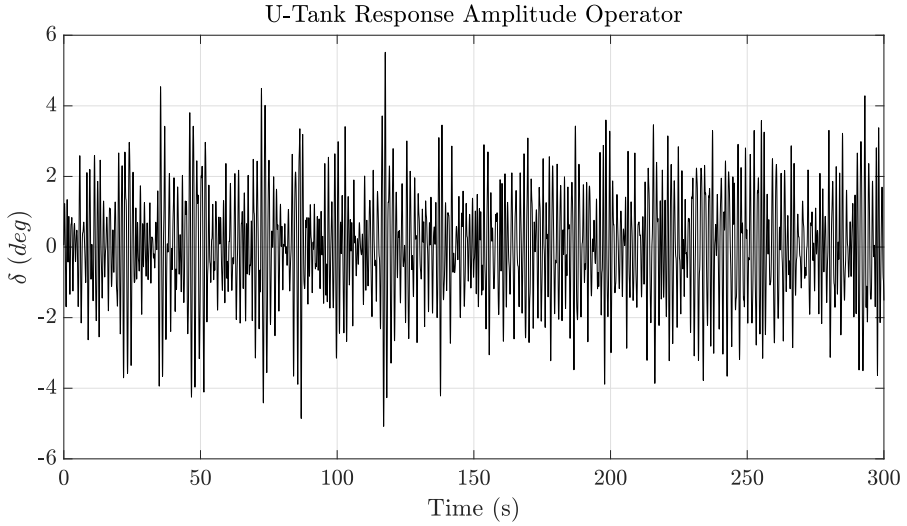

Figure 3.16 Irregular imposed pitch motion $\delta(t)$ to the U-Tank.

The irregular pitch oscillation $\delta(t)$ is used to simulate in CFD environment the response of the U-Tank in irregular conditions. The U-Tank oscillation $\tau(t)$ response calculated through the RANSE model is shown in figure 3.17 and the torque M_τ is shown is given in figure 3.18.

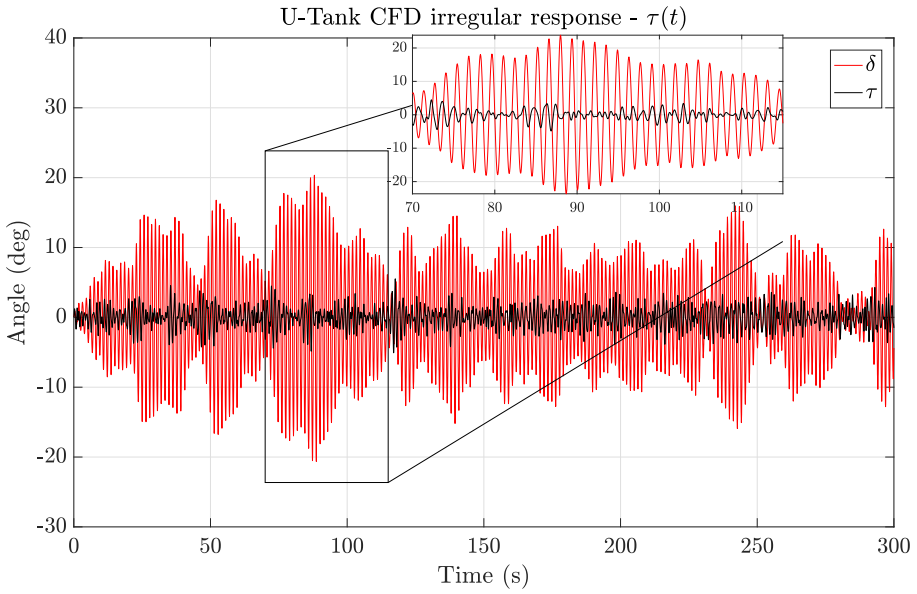

Figure 3.17 CFD Irregular U-Tank response τ compared with the imposed pitch oscillation δ.

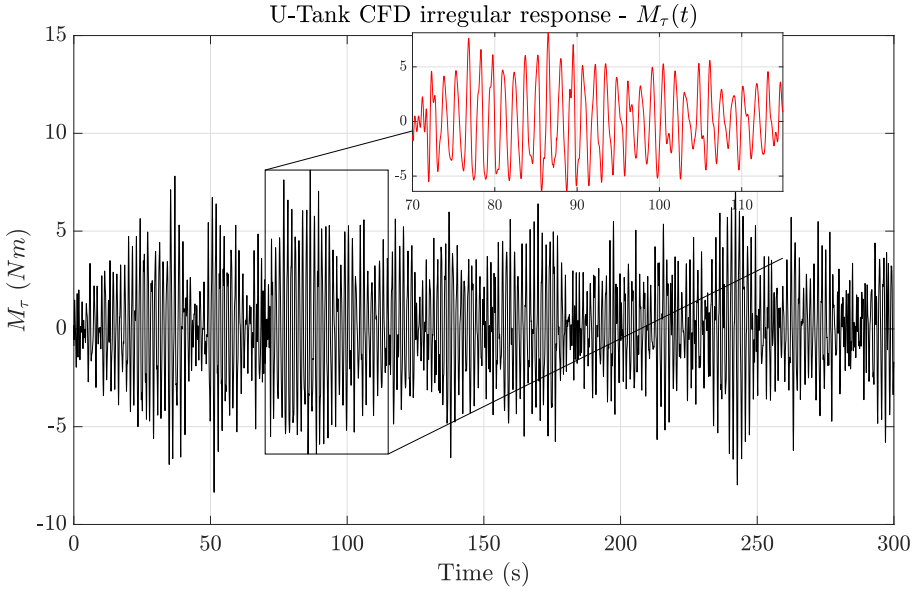

Figure 3.18 CFD Irregular U-Tank torque response M_τ.

A more clear vision of the time histories of the signals is given in figure 3.19 with a spotlight on the phase between the U-Tank torque M_τ and respectively the pitch angle δ and the U-Tank angle τ.

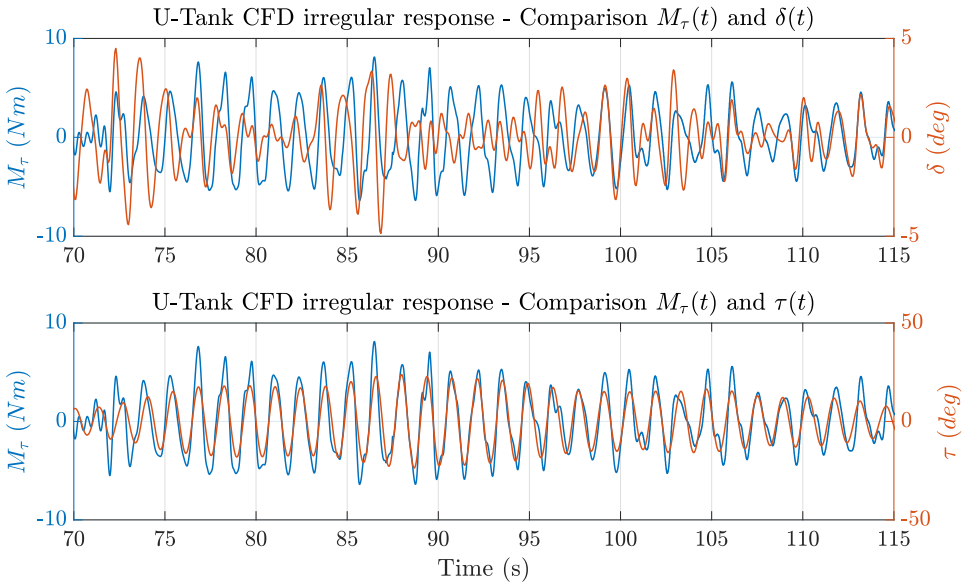

Figure 3.19 Comparison between the U-Tank torque M_τ and the U-Tank oscillation angle τ.

The Power Spectrum Density (PSD) of the U-Tank angle and torque time histories is estimated with the Welch's method also called periodogram method. The frequency energy contribution of the two signals are compared with the PSD of the input signal δ shown in figure 3.20.

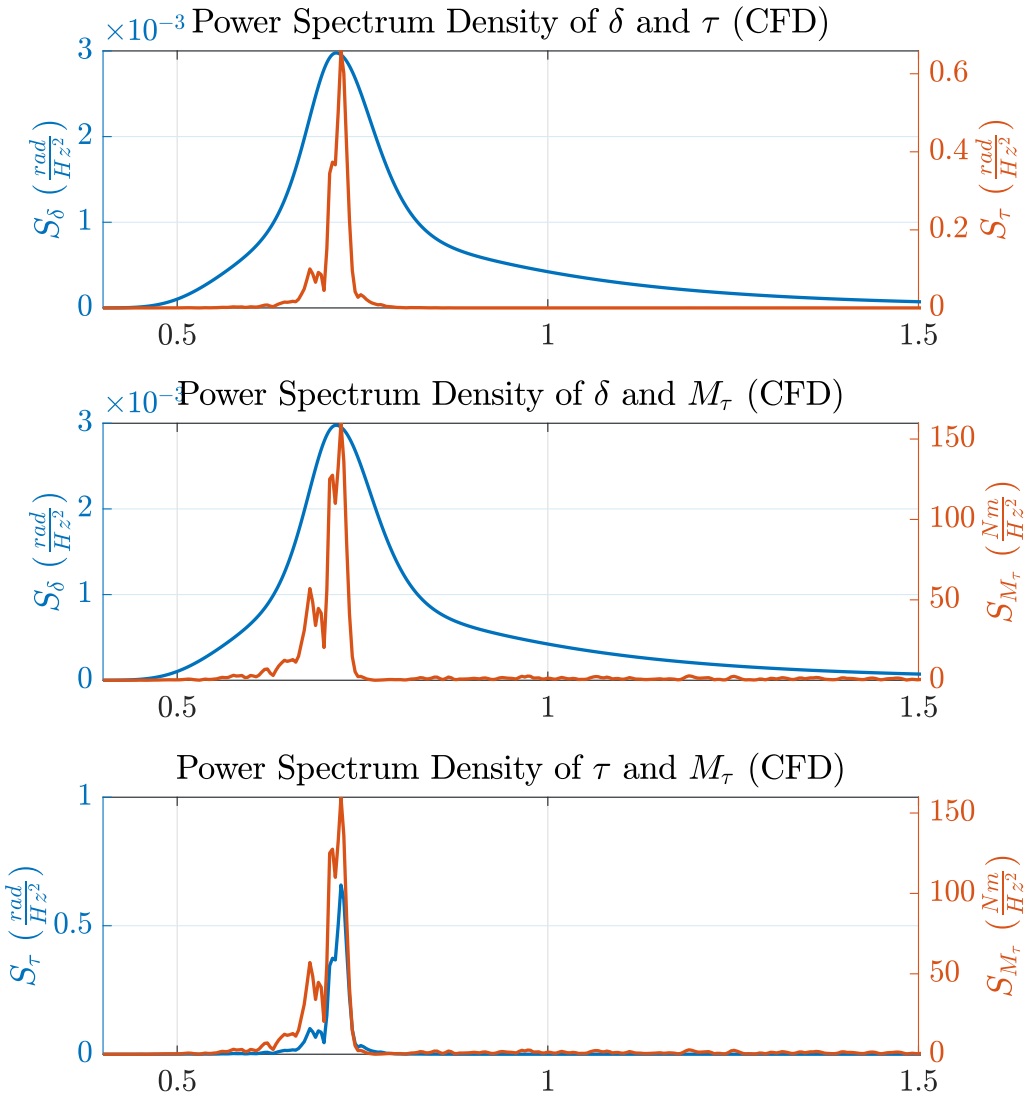

Figure 3.20 Power Spectrum Density of the input signal δ, U-Tank oscillation angle τ and torque M_τ

.

Comparison CFD and lumped parameter model

The linearized U-Tank model with the parameters given in table 3.4 is adopted to simulate the linear response of the U-Tank in irregular conditions with the same

pitch input time history $\delta(t)$ used to simulate the high fidelity response through CFD model.

The comparison between the simulated time histories with high and low fidelity models is given in figure 3.21 and figure 3.22. The low fidelity model shows good agreements in irregular conditions, and tends to underestimates the torque amplitude as shown in regular conditions (see section 3.4). The relative differences of the rms values between the two models are given in table 3.6.

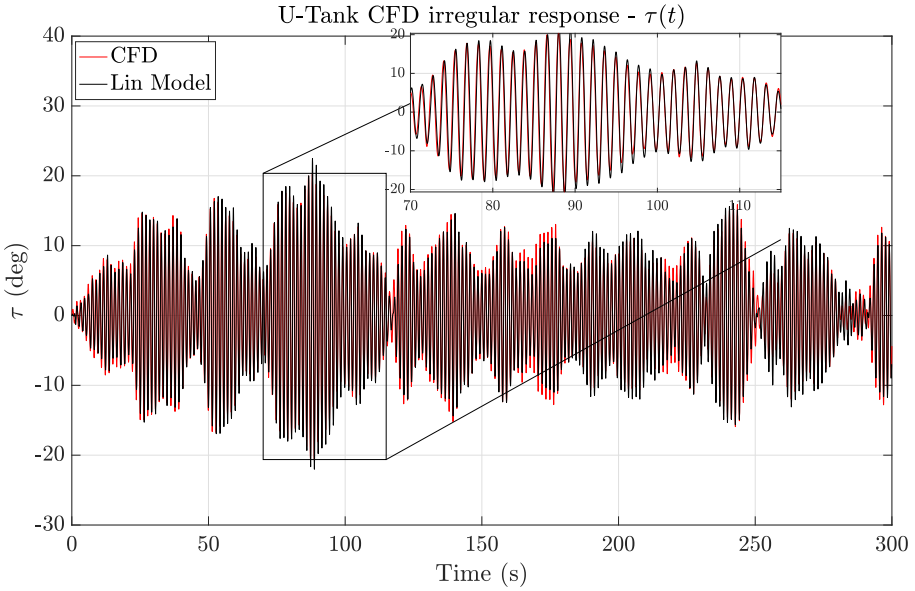

Figure 3.21 Comparison between the high fidelity CFD and low fidelity linear model irregular response of the U-Tank oscillation angle τ.

Table 3.6 Rms values of the CFD and linear model simulation results in irregular conditions.

	CFD	Linear Model	Relative Difference (%)
Rms Angle τ (deg)	7.30	7.54	3.4
Rms Torque M_τ (Nm)	2.54	2.23	-12.3

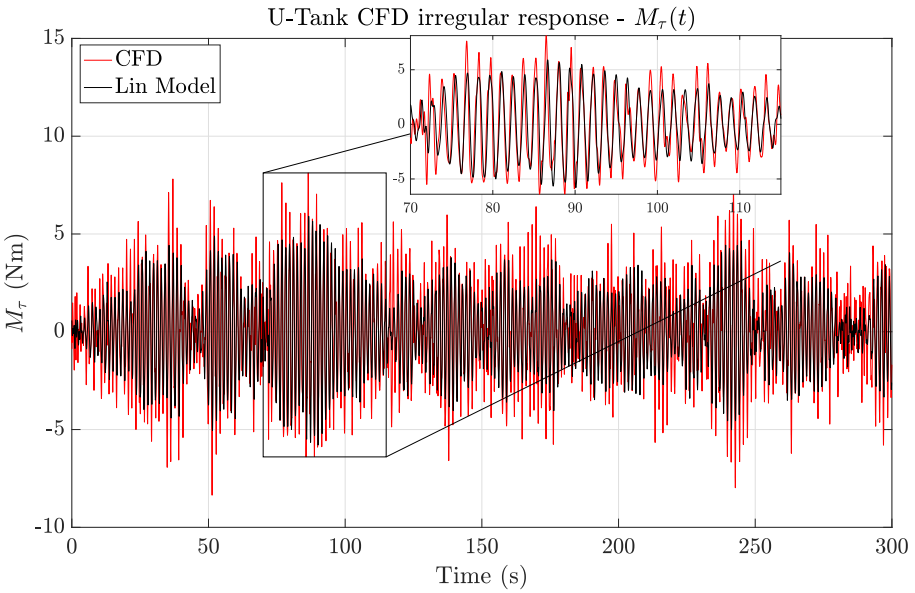

Figure 3.22 Comparison between the high fidelity CFD and low fidelity linear model irregular response of the U-Tank torque M_τ.

The estimated PSD spectrum of the U-Tank angle τ and torque M_τ for both the CFD and linear model are shown in figure 3.23.

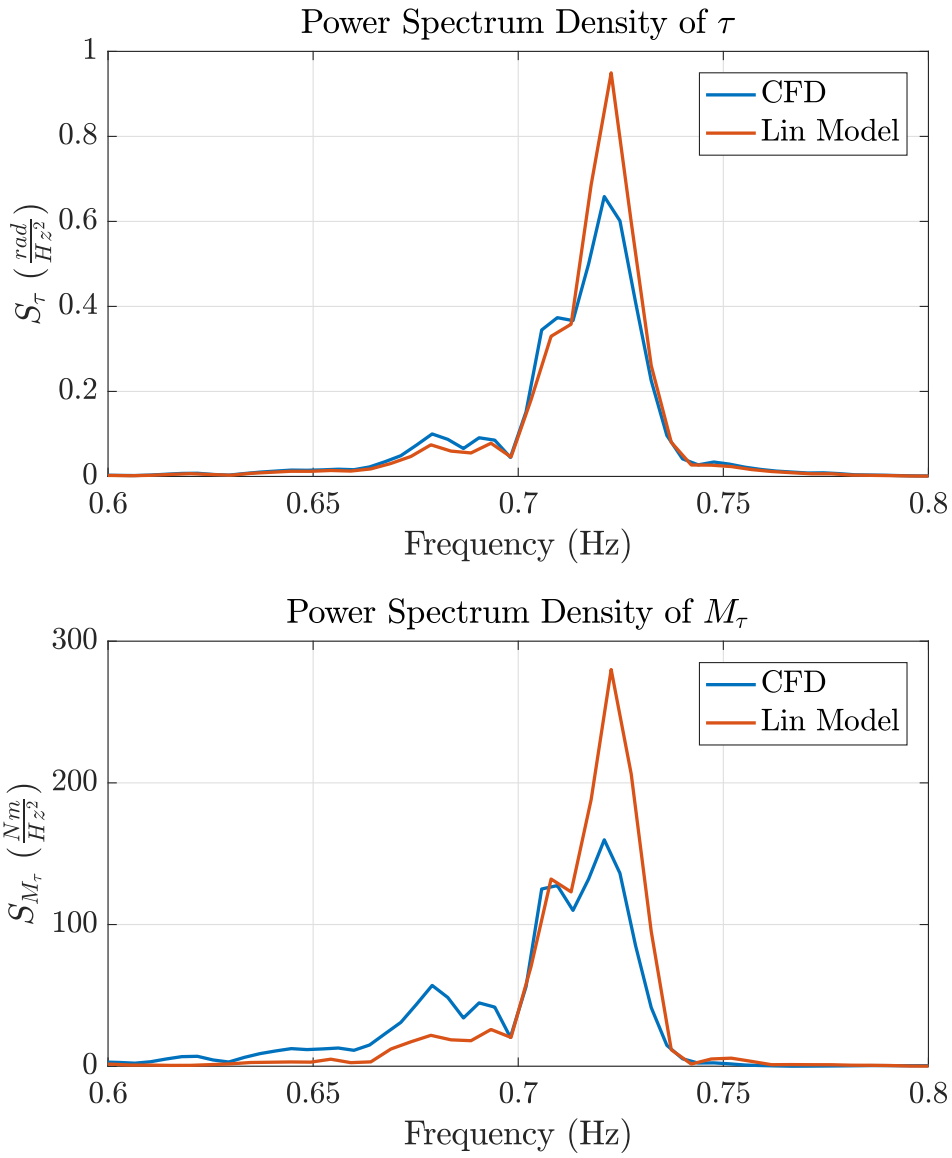

Figure 3.23 Comparison between the high fidelity CFD and low fidelity linear model irregular response of the U-Tank torque M_τ.

3.6 Experimental tests and validation of the numerical models

An experimental test campaign was carried out in Polytechnic of Turin on the scaled model of the U-Tank with the same properties of the CFD simulation (see table 3.1). The objective of the experimental campaign is to validate the CFD model and use the numerical tool to simulate the behavior of the U-Tank in full-scale size with high confidence of the results. The model was tested in regular wave conditions.

3.6.1 Experimental set-up

The U-Tank model is made of transparent PVC material in order to catch the motion of the water inside the tank (see figure 3.24).

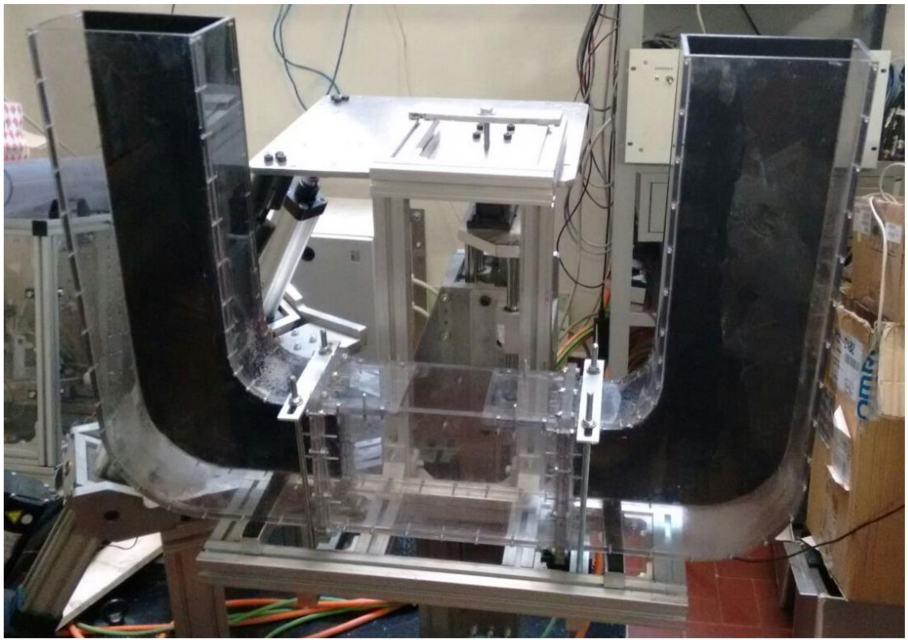

Figure 3.24 U-Tank prototype realized in PVC material used during the experimental campaign tests.

The U-Tank model is fixed on a HPR (Heave, Pitch and Roll) platform shown in figure 3.25.

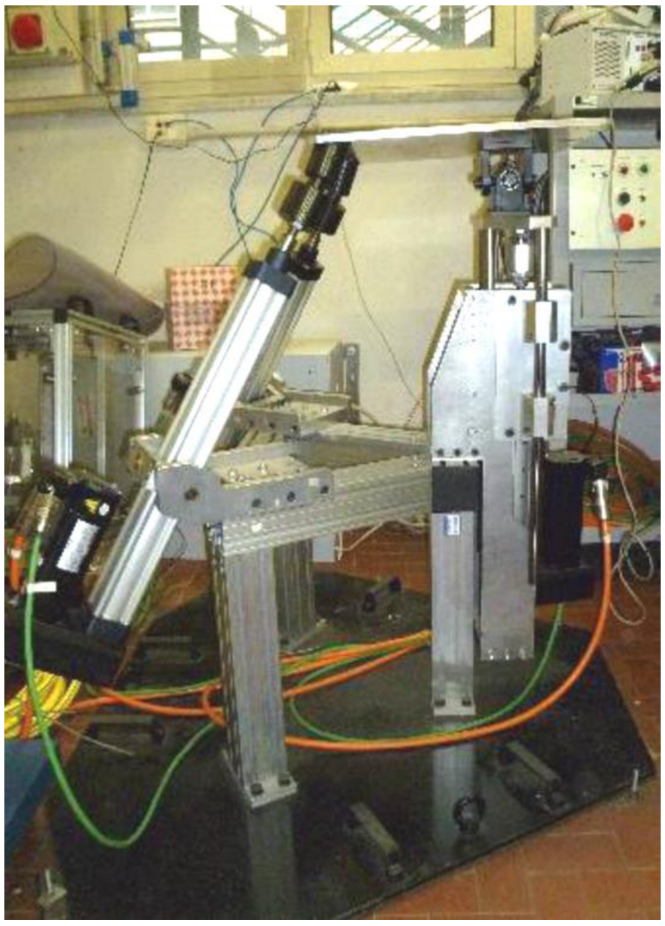

Figure 3.25 Picture of the HPR platform in the mechatronic systems laboratory of Polytechnic of Turin.

The HPR platform is a three degrees of freedom electro-actuated device, that let the platform to describe trajectories in a certain working space among the working space limits:

- Roll motion $\pm$ 25 (deg).
- Pitch motion $\pm$ 25 (deg).
- Heave maximum excursion 100 (mm).

The HPR platform is controlled by a DSP processor that includes a numerical model implemented in Matlab/Simulink environment that represents the dynamics of the platform. More in detail, the electro-mechanical actuators are controlled in

velocity. The reference position signal in this experimental campaign is sinusoidal in order to test the frequency response of the system. The distance r_D between the center of rotation of the platform (that represents the COG of the floater) and the duct center-line of the U-Tank can be regulated and it this experimental campaign is set to 63 (mm) equal to the CFD numerical setup.

Vision acquisition system

The motion of the U-Tank and the water level in the two reservoirs is measured trough a vision acquisition system. Figure 3.26 shows the layout of the vision markers mounted on the system:

- One marker on the Center of Rotation (CR) of the HPR platform.
- Four markers on the U-Tank structure to measure the pitch motion of the system.
- Two markers fixed to two thin polyurethane plates floating on the free surface of the reservoirs of the U-Tank to measure the instantaneous water levels.

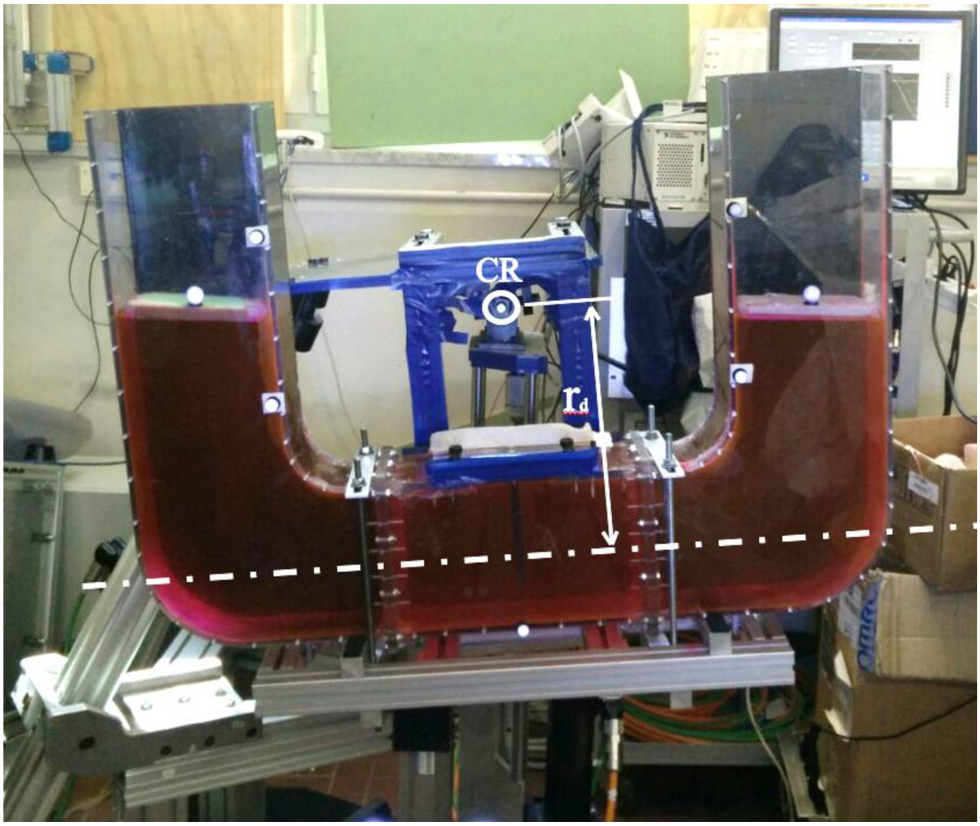

Figure 3.26 Experimental setup during an aquisition.

The vision acquisition system is constituted by a camera (not shown in figure) that tracks the motion of the markers. A post-processing software analyses the recorded frames and identify the position of the reflecting markers at every instant in time.

Signal post-processing

The range of the tested periods for the forced sinusoidal motion goes from 1 to 2 seconds and it has been chosen compatibly with the platform working limits. To perform an accurate characterization of the system, four different motion amplitude were tested: 2 and 2.5 deg.

The position of the markers are acquired in the Fixed Reference Frame (FRF) and the pitch motion of the tank can be calculated. The position of the floaters inside the reservoirs is also defined in the fixed reference frame and through a rotation transformation their position is defined also in the Local Reference Frame (LRF)

anchored to the tank. We can assume that the markers on the floaters represent the free surface level in each reservoir. The positions signals are elaborated in Matlab environment and the data have been filtered with a low pass filter with a frequency cut $Fs = 4\ (Hz)$.A FFT algorithm is adopted in order to identify the oscillation amplitudes in stationary conditions to identify the Response Amplitude Operator of the U-Tank for each test.

3.6.2 Results

An example of experimental post-processed signals is shown in figure 3.27 for both tank and water oscillation in resonance conditions.

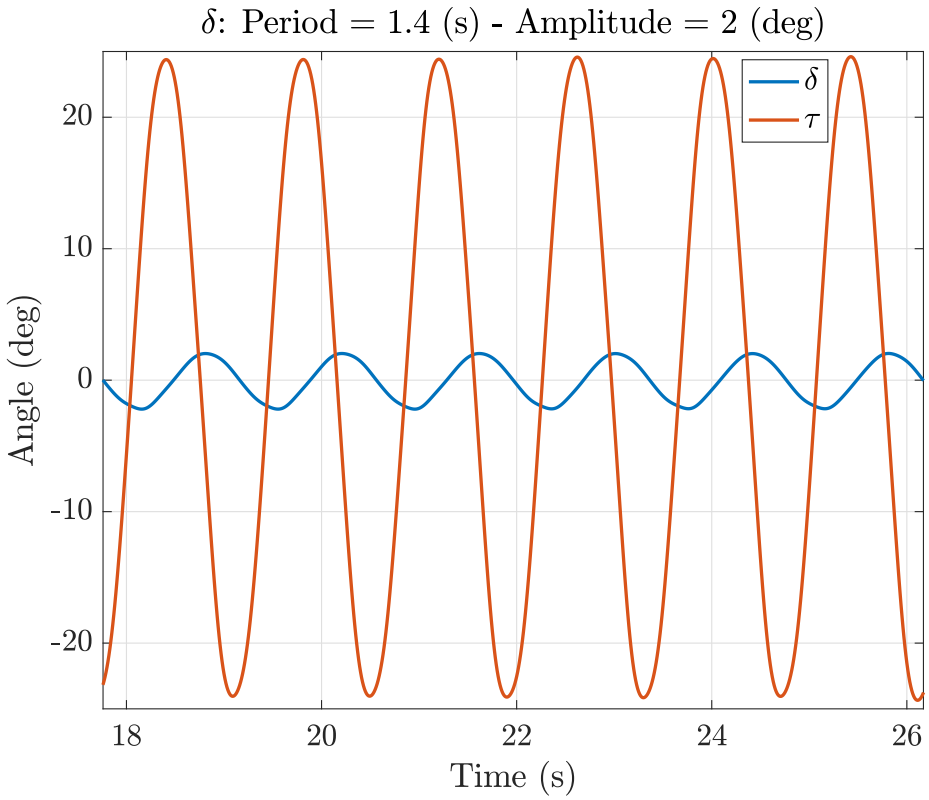

Figure 3.27 Example of elaborated time histories signals in stationary conditions.

The Response Amplitude Operator of the water angle τ is shown in figure 3.28 considering an oscillation forced amplitude of the pitch angle δ of 2 and 2.5 deg. A missing point occurs in resonance condition $T = 1.4\ (s)$ for a pitch amplitude

$\delta_0 = 2.5(deg)$ because during the test there was a leakage of the water from the tank caused by the large amplitude of the sloshing motion in resonance conditions.

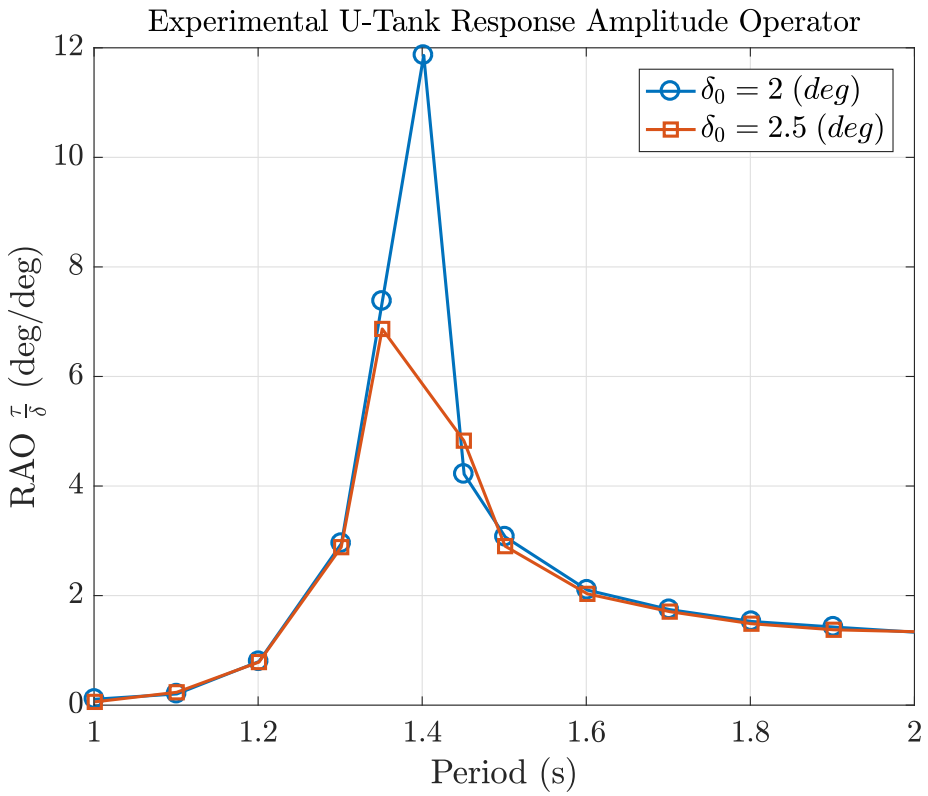

Figure 3.28 Experimental Response Amplitude Operator of the U-Tank

The RAO of the U-Tank of the experimental test, CFD and linear model are compared in figure 3.29 and the amplitudes of the U-Tank oscillation τ are given in table 3.7.

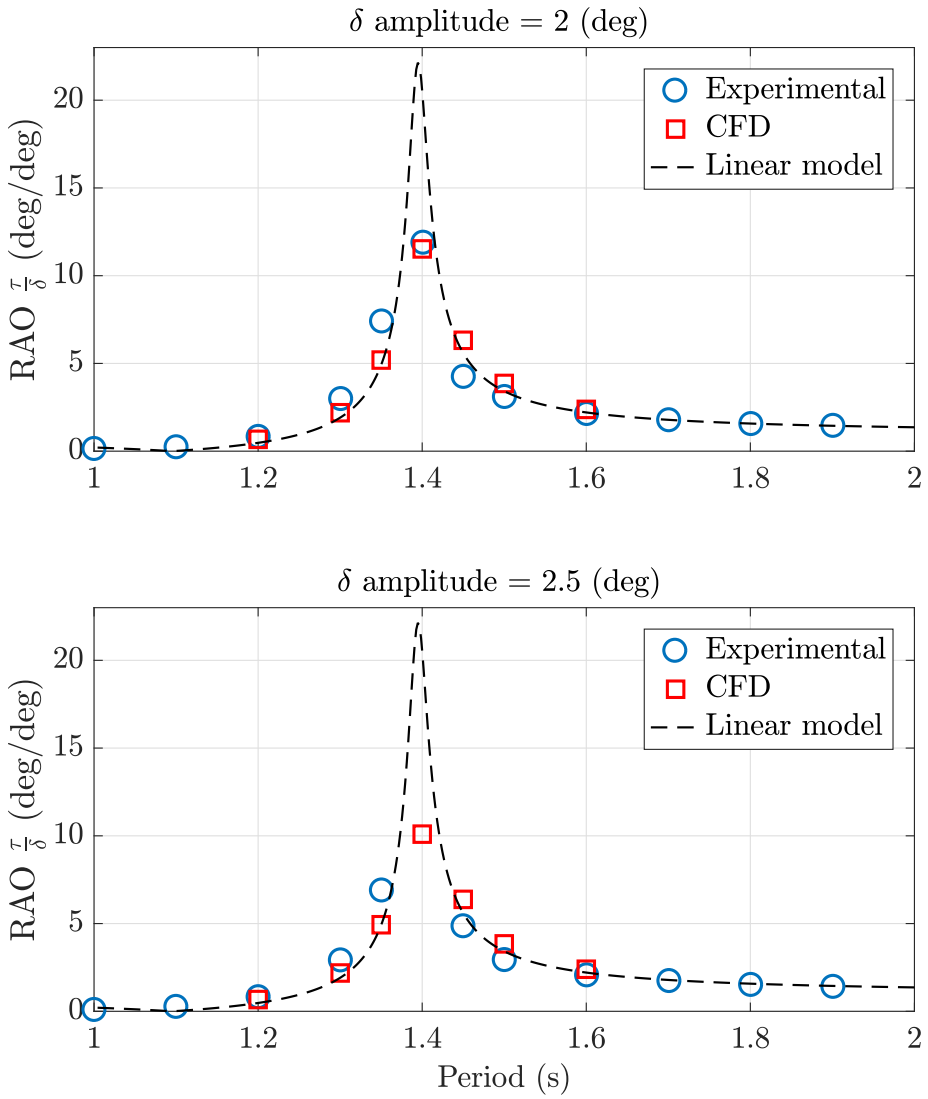

Figure 3.29 CFD and numerical model U-Tank RAO compared to experimental RAO.

The CFD results show good agreement with the experimental data, with higher differences close to the resonance condition. These differences in amplitude values can be addressed mostly to experimental uncertainties that can affect the result such as the acquisition error of the markers' position and also the presence of the floaters in the reservoir can affect negatively the results. The CFD tool is able to catch the dynamics and the sloshing phenomena, and it can be used as design tool in order to calibrate the numerical lumped parameter model, also in full-scale conditions and

Table 3.7 Experimental, CFD and linear model results in regular wave conditions.

(a) Amplitude δ_0 = 2 (deg)

Period (s)	Exp τ_0 (deg)	CFD τ_0 (deg)	Lin Model τ_0 (deg)
1.0	0.22	-	0.42
1.1	0.43	-	0.03
1.2	1.63	1.35	0.95
1.3	5.88	4.38	3.82
1.35	14.91	10.39	9.84
1.4	24.81	23.05	41
1.45	8.84	12.64	11.19
1.5	6.45	7.72	6.84
1.6	4.38	4.76	4.42
1.7	3.62	-	3.57
1.8	3.16	-	2.89
1.9	2.93	-	2.89
2.0	2.79	-	2.72

(b) Amplitude δ_0 = 2.5 (deg)

Period (s)	Exp τ_0 (deg)	CFD τ_0 (deg)	Lin Model τ_0 (deg)
1.0	0.15	-	0.53
1.1	0.59	-	0.04
1.2	2.02	1.67	1.19
1.3	7.28	5.46	4.78
1.35	17.05	12.33	12.30
1.4	-	25.24	51.36
1.45	12.27	15.95	13.99
1.5	7.50	9.61	8.55
1.6	5.26	6.00	5.52
1.7	4.39	-	4.46
1.8	3.83	-	3.61
1.9	3.54	-	3.61
2.0	3.11	-	3.40

for different geometrical shapes, with high time and cost reduction compared to the experimental tests. Moreover, it has been demonstrated that a calibrated lumped parameter model is representative of the real dynamics of the U-Tank, and it can be used with confidence for the performance assessment of the device and, in future, to be implemented in a on-board control logic.

Chapter 4

IOwec Numerical Design Tool

In this chapter the development of a numerical design tool for the assessment of the IOwec device performances is discussed. The core of the design tool is the linear numerical model presented in the previous chapter that allows to simulate the dynamics of the device given the properties of the floater, gyroscope and U-Tank systems. The amount of parameters that describes the IOwec device can be very high and not handy to manage, especially in a preliminary design phase. Therefore, it is worth to make some simplifications and assumptions that relate some system parameters in order to reduce the design variables that defines uniquely the device. The goal is to have a set of limited but significant design variables that identify the remaining geometrical and inertial properties necessary fo the numerical model. Once the device is given uniquely, the hydrodynamic parameters of the floater are calculated through the BEM open source code Nemoh and the wave forces acting on the hull can be computed. Then the numerical simulation can be carried out in order to assess the dynamics of the device and its performance. All the stages of this numerical tool have been coded in matlab environment in order to have a flexible design and simulation tool.

4.1 Design Parameters and assumptions

The choice of the design parameters that uniquely define the device plays a strategic role, which is the result of the experience and sensibility of the system engineer. In fact, once the design parameters are defined, they can be optimize with a global-

search optimization algorithm to minimise the cost of energy for a given installation site. During the early design stage, some parameters need to be set to avoid an excessive abundance of variables that define the device.
The IOwec device can be divided into three macro-subsystems:

- Floater.
- Gyroscope.
- Water Sloshing Tanks.

The determination of the parameters of each subsystem will be addressed in the following sections.

4.1.1 Floater Design Parameters and Assumptions

The floater shape and inertial properties play an important role in the dynamics and power absorption of the device. IOwec is a pitching-resonant device and therefore its performance is strictly linked to the pitch Response Amplitude Operator (RAO). As a starting point, the shape of IOwec is assumed to be similar to the ISWEC device, [49]. The hull profile is defined by the arcs of two circumferences tangent internally and parametrized as a function of some geometrical quantities as shown in figure 4.1. The floater is symmetrical with respect to the *z-y* and *z-x* planes and it is given by the extrusion of the profile of the hull along the y-axis.

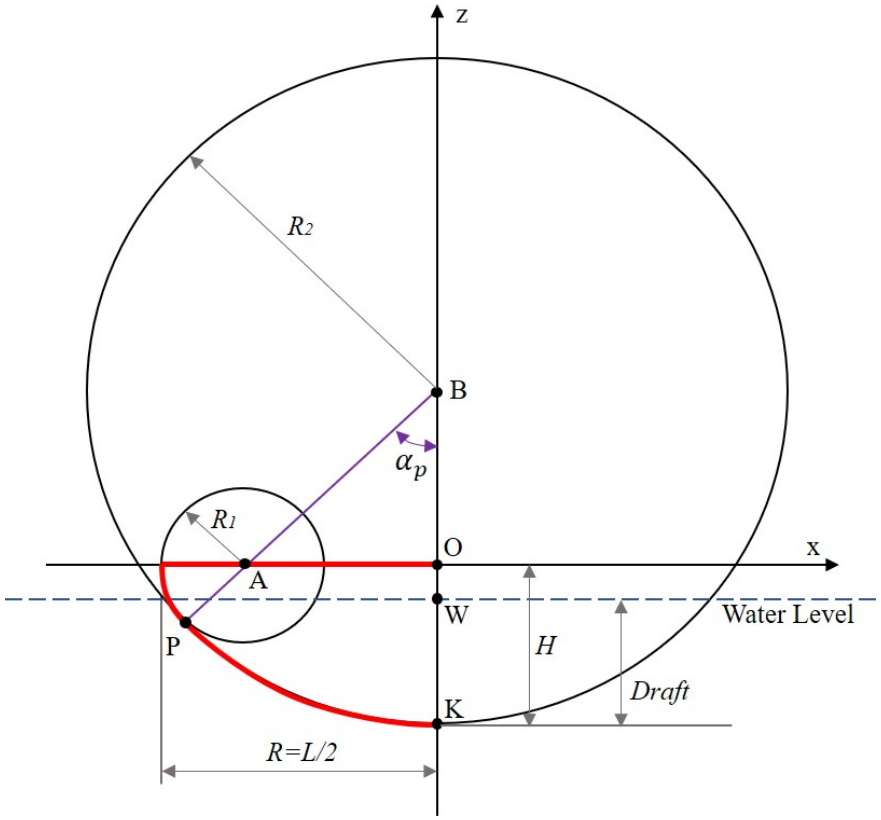

Figure 4.1 Parametrization of the floater profile.

The origin O lies on the middle of the deck, the x-axis coincides with the floater deck and the z-axis and the z-axis points upwards. The parameters involved in the hull profile function are:

- **R**: Semilength of the floater, $R = \frac{L}{2}$
- **H**: Overall height of the hull. Distance between keel and deck.
- **R_1 and x_A**: radius of the circumference C_1 and the x-coordinate of its center (z_A is fixed, $z_A = 0$)
- **R_2 and z_B**: radius of the circumference C_2 and the z-coordinate of its center (x_B is fixed, $x_B = 0$)
- **α_P**: angle $\angle PBO$

The hull profile is described by two circumferences C_1 and C_2 internally tangent. Therefore, from the tangency relation we can write:

$$|R_2 - R_1| = \overline{AB} = \sqrt{x_A^2 + z_B^2} \tag{4.1}$$

For the sake of simplification, the hull profile may be expressed as a function of geometrical ratios. These parameters, with the hull overall length L and the overall width W will constitute the design parameters of the floater system:

- **L**: Overall length of the hull
- **W**: Overall width of the hull
- **h**: ratio between x_A and the semilenght of the hull $R \longrightarrow h = \frac{x_A}{R}$
- **k**: ratio between H and the semilength of the hull $R \longrightarrow k = \frac{H}{R}$

Therefore, all the floater profile can be expressed in uniquely as a function of these design parameters:

$$R_1 = R - x_A = R(1-h) \tag{4.2}$$

$$z_B = R\frac{k^2 + 1 + 2kh - 2h - 2k}{2 - 2h - 2k} \tag{4.3}$$

$$R_2 = z_B + H = z_B + kR \tag{4.4}$$

$$\alpha_P = asin\left(\frac{z_B}{x_A}\right) \tag{4.5}$$

Where z_B has been calculated subsituting the known design parameters into Equation (4.1). Hence, the floater profile function $z(x)$ can be defined as:

$$z(x) = \begin{cases} z_A - \sqrt{R_1^2 - (x - x_A)^2}, & when \quad -R < x \leq -R_2 sin(\alpha_P) \\ z_B - \sqrt{R_2^2 - (x - x_B)^2}, & when \quad -R_2 sin(\alpha_P) < x \leq 0 \end{cases} \tag{4.6}$$

Figure 4.2 shows an example of how the hull profile is drawn in Matlab starting from specific design parameters and Figure 4.3 explain how the geometrical ratios k and h influence the hull profile for a fixed hull length.

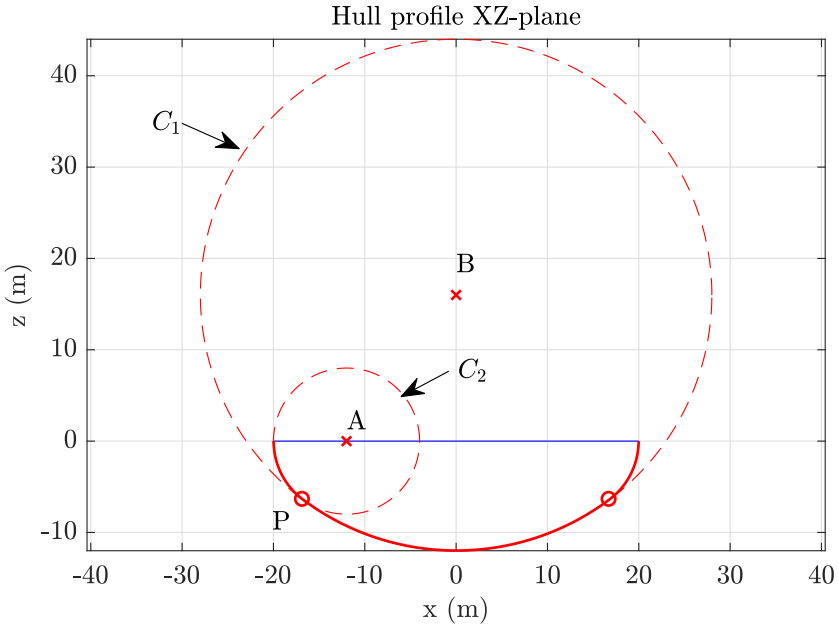

Figure 4.2 Example of a hull XZ-plane profile drawn in Matlab.

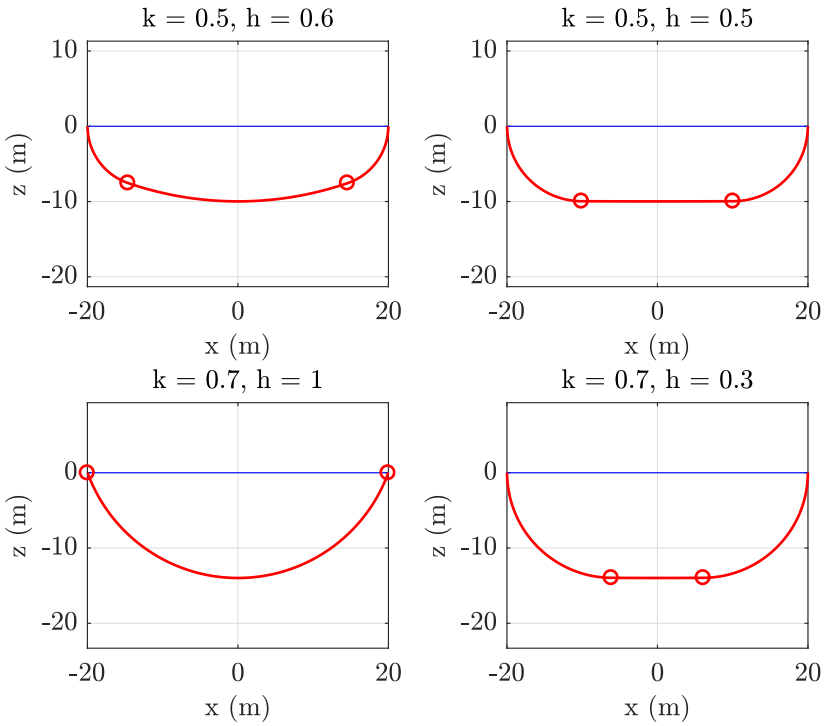

Figure 4.3 Examples of hull profiles drawn in Matlab as a function of the design parameters k and h considering a fixed hull length of $L = 20(m)$.

Floater inertial design parameters

The ballast mass and its spatial distribution influences the inertial properties of the device and therefore its dynamics. It is possible, for a given device, to identify the best ballast configuration in order to maximize the energy harvesting for a specific site. The advantage, is also the possibility to tune, in a certain range, the hydrodynamic resonance period with the prevalent wave of different installation sites avoiding the re-engineering of the device.
The ballast mass influences the draft of the floater, and its spatial distribution modify the inertia and center of gravity of the whole device. In the light of these considerations, two other design parameters related to the floater are introduced:

- **j**: ratio between the $draft$ and the height H of the Hull $\longrightarrow j = \frac{Draft}{H}$.
- **Ballast Filling Ratio (BFR)**: It determines the percentage of ballast located in aft/fore and bottom ballast tanks ($BFR = 1 \longrightarrow$ all the ballast is stored in

aft/fore ballast tanks, $BFR = 0 \longrightarrow$ all the ballast is stored in bottom ballast tank).

The ballast mass M_{bal} is uniquely defined when the device displaced mass M_{tot} and the gyroscope units mass M_{gyros}, floater structural mass M_{hull}, and U-Tank mass M_{Utank} are given:

$$M_{bal} = M_{tot} - M_{gyros} - M_{hull} - M_{Utank} \tag{4.7}$$

Figure 4.4 shows some examples of how the ballast mass can be allocated between the fore/aft and bottom ballast compartments for a given hull geometry and draft. The ballast material is assumed to be concrete, as a compromise between low material cost and density($\rho_{bal} = 3000\ \mathrm{kg\,m^{-3}}$) . The fore and aft ballast compartments are filled from the ends inwards, while the bottom ballast compartment is filled from the bottom upwards.

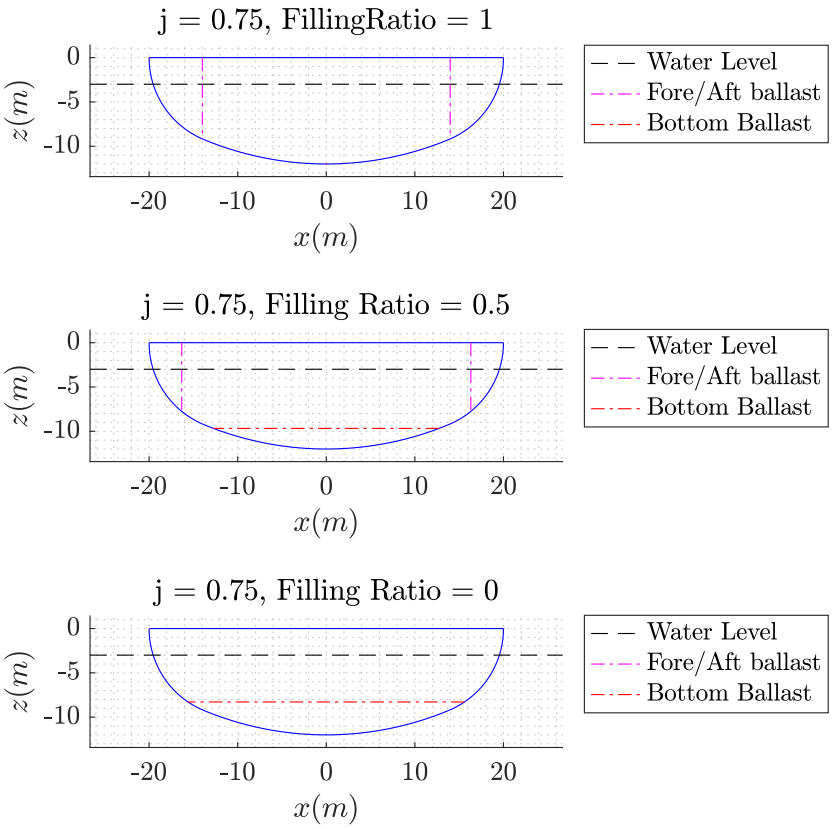

Figure 4.4 Examples of ballast mass distribution between the fore/aft and bottom compartments for a given hull geometry and draft.

As regards the hull, the chosen material is standard naval carpentry steel ($\rho_{hull} = 7800\ \mathrm{kg\,m^{-3}}$). For the sake of simplicity, an equivalent thickness of the hull structure is adopted to calculate the inertial properties of the floater. The total mass of the device is given as a function of the overall volume of the device. This relation is derived from the mass and geometrical properties of full-scale ISWEC floater:

$$M_{hull} = 90 \times V_{hull,tot}\ (kg) \tag{4.8}$$

Where $V_{hull,tot}$ is the overall volume of the floater. Since it is assumed that the walls of the floater are considered as thin plates, the equivalent structural thickness can be calculated.

4.1.2 Gyroscope Design Parameters and Assumtions

The gyroscope represents the core of the IOwec energy conversion process, and its geometrical optimization influences the maximization of power absorption, its costs and construction feasibility. Figure 4.5 shows the technological solution that is considered in this work, with reference to the gyroscope installed on the ISWEC full-scale device.

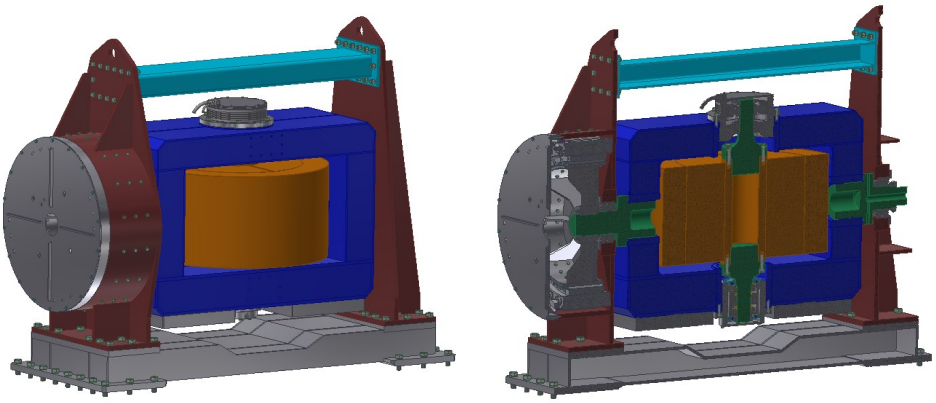

(a) (b)

Figure 4.5 (a) Gyroscope layout (b) Section of the Gyroscope: (blue)Support frame (Orange)Flywheel, (Green) Shafts and bearings.

The flywheel can rotate about its symmetrical axis driven by an electrical motor and its speed can be regulated. Two radial and axial bearings constrain the flywheel on a support frame. Other two radial bearings constrain the support frame on the hull structure. The precession oscillation of the gyroscope can be transformed into electricity by a suitable Power Take Off system (Direct Drive, Gearbox and electrical generator, hydraulic system etc.). An eccentric mass is mounted on the bottom of the support frame: as explained in Section 2.2.1 it avoids the gyroscope to reach its equilibrium position at 90° providing a stiffness torque. Moreover the eccentric mass modify the dynamic properties of the gyroscope about its precession axis ε that can be tuned to maximize the power extraction. Two design parameters for the gyroscopic system are defined:

- **J**: Flywheel inertia about its rotational axis.
- $\mathbf{m_p}$: mass of the eccentric steel block mounted on the bottom of the support frame.

All other gyro parameters are derived from these design parameters, on the basis of certain assumptions.

Flywheel

With reference to the Figure 4.6, the flywheel structure can be simplified as a hollow cylinder, identified by an external diameter, $D_{e_{fw}}$, an internal diameter $D_{i_{fw}}$ and a height H_{fw}.

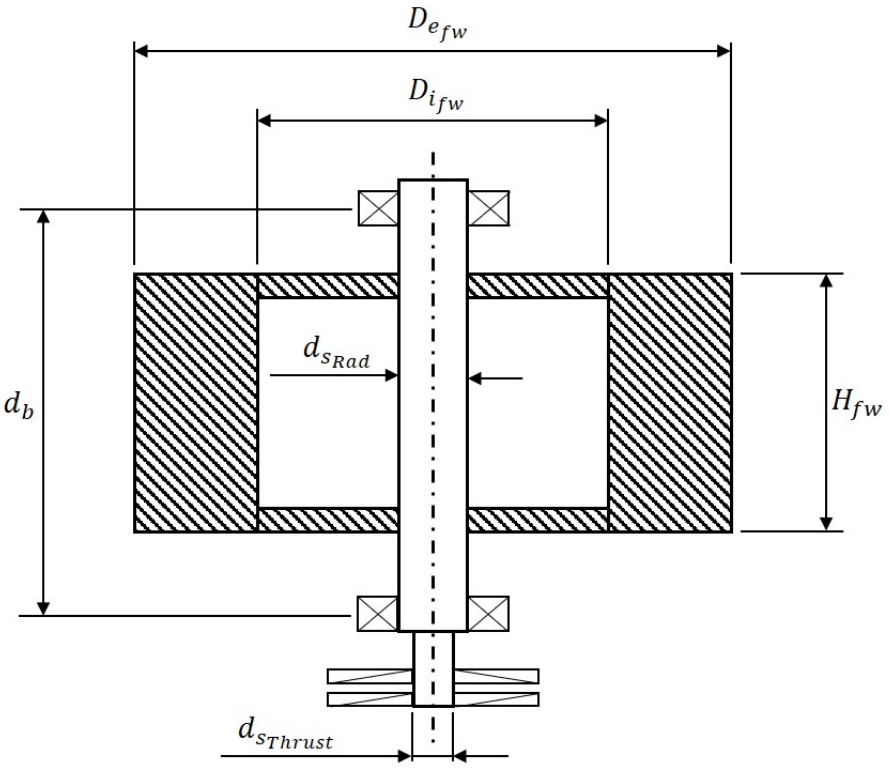

Figure 4.6 Sketch of the flywheel and its geometrical parameters.

First, the geometrical properties of the flywheel are related with geometrical ratios as a function of the external diameter $D_{e_{fw}}$ (the values of the geometrical ratios are derived from the flywheel of ISWEC device):

- k_{fw}: ratio between the flywheel height H_{fw} and the external diameter $D_{e_{fw}}$, $\longrightarrow k_{fw} = \frac{H_{fw}}{D_{e_{fw}}} = 0.5$.

- w_{fw}: ratio between the flywheel internal diameter $D_{i_{fw}}$ and the external diameter $D_{e_{fw}}$, $\longrightarrow w_{fw} = \frac{D_{i_{fw}}}{D_{e_{fw}}} = 0.75$.

The principal moments of inertia for a hollow cylinder about the rotational axis are:

$$I_{fw_{xx}} = \frac{m_{fw}}{12}\left(3\left(R_{e_{fw}}^2 + R_{i_{fw}}^2\right) + H_{fw}^2\right) \tag{4.9}$$

$$I_{fw_{yy}} = \frac{m_{fw}}{12}\left(3\left(R_{e_{fw}}^2 + R_{i_{fw}}^2\right) + H_{fw}^2\right) \tag{4.10}$$

$$I_{fw_{zz}} = J = \frac{m_{fw}}{2}\left(R_{e_{fw}}^2 + R_{i_{fw}}^2\right) \tag{4.11}$$

$$m_{fw} = \rho_{steel}\pi H_{fw}\left(R_{e_{fw}}^2 - R_{i_{fw}}^2\right) \tag{4.12}$$

Where $I_{fw_{ii}}$ is the moment of inertia about the i-th axis, m_{fw} is the mass, $R_{e_{fw}}$ and $R_{i_{fw}}$ are the external and internal radius, ρ_{steel} is the density of the flywheel ($\rho_{steel} = 7800\ \mathrm{kg\,m^{-3}}$). The flywheel geometry and moments of inertia about the x and y axis are uniquely defined given the design parameter J and the fixed geometrical ratios:

$$R_{e_{fw}} = \sqrt[5]{\frac{J}{\rho_{steel}\pi k_{fw}\left(1 - w_{fw}\right)}} \tag{4.13}$$

Flywheel support frame

The moments of inerzia $I_{s_{ii}}$ of the support frame about the i axis are given as function of the flywheel moment inertia $I_{fw_{ii}}$. The inertial ratios are derived from the ISWEC full-scale device:

- $h_{s_{xx}} = \frac{I_{s_{xx}}}{I_{fw_{xx}}} = 0.746$.
- $h_{s_{yy}} = \frac{I_{s_{yy}}}{I_{fw_{yy}}} = 1.80$.
- $h_{s_{zz}} = \frac{I_{s_{zz}}}{I_{fw_{zz}}} = 0.855$.

- $h_{s_m} = \frac{m_s}{m_{fw}} = 0.55$.

Where I_s and m_s are respectively the moment of inertia and the mass of the support frame.

Gyroscope Unit

It is assumed that the overall dimensions and moments of inertia of the gyroscope unit are a linear function respectively of the flywheel external diameter $D_{e_{fw}}$ and its momenta of inertia. Therefore, The following relationships can be obtained (derived from the ISWEC device):

- $Unit_{length} = 2.33 D_{e_{fw}} + 3.2$.
- $Unit_{width} = D_{e_{fw}} + 1.2$.
- $Unit_{Height} = 3.6 D_{e_{fw}}$.
- $I_{unit} = I_{fw} + I_s$.
- $mass_{unit} = 3 mass_{fw}$.

Where I_{unit} is the inertial tensor of the whole gyroscopic unit. The calculation of the gyro unit overall dimensions and inertial properties are useful to to verify the encumbrances inside the hull and to estimate as accurately as possible the inertial properties of the device. For the sake of simplification, the centre of gravity of the gyroscopic unit is assumed to coincide with its geometrical centre.

Gyroscope Units Layout

The realization of a single gyroscope with a high inertia J can result in technological and performance problems, high loads and costs. One solution is to distribute the inertia on different units of gyroscopes, with a consequent reduction of the loads on the single units. In addition, the number of gyro units becomes a new design parameter. It is assumed that the gyroscopic units are in even number to avoid roll torques on the hull as explained in section 2.2.1. First, the algorithm tries to locate

the units along the y-axis, and if the total width exceed the hull width, then it tries to arrange the units in two parallel and adjacent lines as shown in figure 4.7.

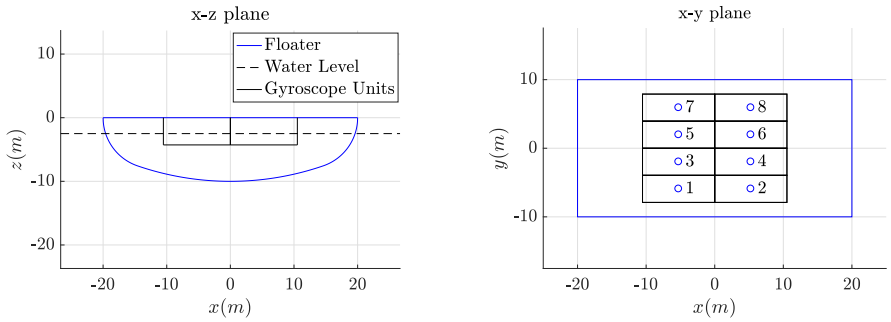

(a) (b)

Figure 4.7 Example of the gyroscope units layout (a) Plane X-Z (b) Plane X-Y.

Gyroscope eccentric mass

Figure 4.8 shows the sketch of the gyroscope in the reference plane $x-z$ and how the eccentric mass is mounted on the system.

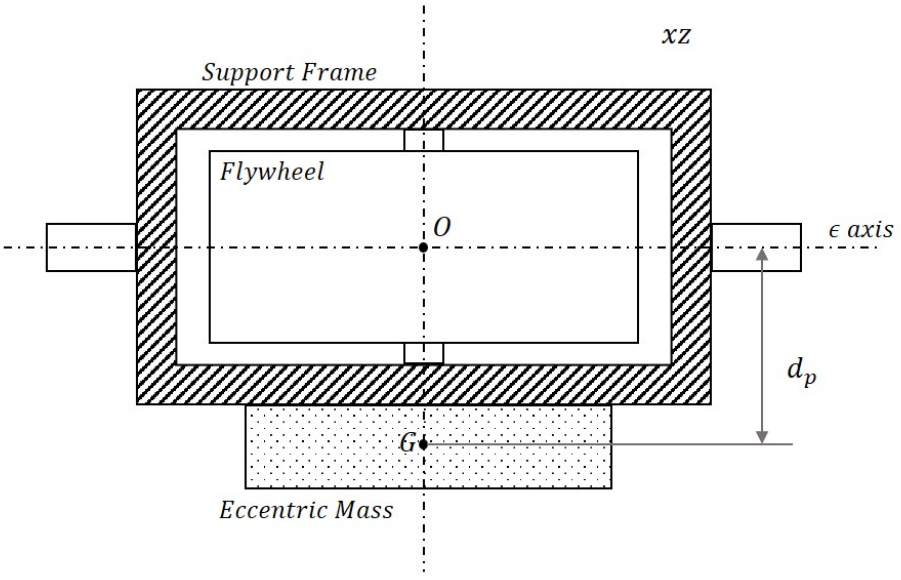

Figure 4.8 Sketch of the eccentric mass mounted on the gyroscope.

It is assumed that the distance d_p between the origin of the inertia tensor of the gyroscope and the centre of gravity of the eccentric mass is a function of the flywheel height:

- $p = \frac{d_p}{H_{fw}} = 1$

On the other hand, the mass m_p is chosen to be a design parameter as discussed in Section 4.1.2. Therefore, it is possible to define the linearized stiffness due to the eccentric mass about the ε- axis:

$$k_\varepsilon = m_p g d_p \tag{4.14}$$

With reference to equation (2.108) the inertia of the gyroscope about the ε can be computed, taking into account the mass of the eccentric mass and neglecting its inertia:

$$I_g = I_{fw_{xx}} + I_{s_{xx}} + m_p d_p^2 \tag{4.15}$$

Flywheel Bearings

The main sources of energy dissipation in the ISWEC [49] and then IOwec system are principally:

- energy loss due to the flywheel radial and axial bearings.
- efficiency of the Power Take Off system. In the case of ISWEC is due to the mechanical losses of the gearbox and electrical efficiency of the electrical torque generator.
- aerodynamic dissipation of the flywheel.
- electrical efficiency of the flywheel motor.
- fixed electrical energy consumption due to auxiliary systems (control systems, cooling pumps, electronic panels etc.).

Some of these losses, such as the PTO losses and the efficiency of the electrical motors can be estimated only in a later design phase, when the project of the device is more mature. For the sake of simplicity, only the losses due to the flywheel radial and axial bearings are considered. The bearings layout and type of IOwec is assumed to be the same of the ISWEC device:

- two spherical roller bearings that allows the rotation of the flywheel and support the radial flywheel force components.
- two axial roller thrust bearings that balance the flywheel axial force due mainly to the weight force.

The mechanical design of the flywheel bearings involves a static and fatigue verification. The axial load are due mainly to the weight force, and then the fatigue verification is more restrictive. Instead, the radial bearings are subject to the radial forces, that are a combination of the weight force and the gyroscopic torque T_λ (see eq. 2.57) which is more relevant. As regards the radial bearings, the static verification is more restrictive than the fatigue verification. The maximum static load that the bearings can allow is given in the bearings catalogue and named C_0. The Safety Factor SF_{bear} of the bearings is set at a value of 4 and imposed during the optimization of the control parameters (see section 4.4):

$$SF_{bear} = \frac{C_0}{F_{rad,eq}} = 4 \tag{4.16}$$

To simplify the problem the same series of radial bearings of the ISWEC device have be adopted for this preliminary study: spherical roller bearings of the SKF 232 series [97]. A set of 7 representative bearing size has been extrapolated from the SKF catalogue and their static radial load C_0 are given as a function of the inner diameter of the bearings d_s in figure 4.9:

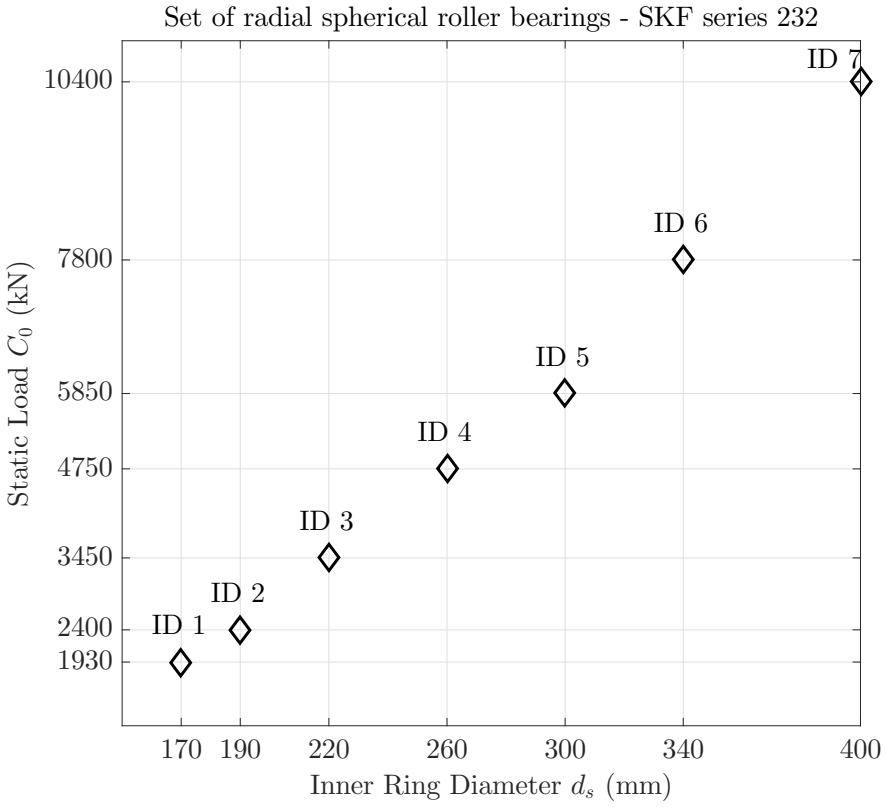

Figure 4.9 Set of selected radial spherical roller bearings SKF series 232.

This set of 7 radial bearings will be use in the genetic optimization of the device discussed in chapter 6. On the other hand, the axial bearings are considered fixed in the optimization tool, and the fatigue verification is not carried out. It is considered an inner diameter of 110 (mm) of the fixed axial bearing for the losses estimation. The distance between the radial bearings d_b is supposed to be related with the flywheel height H_{fw} (relationship derived from ISWEC device):

$$d_b = 1.75 H_{fw} \tag{4.17}$$

A first simplified equation in order to quantify the bearing losses is given in the SKF baerings catalogue and manual [97]. The time-varying power loss P_{loss} is calculated as the product of the bearing friction moment M_b and the rotational velocity of the shaft, in this case coincident with the flywheel speed $\dot{\phi}$:

$$P_{loss} = M_b \dot{\phi} \tag{4.18}$$

The bearing friction moment M_b is defined as:

$$M_b = \frac{1}{2} \mu_b F_{rad,eq} d_s \tag{4.19}$$

Where μ_b si the friction coefficient depending on the bearing type and reported in the SKF manual ($\mu = 0.0018$ for both radial and axial bearings considered).

4.1.3 Water Sloshing Tank Design Parameters and Assumptions

The geometrical and inertial properties of the U-Tank influences the dynamics of the device. With reference to Figure 4.10, the following assumptions are considered:

- According to the LLoyd theory [86], the U-Tank shape is assumed right-angled, as shown in figure 2.4. The U-Tank shape optimization with round corners to avoid flow separation will be considered at a later stage of design.
- The water mass in the U-Tank can be no more than 30 % of the total mass of the device. Once the U-Tank profile is determined by the design parameters, the tool try to calculate the U-Tank width x_t to set the water mass equal to the 30 % of the total mass of the device. If the computed x_t value is longer than the floater width, then x_t is set equal to this value.
- The upper wall of the central duct is in contact with the gyroscopic unit
- The water level h_r is given as a function of the U-Tank length w (see figure 2.4) and a U-Tank angle τ of 22 (deg). This assumption is made in order to avoid the unwanted case of no water in one of the two reservoirs (phenomenon not modelled by the Lloyds equations).

With reference to figure 2.4 the design parameters of the U-Tank system are:

- $\mathbf{UT_{W_r}} = \frac{W_r}{W_d}$.
- $\mathbf{UT_{H_d}} = \frac{H_d}{W_r}$.

- $\mathbf{UT_{W_d}} = \frac{W_d}{W_{d_{min}}}$.

$W_{d_{min}}$ defines the lower limit value of the duct length W_d and it is equal to the total length of the gyroscope units.

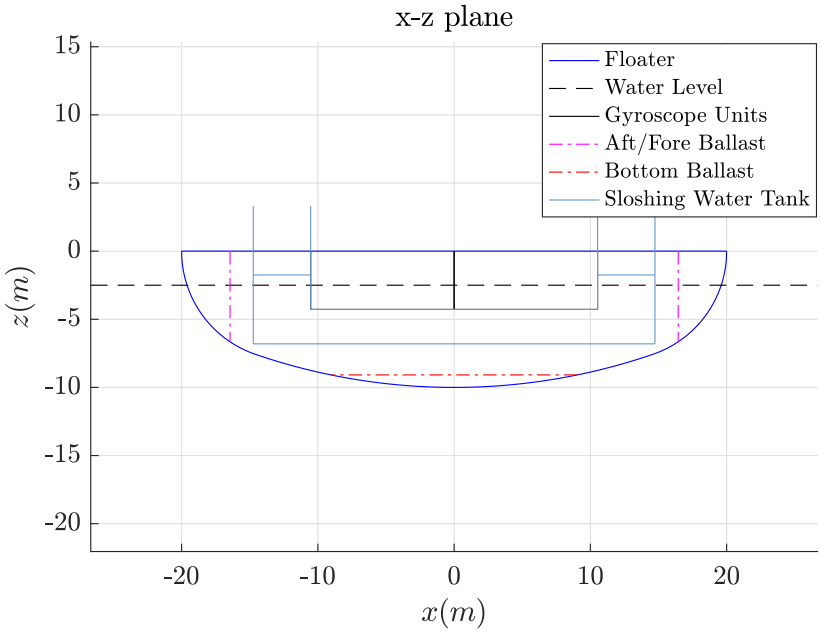

Figure 4.10 Arrangement of the U-Tank, ballast and gyro units inside the floater for a given set of design parameters.

The width x_t of the U-Tank can be calculated as:

$$x_t = \frac{\text{Volume of water}}{2w_r h_r + w_d h_d} \tag{4.20}$$

Once all the geometrical parameters are defined, the dynamical coefficients of the U-Tank can be calculated as discussed in Section 2.3.1.

4.2 Device Inertial Properties Calculation

Once all the geometrical and inertial quantities of each subsystem have been calculated, the center of gravity and the moment of inertias of the device can be defined consequently using a Matlab routine.The CoG and inertia tensor of the gyroscopic

units were defined in Section 4.1.2, while the inertial properties of the hull structure, ballast and U-Tank must be calculated. As example, the x-coordinate of the COG and the moment inertia about the same axis can be calculated as follows:

$$x_G = \frac{\int x dA}{A} \tag{4.21}$$

$$I_x = \rho \int \left(y^2 + z^2\right) dV \tag{4.22}$$

Once the center of gravity and moments of inertia of all subsystem are known, the inertial properties of the whole device can be calculated taking into account each contribution. As example, the CoG and moment of inertia about the x-axis of the device can be calculate as follows:

$$x_{G_{Device}} = \frac{\sum x_{G_i} m_i}{\Delta} \tag{4.23}$$

$$I_{x_{Device}} = \sum I_{x_i} \tag{4.24}$$

Where x_{G_i}, m_i and I_{x_i} are respectively the CoG, mass and moment of inertia of the i-th subsystem (e.g, gyroscopic units, ballast tanks) and Δ is the displacement mass of the device. All the i-th moments of inertia are calculated with reference to the device CoG. Figure 4.11 shows an example of the calculated CoGs for each subsystem and for the whole device.

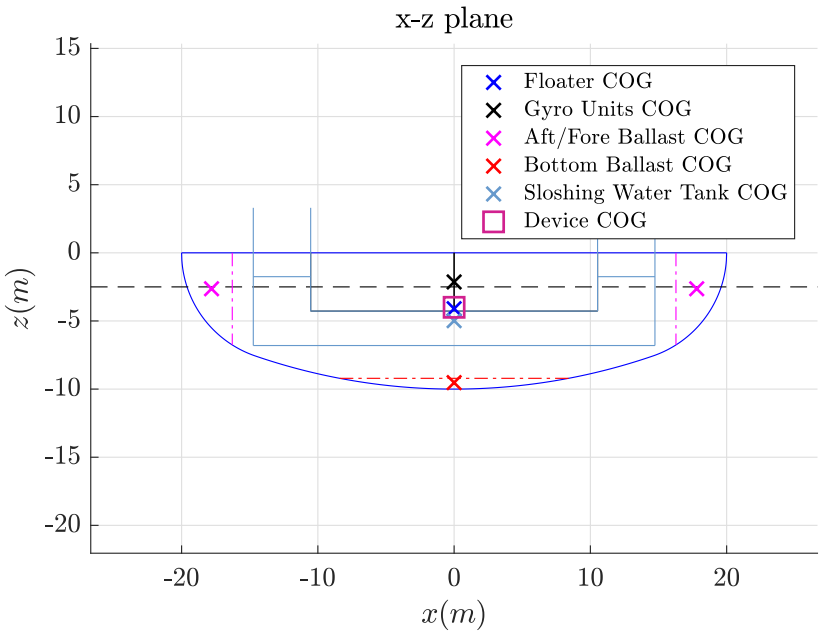

Figure 4.11 Center of gravity of each subsystem and device.

4.2.1 Feasibility check of the design solution

The device is now uniquely defined by 13 design parameters discussed in the previous sections. But some combinations of these parameters can lead to unfeasible solutions. The most common reason of solution unfeasibility are the geometrical intersection of the subsystems, for example:

- The gyroscope length, height and width are longer than respectively the hull length, height, width.
- The U-Tank system does not fit inside the device.
- There is not enough space for the desired quantity of ballast in the aft/fore or bottom compartment.
- Geometrical collisions between ballast and the gyroscope units or the U-Tank system.

These were examples of issues that lead to infeasible solutions. The tool implemented in Matlab environment is able to recognize any type of geometrical collision,

and the solution is labelled as unfeasible and the simulation is not run. If the device succeed the geometrical feasibility check, the hydrodynamic parameters of the floater are calculated.Afterwards, another check is made on the stability of the floater. In fact, a combination of design parameters can lead to a solution that is not stable at roll or pitch. A simplified routine is implemented in the tool to discard those devices that not satisfy the roll/pitch stability criteria. A floater, to be stable at roll/pitch DoF, must have its metacentric height $\overline{GM}$, defined as the distance between the device CoG G and the transverse metacentre M_T for roll and longitudinal metacentre M_L for pitch, greater than a safety value :

$$\overline{GM}_T \, , \overline{GM}_L > 1m \tag{4.25}$$

The safety value is set equal to 1 (m).

4.2.2 Device cost estimation

A preliminary evaluation of the total cost of the device can be accomplished with the following assumptions:

- The cost of the floater C_{hull} is proportional to its structural mass. In naval carpentry sector, the cost per unit mass produced c_{hull} can be reasonably assumed to be $c_{hull} = 3500$ (€/ton).
- The cost of the gyroscope C_{gyro} (flywheel, support frame, basement etc.) is proportional to its structural mass. In mechanical manufacturing, the cost per unit mass produced c_{gyro} can be reasonably assumed to be $c_{gyro} = 6500$ (€/ton).
- Since at this stage the PTO technology solution is unknown, it is assumed that the cost related to the PTO and the other auxiliary system (electronics, cooling systems etc.) is equal to the cost of the gyroscopes: $C_{PTO} = C_{Gyro}$.

The overall cost of the device C_{tot} is given by the sum of the costs of each subsystem:

$$C_{tot} = C_{hull} + C_{gyro} + C_{PTO} = c_{hull} m_{hull} + 2 c_{gyro} m_{fw} \tag{4.26}$$

4.3 Hydrodynamics Calculation

In this chapter, the numerical calculation of hydrodynamics parameters and forces acting on the hull are discussed. The previous sections described how determine the geometry and inertial properties of the whole device given the design parameters. The geometrical and inertial properties of the device are inputs of the hydrodynamics calculation tool. The floater geometry is meshed with a Matlab routine and the mesh panel dimension and number are parametrized as a function of the dimensions of the device. The hydrodynamic parameters (e.g., added mass, radiation damping, diffraction forces) are calculated using the open source Boundary Element Method (BEM) code Nemoh [65]. In order to use the time domain Cummins' equation, a state space representation of the radiation convolution term is identified using the Perez method and Matlab toolbox [71], [72]. At the end, the calculation of the irregular diffraction forces is calculated using the equations discussed in section 2.1.4. A summarized diagram of the whole hydrodynamic tool calculation is shown in Figure 4.12

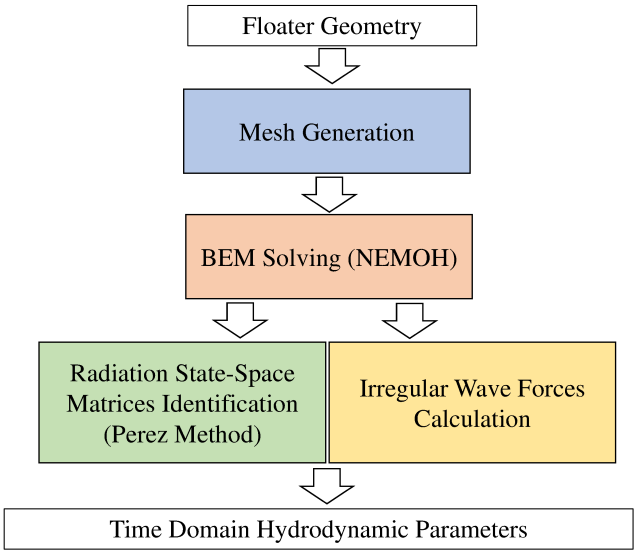

Figure 4.12 Flow diagram of the hydrodynamic parameters calculation process.

4.3.1 Hydrodynamic Frequency Domain Parameters Calculation

In this work, the hydrodynamic parameters of the floater in frequency domain are calculated using the open source BEM code Nemoh developed by the Ecole de Nantes [65]. The reason of using this tool is that this code is written in Matlab environment and therefore it can be directly implemented into the IOwec Design Tool entirely coded in Matlab. Nemoh solves the Boundary Values Problem (BVP) based on the linear potential flow theory and calculates the pressure distribution around the floater and the frequency domain parameters (see section 2.1):

- **Added Mass**.
- **Radiation damping**.
- **Froude-Krylov coefficients**.

A recent study [98], compared the Nemoh open-source code with the commercial BEM code Wamit for different wave energy converters, with good agreements for simple floater geometries as the case of IOwec device. The choice of the shortest and longest wave length λ_{min}, λ_{max} under analysis is a function of the overall length of the device L_{tot}, in order to have a flexible tool able to manage different hull geometries:

- $\lambda_{min} = L_{tot}/3$
- $\lambda_{min} = 10L_{tot}$

Within this wave length range the hydrodynamics of the device is well described and 30 values of equidistant frequencies have been adopted for the analysis.

Hull Geometry Mesh

The Nemoh tool needs in input the mesh of the floater geometry. The mesh is created by a Matlab custom routine to have more control over the number and size of mesh panel, which are expressed as a function of the dimensions of the hull. The wet geometry of the hull is described by flat quadrilateral panels, and the four vertices are defined anticlockwise as Nemoh requests. The mesh refinement influences the accuracy of the hydrodynamic parameters and the computational cost. Therefore,

the mesh size must be a compromise between calculation time and quality of the results. The Ansys Aqwa manual [99] suggests to use a panel size small relative to the shorter wave length analysed:

$$L_{max} = \frac{1}{7}\lambda_{min} \tag{4.27}$$

Where L_{max} is the maximum mesh panel size and λ_{min} is the minimum wave length analysed. A grid convergence analysis is carried out to verify this rule of thumb. The hydrodynamic properties added mass and radiation damping have been considered to evaluate the grid convergence of the hull. The analysis was performed on a single core machine Intel® Core i/-6700HQ CPU @ 2.60 GHz. The mean relative error MRE of the hydrodynamic parameters calculated with the various meshes with respect to a refined one is used as a parameter of goodness:

$$MRE = \frac{\sum_{i=1}^{n} \left| \frac{x_i - \overline{x_i}}{\overline{x_i}} \right|}{n} \tag{4.28}$$

Where x_i is the hydrodynamic property of interest (i.e. the added mass) of the coarser mesh case for the i-th wave frequency of analysis, $\overline{x_i}$ is the respective value of the very-fine reference mesh case and n is the total number of analysed wave frequencies. For the mesh convergence analysis, a floater with an overall length of 40 m has been chosen, and therefore the shorter analysed wave length λ_{min} is equal to 13.3 m (2.9 s of wave period). In Table 4.1 the properties of the meshes under study are given.

Table 4.1 Characteristics of the hull meshes used for the convergence analysis.

Mesh ID	max panel size	n° of panels
	m	-
G1	$\lambda_{min}/3$ - 4.5 m	58
G2	$\lambda_{min}/5$ - 2.7 m	150
G3	$\lambda_{min}/7$ - 1.9 m	282
G4	$\lambda_{min}/9$ - 1.5 m	510
G5	$\lambda_{min}/11$ - 1.2 m	738
G6	$\lambda_{min}/13$ - 1.0 m	1006
G7	$\lambda_{min}/15$ - 0.9 m	1344

Figure 4.13 shows an example of the generated mesh for the G3 mesh case.

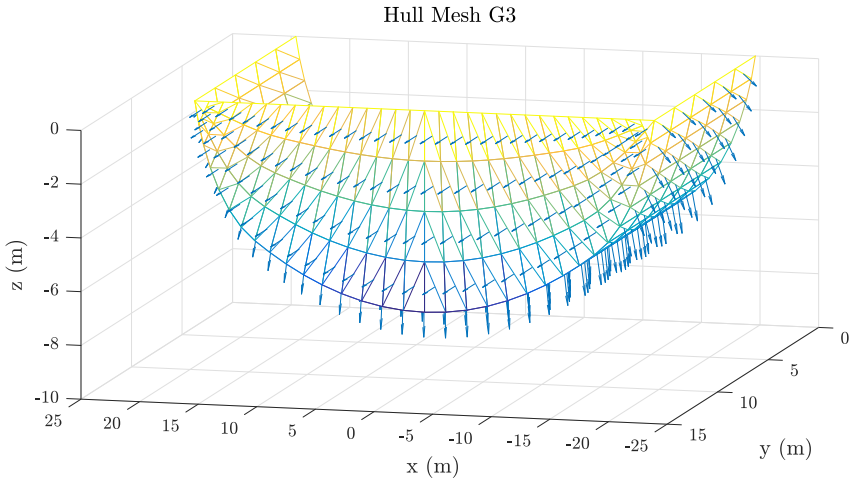

Figure 4.13 Example of the floater geometry mesh G3 used for the convergence analysis.

The computational time for the calculation of the hydrodynamic parameters is proportional to the square of the number of panels as shown in Figure 4.14.

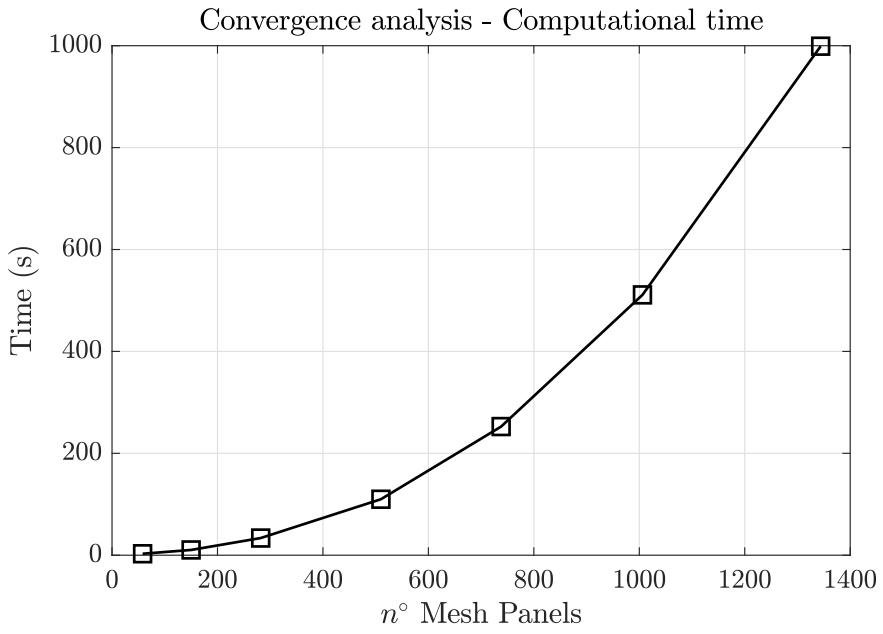

Figure 4.14 Computational time of the hydrodynamic parameters computation.

The influence of the mesh grid on the calculation of the hydrodynamic parameters is highlighted in Figure 4.15 with a comparison between the very coarse mesh G1, a medium-fine mesh G3 and the very-fine mesh G7. For higher frequencies the coarser mesh shows high irregularities and therefore can not be used for the computation. Instead, the medium-fine mesh shows similar results compared to the very-fine mesh.

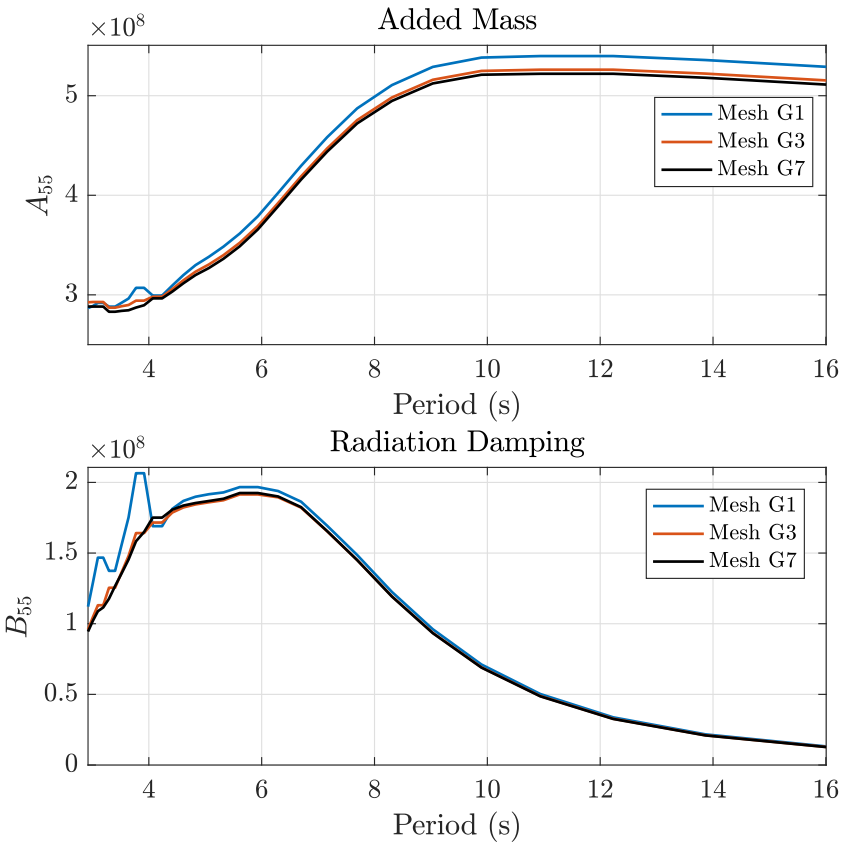

Figure 4.15 Added mass and radiation damping for different mesh grids.

These considerations are summarized in Figure 4.16 where the MRE trends of the added mass and radiation damping are plotted as a function of the number of panels of the mesh. The reference is the very-fine mesh G7 and the MRE shows a good convergence towards the finest mesh. These results show that the mesh G3 is a good compromise between the computational time and quality of the results: the MRE of the hydrodynamic parameters are less than the 2% with reference to the finest mesh analysed.

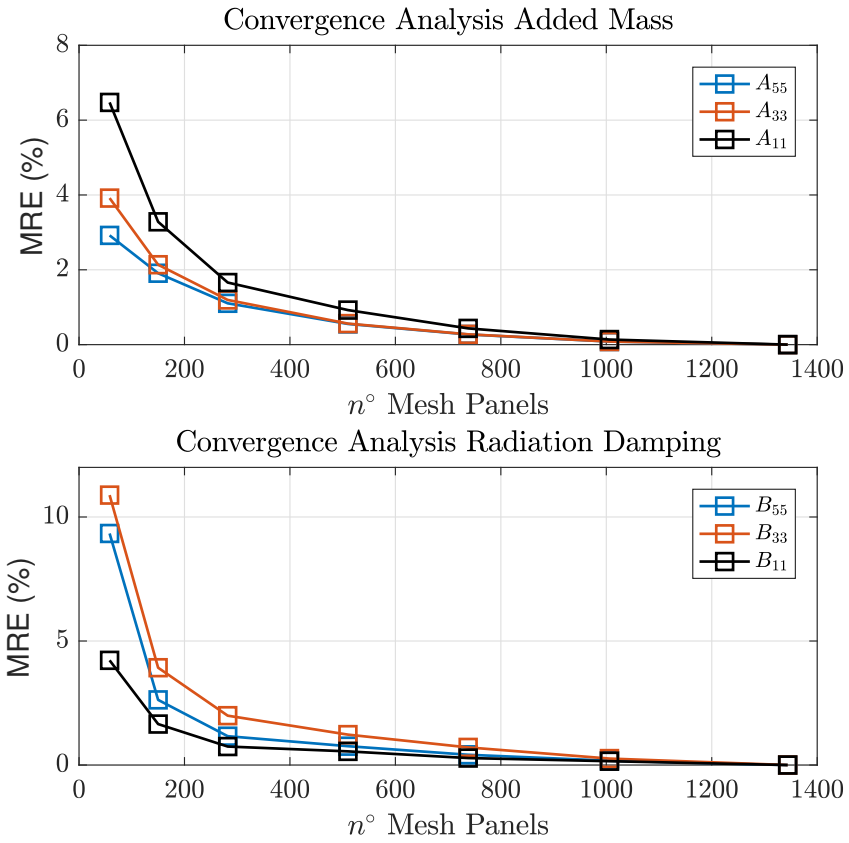

Figure 4.16 Convergence analysis of the hull mesh.

4.3.2 State Space realization of the radiation damping

The BEM tool Nemoh allows the user to compute the all the hydrodynamic parameter of a hull in frequency domain, but a further effort must be done to simulate the floater dynamics in time domain. As discussed in section 2.1.3 the dynamics of the floater in time domain can be described by the Cummins' integro-differential equation where the time domain hydrodynamic properties added mass at infinite frequency and the radiation impulse response can be calculated thanks to the Ogilvie relations. In this model the radiation forces are represented by a convolution term, and it constitutes a drawback in terms of calculation time and a flexible representation of the model for control and analysis purposes. Therefore, it is convenient to approximate the convolution term with a state-space representation:

$$F_r = \int_0^t h_r(t-\tau)\dot{X}d\tau \simeq \begin{cases} \dot{\zeta}_r = A_r\zeta_r + B_r\dot{X} \\ F_r = C_r\zeta_r + D_r\dot{X} \end{cases} \tag{4.29}$$

The state space matrices A_r, B_r, C_r and D_r in this work are identified using the method proposed by Perez [71, 72] and his toolbox is implemented in the IOwec Design Tool. The determination of the state-space order that best approximates the convolution term is given by a Matlab routine which involves the following steps:

- The radiation state-space model is identified through Perez routine and calculated four different state-space orders within the range [2-5].
- The Normalised Root Mean Square Error (NRMSE) is calculated between the estimated added mass $\hat{A}$ and radiation damping $\hat{B}$ and the added mass A and radiation damping B calculated originally trough Nemoh.
- The state-space order with the smallest NRMSE is chosen and used later in the simulation.

This routine is repeated for each degree of freedom involved in the numerical model. Figure 4.17 shows an example of the results of the State-space approximation of the radiation forces.

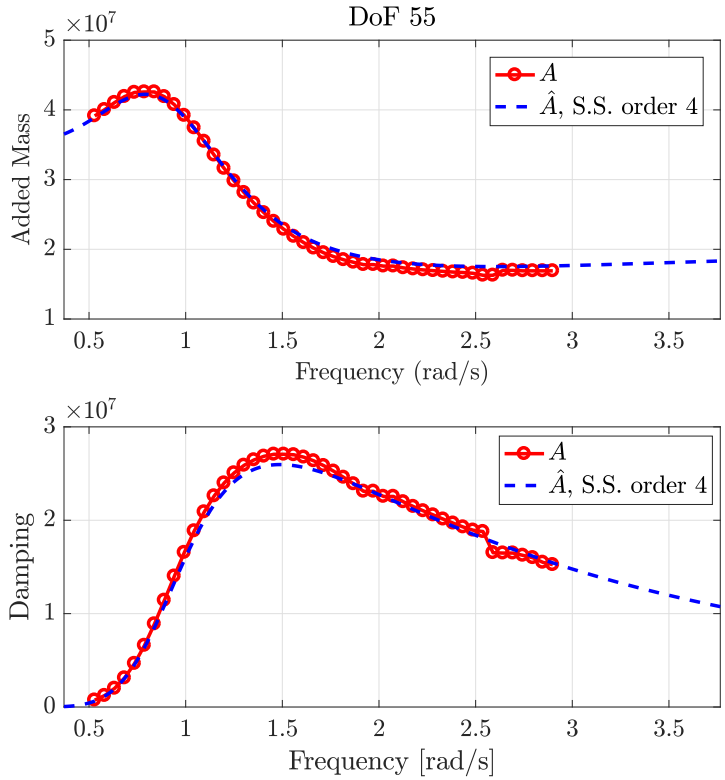

Figure 4.17 Example of identification results for pitch DoF. The estimated added mass $\hat{A}$ and radiation damping $\hat{B}$ are compared with the added mass A and radiation damping B calculated originally trough Nemoh. The optimal device ID 2761 has been chosen for the study (see section 6.3.2).

4.3.3 Irregular wave forces calculation

The performances of the floater are evaluated in irregular wave conditions and the first order wave excitation forces as stated are the only external forces considered in this preliminary work.

Given a wave spectrum model characterized by a significant wave height H_s and energetic period T_e, the pseudorandom unidirectional wave profile $\eta(t)$ can be calculated as superposition of sinusoidal wave components:

$$\eta(t) = \sum_{i=1}^{n} a_i sin(\omega_i t + \theta_i) \tag{4.30}$$

$$a_i = \sqrt{2 S_{\eta_i} \Delta\omega} \tag{4.31}$$

Where $\Delta\omega$ is the frequency resolution, n is the total number of frequencies, ω_i is a discrete spectrum frequency and S_{η_i} is the associated value of spectral energy density, θ_i is the associated pseudo-random phase in the range $[0, 2\pi]$, a_i is the amplitude of the sinusoidal i-th wave component. Therefore, it is possible to calculate the first order excitation forces associated to a specific floater geometry and sea state condition acting on the j_{th} DoF:

$$F_{w_j}(t) = \sum_{i=1}^{n} \left| f_{FK_{j,i}} \right| a_i sin\left(\omega_i t + \theta_i + \angle f_{FK_{j,i}}\right) \tag{4.32}$$

Where $f_{FK_{j,i}}$ is the Froude-Krylov diffraction coefficient calculated by Nemoh associated to the j_{th} DOF and the i_{th} wave frequency.

4.4 Time Domain Simulation

Once all the device parameters are defined and the hydrodynamic properties and external forces are computed, the time domain simulation of the device can be carried out under some hypothesis and restrictions described in this section.
The time domain model is based on the Iswec Design Tool work presented in [100] and it presents several improvements:

- Implementation of a 3-DoF hydrodynamical model (surge,pitch,heave) instead of the 1DoF model.
- The gyroscope stiffness term is now provided by an eccentric mass, reducing also the control parameters.
- The IOwec Design Tool calculates the geometrical, inertial and hydrodynamic properties of the device through Matlab routines in a unique flexible tool. The ISWEC Design Tool did not provided these features: the geometrical and inertial properties used to be calculated with the CAD software SolidWorks ® and the hydrodynamic parameters with Ansys Aqwa®.
- Implementation of the U-Tank lumped parameters model.

At this preliminary assessment stage, the Power Take Off is not modeled, and also the technology solution adopted is not specified and it will be carried out in a later stage of the project. In fact, the range of possible PTO solutions is wide and they depend on the entity of the gyroscopic torques, velocities and technology cost and feasibility: spacing from an electrical to an hydraulic PTO solution [84]. Therefore, also the losses related to the PTO system are neglected at this phase, because they depend on the adopted technology solution.

With reference to section 2.2.1, the PTO torque is controlled with the following law:

$$T_{PTO} = c\dot{\varepsilon} \tag{4.33}$$

Where c is the PTO damping coefficient which should be tuned with the sea-state. The net absorbed mechanical power P_{net} avaible at the PTO can be calculated as:

$$P_{net} = c\dot{\varepsilon}^2 - P_{loss} \tag{4.34}$$

Where P_{loss} are the power losses due to the radial and axial bearings and explained in detail in section 4.1.2. Both the PTO damping parameter c and the flywheel speed $\dot{\phi}$ constitute the control parameters and they can be optimized to maximize the power extraction for a specific sea state condition.

4.4.1 State variables constraints

A constrained local-search optimization algorithm is implemented to find the optimal control parameters $\left[c, \dot{\phi}\right]$ given the sea-state condition. In this work, a Matlab routine that implements the Nelder-Mead simplex algorithm [101], is adopted. This Matlab routine is called *fminsearchbnd* [102] and it is a modified version of the original Matlab function *fminsearch* [103] (for unconstrained problems) that permits the inclusion of boundaries on the problem.
As discussed in [100], when an optimization algorithm is applied to a linear system there is the probability that some state variables overcome the linear limit conditions and then the results are not reliable or representative. Therefore, soft constraints on

these state variables should be added. Moreover, the constraint of other simulation output may be of interest, such as the forces acting on the flywheel bearings. A way to consider soft constraints it's to add penalty functions to the optimization problem, and the fitness value Y to be minimized can be written as:

$$Y = P^*_{net} + \sum J_i \tag{4.35}$$

Where P^*_{net} is the net power term,negative when absorbing power, and the penalty functions J_i related to the system variables are considered always positive. Both the net power term and the net variables in the cost functions are normalized to assume the same order of magnitude and being comparable:

$$P^*_{net} = \frac{P_{net}}{P_0} \tag{4.36}$$

$$x^* = \frac{x}{x_{constr}} \tag{4.37}$$

where x is a specific simulation output of interest, P_0 is a reference value for the normalization of the net power and x_{constr} is the soft constraint associated with the output x. The generic penalty function $J(x^*)$ is defined as:

$$J(x^*) = \frac{1 + tanh\left(k\left|x^*\right| - 1\right)}{2} + H\left(x^*\right)\left(\left|x^*\right| - 1\right) \tag{4.38}$$

Where k is a constant value that influence the steepness of cost function and $H\left(x^*\right)$ is the Heaviside function:

$$H\left(x^*\right) = \begin{cases} 0, \left|x^*\right| < 1 \\ 1, \left|x^*\right| > 1 \end{cases} \tag{4.39}$$

Figure 4.18 shows the plot of a generic penalty function: when the output x is lower than the limit value x_{constr} no penalization is added, and when it overcomes the soft constraint an increasing penalization is applied.

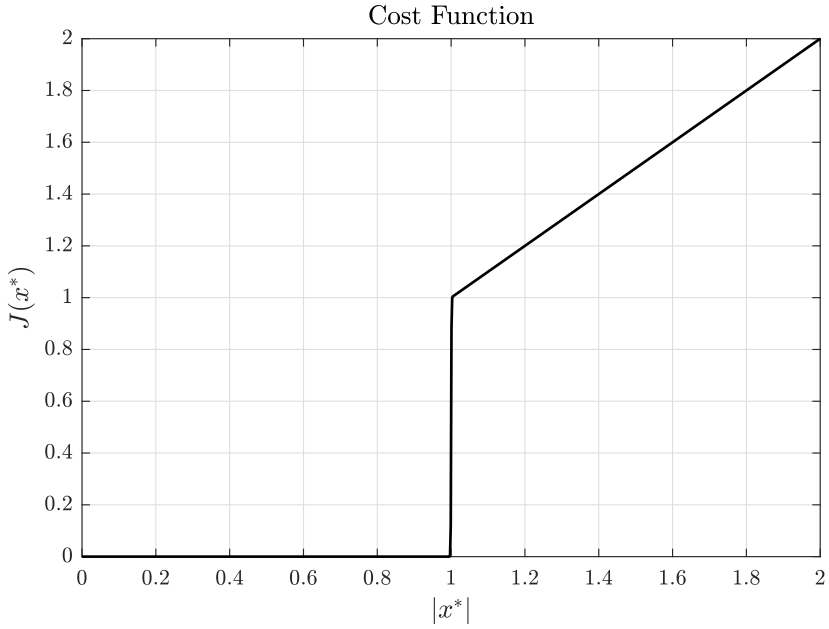

Figure 4.18 Cost function associated to the generic normalized state variable x^*

In this work, the simulation output considered to be constrained are:

- ε_{rms} : rms value of the precession oscillation of the gyroscope.
- τ_{rms} : rms value of the angle between the water level in the two reservoirs of the U-Tank.
- $Frad,max$: maximum value of the radial bearing force.

The chosen maximum rms value of the gyroscope precession oscillation ε_{rms} is 60°. The maximum value of τ_{rms} is chosen from geometrical considerations: the two water reservoirs should not get empty in order to guarantee the assumptions of the Lloyd's model [86]:

$$\tau_{rms_{constr}} = atan\left(\frac{2h_r}{w_d + w_r}\right) \tag{4.40}$$

The maximum value of the radial force bearing $F_{rad,max}$ is set equal to the static load C_0 of the bearing divided by the safety factor $SF = 4$ (see section 4.1.2). Since the PTO technology is not defined at this stage, no considerations can be made on

possible limitations of the control PTO torque and PTO velocity, and then any cost function is applied to these system outputs.

4.4.2 Control parameters boundaries

The flywheel speed control parameter should be also constrained during the optimization to not overcome the centrifugal flywheel stresses. A spinning flywheel is subject to centrifugal forces that must be taken into account during the preliminary design of the system, and the ranges of maximum permissible peripheral speeds for different materials are listed in Table 4.2.

Table 4.2 Suggested limits range of the maximum permissible flywheel peripheral speeds.

Material	$V_{p_{max}}$
	m/s
Iron	35 to 40
Steel	70 to 90
High quality steel	100

The centrifugal stress can be calculated as follows:

$$\sigma_c = \frac{\rho V_p^2}{10^6} \tag{4.41}$$

Therefore, the permissible stress related to the maximum allowable peripheral flywheel speeds can be calculated and they are shown in Table 4.3.

Table 4.3 Maximum allowable stresses for different flywheel materials.

Material	σ_{max}
	MPa
Iron	12
Steel	63
High quality steel	78

Therefore, the maximum flywheel speed $\dot{\phi}_{max}$ can be calculated given the geometry and the material as:

$$\dot{\phi}_{max} = \frac{V_{p_{max}}}{R_e} \tag{4.42}$$

Where R_e is the external flywheel radius. Also the PTO damping c can be constrained during the optimization with a maximum value c_{max}, that depends on the PTO characteristics. Since the PTO is not considered at this stage, no constraints are applied to this control parameter.

4.4.3 Time domain simulation tool

Figure 4.19 shows a diagram of the time domain simulation optimization tool. In this work, only the flywheel speed boundary is considered because as stated before the PTO system is not modelled at this design stage.

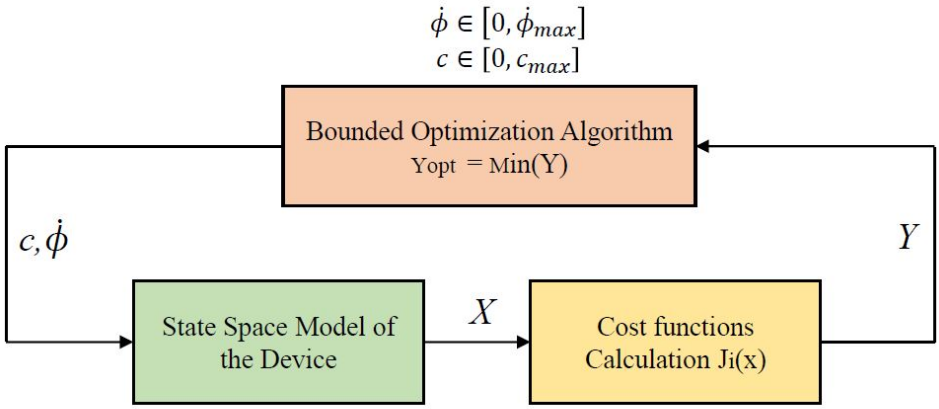

Figure 4.19 Sketch of the power net optimization process

The temporal discretization dt and the simulation time T_{sim} influence both the computational time and the standard deviation of the results. Hence, a convergence analysis of the computed mean net power is necessary to reach a good compromise

between low variance of the power and low computational time.

First, the influence of the simulation time T_{sim} on the standard deviation of the absorbed power for a fixed time step $dt = 0.2s$. The Relative Standard Deviation (RSD) of the absorbed power has been calculated for different values of simulation time. For each configuration, a sample of 100 simulations have been considered. Figure 4.20 shows the relative standard deviation *RSD* and the computational time calculated as a function of the simulation time T_{sim}. Folley et al. carried out a similar study [56], considering both linear and non-linear hydraulic PTO case. The results are in line with those proposed in this section and they stated that the precision of the absorbed power increases with the square root of T_{sim}. In conclusion, a simulation time of 1800 s (30 min) can be considered as good compromise between computational time and low standard deviation of the results.

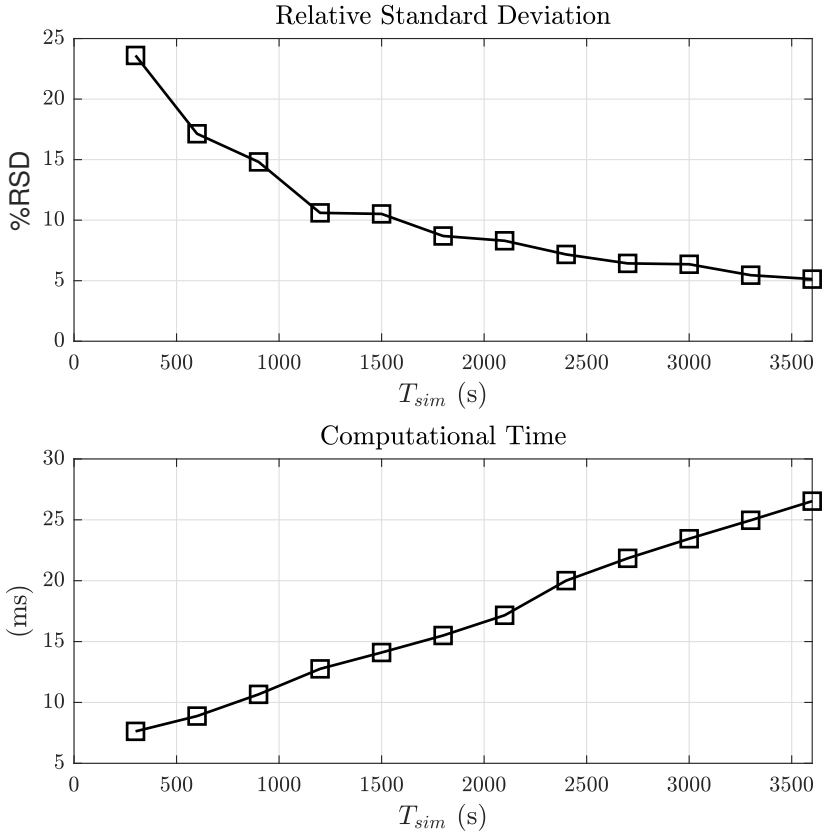

Figure 4.20 Convergence analysis on the total simulation time T_{sim}.

The convergence analysis of the simulation time step dt and the relative computational time analysis for a fixed value of total simulation time T_{sim} is shown in Figure 4.21. The relative error RE between the mean power of the coarser time steps and the finest one is calculated in order to evaluate the convergence property. In conclusion, a time step $dt = 0.2s$ has been chosen for the simulations.

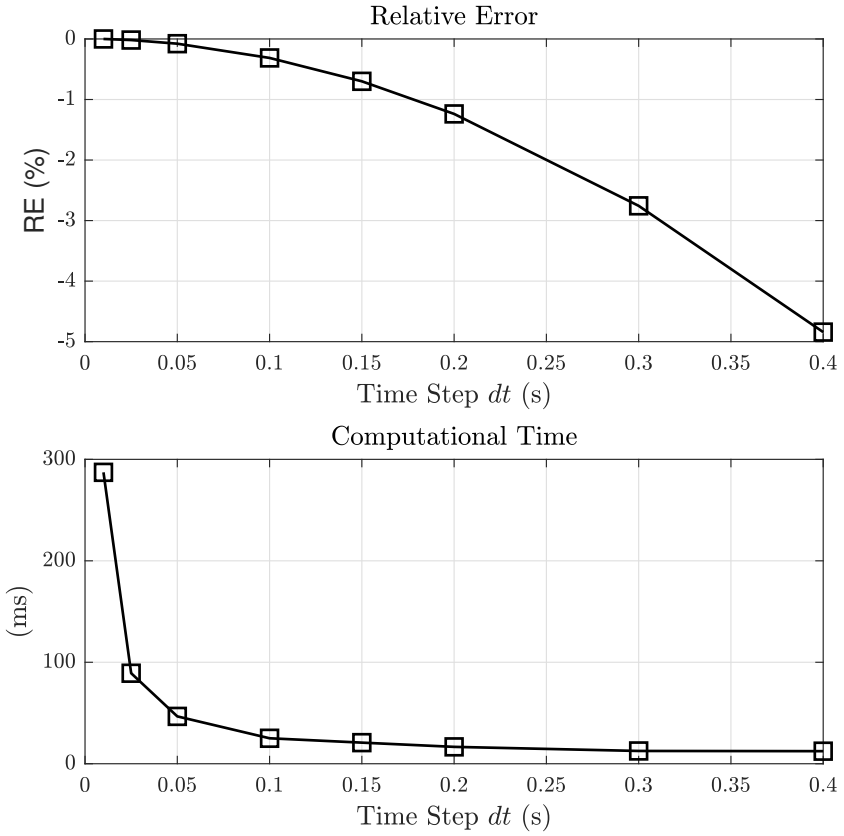

Figure 4.21 Convergence analysis of simulation time step dt.

Chapter 5

Performance assessment of the IOwec device

In this chapter a first draft of the IOwec device with the integration of the U-Tank technology is presented and its performances are discussed in different wave conditions. A first control logic of the U-Tank based on the tuning of the resonance period of the device with the incoming wave period. Then, the IOwec dynamics is analyzed in regular and irregular wave conditions. Moreover, the behavior of the IOwec system is studied in complex sea-state condition, constitute of local wind sea state and swell generated from distant storms.

5.1 Wave resource analysis

The IOwec device has been designed in order to be deployed in ocean sites where the energy resource is considerable high [1],[104]. For this work two different sites have been chosen in order to study the performance of this novel technology solution:

- Humboldt Bay, California (USA).
- Wave Energy Test Site, Hawaii, (USA).

The Department of Energy (DOE) of the United States suggested to adopt the scatter table provided by the DOE [105] in order to assess the performance of the

proposed WEC technology. The bathymetry of the site is about 50 m and the distance from the coast is 70 km, which are reasonable values for a techno-economic analysis. The US Navy Wave Energy Test Site (WETS) is located offshore of the Marine Corps Base in Kaneohe, Oahu (Hawaii, USA). The WETS is first grid-connected test site of this kind as reported by the *Hawaii Natural Energy Institute* [106]. The wave occurrences diagram of the WETS site is provided by the *University of Hawaii* [107] with an extensive study on the wave energy resource in different sites of interest along the coast of the Hawaiian islands. The occurrences tables of both sites of interest are shown in figure 5.1 and 5.2. The wave resource data was elaborated and the synthetic results are given in table 5.1.

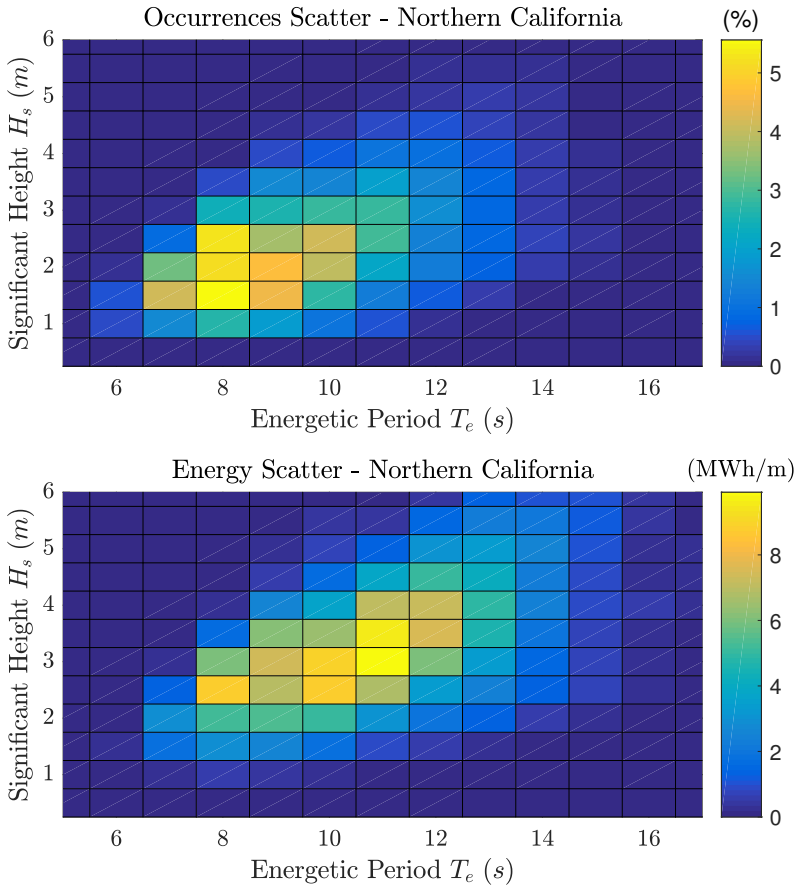

Figure 5.1 Scatter and energy diagram Northern California

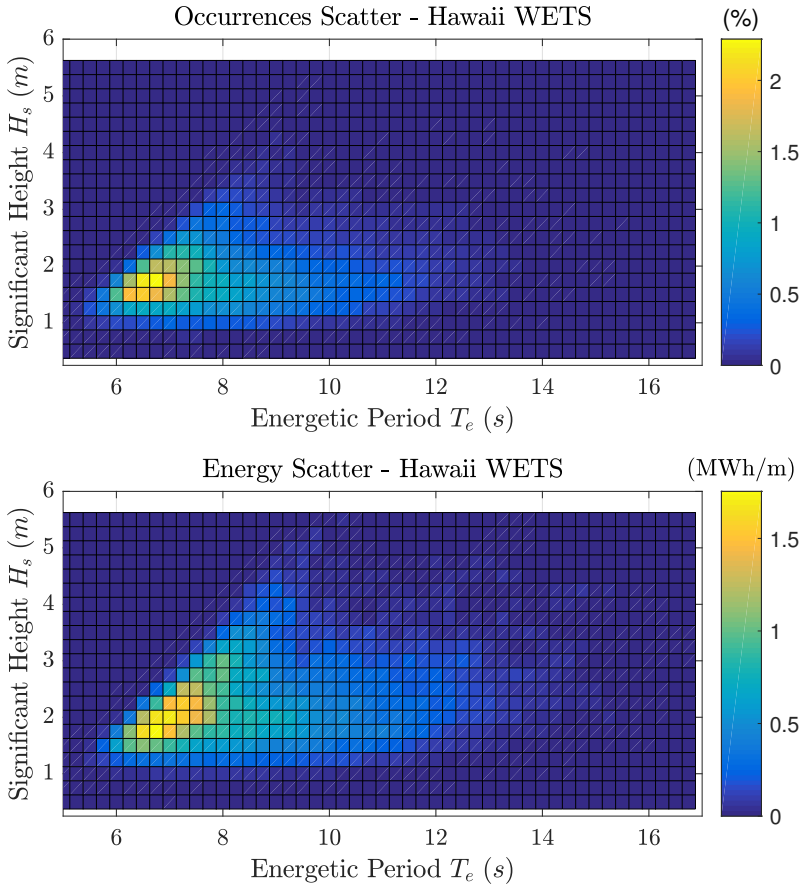

Figure 5.2 Scatter and energy diagram WETS Hawaii

The occurrences and energy diagrams of the two sites are given in figure 5.3 as a function of the energetic period. The cumulative diagrams are shown in figure 5.4. It is worth to notice that the occurrence and energy distribution of the two sites differ considerably. Californian wave resource show a spreader occurrence of sea state periods and high energetic periods. Differently, the Hawaiian test site present a concentration of sea states occurrences towards lower energetic periods compared to the wave resource of Humboldt Bay site.

Table 5.1 Wave Energy resource properties of the chosen sites of analysis

Northern California

Property	Symbol	Unit	Value
Most Probable Sea State Energetic Period	T_e	s	7.50
Most Probable Sea State Significant Height	H_s	m	1.5
Most Probable Sea State Power	P	kW/m	8.43
Most Energetic Sea State Energetic Period	T_e	s	10.50
Most Energetic Sea State Significant Height	H_s	m	2.75
Most Energetic Sea State Power	P	kW/m	39.71
Average Annual Wave Power	P_w	kW/m	27.1
Total Annual Energy	E_{tot}	MWh/m	238.2

WETS Hawaii

Property	Symbol	Unit	Value
Most Probable Sea State Energetic Period	T_e	s	6.62
Most Probable Sea State Significant Height	H_s	m	1.63
Most Probable Sea State Power	P	kW/m	8.75
Most Energetic Sea State Energetic Period	T_e	s	6.62
Most Energetic Sea State Significant Height	H_s	m	1.63
Most Energetic Sea State Power	P	kW/m	6.62
Average Annual Wave Power	P_w	kW/m	14.1
Total Annual Energy	E_{tot}	MWh/m	123.3

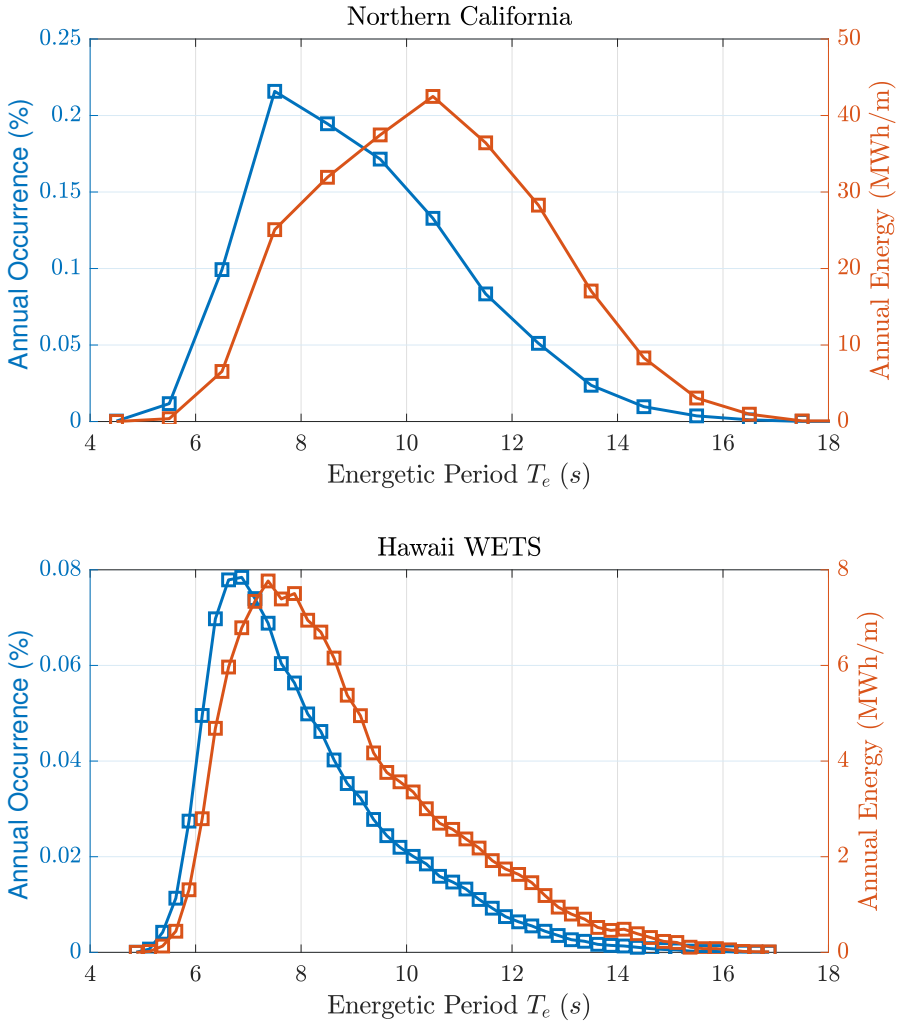

Figure 5.3 Occurrences and energy diagrams as a function of the energetic period T_e.

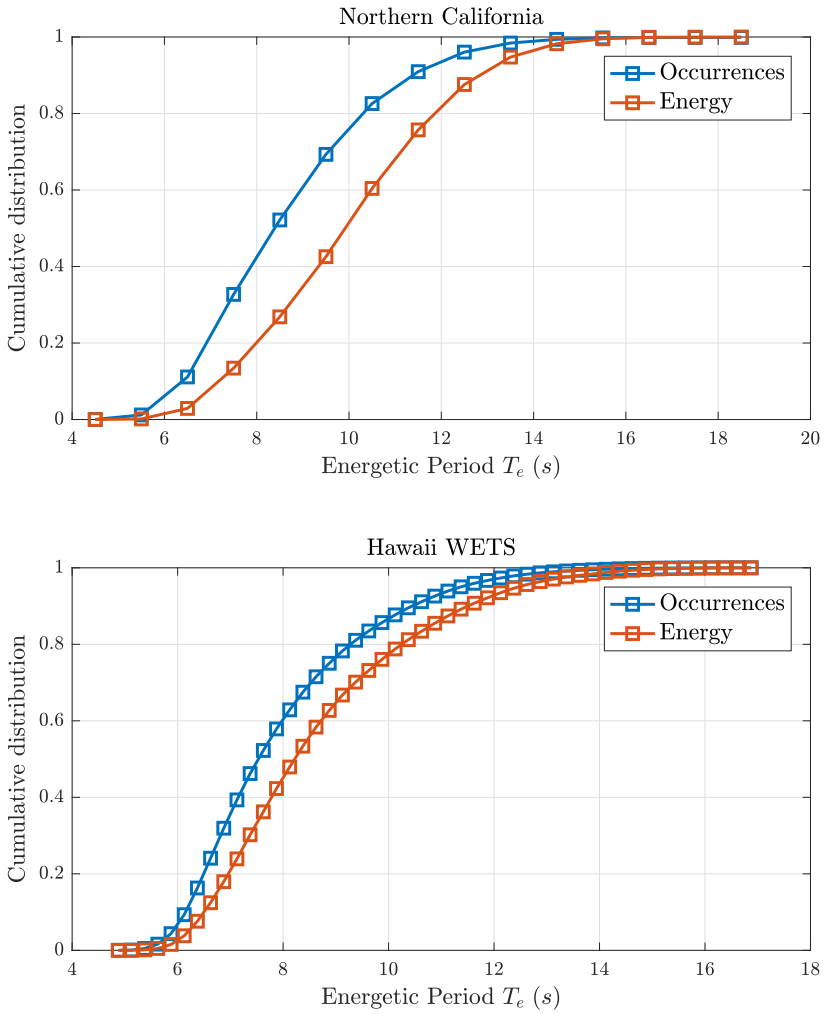

Figure 5.4 Occurrences and energy cumulative diagrams as a function of the energetic period T_e.

The design of a floating wave energy converter that exploits energy from the pitching motion of the hull is heavily influenced by the wave climate of the sites of interest, especially by the most frequent wave periods in a year. In fact, longer is the wave period longer should be the hull length in order to be in resonance condition with the most probable sea states of the deployment site. A drawback of this WEC technology is the strong dependence of the design of the device on the a certain wave climate. Moreover, the design of a pitching floating device in sites with long waves leads to enormous devices that can show significant techno-

Table 5.2 Design parameters of the first draft of IOwec.

Parameter	Symbol	Unit	Value
Hull lenght	L	m	23
Hull width	W	m	20
Hull shape coefficient 1	h		0.420
Hull shape coefficient 2	k		0.675
Hull draft ratio	j		0.65
Ballast Filling Ratio	BFR		1
Flywheel Inertia	J	kgm^2	25000
Eccentric Mass	M_p	kg	12000
number of gyroscope units	$nGyros$		2
Radial Bearings ID	$BearID$		3
U-Tank shape coefficient 1	UT_{W_r}		0.37
U-Tank shape coefficient 2	UT_{H_d}		0.23
U-Tank shape coefficient 3	UT_{W_d}		1

economic, manufacturing and installation issues. Therefore, the idea is to design a unique compact and adaptable device with a hydrodynamic resonance period tuned with the most frequent local wind waves. The energetic periods of wind waves are shorter than those of swells and generally in the range of 5-7 (s). The tuning of the hydrodynamic resonance of a pitching device like IOwec on longer waves would result in longer hull lengths and mass, therefore, higher costs. The dynamic response of the device can be tuned on longer waves by the integration onboard of the U-Tank and the adoption of a "slow control logic".

5.2 IOwec device characteristics

The first draft of IOwec is designed taking into account the wave resource analysis presented in the previous section. The hull length and the inertia have been determined to have a pitch resonance period of the hull at around 6.5 (s), typical of the local-wind generated sea-states. The U-Tank technology, as explained in the next chapter, allows to tune the resonance of the device to longer wave periods.
The geometrical, inertial and hydrodynamic properties of the IOwec device are computed with the design tool discussed in section 4. The chosen input design parameters are defined in table 5.2.

Figure 5.5 shows the front and plan view of the device, with the arrangement of the gyro units, U-Tank and ballast inside the hull.

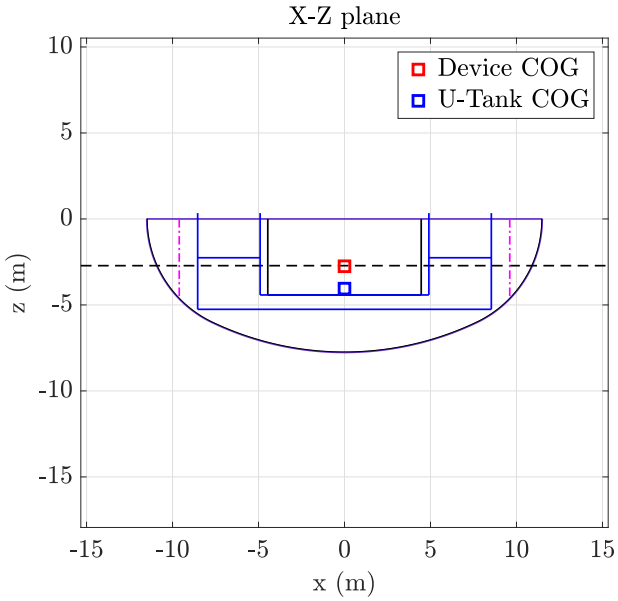

(a)

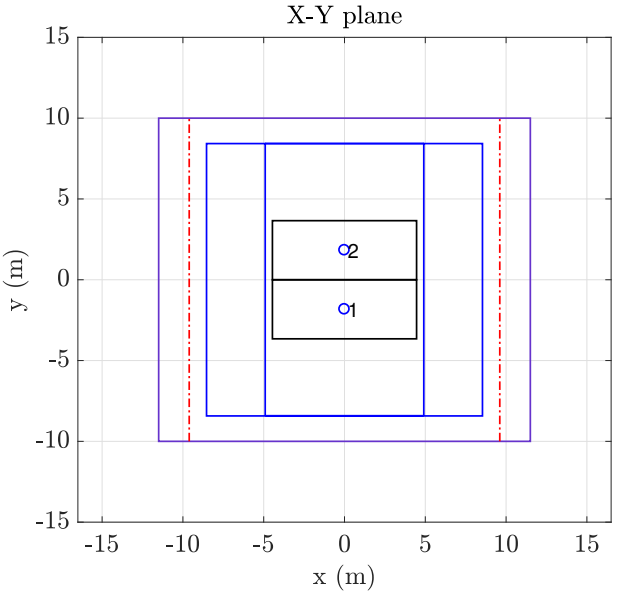

(b)

Figure 5.5 Side and Plan view of the first draft of IOwec.

The relevant characteristics of the device are given in table 5.3 and the pitch RAO is shown in figure 5.6, which has a resonance period of approximately 6.5 (s) and a maximum response amplitude of 7 (rad/rad).

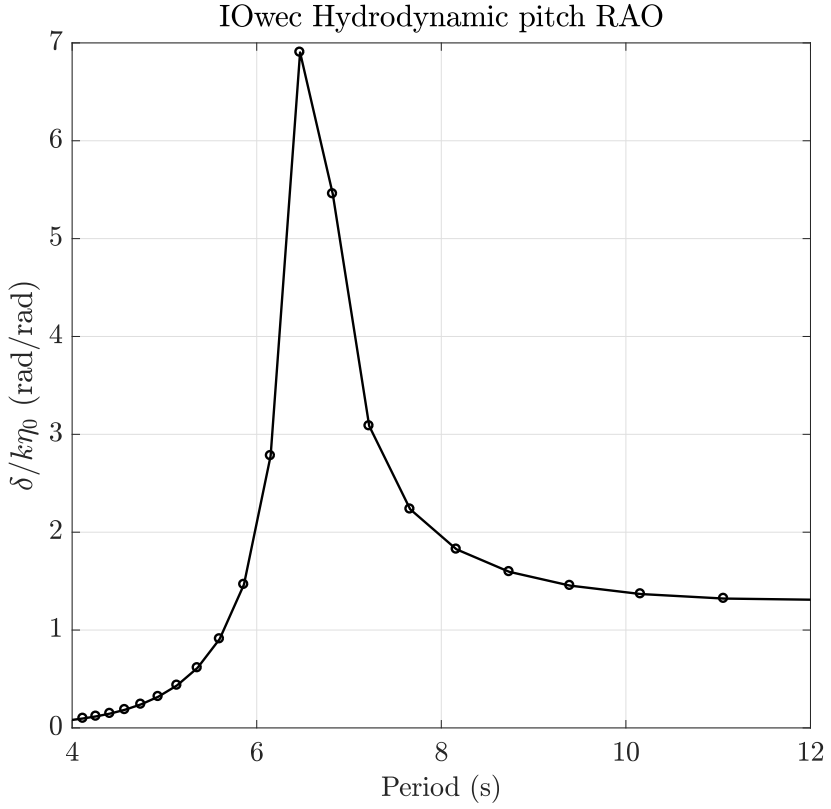

Figure 5.6 Hydrodynamic pitch Response Amplitude Operator of the first draft of IOwec.

5.3 U-Tank sea-state control logic

The integration of the U-Tank technology in a pitching-resonant WEC is based on the idea of implementing a slow-tuning control logic of the U-Tank to tune the resonance of the device to the current sea-state. In this section a possible slow-tuning control logic is proposed and discussed.

Table 5.3 Characteristics of the first draft of IOwec.

Property	Symbol	Unit	Value
Floater			
Length	L	m	23
Width	W	m	20
Height	H	m	7.76
Draft	Dr	m	5.05
Global COG from deck	COG	m	2.75
Device Pitch Inertia	I_{yy}	kgm^2	1.17e08
Total mass	M	ton	1684
Total Device cost	C_{tot}	M EUR	2.7
Hull mass	M_{hull}	ton	321
Ballast mass	M_{ball}	ton	726
Gyroscope			
Units	nGyros	-	2
Flywheel Inertia	J	kgm^2	25000
Flywheel External Diameter	D_e	m	2.46
Eccentric Mass	m_p	ton	12
Eccentric Mass Arm	d_p	m	1.23
Gyro Unit Mass	M_{gyro}	ton	66
U-Tank			
Water mass	M_{Utank}	ton	505
Width	X_t	m	16.9
Duct Height	H_d	m	0.83
Duct Lenght	W_d	m	9.81
Reservoir length	W_r	m	3.63
Datum level (Lloyd ref)	H_r	m	2.58
Device COG distance from duct centerline	r_D	m	2.08
Total U-Tank length	W_{tot}	m	17.08

5.3.1 U-Tank Control Logic

In literature, different active control logics for the U-Tank have been discussed. Winden [108] analyses two types of active controls to reduce the roll motion of ships:

- **Active Pump System**: the flow in the U-Tank is controlled by a water pump located in the central duct of the U-Tank.
- **Active Air Throttle Valve System**: the two U-Tank reservoirs are connected by an air duct and through an air throttle valve the fluid motion can be halted in specific moments in order to tune the U-Tank and reduce the roll motion of the ship.

The first method requires a high energy consumption by the pump, which is not an ideal solution for wave energy devices. The second method appears more suitable to be applied on IOwec, but it requires a wave-by-wave control logic that is too advanced to be studied at this design stage.

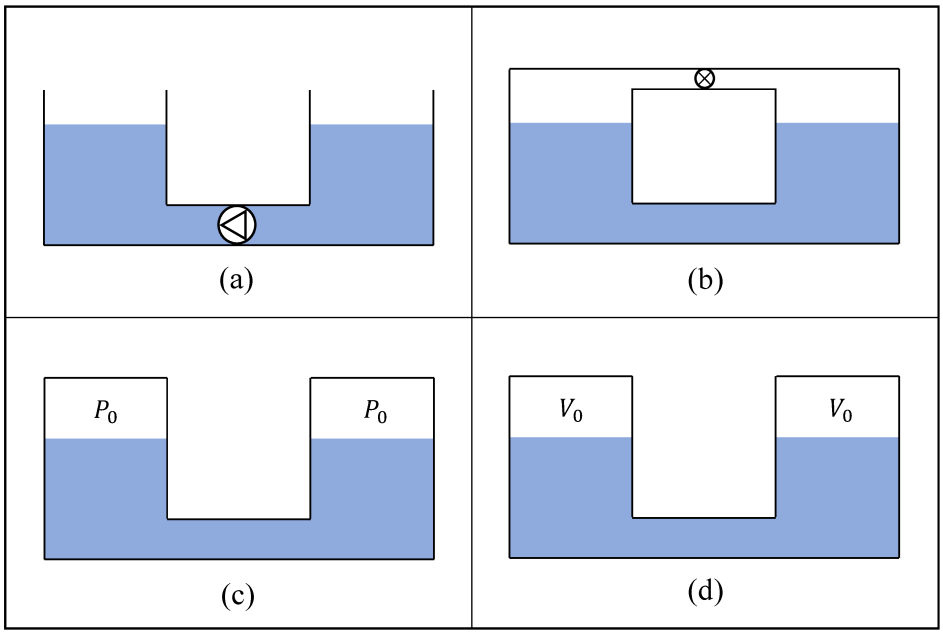

Figure 5.7 Different types of U-Tank active control systems. (a),Active Pump System (b),Active Air Throttle Valve System (c), Initial Pressure Control, (d), Initial Volume Control

Another control philosophy is to modify certain dynamic parameter of the U-tank to seek the slow-tuning of the device with the incoming sea-state, avoiding the

complexity of a wave-by-wave control logic. The idea is to find a characteristic parameter of the U-Tank that can be varied to modify the frequency response of the U-Tank and consequently of the device. Equation (2.101) highlights the parameters of the U-Tank that influence the resonance frequency of the system. All of these parameters are related to the geometry of the U-Tank or to the water level, and their modification is not a trivial problem during the operation of the machine. A solution to this problem may be closure of two reservoirs in order to have a determined air pressure P_0 and volume V_0 in resting condition of the U-Tank. The fluid motion inside the tank will compress and expand the air in the two chambers that will generate a restoring force acting on the opposite direction of the fluid motion. The air stiffness will depend on the initial pressure P_0 and volume V_0 of the air in the chambers. The added stiffness of in the U-Tank dynamics can be varied in two ways:

- **Initial Pressure Control**: The air pressure P_0 of the air in the two chambers is modified through a vacuum pump in resting conditions.
- **Initial Volume Control**: The air volume V_0 of the air chambers is modified through a system of different volumes that can be activated or deactivated with on/off air valves.

The *Initial Pressure Control* needs a high amount of energy in order to set the pressure in the air chambers of the U-Tank and therefore only *Initial Volume Control* will be studied in this thesis.

Initial Volume Control

The working principle of the Initial air Volume Control is shown in figure 5.8. The air chambers of the two U-tank reservoirs are independent and connected to n volumes through n on/off air valves. For example if the valves v_1 are open, and the valves v_2 closed then the air in the two reservoirs can compress and expand in a initial volume in rest conditions $V_0 = V^* + V_1$, where V^* is the air volume in the two reservoir chambers. Then, if we have n discrete volumes and n open valves per reservoir the generic initial volume V_0 is given by:

$$V_0 = V^* + \sum_{i=1}^{n} V_i \tag{5.1}$$

Where V_i is the i-th air volume considered.

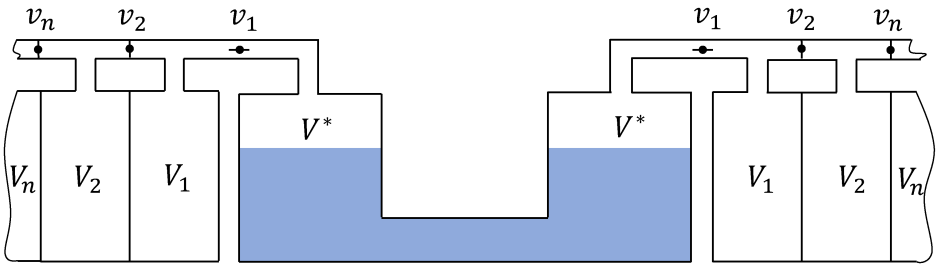

Figure 5.8 Working principle of the Initial Volume Control of the U-tank system.

In order to calculate the stiffness contribution due to the compression/expansion of the air some assumptions must be made:

- The air is considered as a perfect gas.
- There is no air leakage. The air mass is considered constant.
- The initial air pressure is equal to the atmospheric pressure: $p_0 = 10^5\ (Pa)$.
- The air transformation can be considered isothermal: the water sloshing in the U-Tank and therefore the transformation of the gas in the air chambers occur at a low frequency range, and the walls are not adiabatic. Therefore, the temperature of the air can be considered almost constant during its transformation.

The isothermal transformation of the air in the two air chambers can be expressed as:

$$p(t)V(t) = p_0V_0 = const \tag{5.2}$$

Where $p(t)$ and $V(t)$ are the instantaneous air pressure and volume and p_0 and V_0 are their values in resting conditions. The instantaneous air volume for bow chamber V_B and stern chamber V_S can be written as a function of the U-Tank angle τ (see the reference system in shown in figure 2.4):

$$\begin{cases} V_B = V_0 - \frac{ww_r x_t}{2}\tau \\ V_S = V_0 + \frac{ww_r x_t}{2}\tau \end{cases} \tag{5.3}$$

Combining equation 5.2 and 5.4 the following relations can be derived:

$$\begin{cases} p_B(V_0 - \frac{ww_r x_t}{2}\tau) = p_0 V_0 \\ p_S(V_0 + \frac{ww_r x_t}{2}\tau) = p_0 V_0 \end{cases} \rightarrow \begin{cases} p_B = \frac{p_0 V_0}{V_0 - \frac{ww_r x_t}{2}\tau} \\ p_S = \frac{p_0 V_0}{V_0 + \frac{ww_r x_t}{2}\tau} \end{cases} \tag{5.4}$$

Therefore, we can define the pressure difference ΔP :

$$\Delta P = p_B - p_S = p_0 \left(\frac{1}{1 - \frac{ww_r x_t}{2V_0}\tau} - \frac{1}{1 + \frac{ww_r x_t}{2V_0}\tau} \right) \tag{5.5}$$

Linearizing the previous equation around the equilibrium position $\tau = 0$ we obtain:

$$\Delta P = \frac{ww_r x_t}{2} \frac{p_0}{V_0} \tau \tag{5.6}$$

The pressure difference ΔP is expressed as a linear function of the U-Tank angle τ and it is proportional to the initial air pressure p_0 inversely proportional to the initial air volume V_0. Then, the terms of equation (5.6) can be multiplied by the moment of area of the reservoirs (see eq. (2.95)) in order to obtain the torque M_{air} due to the air difference pressure and include it in the U-Tank equation (2.96):

$$M_{air} = \frac{w^2 w_r^2 x_t^2}{4} \frac{p_0}{V_0} \tau = c_{\tau\tau_{air}} \tau \tag{5.7}$$

Where with $c_{\tau\tau_{air}}$ we define the stiffness coefficient of the U-Tank equation due to the pressure difference in the two air chambers and then the equivalent stiffness term $c^*_{\tau\tau}$ becomes:

$$c^*_{\tau\tau} = c_{\tau\tau} + c_{\tau\tau_{air}} \tag{5.8}$$

The resonance frequency of the U-Tank (see eq. (2.101)) becomes:

$$\omega_{res} = \sqrt{\frac{c_{\tau\tau} + c_{\tau\tau_{air}}}{a_{\tau\tau}}} \tag{5.9}$$

Therefore, changing the initial air volume V_0 is possible to shift the resonance frequency of the U-Tank and of the device. The Active Volume control can constitute a simple, cheap and effective solution for the U-tank active control.
The maximum volume of air $V_{0_{max}}$ per reservoir that can be derived in the proposed device layout is equal to around 350 (m^3) and it can be partialized in equal volumes V_i in order to implement the air volume control strategy of the U-tank. Instead, the minimum volume of air V^* per reservoir in correspondence of all closed air valves is equal to 13.42 m^3.
The diagram of the torque due to the hydrostatic pressure and the non-linear and linear air pressure (see equations (5.5) and (5.6)) are shown in figure 5.9 for the case of $V_0 = V_{0_{min}}$ and $V_0 = V_{0_{max}}$. The range of the increment of stiffness ratio $c^*_{\tau\tau}/c_{\tau\tau}$ is:

$$2.2 < c^*_{\tau\tau}/c_{\tau\tau} < 4.9 \tag{5.10}$$

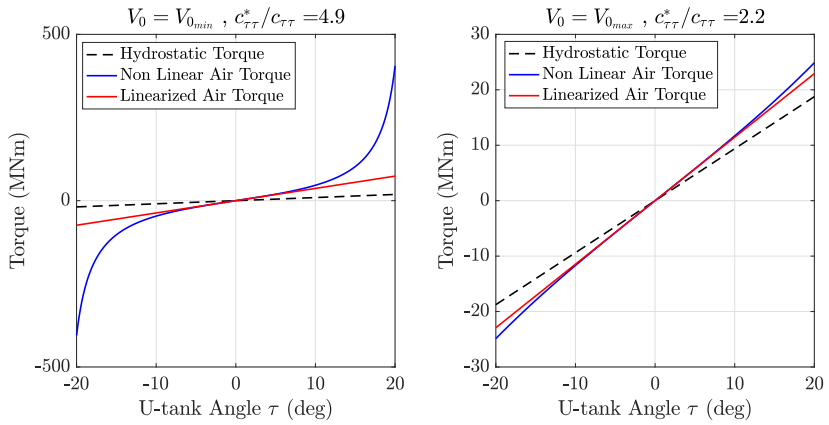

Figure 5.9 Diagram of the torque due to the hydrostatic pressure of the U-Tank and the air pressure as a function of the U-tank angle τ.

The diagram of the pressure difference ΔP between the two chambers as a function of the U-tank angle is shown in figure 5.10.

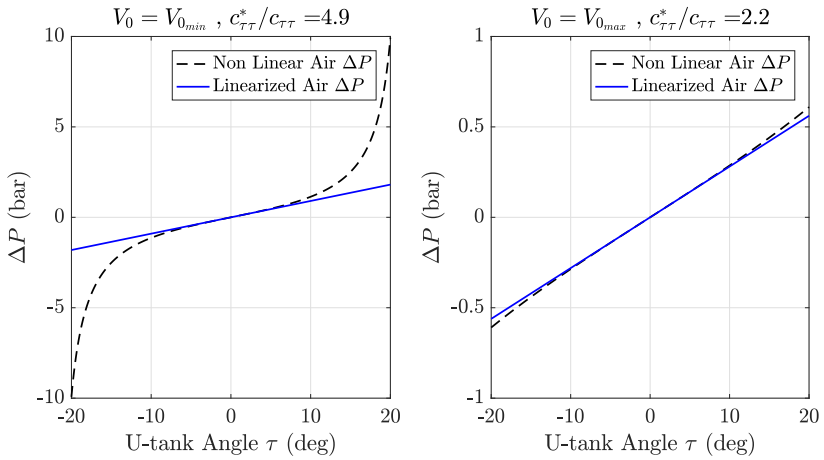

Figure 5.10 Diagram of the air pressure difference as a function of the U-tank angle τ.

The influence of the air active control of the U-Tank on the Response Amplitude Response of water motion is shown in figure 5.11, and it can be notice how the frequency response shifts as a function of the stiffness ratio $c^*_{\tau\tau}/c_{\tau\tau}$.

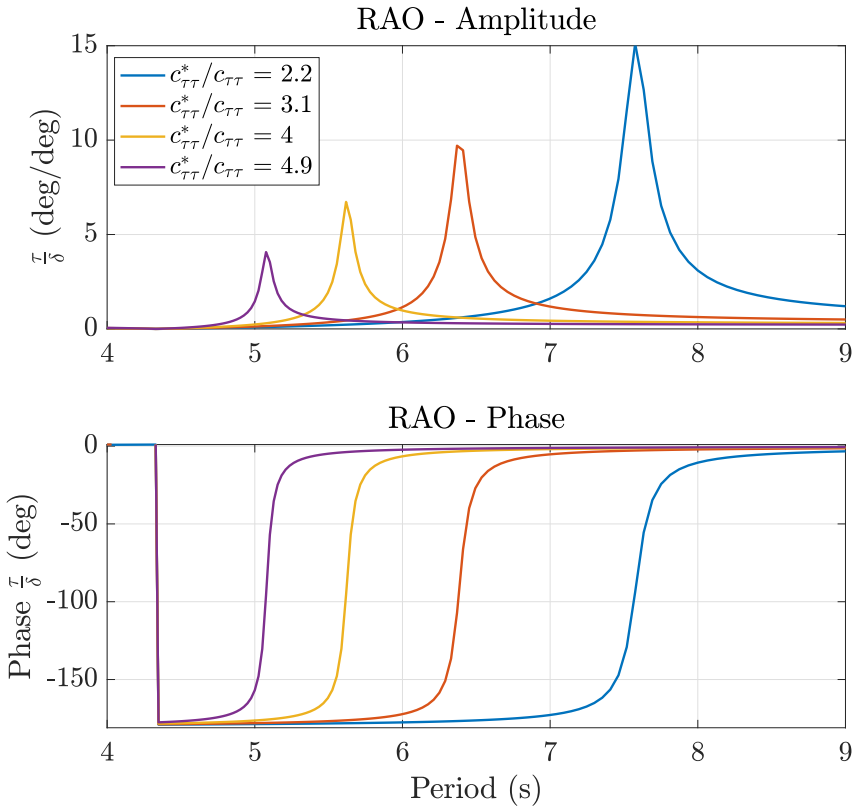

Figure 5.11 U-Tank Response Amplitude Operator for different values of the stiffness ratio $c^*_{\tau\tau}/c_{\tau\tau}$.

The effect of the control and change of the initial air volume of the U-Tanks on the response of the floater is explained in figure 5.12 considering the gyroscope units turned off. The device dynamics is represented by a 4-th order linear system, given by the coupling of two 2nd order underdamped systems. Thus the frequency response shows an antiresonance in correspondence of the frequency resonance of the U-Tank and the device results almost stable. Two resonance peaks occur at high and low frequency, and they can be shifted with the air control system in order to tune the device with the incoming wave.

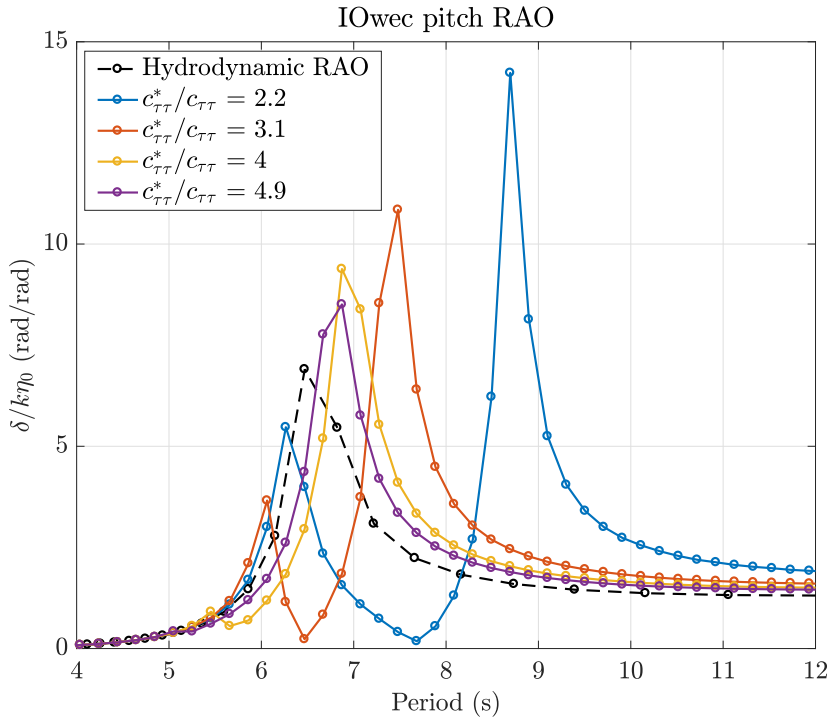

Figure 5.12 IOwec (first draft) Response Amplitude Operator for different values of the U-Tank stiffness ratio $c^*_{\tau\tau}/c_{\tau\tau}$ compared with the hydrodynamic RAO of the device with the gyroscope units turned off (flywheel speed $\dot{\phi} = 0$).

5.4 Regular wave analysis

The IOwec dynamics with the active control of the U-Tank is assessed firstly in regular wave conditions. This preliminar analysis is fundamental in order to understand how the dynamics of the system is influenced by the U-Tank and the power response curve can be enlarged thanks to the integration of this novel technology.
The simulation is carried out with a set of regular waves with a periods range of [5-15] and a 1:60 constant steepness has been chosen for the analysis to do not overcome the linear assumptions of the model (see figure 5.13).

For each simulation the mechanical net power of the gyroscopes is maximized through the constrained optimization of the control parameters flywheel speed $\dot{\phi}$ and PTO damping coefficient c (see section 4.4). Moreover, because this study is more qualitative than quantitative the simulation constraint on the gyroscope

precession angle ε is avoided to not affect the results trends. Only the constraint on the maximum equivalent radial force acting on the radial bearings is considered.

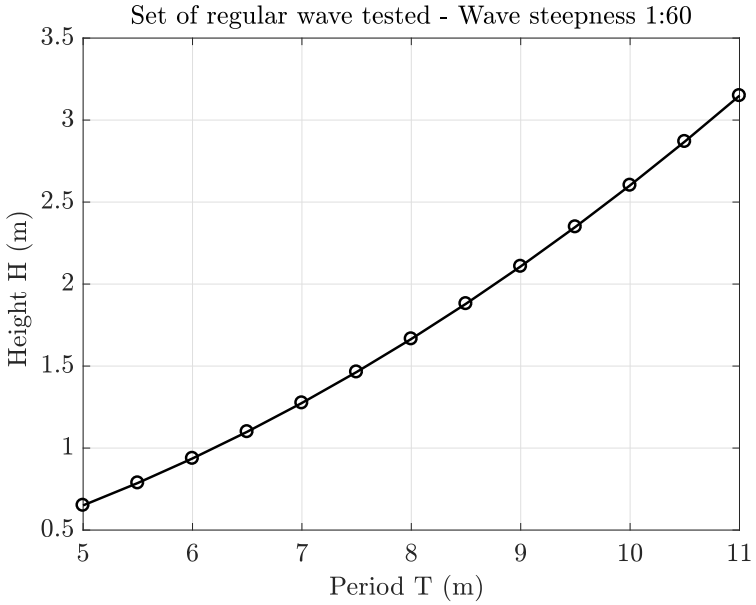

Figure 5.13 Regular waves with constant steepness 1:60 under testing for the assessment of the IOwec device.

The results of the simulation of the IOwec device in regular wave conditions are shown in figure 5.14, 5.15, 5.16. For the sake of clarity three different U-Tank control conditions have been considered:

- **Inactive U-Tank**: In this conditions through a closed hydraulic valve located in the central duct of the U-Tank there is no liquid sloshing. Therefore, the U-Tank dynamics is negligible and the mass of water act as simple inertial ballast.
- **Active U-Tank**: The water is free to move inside the U-Tank and two control conditions of the U-Tank stiffness are considered: $c^*_{\tau\tau}/c_{\tau\tau} = 2.2$ and $c^*_{\tau\tau}/c_{\tau\tau} = 3.1$.

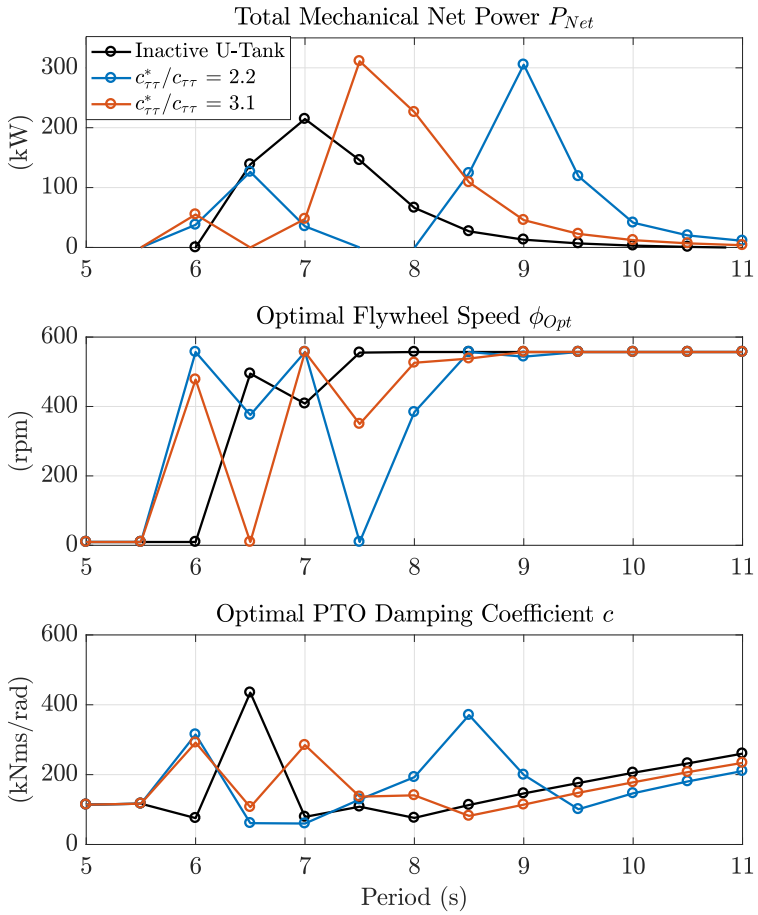

Figure 5.14 Simulation results of the IOwec device under regular waves: Net Power P_{net}, optimal flywheel speed $\dot{\phi}_{opt}$ and optimal PTO damping coefficient c_{opt}. Comparison of Inactive U-Tank and active U-Tank control with two different values of stiffness ratio control $c^*_{\tau\tau}/c_{\tau\tau}$.

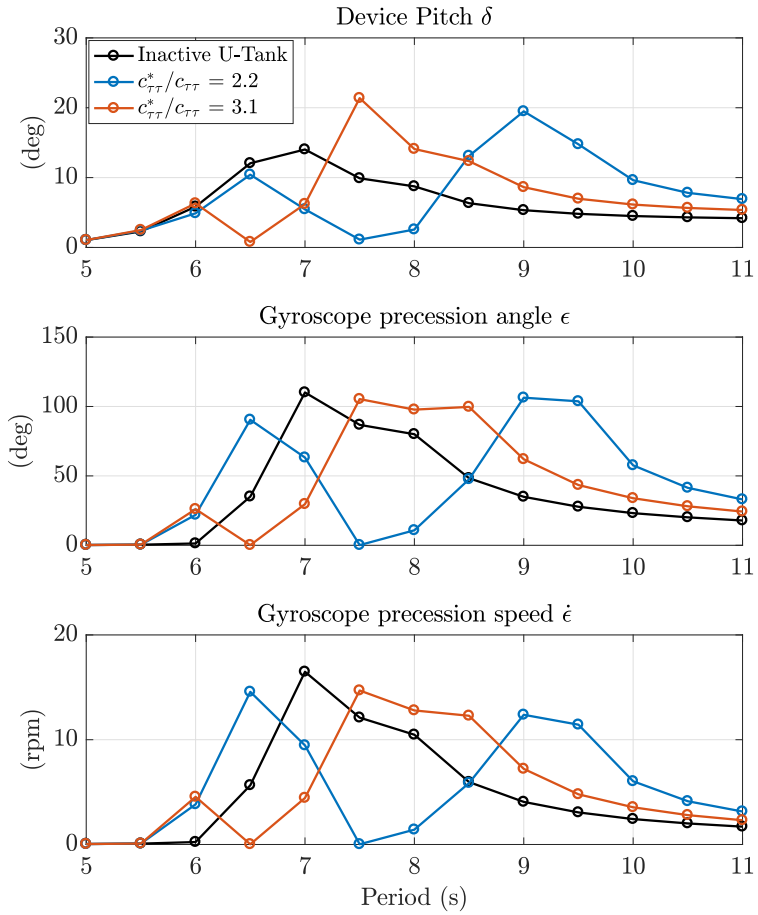

Figure 5.15 Simulation results of the IOwec device under regular waves: floater pitch angle δ, gyroscope precession angle ε and gyroscope precession velocity $\dot{\varepsilon}$. Comparison of Inactive U-Tank and active U-Tank control with two different values of stiffness ratio control $c^*_{\tau\tau}/c_{\tau\tau}$.

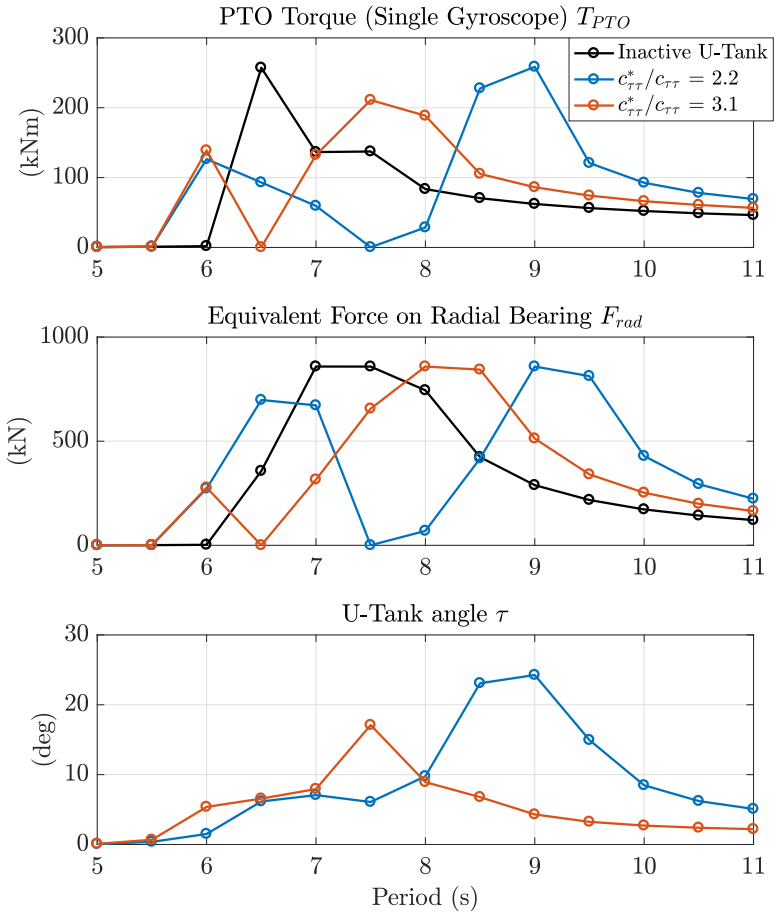

Figure 5.16 Simulation results of the IOwec device under regular waves: Net Power P_{net}, PTO torque T_{PTO}, force on radial bearings F_{rad} and U-Tank angle τ. Comparison of Inactive U-Tank and active U-Tank control with two different values of stiffness ratio control $c^*_{\tau\tau}/c_{\tau\tau}$.

The influence of the dynamics of the U-Tank on the IOwec device performance is clear observing the curves of the mechanical net power that can be extracted by the PTO: A correct choice of the resonance period of the U-Tank through the air volume control allows the tuning of the device dynamics with an increase of performance in different wave conditions. In fact, if we do not consider the dynamics of the U-Tank, the performance of the device is represented by the black curve (Inactive U-Tank), where the energy extraction is high close to the hydrodynamic resonance period of the floater and decrease when the wave period increase or decrease. Due to the integration of the U-Tank technology is possible to shift the resonance period of the system and increase the performances also when longer waves are encountered.

In some wave conditions the precession angle of the gyroscope ε reaches maximum values that exceed the linear assumptions of the model (see figure 5.15). But as stated before, this analysis is meant to be qualitative, and simulations constraints on the rms value of the precession angle ε will be imposed in irregular wave conditions where the quantitative consideration will be more significant.
The analysis in regular wave conditions is also a first demonstration of the optimization process of the maximization of the extracted net power through the optimization of the control parameters [c $\dot{\phi}$] with a constrain on the equivalent radial force on the bearings. In fact, the radial bearing force do not exceed the limit value imposed in the simulation (see figure 5.16).

Varying the stiffness ratio $c^*_{\tau\tau}/c_{\tau\tau}$ between the range [2.2 - 4.9] is possible to define the envelope curve of the maximum net power extraction in regular wave conditions as shown in figure 5.17. The envelope net power curve of the active U-Tank control is compared with the inactive U-Tank case, highlighting the performance increase of the device due to the U-Tank tuning.

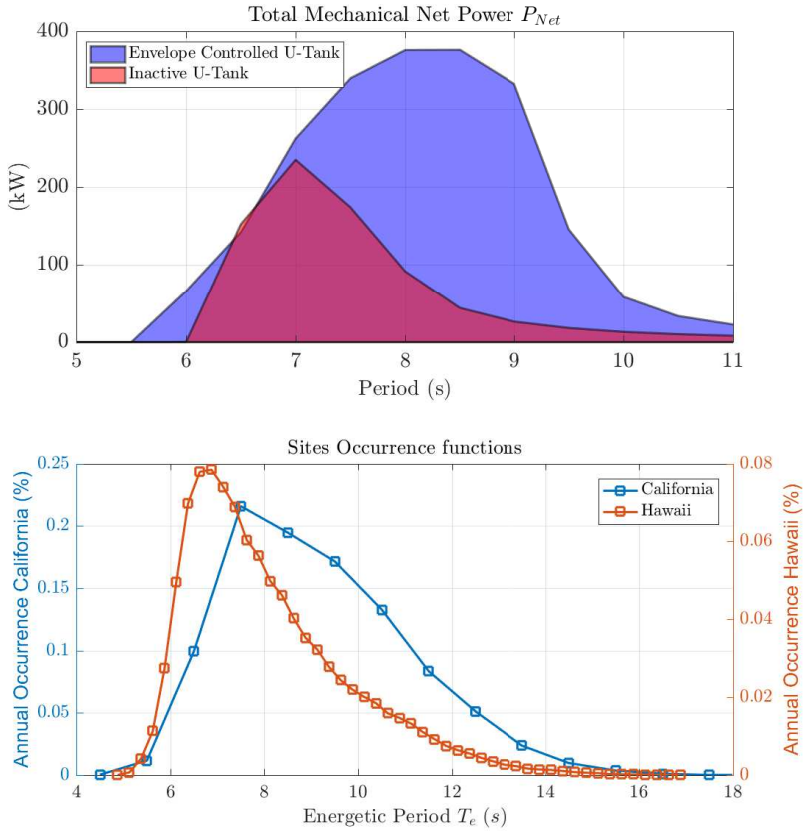

Figure 5.17 Comparison of the IOwec performance in regular wave between inactive U-Tank case and the envelope of the controlled U-Tank power curves for different stiffness ratios values.

In order to take into account the occurrences of the site is convenient to weight the net power curve with the occurrences curves of the two chosen sites, Hawaii and California, that are shown in figure 5.18 as a function of the energetic period. For the sake of simplicity the energetic period T_e, that is a statistical parameter, can be confused with the regular wave period T in this qualitative assessment.

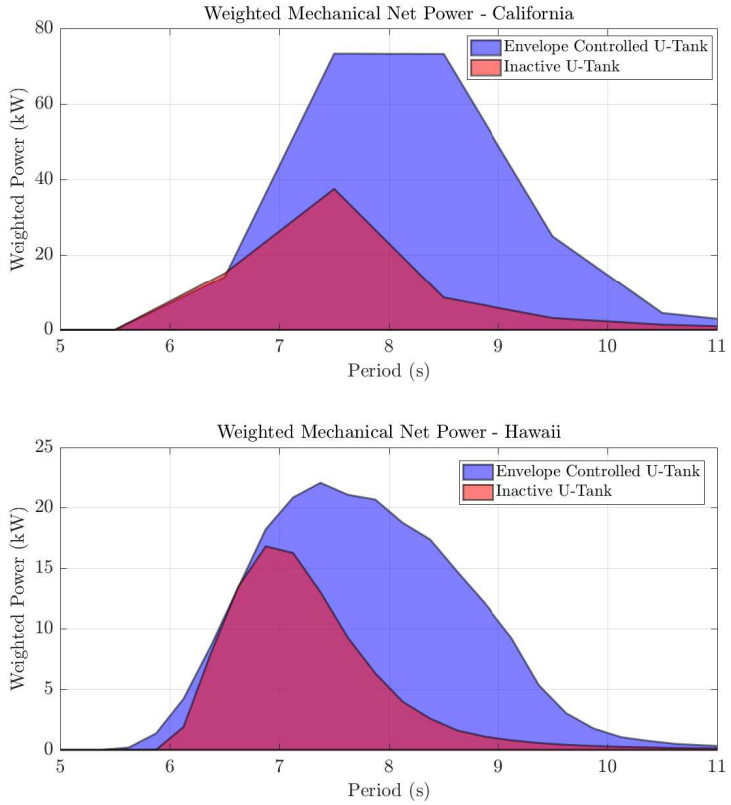

Figure 5.18 Comparison of the IOwec weighted power curves in regular wave between inactive U-Tank case and the envelope of the controlled U-Tank power curves considering the Californian and Hawaiian deployment site.

5.4.1 Time Domain Analysis

The time domain analysis of the dynamics of the IOwec device with active U-Tank control is shown if figure 5.19 and 5.20. In this example a regular wave with period $T = 7.5\ (s)$ and the U-Tank stiffness ratio $c^*_{\tau\tau}/c_{\tau\tau} = 3.1$ that maximize the net power of the device is considered. The optimal control parameters are $\dot{\phi}$ = 350 (rpm) and c = 137 (kNm) (see figure 5.14). It is interesting to notice that the U-Tank water oscillation τ is antiphase to the floater pitch oscillation δ, and hence the the U-Tank torque M_τ is perfectly in phase with the floater pitch. It can be also noticed that the wave excitation pitch torque F_{exc_δ} and the U-Tank torque M_τ are in quadrature.

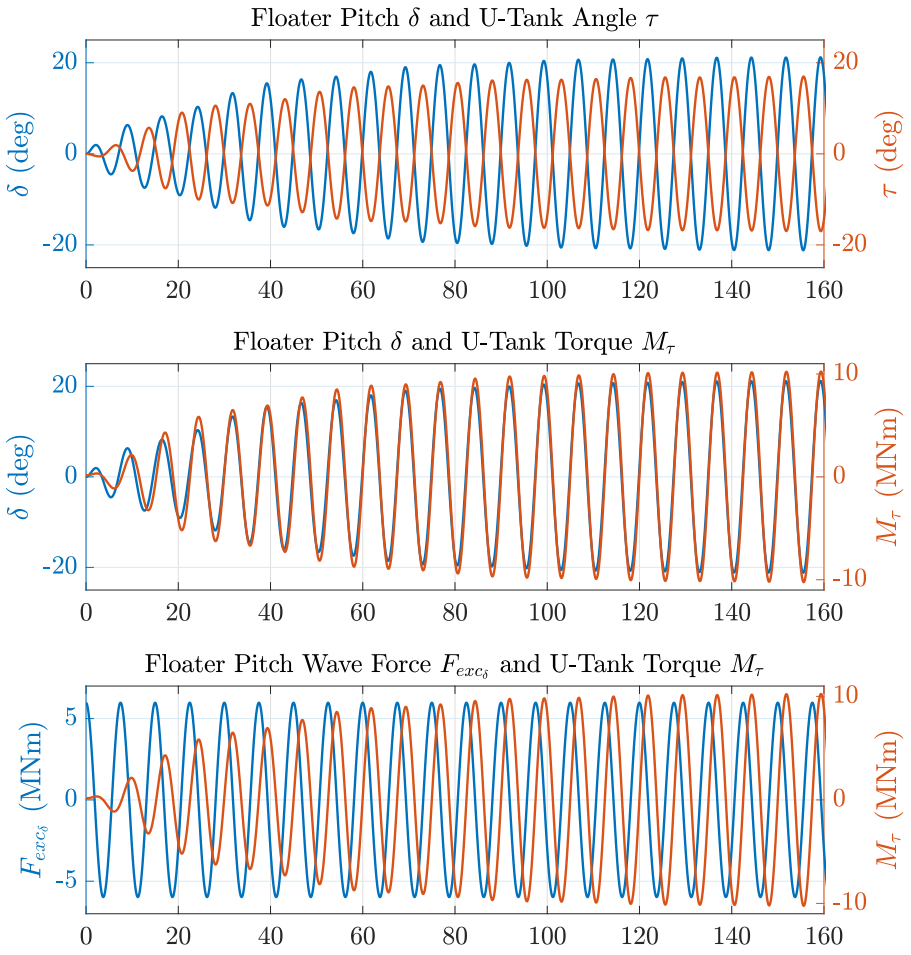

Figure 5.19 Time domain results of the IOwec dynamics with active control of the U-Tank (1).

Figure 5.20 highlights the time histories of the gyroscope kinematics compared with the floater kinematics, and the instantaneous PTO torque and mechanical power.

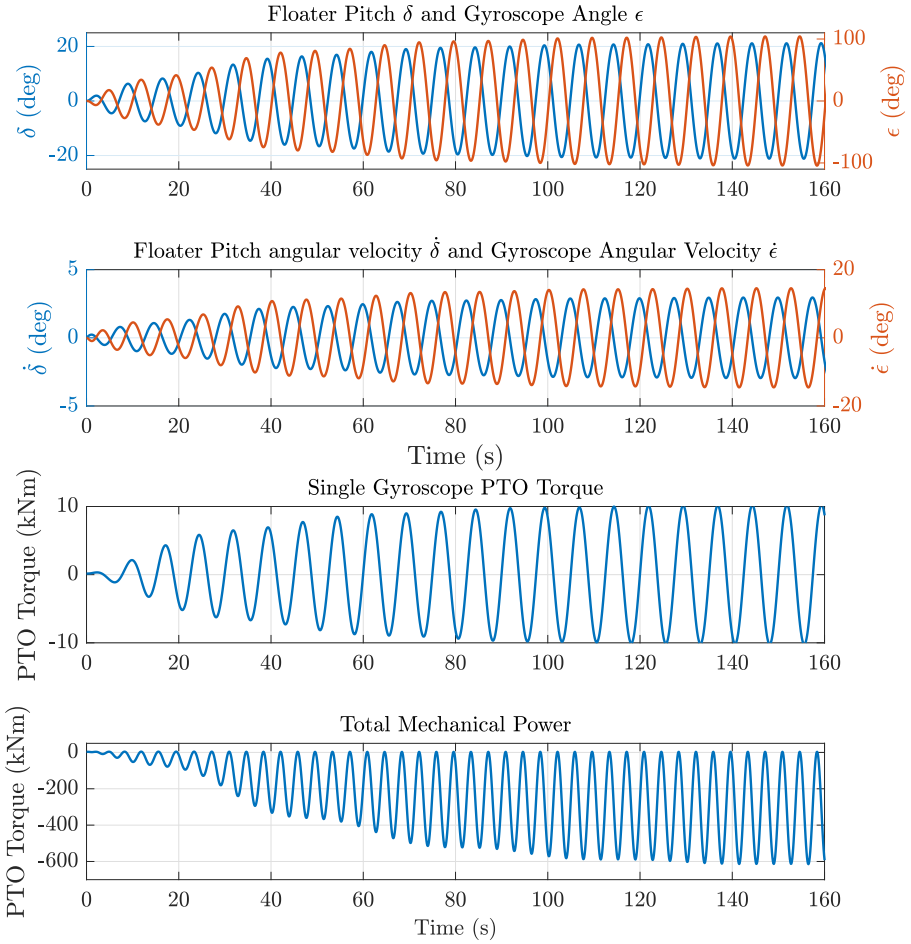

Figure 5.20 Time domain results of the IOwec dynamics with active control of the U-Tank (2).

5.5 Irregular wave analysis

In this section the performance of the IOwec device with active control of the U-Tank is evaluated in irregular wave conditions. Real sea states are combination of several independent wave systems, often result of the superposition of a local wind generated waves and swells generated by distant storms [76].

It is common practice to evaluate numerically the performance of wave energy converters with analytical spectral density functions that represent the wave energy

distribution [56]. The most adopted spectral functions are the JONSWAP and the Bretshneider spectra, where the former is suggested in case of wind seas with limited fetch and the latter for fully developed seas. Sandia Laboratories [109] elaborated the meteocean data of different sites in the United States and the results show how the sea state conditions can be very complex. They found that the average measured spectrum, representative of a sea-state, can be fairly represented by the Bretschneider spectrum. A limitation of the Bretschneider spectrum is the impossibility to capture the bimodal nature of some sea-states. Ochi and Hubble [110] proposed a six-parameters spectrum given by the superposition of two Pierson-Moskovitz spectra to model bimodal sea-states. Guedes Soares [111] similarly developed a 4-parameters spectra based on the the superposition of two JONSWAP spectra.

Established the variety of spectral shapes that sea-states can assume, the performance of IOwec are studied considering two types of spectra:

- Single-wave system (Jonswap and Bretshneider spectra).
- Complex sea-state (Measured spectra).

This analysis is carried out to investigate the influence of different spectral shapes and their energy distributions on the dynamics of the device.

5.5.1 Single-wave system analysis

Three sea states conditions have been considered for the irregular wave analysis: the most occurrent and energetic sea states in Hawaii test site (they coincides), and the most occurrent and energetic sea states in Californian site, whose properties are resumed in table 5.4 and 5.5. Because of the inherent variability of the spectra shape of real sea states it is also interesting analyze the dynamics of the system with different wave spectral shapes with the same sea state parameters T_e and H_s and analyize the sensitivity of the performance of the device. Hence, Jonswap spectrum with $\gamma = 1$, $\gamma = 2$ and $\gamma = 3.3$ is considered for the analysis. γ representes the peakedness factor of the spectrum function, higher is the value of this parameter, higher is the concentration of energy among a narrow range of frequency. It is important to note that a Jonswap spectrum with $\gamma = 1$ correspond to the Bretshneider spectrum.

Table 5.4 Set of irregular sea states tested (a).

			Wave ID					
			1a	1b	1c	2a	2b	2c
Property	Symbol	Unit						
Peakedness Factor	γ		1	2	3.3	1	2	3.3
Energetic Period	T_e	(s)	6.6	6.6	6.6	7.5	7.5	7.5
Peak Period	T_p	(s)	7.68	7.48	7.30	8.73	8.49	8.30
Significant Height	H_s	(m)	1.63	1.63	1.63	1.5	1.5	1.5
Wave Power	P_w	(kW/m)	8.75	8.75	8.75	8.43	8.43	8.43

Table 5.5 Set of irregular sea states tested (b).

			Wave ID		
			3a	3b	3c
Property	Symbol	Unit			
Peakedness Factor	γ		1	2	3.3
Energetic Period	T_e	(s)	10.5	10.5	10.5
Peak Period	T_p	(s)	12.22	11.89	11.62
Significant Height	H_s	(m)	2.75	2.75	2.75
Wave Power	P_w	(kW/m)	39.71	39.71	39.71

A pseudorandom wave with a duration of 1800 (s) is generated for each sea state to simulate the dynamics of the device. As in the case of regular wave analysis two conditions are considered: inactive U-Tank and active U-Tank with the tuning of the resonance period through the stiffness ratio $c^*_{\tau\tau}/c_{\tau\tau}$. The stiffness ratio $c^*_{\tau\tau}/c_{\tau\tau}$ of the U-Tank that maximize the net power is search with a brute-force approach considering a range variation of [2.2 - 4.9].
The summary results of the simulations are provided in Table 5.6, B.1 and B.2 (see Appendix B). The positive effect of the active control of the U-Tank on the net power extraction is higher when the peakedness factor γ of the wave spectrum is higher. The average percentage increase of net power due to the active U-Tank control is approximately 20 % with a peak of 44 % for the Wave ID 2c case.

Table 5.6 Simulation results in irregular wave. Peakedness factor $\gamma = 2$.

		Inactive Utank			Active U-Tank		
		Wave ID			Wave ID		
Parameter	Unit	1b	2b	3b	1b	2b	3b
Tot. Net Power, P_{net}	kW	45.5	22.4	29.8	54.2	27.6	36.5
Tot. Gross Power, P_{gross}	kW	56.4	34.6	42.3	65.5	40.2	50.3
Flywheel Speed, $\dot{\phi}_{opt}$	rpm	455	511	517	454	513	533
PTO Damping Coeff., c_{opt}	kNms/rad	161	126	153	159	133	155
Utank Stiffness Ratio, $c^*_{\tau\tau}/c_{\tau\tau}$	-				4.2	3.6	3.8
Floater Pitch Angle rms, δ_{rms}	deg	4.4	3.2	3.7	4.8	3.6	4.1
U-Tank Angle rms, τ_{rms}	deg				2.1	2.1	2.1
Gyro. Angle rms, ε_{rms}	deg	26.1	23.8	24.3	29.3	26.2	27.6
Gyro. Velocity rms, $\dot{\varepsilon}_{rms}$	rpm	4.0	3.5	3.5	4.3	3.7	3.8
PTO Torque rms, T_{PTO}	kNm	67.5	46.7	57.0	72	51.7	62.5

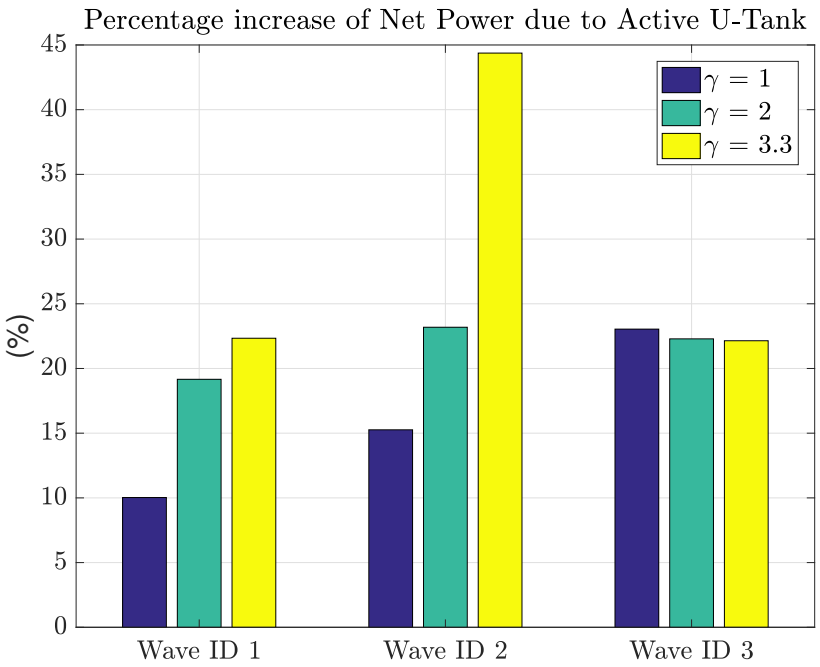

Figure 5.21 Increment of extracted net power due to the active control of the U-Tank compared with the case of inactive U-Tank.

It is interesting to analyze the different PSD response of the floaters pitch δ and gyroscope angle ε for inactive and active U-Tank (see figures 5.22, A.1 and A.2). The active U-Tank control shifts the dynamics response of the floater and gyroscope

towards a range of frequencies that maximize the power extraction of the system. Differently from the case of regular wave condition, the best stiffness ratio for sea state with long periods like the Wave ID 3 does not shift the resonance of the system toward that period (10.5 (s) in this case), but toward a shorter period. When we consider a real sea state, with energy spread over a range of frequencies, it is normal that such complex systems, constitute by the superposition of different dynamics show optimal energy extraction that seem to disagree the considerations made in regular wave analysis.
Moreover, an important parameter that should be tuned as well is the gyroscope stiffness due to the eccentric mass, that influences the dynamics of the gyroscope.

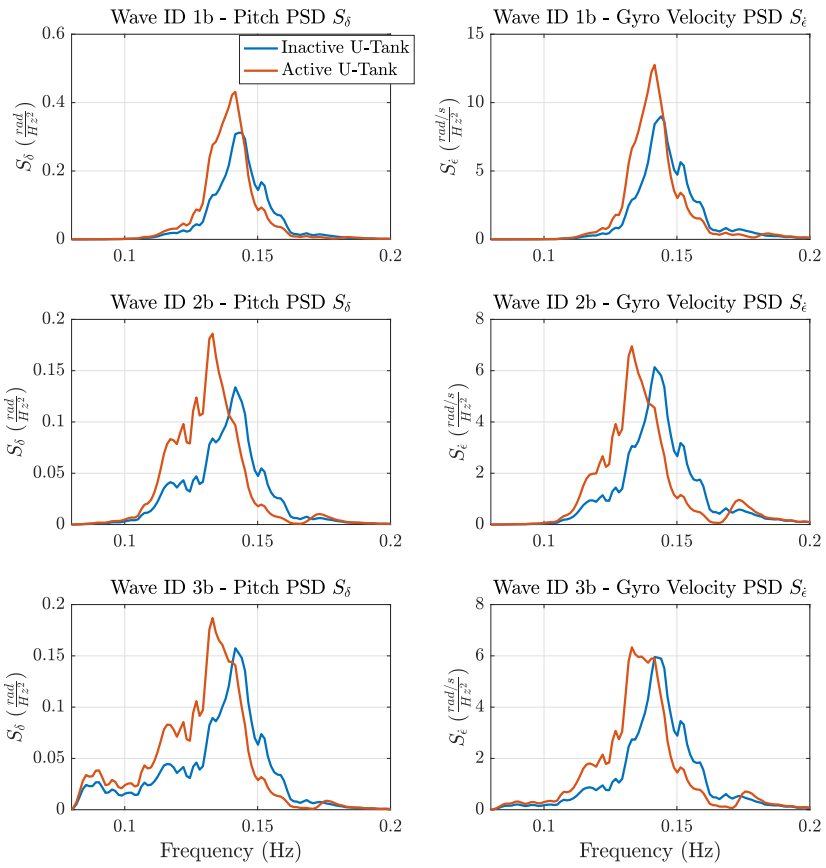

Figure 5.22 Comparison of the floater pith and gyroscope velocity PSD for the inactive and active U-Tank case. peakedness factor $\gamma = 2$

The influence of the spectral narrowness described by the peakedness factor γ on the dynamics and performance of the device is analyzed in figure 5.23 for wave ID 2 and in Appendix A the analysis of for Wave ID 1 and 3 are provided. The peakedness factor influences the optimal value of the flywheel speed $\dot{\phi}$ and PTO damping coefficient c and the net power extracted power. Since the hydrodynamic resonance period of the device is approximately 6.5 (s), a narrower sea state spectrum with longer period adversely affects the performance of the system, because the wave energy is concentrated more on a different range of frequencies. On the other hand, the possibility to modify the dynamic response of the U-Tank enhances the flexibility and adaptability of the system with different spectrum energy concentration, increasing the efficiency of the machine.

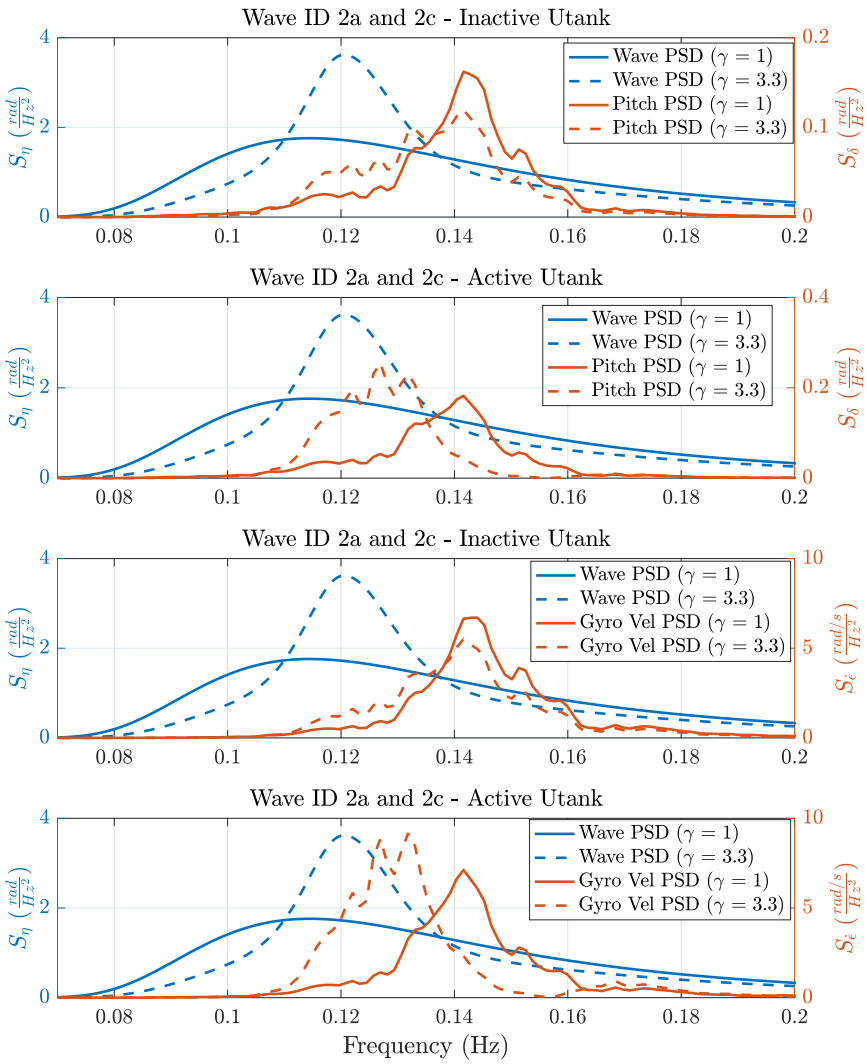

Figure 5.23 Influence of the peakedness factor γ on the PSD response for the case of inactive and inactive U-Tank.

Time Domain Analysis

An example of time domain response of the most significant variables of the IOwec system is shown in 5.24 for Wave ID 2b with active U-Tank control. Instead, figure 5.25 provides a more interisting zoom of the same record. As discussed in section 5.4.1 also in irregular wave condition the U-Tank torque is in phase with the floater's

pitch. This information can be exploited in future in order to develop a short-term control logic of the U-Tank.

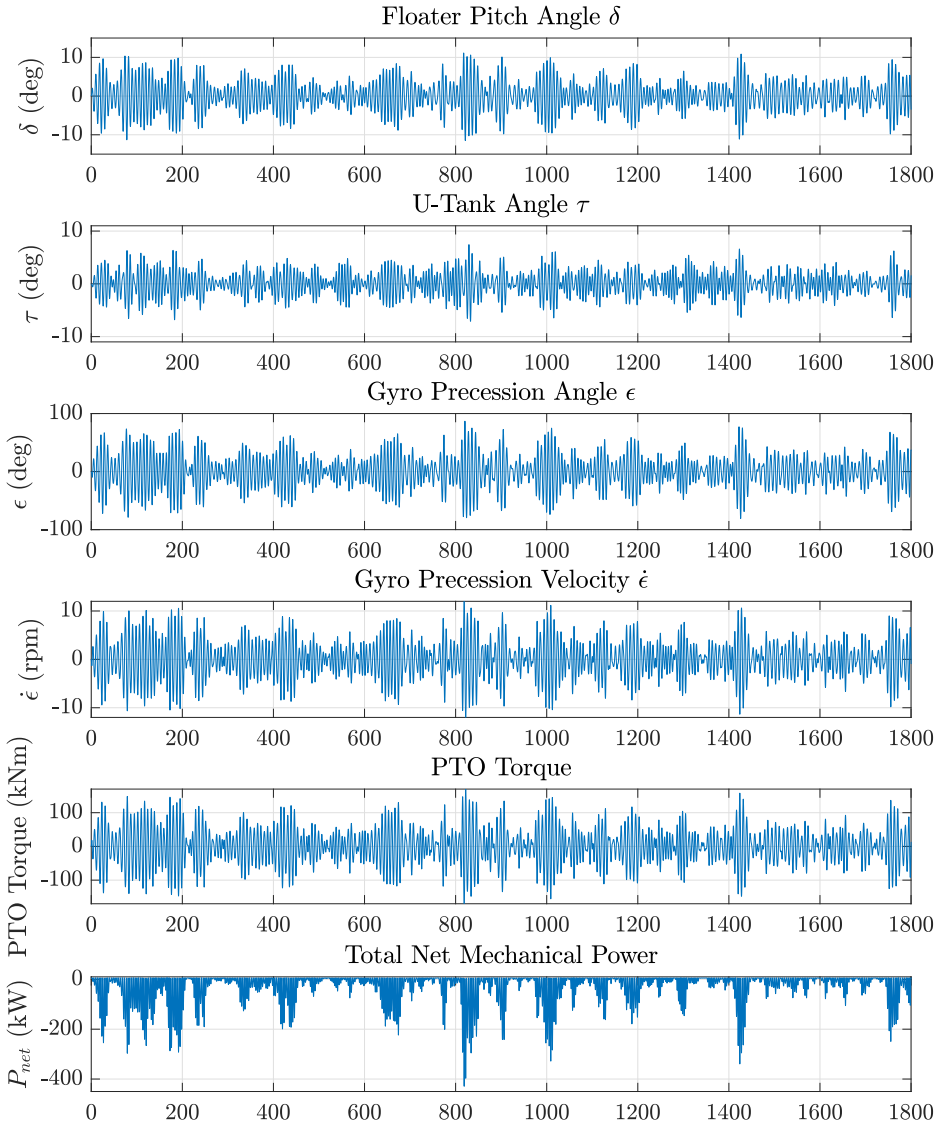

Figure 5.24 Time domain response of the IOwec device with active U-Tank for the WAVE ID 2b.

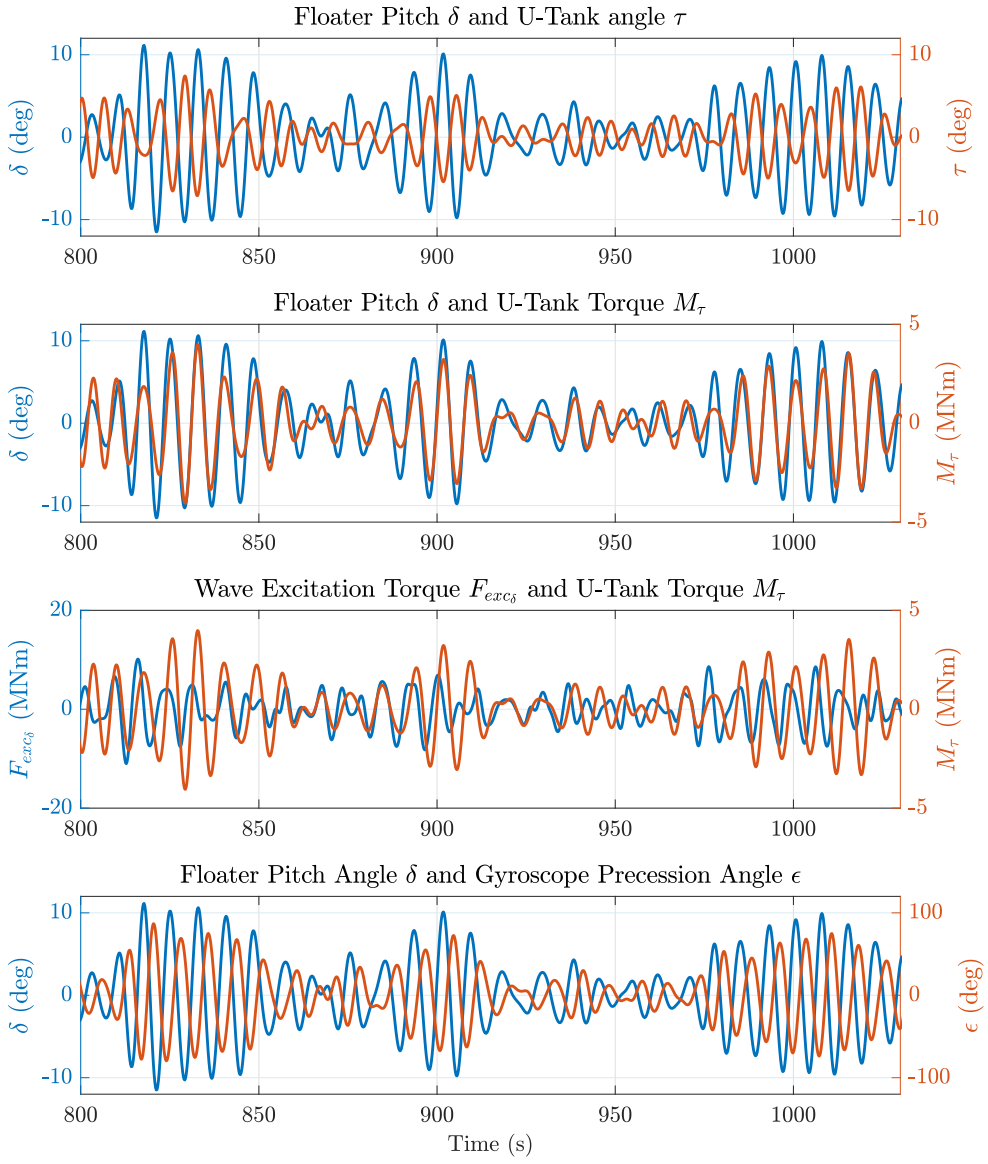

Figure 5.25 Time domain response of the IOwec device with active U-Tank for the WAVE ID 2b.

5.5.2 Complex sea-state analysis

The performance assessment of a wave energy converter and the comparison of technological solution in early development stage is usually made numerically using the standard analytical spectral functions to describe the sea states. This procedure is effective in order to have a common and standard background of comparison for technology developers and stakeholders.
It can be also interesting to simulate and test the behavior of a device in real sea state conditions using measured power spectral densities provided by wave buoys installed in the site of interest. In fact, the wave climate in certain sites can be particularly complex characterized by the superposition of several wave systems as local wind sea and swells generated by distant storms [112]. Moreover, these wave systems travel with different directions and energy is not concentrated in one direction (unidirectional wave) but is spread.
Therefore, the energetic spectral parameters, energetic period T_e and significant height H_s, that are used to describe the sea-state and define uniquely the spectral shape in case of analytical spectra, are not longer sufficient to describe the energy distribution in case of real complex sea states. In view of this fact, the choice of control parameters is a not trivial problem when they are mapped offline assuming a specific energy distribution function of the energetic period T_e and significant height H_s. In this section, a preliminary analysis of the influence of different energy distribution on the device behaviour and performance is carried out.
The data provided by the wave buoy NOAA 51003 is analyzed as it is representative of the wave climate close to the WETS site in Hawaii and the closest buoy with also measured PSD of the measured sea states. The buoy data is analyzed to find three representative sea states with the same energetic period T_e and significant height H_s of Wave ID 2 of the previous section ($T_e = 7.5$ (s), $H_s = 1.5$ (m)). The power spectral density functions of the chosen sea states are shown in figure 5.26 compared with the Bretshneider spectrum with the same spectral parameters. The energy distributions of the measured sea states are different and the Bretshneider spectrum is suited to represent only the sea state C3. Two distinct wave systems can be observed for the sea state C1 and the sea state C2 show a spread energy distribution among a large range of frequencies.

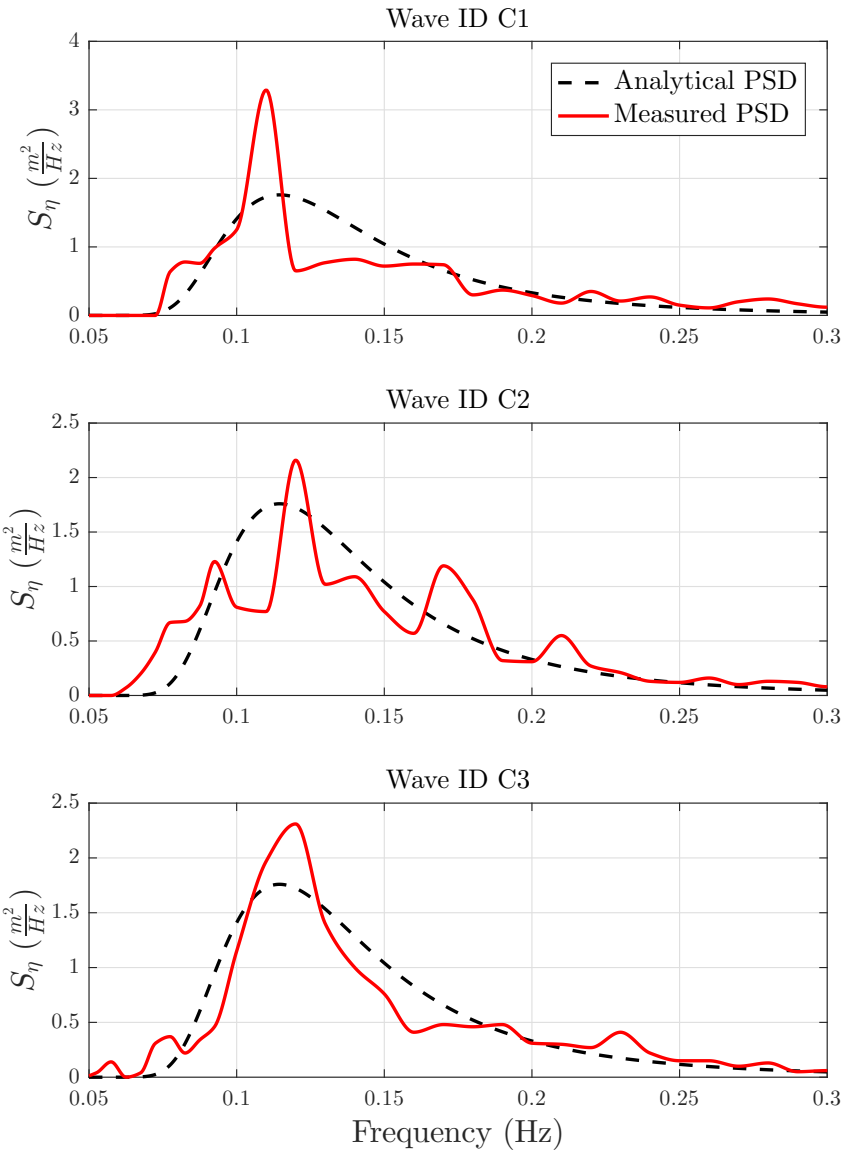

Figure 5.26 Power spectral density functions of measured wave data (Wave buoy NOAA 51003, Hawaii).

For the sake of simplicity, it is assumed that the pseudorandom wave generated from these measured sea states are unidirectional and the wave direction of the single wave systems travels with the same direction. Therefore, it is possible to use the proposed numerical model based on a 3-DoF model to give a preliminary assessment

Table 5.7 Simulation results in irregular wave with measured PSD.

		Inactive Utank			Active U-Tank		
		Wave ID			Wave ID		
Parameter	Unit	C1	C2	C3	C1	C2	C3
Tot. Net Power, P_{net}	kW	13.6	17.5	15.3	20.4	21.8	22.0
Tot. Gross Power, P_{gross}	kW	22.1	28.1	27.2	32.6	32.3	34.0
Flywheel Speed, $\dot{\phi}_{opt}$	rpm	451	489	517	532	488	509
PTO Damping Coeff., c_{opt}	kNms/rad	154	139	121	157	156	131
Utank Stiffness Ratio, $c^*_{\tau\tau}/c_{\tau\tau}$	-				2.2	3.2	3.2
Floater Pitch Angle rms, δ_{rms}	deg	2.77	2.87	2.17	3.62	3.32	3.45
U-Tank Angle rms, τ_{rms}	deg	16.6	19.8		4.32	2.61	2.48
Gyro. Angle rms, ε_{rms}	deg			21.6	23.1	21.1	24.6
Gyro. Velocity rms, $\dot{\varepsilon}_{rms}$	rpm	2.56	3.03	3.2	3.1	3.1	3.4
PTO Torque rms, T_{PTO}	kNm	41.3	44.2	40.6	50.6	50.3	47.3

of the device in complex sea states. The simulation results for the inactive U-Tank and active U-Tank control are given in table 5.7.

It is clear how the power extraction is sensitive with the energy distribution, even if the sea state parameters T_e and H_s remain the same. Also the the control parameters change and a sensitivity analysis should be carried out in the future. A relevant result is the capability of the active U-Tank control to tune the device as best as possible to increase the power extraction demonstrating the adaptability of the device with different wave conditions (see figure 5.27).

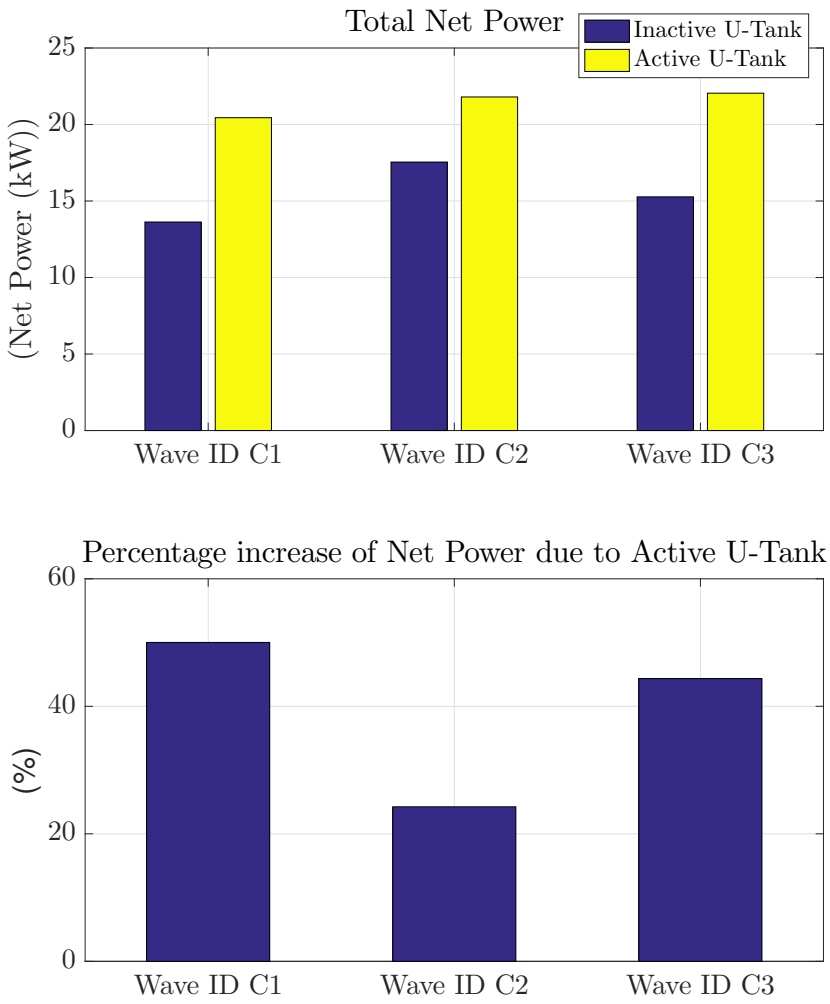

Figure 5.27 Total power net of IOwec with real sea state PSD wave and efficiency increase due to active U-Tank Control.

The influence of the active U-Tank control on the energy distribution of the response of the device is highlighted in figures 5.28 and 5.29, showing the effect of the U-Tank dynamics that shifts the device response in order to maximize the energy extraction.

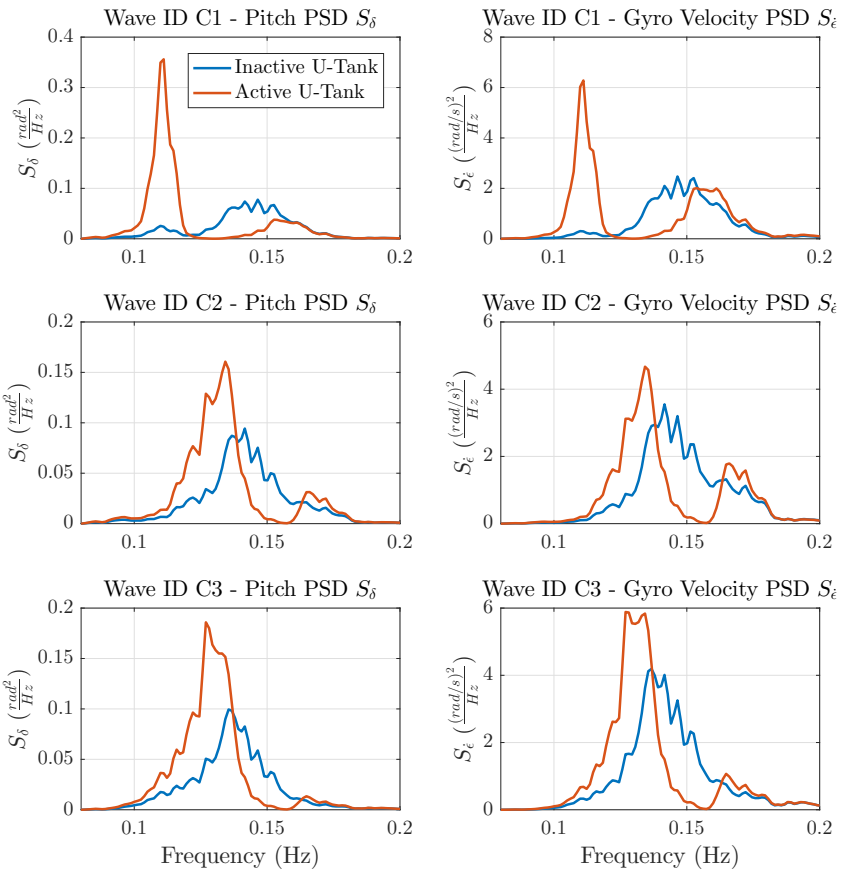

Figure 5.28 Comparison of the floater pith and gyroscope velocity PSD for the inactive and active U-Tank case. Measured wave PSD.

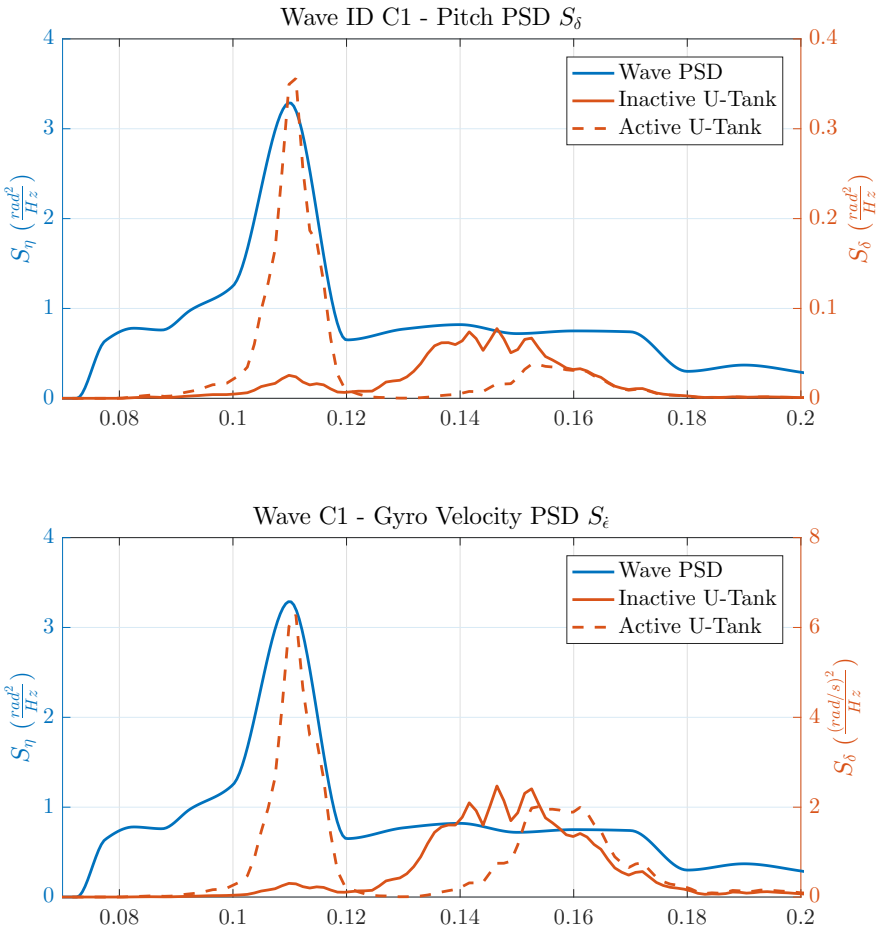

Figure 5.29 Influence of the active U-Tank control on the energy distribution of the device response with measured wave PSD.

5.5.3 On-Board Sea State Estimation

In conclusion, the performance and the values of control parameters are suboptimal if mapped offline only as a function of the energetic period T_e and significant height H_s. For a preliminar assessment the use of standard analytical wave spectral function good practice, but the real energy distribution of the sea state should be taken into account when operating in real sea states. Therefore, a technical solution can be the installation of a wave buoy close to the hypothetical array of devices. An other solution can be the on-board estimation of the wave PSD through the measurement

of the floaters heave. The main idea is to measure the heave motion of the floater through an Inertial Measurement Unit (IMU) and with the knowledge of the heave RAO calculate the wave PSD under the assumption of linearity:

$$S_\eta(f) = \frac{S_z(f)}{|RAO_{33}(f)|^2} \tag{5.11}$$

Where f is the frequency considered, RAO_{33} is the response amplitude operator for the heave DoF, S_z is the measured heave PSD and S_η is the estimated wave PSD. The heave RAO of the device can be estimated experimentally or numerically through a Boundary Element Method software like Nemoh or Ansys Aqwa. The heave motion of the ISWEC and IOwec device is totally uncoupled with the other DoF, and in particular with the pitch DoF that is strongly affected by the gyroscope and U-Tank dynamics. The uncoupling of the heave is due to geometrical symmetry of the floater around its longitudinal and transversal plane and because the center of gravity is coincident with the geometrical center (except for the z-axis) due to the symmetrical distribution of the masses.

This sea state estimation method from heave measurement was developed and validate [10] through the data of an experimental campaign on the full-scale prototype ISWEC deployed from September to December 2015. The heave motion of the ISWEC was acquired by an IMU system and the wave elevation was measured by a wave measurement instrument (Nortek AWAC,a current profiler and a wave directional system) installed nearby the device. In this preliminary analysis the heave RAO of the ISWEC was calculated numerically with the BEM software Ansys Aqwa with the assumption of linearity and assuming that the mooring forces were negligible. An example of elaborated measured wave PSD and heave PSD is given in figure 5.30 compared with the numerical heave RAO and it is clear that the floater behave like a low pass filter for what concern the heave DoF.

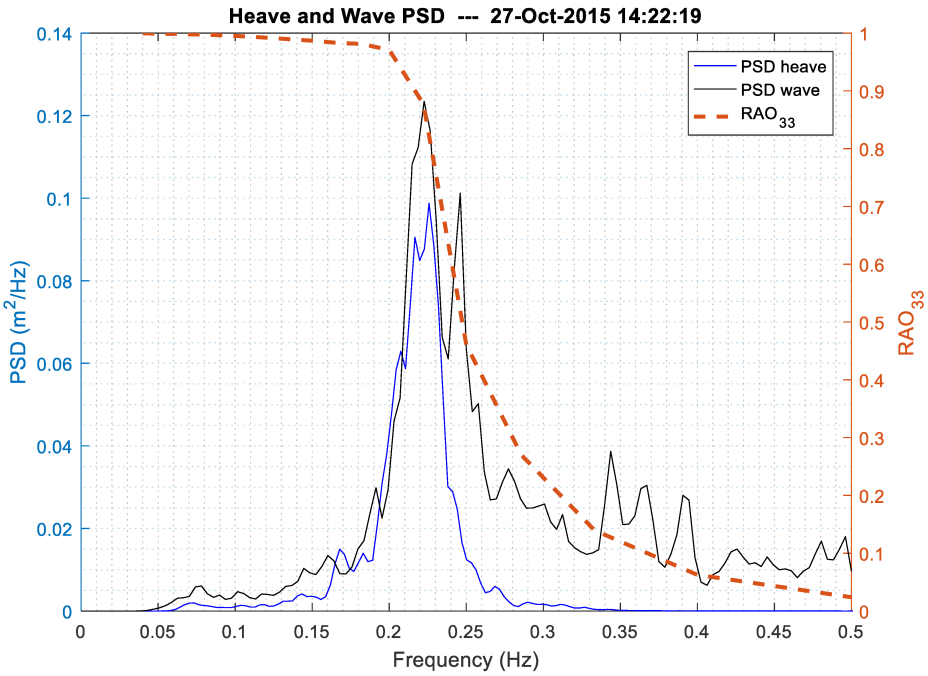

Figure 5.30 Measured wave PSD compared with measured heave PSD and floater heave RAO [10].

The measured wave and estimated wave PSD are compared in figure 5.31 showing good agreement between the two curves and more details of the validation process are provided in the paper work.

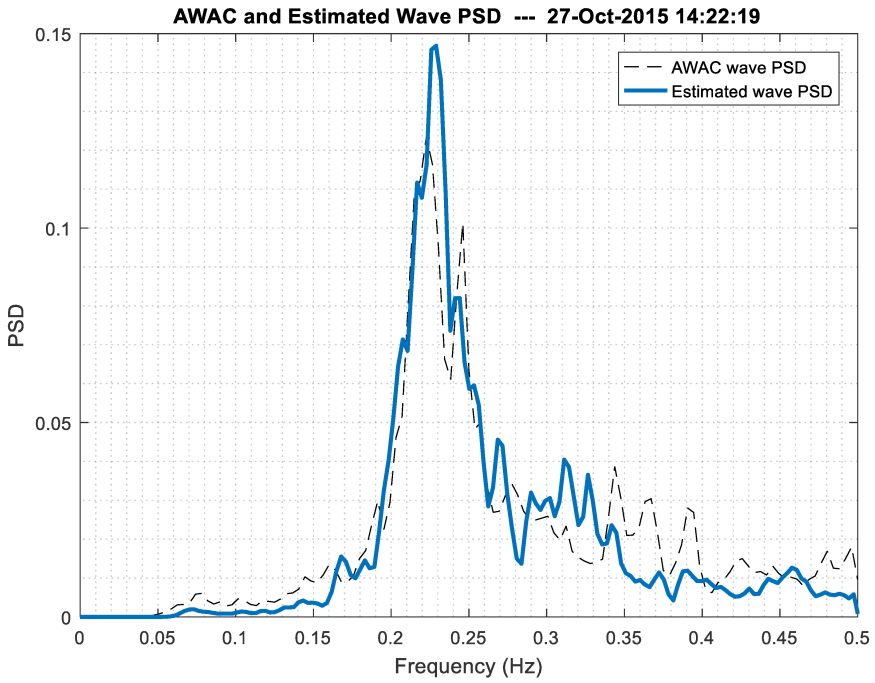

Figure 5.31 Measured wave PSD compared with the estimated wave PSD from floater heave measurement [10].

This estimation method can be very useful and easy to implement on-board and allows the calculation of not only the important sea states parameters T_e and H_s but also the energy distribution is given. Therefore, it is possible to implement more sophisticated sea-state based control logics, especially for the choice of the correct stiffness ratio for the active U-Tank control.

5.6 Annual Productivity Assessment

In the previous section, the analysis of the dynamics and performance of the IOwec system were discussed in detail, highlighting the adaptability of the device in different sea-state conditions through the slow-tuning control of the U-Tank. In this section, the annual productivity of the first draft of IOwec is evaluated considering the two selected sites, Humboldt Bay in California and WETS site in Hawaii.
To perform such analysis, a set 70 pseudo-random waves with duration of 1800 (s) has been chosen. The Bretshneider spectrum is adopted for the following reasons:

- in wave energy field the Bretshneider spectrum is widely used [56, 57].
- The U.S. Department of Energy recommends the Bretshneider spectrum when assessing the performance of a WEC to have standardised method of comparison [105].
- The representative mean spectra of the analyzed sites are fairly represented by the Bretshneider spectra, even if bimodal sea-states can occur during the year.

The chosen sea-state conditions form a grid in which the energetic period T_e and significant height H_s are equally spaced in the following ranges:

- Significant height H_s: 7 values evenly spaced in the range: [0.5 5.25].
- Energetic period T_e: 10 values evenly spaced in the range: [5 14].

The H_s and T_e vectors form a grid of sea states that cover the occurrence matrices of both sites of interest. The total number of waves under analysis are a compromise between grid size and computational time.
For each wave the produced net mechanical power is maximized optimizing the flywheel speed $\dot{\phi}$ and PTO damping c using the Time Simulation Tool discussed in section 4.4. The simulation constraints and optimization boundaries are defined in the same section. Since the objective is to evaluate also the performance improvement due to the U-Tank control, two cases are analyzed: Inactive and Active U-Tank control. As discussed previously the inactive U-Tank control means that a closed hydraulic valve prevent the water to flow inside the tank and no motion and dynamics occur (the water acts as standard ballast). In the active U-Tank control case, through a brute-force approach the best stiffness ratio $c^*_{\tau\tau}/c_{\tau\tau}$ (see section 5.3.1) that maximize the net power for each sea-state is chosen among the range:

- U-Tank stiffness ratio range: [2.2, 2.6, 3, 3.5, 4.9].

The calculated net power matrix is then interpolated on the occurrences matrices of the two sites and then the calculation of the net annual productivity is straightforward. The "weighted" results are calculated weighting the results matrix with the occurrences of the specific site in analysis. The improved productivity due to the active control of the U-Tank compared with the inactive U-Tank case is 20 % in

Table 5.8 Results summary of the first draft of IOwec performances in Humboldt Bay (California) and WETS (Hawaii) sites.

Parameters	Unit	California		Hawaii	
		Inactive Utank	Active Utank	Inactive Utank	Active Utank
Annual Net Productivity	MWh/y	280	335	270	306
Annual Gross Productivity	MWh/y	375	421	360	396
Mechanical Efficiency, η_{mech}	%	75	80	75	77
Weighted $\dot{\phi}$	rpm	456	462	461	460
Weighted c	kNms/rad	205	208	228	200
Weighted δ	deg	3.5	4.0	3.4	3.8
Weighted τ	deg		2.0		1.5
Weighted ε	deg	18.4	20.2	19.2	20.0
Weighted $\dot{\varepsilon}$	rpm	2.8	4.0	2.9	3.0
Weighted T_{PTO}	kNm	62	69	59	65
Weighted Net Power P_{net}	kW	31	39	30	35
Weighted Gross Power P_{gross}	kW	41	48	40	45

California and 13 % in Hawaii. The wave periods in the Californian site are longer and spreader than Hawaiian site and then the performance improvement de to the U-Tank control is more evident.
The mechanical efficiency of power conversion is about 80 %, and therefore 20 % of the mechanical energy of the gyroscope is dissipated by the flywheel bearings.

5.6.1 Results

The synthetic results of the simulations are summarized in table 5.8.

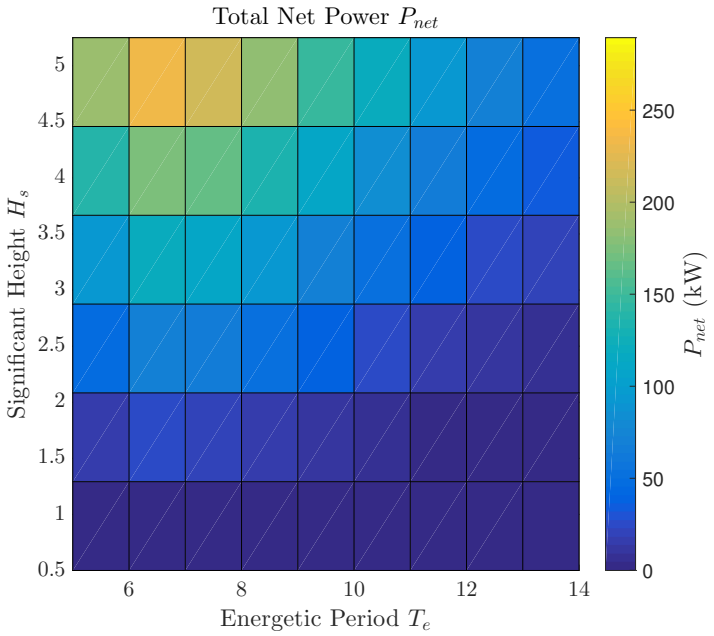

Figure 5.32 Total mean net mechanical power P_{net} plot grid. First IOwec draft - Active Ut-Tank control case.

The net power matrix, the annual productivity matrices in the two deployment sites and the system variables of interest are given in figures for the the case of IOwec with active control. The results regarding the case of inactive U-Tank are provided in Appendix A. The optimal flywheel speed increase with the signficant wave height H_s and with wave power: the flywheel bearings losses increases with the flywheel speed, and therefore for sea states with low energy the flywheel speed is kept low. The stiffness U-Tank ratio $c^*_{\tau\tau}/c_{\tau\tau}$ vary accordingly with the consideration made in the previous sections, when the wave period increases the U-Tank control shifts consequently the resonance period of the device (see figure 5.12).

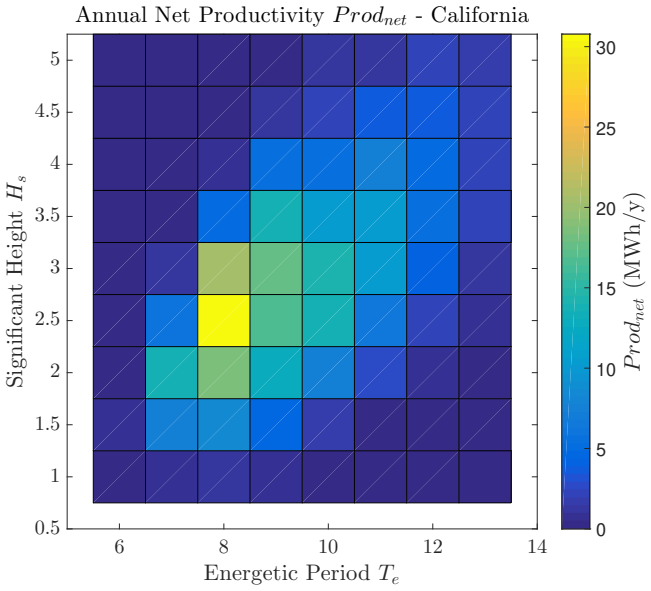

(a)

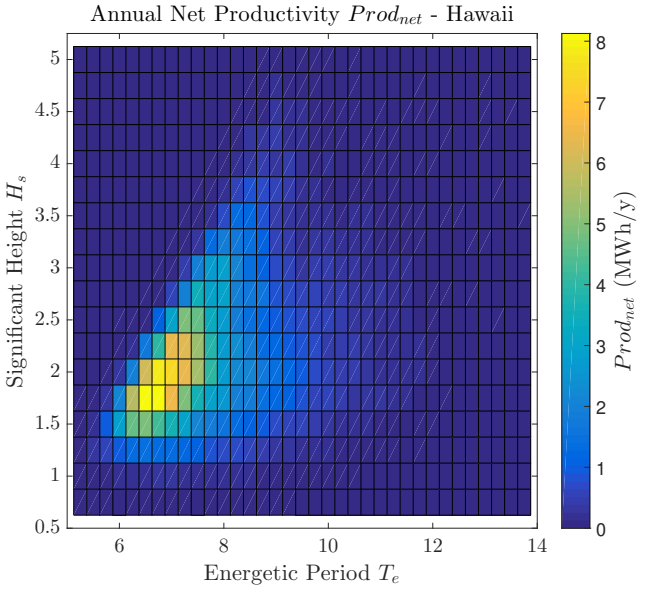

(b)

Figure 5.33 Productivity *Prod* interpolated plot grids. First IOwec draft - Active Ut-Tank control case. Active U-Tank control case.(a) Humboldt Bay (California) (b) WETS (Hawaii).

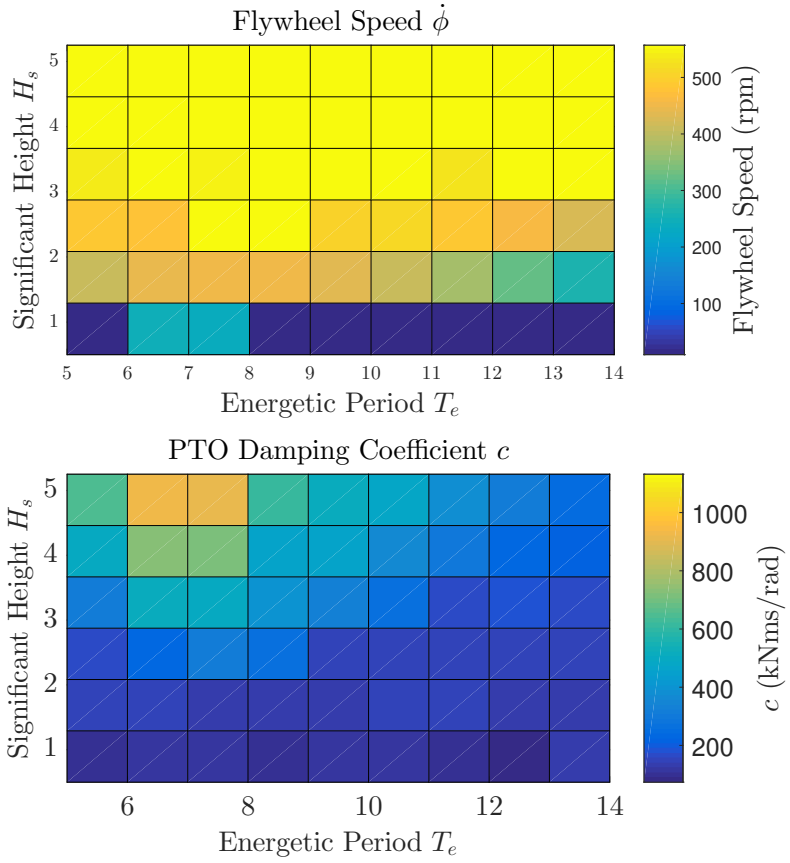

Figure 5.34 Optimal flywheel speed $\dot{\phi}$ and PTO damping coefficient c plot grids. First IOwec draft - Active U-Tank control case.

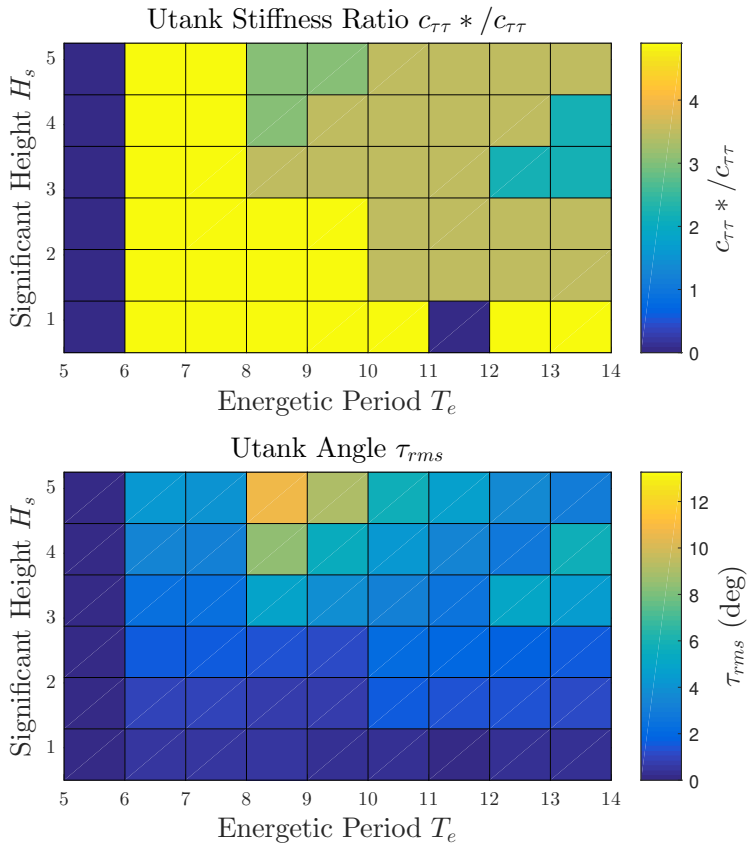

Figure 5.35 U-Tank stiffness ratio $c^*_{\tau\tau}/c_{\tau\tau}$ and U-Tank angle τ_{rms} plot grids. First IOwec draft - Active U-Tank control case.

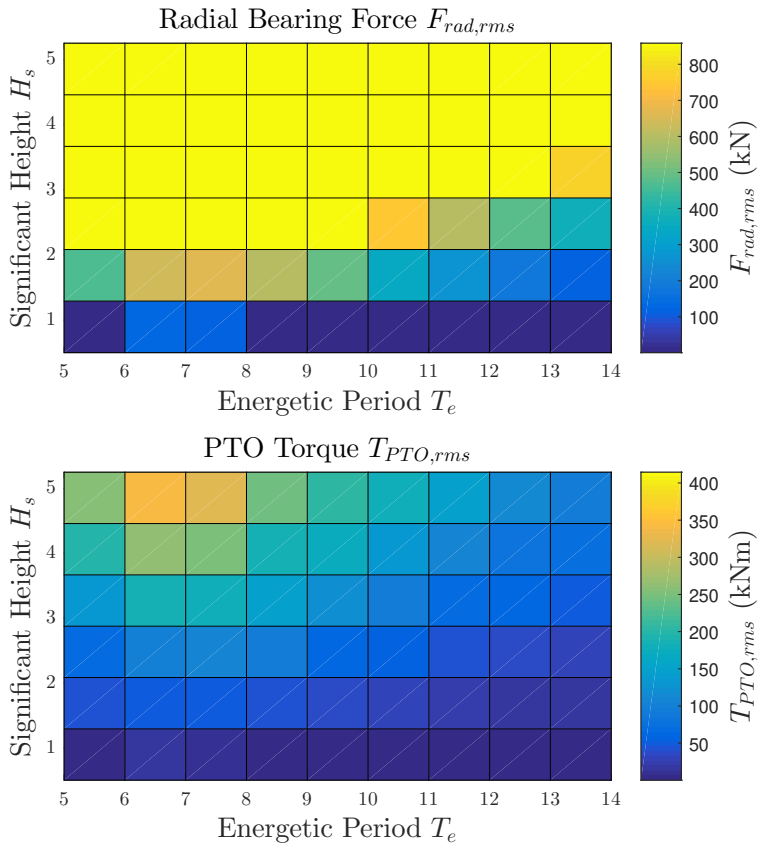

Figure 5.36 Radial bearing forces $F_{rad,rms}$ and PTO torque $T_{PTO,rms}$ grid plots. First IOwec draft - Active U-Tank control case.

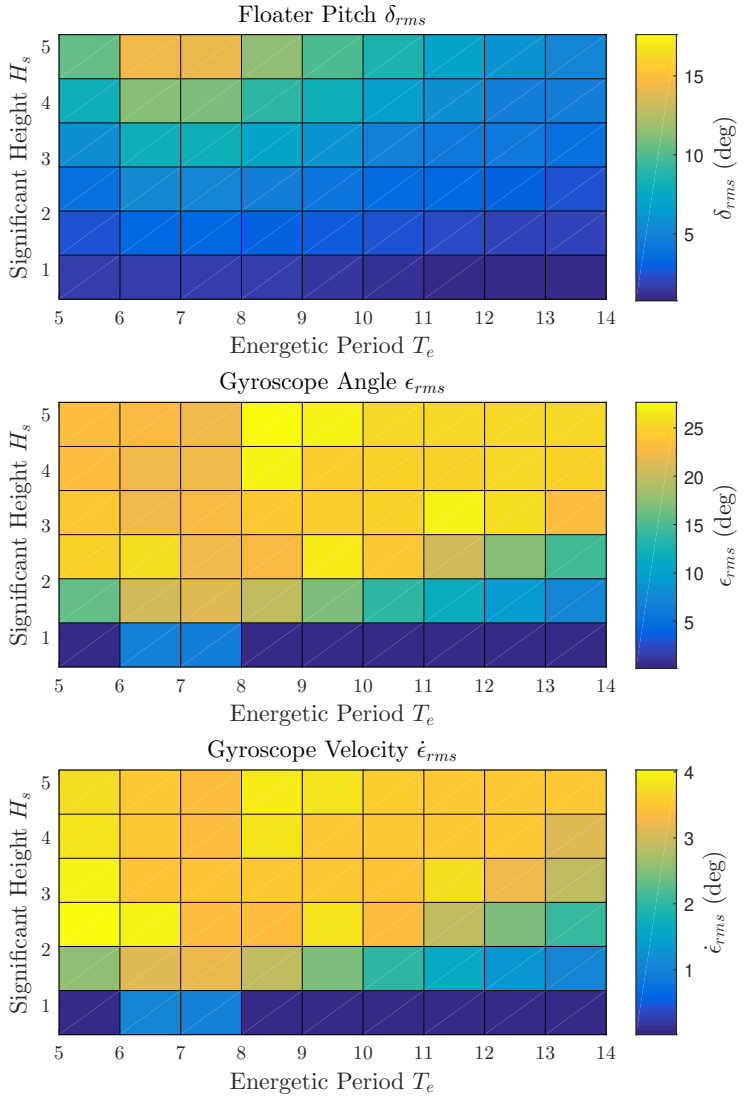

Figure 5.37 Floater pitch δ_{rms}, gyroscope angle ε_{rms} and velocity $\dot{\varepsilon}_{rms}$ grid plots. First IOwec draft - Active U-Tank control case.

In conclusion, this section presented the first draft of the IOwec device, with the analysis of its dynamics highlighting the improvement of the performance of the device due active control of the U-Tank. Since the device show a high complexity, with the dynamic interaction of three systems (floater, gyroscope and U-Tank) and with also the added complexity due to the regulation of the flywheel speed, PTO

damping and U-Tank stiffness ratio, the identification of an optimal design solution is not trivial and beyond the capabilities and sensibility of the system engineer. Therefore, a global-search optimization process is necessary in order to identify the best solution, or a set of optimal solutions, that optimize the performance of the IOwec device for the two chosen sites under analysis. The next chapter will discuss the optimization algorithm, its setup and the results of the optimal configuration of IOwec compared with its first draft version.

Chapter 6

Optimization of the IOwec Device

In this chapter, the optimization of the IOwec device is discussed.
The purpose of the optimization is to identify a device (or a set of devices) as much site-agnostic as possible, i.e. to have one machine that performs well regardless of the location where it is deployed. In fact, extreme specialization of a device to an installation site it's likely to lead to poor performances in sites other than the designed location. In section On the contrary, a device capable to perform well in different locations would significantly reduce production costs, exploiting economy of scales.
Such optimization problem falls within the field of multi-objective optimization (known also as Pareto optimization), where more than one objective needs to be optimized simultaneously. The objective to be minimized, or maximized, is also called fitness function or performance index. The capture width C_w is a common performance indicator for wave energy indicator [113], defined as the ratio of the power absorbed by the WEC P_a to the incident, unidirectional, wave power P_w:

$$C_w = \frac{P_a}{P_w} \tag{6.1}$$

Falnes and Todalshaug [114] have discussed the limits of using the capture width as performance indicator of a WEC. They highlight the urgent challenge to develop a feasible wave energy device, which maximize the power absorption not with respect to the available wave power but directly to the device itself (i.e. its cost or size of the WEC). In this work, a techno-economic metrics related to the cost of energy has been chosen. The two deployment sites discussed in section 5 and the IOwec

Design Tool have been adopted to calculate the fitness value for a given set of design parameters (see section 4 and 5.2).
The first part of this section explains the multi-objective optimization algorithm, the design space and the set-up of the optimization algorithm. The second part discusses the results of the optimization process with a comparison between the first draft of the IOwec device its optimized version.

6.1 Multi-objective optimization problem

The optimization of the device on different deployment sites is carried out considering several design parameters that influence the energy harvesting performance but also the cost of the device and the technology solutions. The choice of the design space (also called decision space), i.e. the investigated range of each design parameter, is strategic and fruit of the experience and sensibility of the system engineer.
The purpose of the multi-objective optimization is to find a solution within the design space in order to minimize some fitness functions, in this case the cost of energy in the two deployment sites. In the simple single-objective optimization problem the superiority of a solution can be determined uniquely comparing the fitness values of all the solutions. Instead, the multi-objective optimization problem involves more than one objective function that must be minimized and the superiority of a solution is given by its **dominance** and then by a set of optimal solution [115–117].
A solution x_1 dominates another solution x_2 (solution x_2 is dominated by x_1) if:

- all the fitness values of solution x_1 are no worse than the fitness values of solution x_2.
- Al least one fitness value of solution x_1 is strictly better than the fitness value of solution x_2.

For a multi-objective optimization problem we can define the **Pareto optimal solutions** as the **non-dominated solution set**: given a set of solutions, the non-dominated solution set is a set of all the solutions that are not dominated by any member of the solution set. The non-dominated set of the entire feasible design space is also called the **Pareto-optimal set** and the frontier made from the union of the

points of the Pareto-optimal set is called **Pareto front** (see figure 6.1). Hence, the goal of the multi-objective problem is to find a set of solutions as close as possible to the Pareto-front and the solutions of the set should also be as diverse as possible.

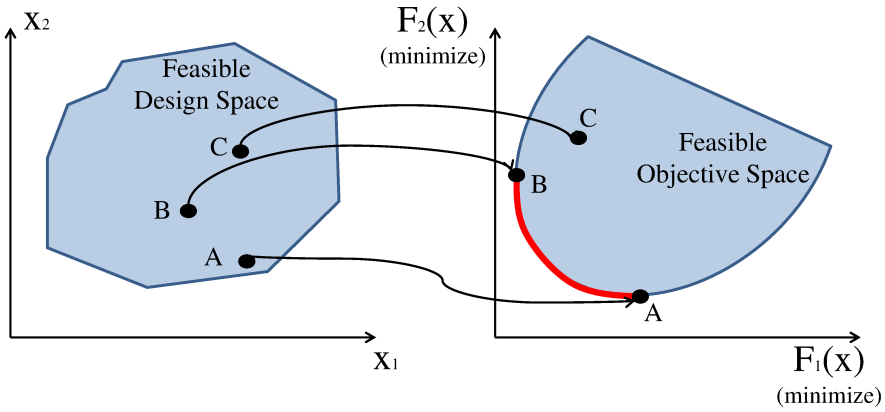

Figure 6.1 Graphical representation of the Pareto-optimal set concept.

6.1.1 Evolutionary optimization

Traditional optimization algorithms are more indicated for single-objective optimization problems and instead evolutionary algorithms present characteristics that fit naturally with multi-objective problems, and they constitute the state of the art in this field [118, 117, 119]. Evolutionary algorithms (EA) are a class of heuristic stochastic optimization methods that replicates the process of Darwinian evolution and natural selection. The evolutionary algorithms have been widely used in multi-objective optimizations problems because of their population-based nature that allows the generation in a single run of several solutions to form the Pareto optimal set. The application of evolutionary algorithms can also be found in the wave energy field. Colby et al. [120] applied evolutionary algorithms to optimize the ballast geometry of a WEC. McCabe [121] uses EA to carry out a constrained optimization of the ge-

ometry of a surge-resonant WEC, with the geometry described by bi-cubic B-spline surfaces. Babarit and Clément [122] implemented a multi-objective optimization based on evolutionary algorithms for the optimization of the pitch-resonance device Searev, considering as objective both the maximization of power production and cost reduction. The main advantages of evolutionary algorithms are:

- They are population-based and direct search methods and do not required any derivative information.
- Since they produce several solutions in a single iteration, it is possible to implement paralleling processing and reduce the computational time.
- They can handle both continue and discrete variables.
- Its stochastic nature permits to find the multi-maxima of the problem.
- They do not require the fitness function to be smooth.

The evolutionary algorithm can be summarized in the following four steps:

- **Initial Population**: The first iteration of the evolutionary algorithm is the random generation of a set of individuals called population. Each individual is a solution of the problem and it is represented by a string (chromosome), where each element (gene) represents the specific design parameter.
- **Fitness function**: for every individual of the population a fitness function is evaluated. The fitness function gives a score to the individual and the probability of reproduction are based on this value.
- **Selection**: In this phase the individuals are ranked by their fitness values and the fittest are allowed to pass their genes to the next generation. pairs of individuals, called parents, are selected for the reproduction.
- **Crossover and Mutation**: Crossover simulate the natural reproduction phase, where the genes of the parents are mixed and transmitted to two children. A crossover point is chosen randomly inside the chromosome of both parents, then the offspring are created by exchanging the genes of parents until the crossover point. In this way, the next population generation will be made of

Table 6.1 Weights used for the scalarization of the multi-objective optimization problem.

Weight set ID	w_1	w_2
1	0.5	0.5
2	1	0
3	0	1

genes of the fittest individuals of the previous generation. Mutation occurs with low probability in order to maintain diversity within the population and avoid a premature convergence in a local minima or maxima. The mutation consists in changing the value of some genes of an offspring.

- **Reiteration and termination**: After the crossover and mutation, a new generation of solution is ready to be evaluated an the iteration can continue until some conditions are reached: convergence thresholds, maximum number of iterations etc.

Scalarization technique

A common procedure is to transform the multi-objective problem into a series of single objective problem with the use of scalarization techniques [123]. The scalarization consists in aggregating the several objectives of the problem into a unique objective that can be optimized with an evolutionary algorithm. Through the choose of different weights that aggregate the objectives it is possible to build the Pareto-optimal set of the multi-objective problem. In this work the linear scalarization is adopted and is it defined mathematically as follows:

$$g(x) = \sum_{1}^{k} w_i f_i(x) \tag{6.2}$$

Where $f_i(x)$ is the i-th objective to minimize of the multi-objective problem, k is the number of objectives, w_i is the weight to be applied to the i-th objective and $g(x)$ is the objective that must be minimized in the reduced single objective-run. In this work, the multi-objective problem consist in minimizing two objectives: the cost of energy of IOwec in the Humboldt Bay site $f_1(x)$ in California and the WETS site in Hawaii $f_2(x)$. And for this purpose three set of weights are investigated:

Where the the weight sets 2 and 3 represent the single-objective optimization of the device respectively in Humboldt Bay and WETS site. In the next section the fitness function for the solutions ranking is discussed.

6.1.2 Fitness Function

The fitness function takes a candidate design solution as input and calculates an output that quantify how good the solution is. The choice of the proper fitness function is not arbitrary and it relies heavily on the purpose of the optimization. For a wave energy converter developer for example one objective is to optimize the design parameters of the device to maximize the annual productivity. Including also the manufacturing cost of the device a techno-economic optimization can be achieved. Several metrics for techno-economic assessment of marine energy converters have been proposed [124–126]. A common used techno-economic indicator is the Levelized Cost Of Energy (LCOE) defined as the net present value of the unit-cost (total capital, operational and maintanance costs included) of electrical energy over the lifetime of the device. LCOE requires detailled assessment of the capital costs, including mooring sytem electrical cable and installation, and operational costs. In a early design stage these costs are difficult to quantify and parametrize in terms of the device parameters. A reduced metrics serving as proxy to LCOE was proposed for the Wave Energy Prize competition [125] to evaluate and compare different low-TRL WEC concepts. The proposed metrics is called *ACE* (Average climate capture width to the Characteristics capital Expenditure) and it is defined as the ratio of the average climate capture width ($\overline{ACCW}$) to the characteristic capital expenditure (CCE):

$$ACE = \frac{\overline{ACCW}}{CCE} \tag{6.3}$$

While the capture width C_w (see eq. (6)) varies from wave to wave, the $\overline{ACCW}$ is a unique indicator evaluated for a set of sea-states representative of a deployment site. The $\overline{ACCW}$ is defined as the weighted average the absorbed energy by the device for different sea-states divided by the incident wave energy [125]. The CCE is defined as structural cost that includes the material and manifacturing costs and it does not include PTO, mooring, electrical cable, installation costs because difficult to assess for early-stage concepts.
In this work, a similar approach is adopted. A performance indicator related to the

cost of energy is adopted as fitness function FiT, defined as the capital expenditure of the device C_tot spread over the project life Y divided by the mechanical net productivity for the site of reference $Prod_{net}$:

$$FiT = \frac{C_{tot}}{Prod_{net} \times Y} \ (MWh/Euro) \tag{6.4}$$

The IOwec Design Tool presented in section 4 allows the calculation of the net annual productivity (see section 5.6) for a chosen deployment site and a preliminary cost assessment of the device. In recent works [127, 128], the importance of including the control strategy during the optimization of the device has been highlight. In fact, the resonance condition of the device depends also on the control strategy adopted. Since the slow-tuning control of U-Tank and gyroscope influence drastically the dynamics of IOwec, they are optimized for each sea-state leading to a "Control-Informed" optimization as discussed by Garcia-Rosa et al. [127].
The adopted fitness function FiT will be used in the evolutionary algorithm to compare and classify the individuals. The capital expenditure C_{tot} takes into account the costs of the floater, gyroscopes and a preliminary assessment of the PTO costs described in section 4.2.2. The expected project life Y is assumed to be 25 years. In this thesis, the fitness function FiT is also called also **Performance Index, (PI)**.

Handling of not feasible solutions

During the assessment of the fitness function, inside an iteration of the evolutionary algorithm, it can happen that certain individuals have a combination of design parameters that produce a not feasible solutions. In fact as discussed in section 4.2.1, the a solution set of design parameters can lead to a not feasible device, usually attributable to size problems of the device subsystems that do not fit inside the floater. In literature, several methods have been discussed to handle unfeasible solutions [129] and the most used is the penalty-based approach [130]. This approach consists in apply a penalty function to the fitness value, and it transforms a constrained into an unconstrained optimization. In this work, the death penalty approach is adopted, that rejects unfeasible solution $\bar{x}$ from the population applying a heavy penalization $P(\bar{x}) = \infty$:

$$eval(\bar{x}) = \begin{cases} f(\bar{x}), & if \bar{x} \in F \\ P(\bar{x}), & otherwise \end{cases} \tag{6.5}$$

Where F is the set of feasible solutions. If no constraint violation occur the fitness value $f(\bar{x})$ of the solution $\bar{x}$ is normally calculated, otherwise the penalization $P(\bar{x})$ is applied.
This is a preliminary approach to the complex problem of handling constraints and unfeasible solution in evolutionary algorithms, and convergence issues of rejecting the unfeasible solutions have been discussed by some researchers [131]. In fact, a solution set with a large number of unfeasible solutions can lead to a premature convergence in a local minima, due to a very low diversity in the population.
The investigation of the influence of unfeasible solutions on the convergence of the evolutionary algorithm for the optimization of IOwec device is beyond the arguments of this work, and it will be analyzed in future more in detail.

6.1.3 Optimization Setup

In this section the set-up of the multi-objective optimization of the IOwec device is discussed. The Dakota [132] (Design and Analysis toolKit for Optimization and Terascale Applications) open-source toolkit developed by Sandia National Laboratories is used for the implementation of the optimization process (high level), and the IOwec Design Tool (low level) is integrated as a black box in Dakota in order to receive the solution set $\bar{x}$ and calculate the fitness functions $f_1(\bar{x})$ and $f_2(\bar{x})$), respectively evaluated in Humboldt Bay and WETS site (see figure 6.2).

Table 6.2 Weights used for the scalarization of the multi-objective optimization problem.

Parameter	Value
Population size	90
Fitness type	Linear rank
replacement type elitist	1
crossover rate	0.8
mutation rate	1
mutation type	offset normal
max iterations	40

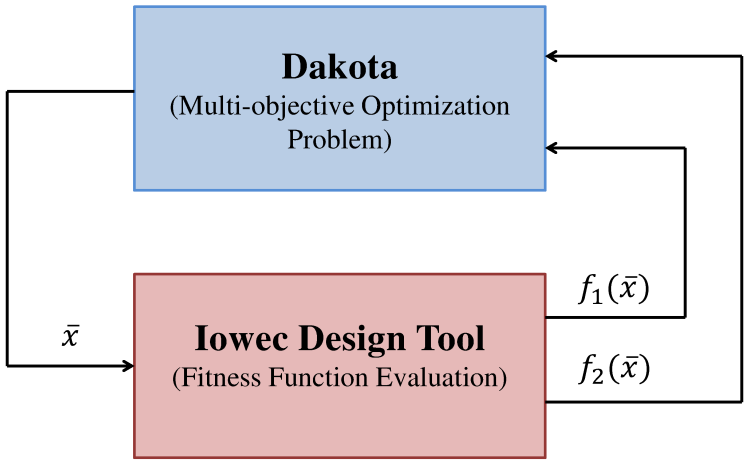

Figure 6.2 Coupling of DAKOTA with the IOwec Design and Simulation Tool.

Evolutionary Algorithm

The DAKOTA evolutionary algorithm tool *Coliny EA* has been adopted in this work with the pareto set optimization approach discussed previously [133]. The three weight sets presented in section 6.1.1 are implemented in the optimization problem. The evolutionary algorithm has a maximum number of 40 iterations as stopping criteria, and a population of 90 individuals is chosen. Therefore, each optimization evaluates 3600 individuals, and the whole optimization process 10800 individuals. The settings of the algorithm are provided in table 6.2.

Table 6.3 Design parameters and design space of the optimization problem.

Parameter	Symbol	Unit	Range	Variable Type
Hull lenght	L	m	[19,20,21,22,23]	Discrete
Hull width	W	m	[15,20]	Discrete
Hull shape coefficient 1	h		[0.3:0.7]	Continue
Hull shape coefficient 2	k		[0.6:0.8]	Continue
Hull draft ratio	j		[0.6:0.7]	Continue
Ballast Filling Ratio	BFR		[0.65:1]	Continue
Flywheel Inertia	J	kgm^2	[10000:35000]	Continue
Eccentric Mass	M_p	kg	[3000:20000]	Continue
number of gyroscope units	$nGyros$		[2,4]	Discrete
Radial Bearings ID	$BearID$		[1,2,3,4,5,6,7]	Discrete
U-Tank shape coefficient 1	UT_{W_r}		[0.2:0.4]	Continue
U-Tank shape coefficient 2	UT_{H_d}		[0.15:0.35]	Continue
U-Tank shape coefficient 3	UT_{W_d}		[1:1.15]	Continue

The advantage of evolutionary algorithms is the possibility to parallelize the computation of the individuals fitness score, and 22 cores are dedicated to fulfill this purpose. Computations are performed on a dedicated node of the high-performance computing (HPC) cluster of Politecnico di Torino, HACTAR, which is provided with 24 cores Intel Xeon E5-2680 v3 2.50GHz.

Design parameter and design space

The 13 design parameters of IOwec that have been chosen to be optimized have been discussed in section 4 and they are the same used to define the first draft of IOwec in section 5.2. The choice of the design space is not arbitrary, and it affects the amount of unfeasible solutions and the convergence of the optimization algorithm. The first draft of IOwec is taken as reference for the definition of the design space, and the ranges of parameters have been defined consequently (see table 6.3).

6.2 Optimization Results Analysis

In this section the results of the multi-objective optimization of the IOwec device are discussed. First, the convergence of the evolutionary algorithm is shown and commented, then techno-economic considerations are made especially on the conver-

gence of some design parameters like the number of gyroscope units. At the end, an optimal solution is chosen from the device solutions with the lowest fittest value and its characteristics are evaluated and compared with the first draft version of IOwec.

6.2.1 Convergence Analysis

The feasible solutions of the multi-objective optimization are shown in figure 6.3 as a function of their perfomance index (PI) evaluated in Hamboldt Bay (California) and WETS (Hawaii) site. The non feasible solutions are 3775 over 10800, which means a mortality rate of 35 %.

With reference with figure 6.4, the results of the optimization do not show any Pareto front and therefore a unique optimal device, that minimize both the fitness value calculated in the two sites of interest is found.

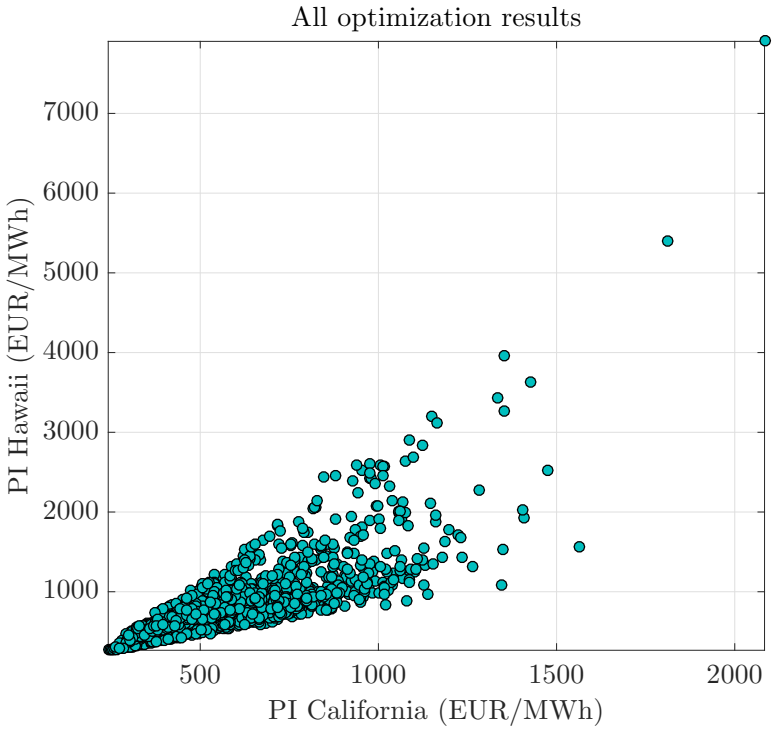

Figure 6.3 All feasible solutions computed as a function of their performance index (PI) evaluated in the Californian and Hawaiian site.

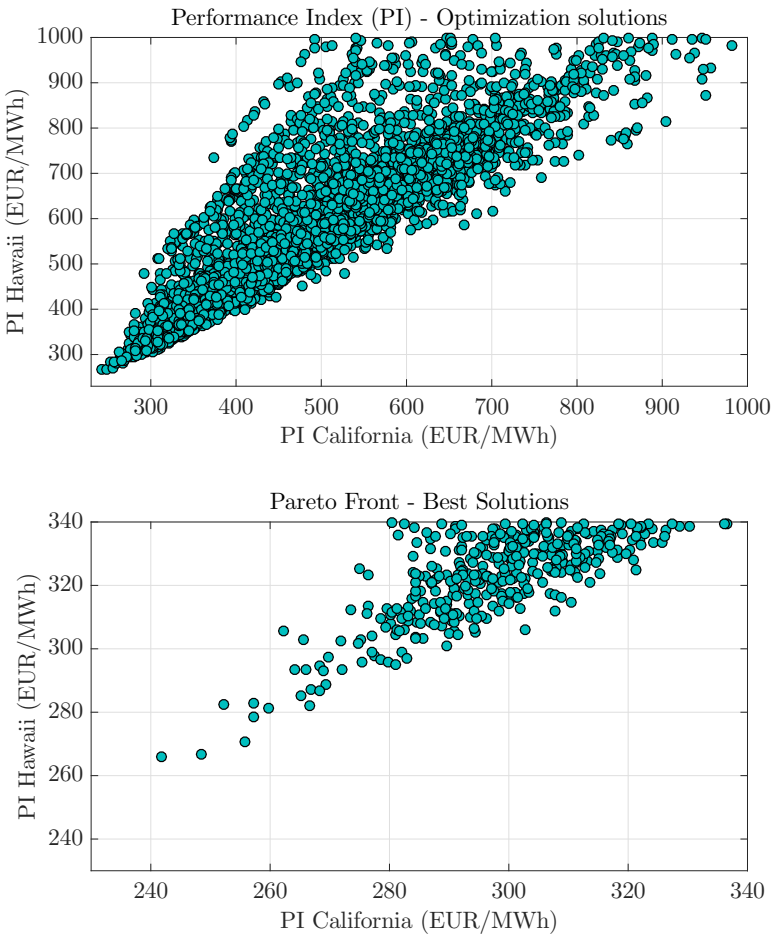

Figure 6.4 Best solutions and Pareto set.

The best solution has ID 1970 and thefore it has generated during the single-objective optimization with weight set ID 1 and it belongs to the 21th generation and it has performance index 242 (€/MWh) in California and 266 (€/MWh) in Hawaii.

6.2.2 Techno-economic analysis

The techno-economic analysis of the feasible configurations is provided in figure 6.5 with the general trends of the optimization and a focus on the most interesting solutions. Data are plotted as a function of the device cost, performance index and net productivity. All the analysis and plots in this section refer to the case of Humboldt

Bay, for the WETS sites analogue considerations can be made and the results are given in Appendix A. With reference to the plotted data, certain considerations can be done:

- Since no constraints were imposed on the rated power of the device during the optimization, several solutions with the same value of performance index but with different cost of the device are found. Therefore, devices with different annual productivity but with the same performance index can be chosen.
- The productivity increase with the investment/cost of the device.
- The best solutions are found around a device cost in the range of [1.5-2.5] (M EUR).

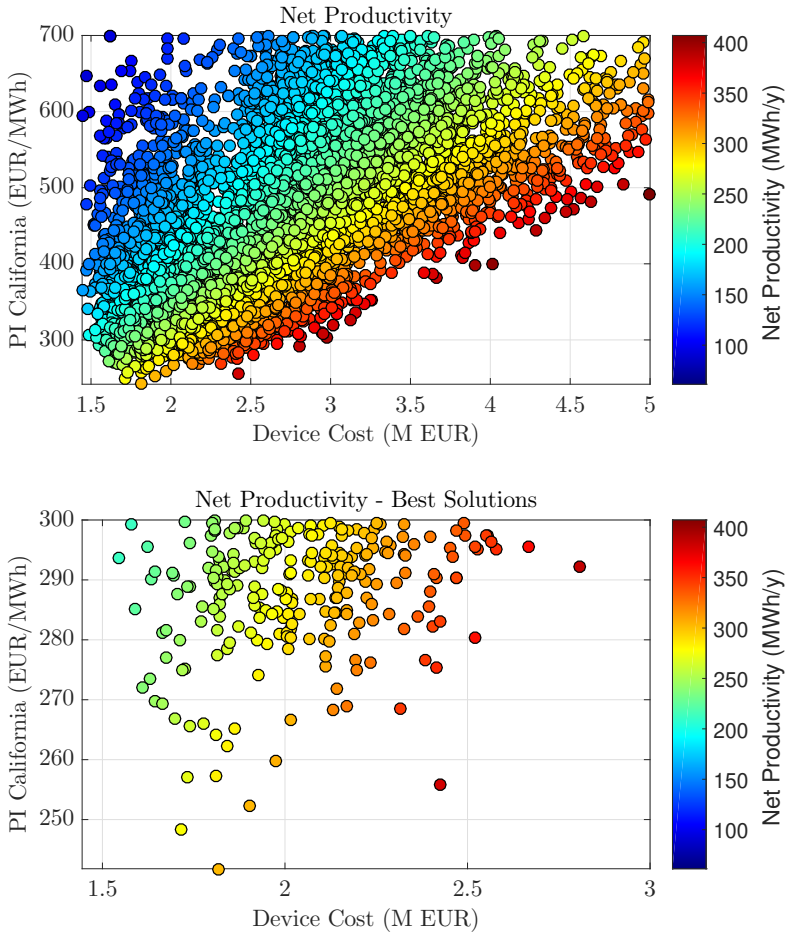

Figure 6.5 Techno-economic analysis: annual net productivity $Prod_{net}$, Performance Index PI and device cost C_{tot}. Evaluated in Hamboldt Bay (California).

The trends and convergence of most meaningful techno-economic design parameters, hull width W, number of gyroscope units $nGyros$ and flywheel inertia J, are analyzed respectively in figure 6.6 6.7 and 6.8. Certain conclusion can be drawn:

- the 4 gyroscope units design solution is clearly not advantageous and the presence of two more gyroscopes and the consequent higher power installed capacity does not justify the higher investment required.
- The optimization does not converge clearly on a certain hull width. With reference to 6.6 it can be concluded that each hull width is optimal in a certain

range of investment. Higher is the hull width, higher is the device cost but also the annual net productivity. From this result it is possible to conclude the future optimizations of the device have to be managed with fixed values of hull width to reach a proper convergence.

- With reference to figure 6.8 and 6.6 the flywheels with higher inertia are disposed in devices with the longer width, because of the higher amount of energy in input.

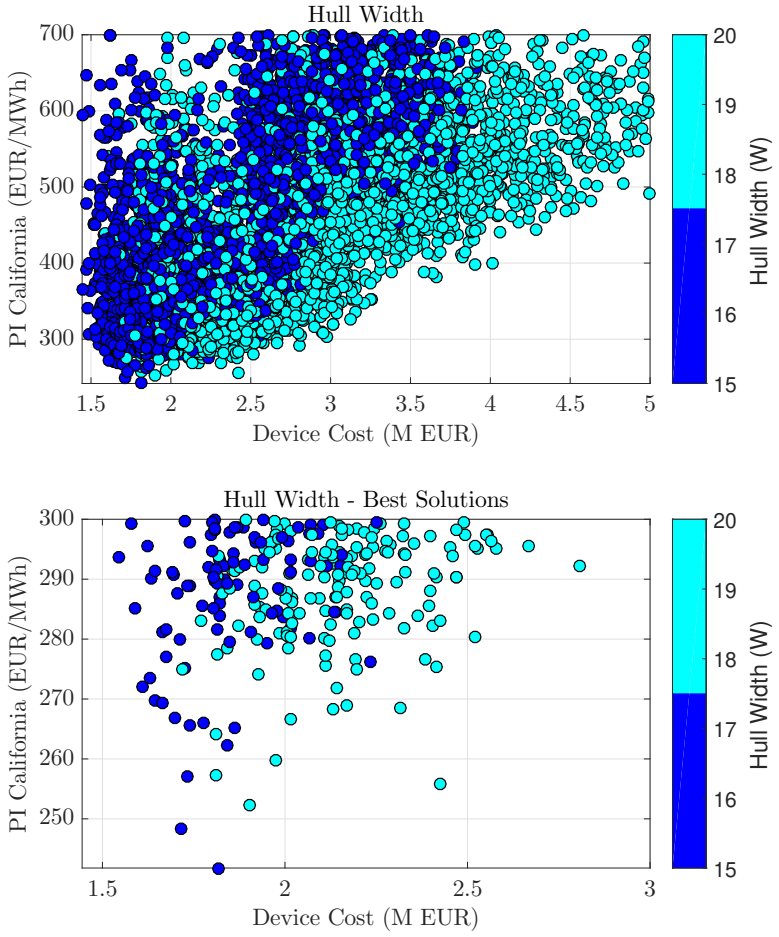

Figure 6.6 Techno-economic analysis: hull width W, Performance Index PI and device cost C_{tot}. Evaluated in Hamboldt Bay (California).

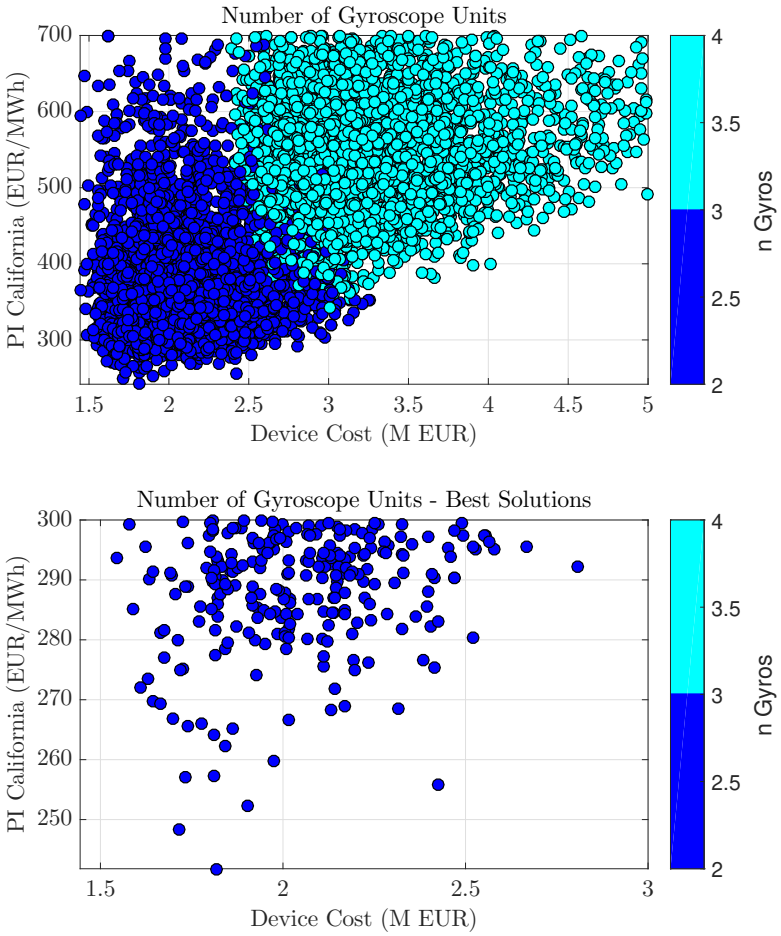

Figure 6.7 Techno-economic analysis: number of gyroscope units *nGyros*, Performance Index *PI* and device cost C_{tot}. Evaluated in Hamboldt Bay (California).

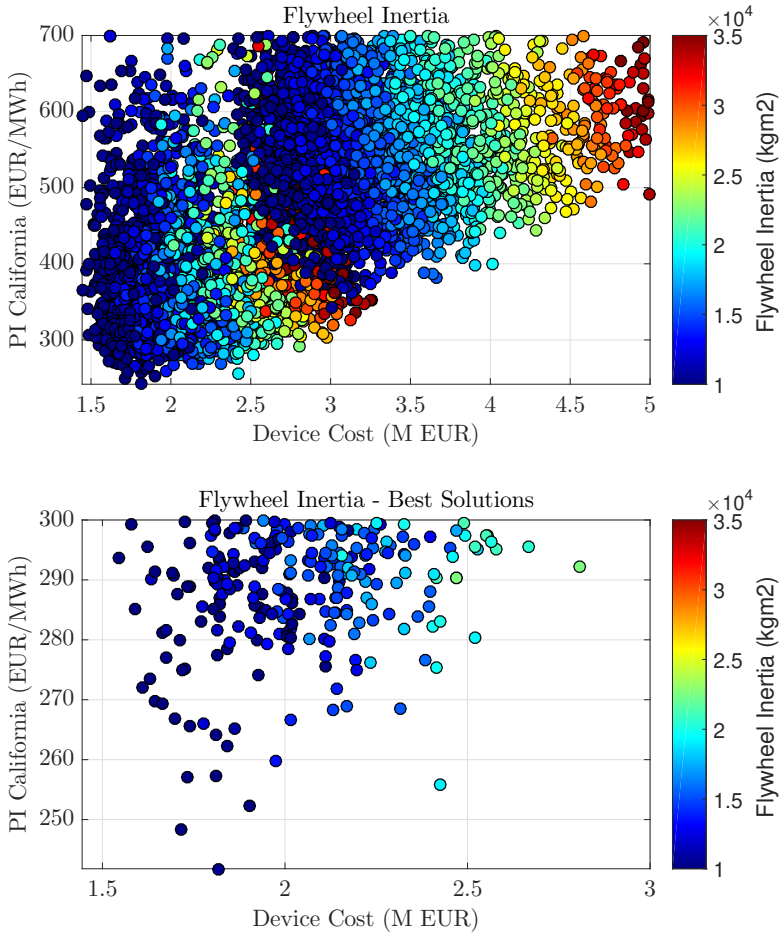

Figure 6.8 Techno-economic analysis: Flywheel Inertia J, Performance Index PI and device cost C_{tot}. Evaluated in Hamboldt Bay (California).

The Techno-economic and convergence analysis on the radial bearings size of the flywheel and related mechanical efficiency η is given in figures 6.9 and 6.10. The best solutions show also the best mechanical efficiencies and the best radial bearings size are found in the ID range [3,4,5], with predominance of ID 3.

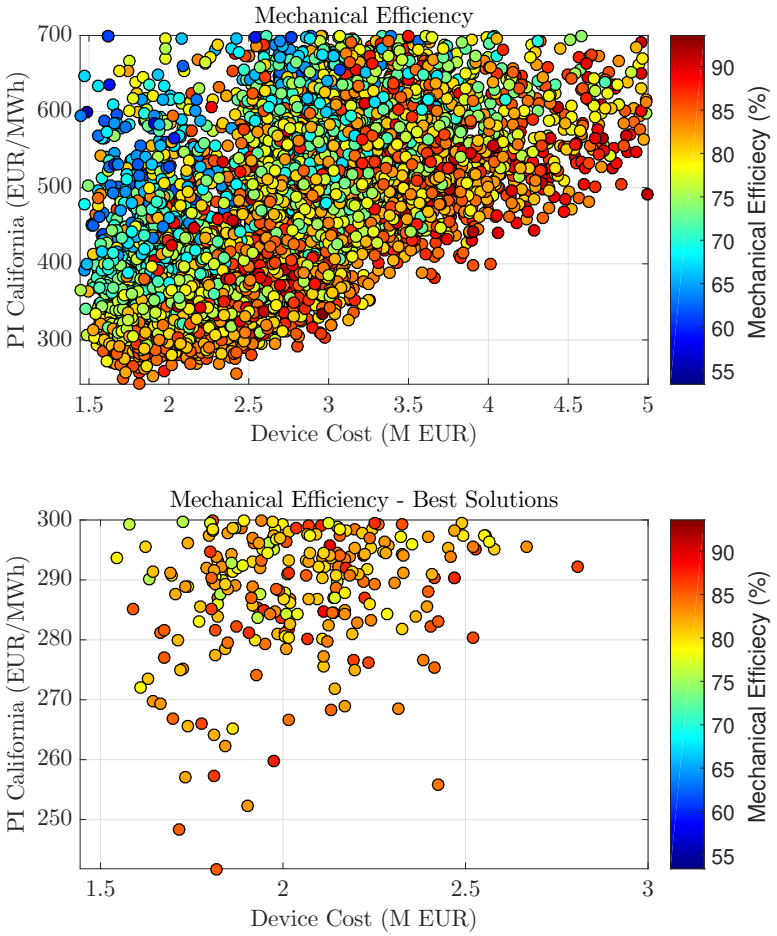

Figure 6.9 Techno-economic analysis: Mechanical Efficiency η, Performance Index PI and device cost C_{tot}. Evaluated in Hamboldt Bay (California).

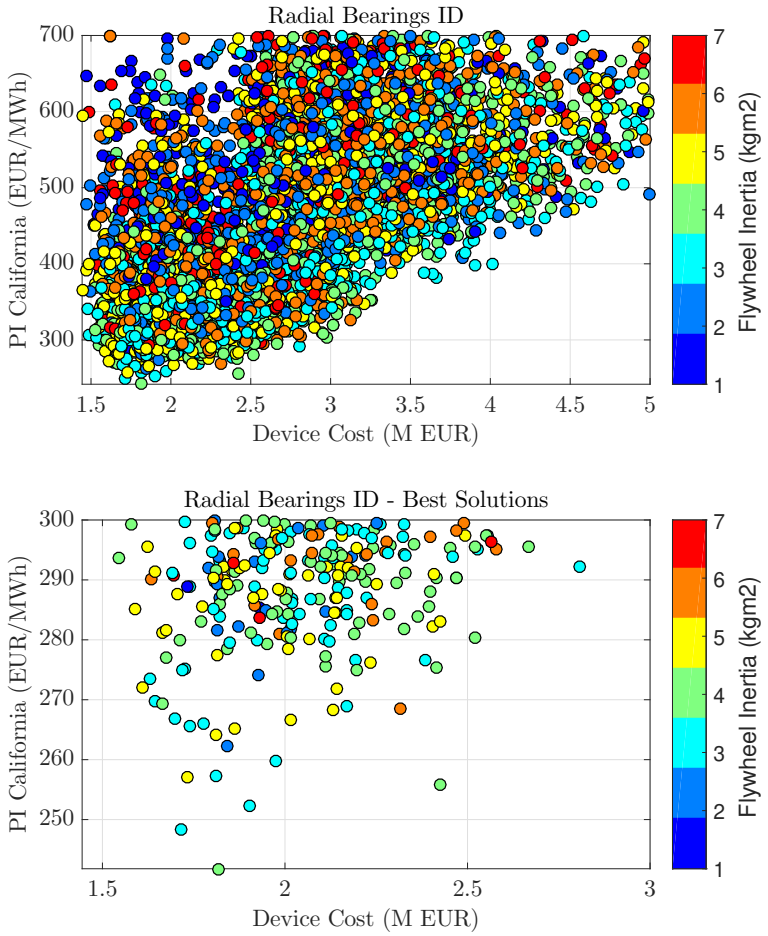

Figure 6.10 Techno-economic analysis: Mechanical Efficiency η, Performance Index PI and device cost C_{tot}. Evaluated in Hamboldt Bay (California).

6.3 Optimal IOwec Device

6.3.1 Decision making

The decision of which device is "more optimal" can be not so straightforward and easy at first sight. In fact, such kind of optimization does not, and can not, take into account all the considerations that can be made, especially when techno-economic aspects are involved. The purpose of a preliminary optimization is more to identify relevant global trends, which parameters influences more the problem and the useful

Table 6.4 Best five solutions of the IOwec optimization process in Humboldt Bay site.

ID	*PI* (EUR/MWh)	$Prod_{Net}$ (MWh/y)	Device Cost M EUR	Hull Widtht (m)	Flywheel Inertia (kgm^2)
1970	242	301	1.82	15	10414
2184	248	276	1.72	15	10000
2208	252	302	1.90	20	10000
2761	256	379	2.426	20	19065
3585	257	269	1.73	15	10000

ranges of the design parameters, as discussed in the previous section.
We have also to take into account that the annual net productivity is calculated with restrictive assumptions:

- The wave spectrum is not "real" or measured but analytical and the Bretshneider spectrum has been chosen in order to standardize the results.
- Only one realization of wave profile with a certain seed of the pseudo-random is considered and therefore there is a certain variance of the results and the optimization can not be considered robust. This aspect has to taken into account especially when comparing and ranking solutions with similar values of performance index.
- The total number of simulated waves (70) is limited and the grid spacing should be larger. A sensibility analysis of the grid dimension should be carried out in further works.

The best five solutions referred to the two deployment sites are given in table 6.4 and 6.5 sorted from the lowest performance index to the highest. The maximum percentage variation of performance index is 10 % and taking into account the previous considerations these solutions can be considered equivalently optimal.

Each device presents a design solution with two gyroscope units, and solutions with a hull width of 15 (m) and 20 (m) are found. Some techno-economic consideration can be made the best device configuration among this pool. Since the development phase of the device is at a preliminary stage no information are given about the costs of the mooring system, electrical connection to the grid, installation and operation and maintenance. Moreover, the IOwec device is intended to

Table 6.5 Best five solutions of the IOwec optimization process in WETS, Hawaii site.

ID	*PI* (EUR/MWh)	$Prod_{Net}$ (MWh/y)	Device Cost M EUR	Hull Widtht (m)	Flywheel Inertia (kgm^2)
1970	266	274	1.82	15	10414
2184	267	257	1.72	15	10000
2761	271	358	2.42	20	19065
2570	278	260	1.81	20	10000
3553	281	281	1.97	20	13404

be deployed as part of a farm, array of several devices to reach a certain installed power. It is reasonable to assess that these mentioned costs can be considered fixed and not so dependent on the hull width. Therefore, since no evidence of large gap of performance index is found, the solution of a device with hull width 20 (m) is preferable. A wider hull implies a higher annual productivity, and therefore all the other fixed cost are more depreciated over the lifetime. Moreover, if the goal is to deploy several devices in a farm layout to reach an certain installed capacity or annual productivity, less devices have to be deployed in the case of wider hull with economic advantages. In view of all these considerations, the device with ID 2761 has been chosen as the best solution to be analyzed.

6.3.2 Analysis of the Optimal IOwec device

The design parameters that distinguish the chosen optimal device are given in table 6.6.

Figure 6.11 shows the front and plan view of the optimal IOwec, with the location of the gyroscope units, U-Tank and ballast inside the hull.

Table 6.6 Design parameters of the optimal IOwec device (ID 2761).

Parameter	Symbol	Unit	Value
Hull lenght	L	m	22
Hull width	W	m	20
Hull shape coefficient 1	h		0.550
Hull shape coefficient 2	k		0.713
Hull draft ratio	j		0.69
Ballast Filling Ratio	BFR		0.86
Flywheel Inertia	J	kgm^2	19065
Eccentric Mass	M_p	kg	3000
number of gyroscope units	$nGyros$		2
Radial Bearings ID	$BearID$		4
U-Tank shape coefficient 1	UT_{W_r}		0.31
U-Tank shape coefficient 2	UT_{H_d}		0.29
U-Tank shape coefficient 3	UT_{W_d}		1.10

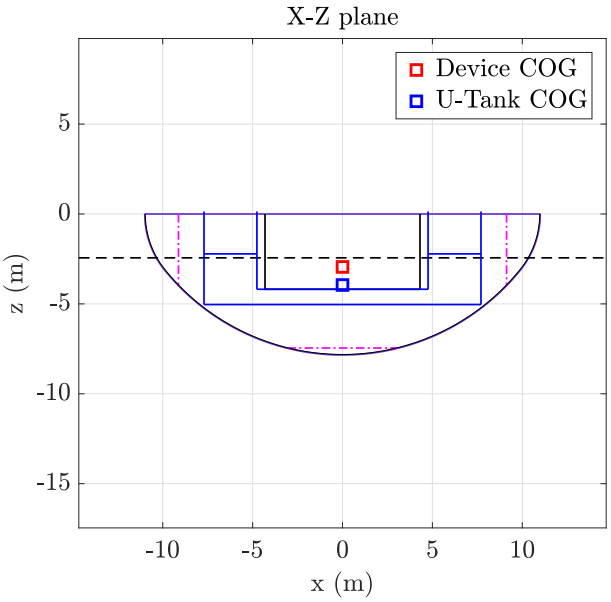

(a) Side view of the optimal IOwec device.

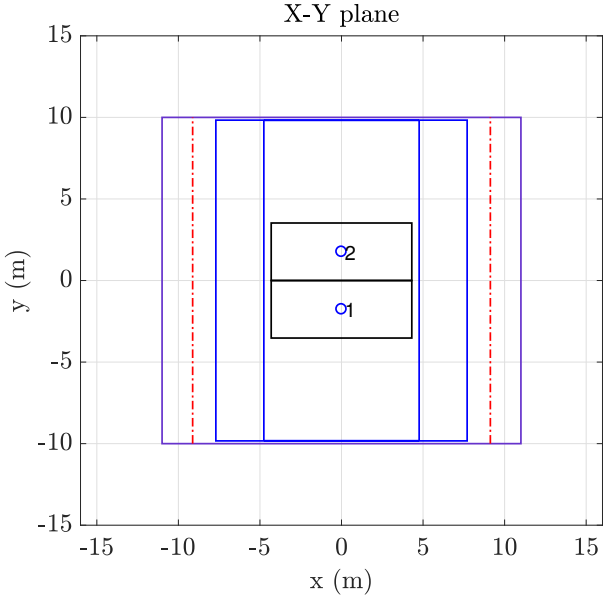

The characteristics of the device are given in table 6.7 and the pitch response amplitude operator is shown in figure 6.12, with a resonance period of approximately 6.3 (s) and a maximum response amplitude of 7 (rad/rad). Figure 6.13 shows the pitch RAO of the device as a function of the U-Tank stiffness ratio values considered in the simulation without the contribution of the gyroscope dynamics (flywheel speed $\dot{phi} = 0$).

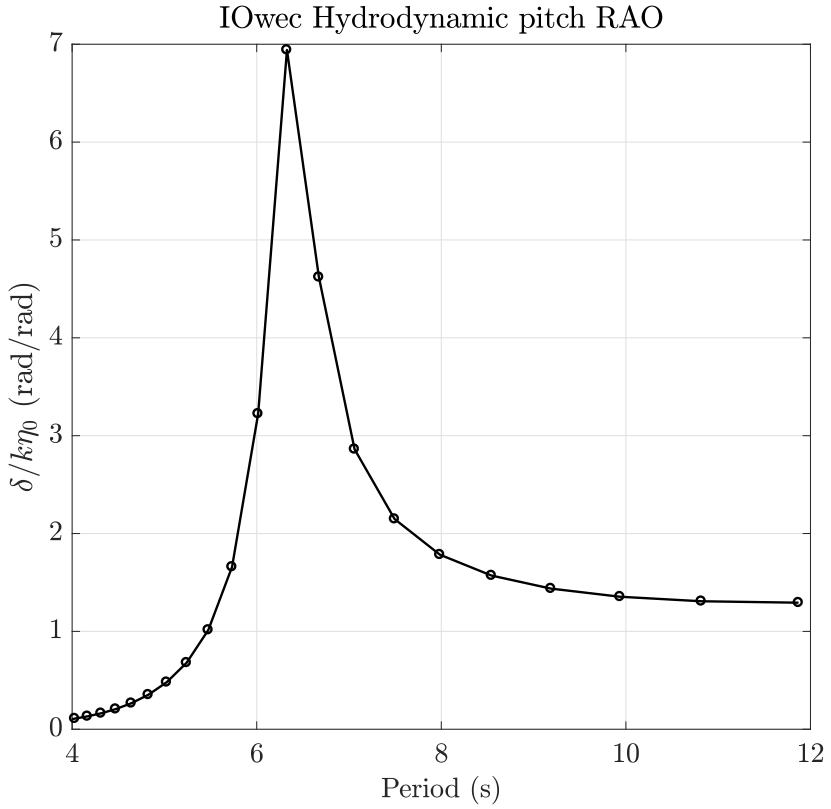

Figure 6.12 Hydrodynamic pitch Response Amplitude Operator of optimal IOwec device.

Table 6.7 Characteristics of the optimal IOwec.

Property	Symbol	Unit	Value
Floater			
Length	L	m	22
Width	W	m	20
Height	H	m	7.84
Draft	Dr	m	5.40
Global COG from deck	COG	m	2.94
Device Pitch Inertia	I_{yy}	kgm^2	9.47e07
Total mass	M	ton	1617
Total Device cost	C_{tot}	M EUR	2.4
Hull mass	M_{hull}	ton	310
Ballast mass	M_{ball}	ton	710
Gyroscope			
Units	nGyros	-	2
Flywheel Inertia	J	kgm^2	19065
Flywheel External Diameter	D_e	m	2.33
Eccentric Mass	m_p	ton	3
Eccentric Mass Arm	d_p	m	1.16
Gyro Unit Mass	M_{gyro}	ton	56
U-Tank			
Water mass	M_{Utank}	ton	485
Width	X_t	m	19.7
Duct Height	H_d	m	0.85
Duct Lenght	W_d	m	9.52
Reservoir length	W_r	m	2.94
Datum level (Lloyd ref)	H_r	m	2.39
Device COG distance from duct centerline	r_D	m	1.67
Total U-Tank length	W_{tot}	m	15.4

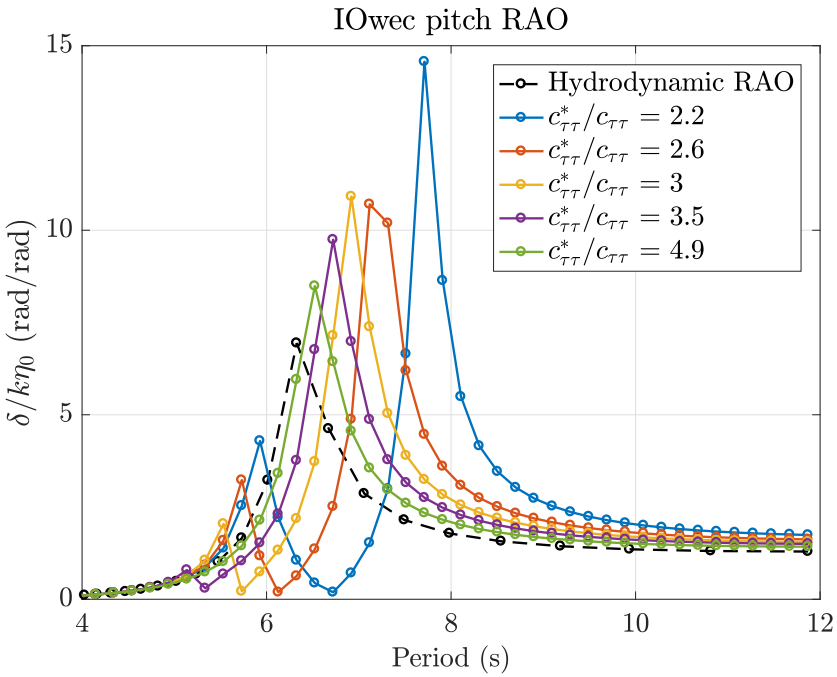

Figure 6.13 IOwec (Optimal) Response Amplitude Operator for different values of the U-Tank stiffness ratio $c^*_{\tau\tau}/c_{\tau\tau}$ compared with the hydrodynamic RAO of the device with the gyroscope units turned off (flywheel speed $\dot{\phi} = 0$).

The simulation results are given in table 6.8 compared with the case of inactive U-Tank: the productivity improvement due to the active U-Tank control is about 20 %, demonstrating the efficacy of such technology integration.

The performance index of the first draft of IOwec is equal to 322 (EUR/MWh) in California and 352 (EUR/MWh) in Hawaii. Therefore, the optimization algorithm has led towards a device that shows a performance index reduction of about 22 % in both sites.

The following figures show the simulation results, and the same considerations discussed in section 5.6.1 can be made. For the sake of completeness, the plotted results regarding the inactive U-Tank case are given in appendix A.

Table 6.8 Results summary of the optimal IOwec performances in Humboldt Bay (California) and WETS (Hawaii) sites.

Parameters	Unit	California		Hawaii	
		Inactive Utank	Active Utank	Inactive Utank	Active Utank
Annual Net Productivity	MWh/y	313	379	292	358
Annual Gross Productivity	MWh/y	386	452	357	427
Mechanical Efficiency, η_{mech}	%	81	84	82	84
Weighted $\dot{\phi}$	rpm	342	346	308	336
Weighted c	kNms/rad	88	92	76	84
Weighted δ	deg	3.6	4.0	3.8	3.9
Weighted τ	deg		2.4		1.8
Weighted ε	deg	27.5	32.0	27.3	33.0
Weighted $\dot{\varepsilon}$	rpm	4.2	4.7	4.3	4.9
Weighted T_{PTO}	kNm	44	48	39	45
Weighted Net Power P_{net}	kW	35	43	32	41
Weighted Gross Power P_{gross}	kW	44	52	39	49

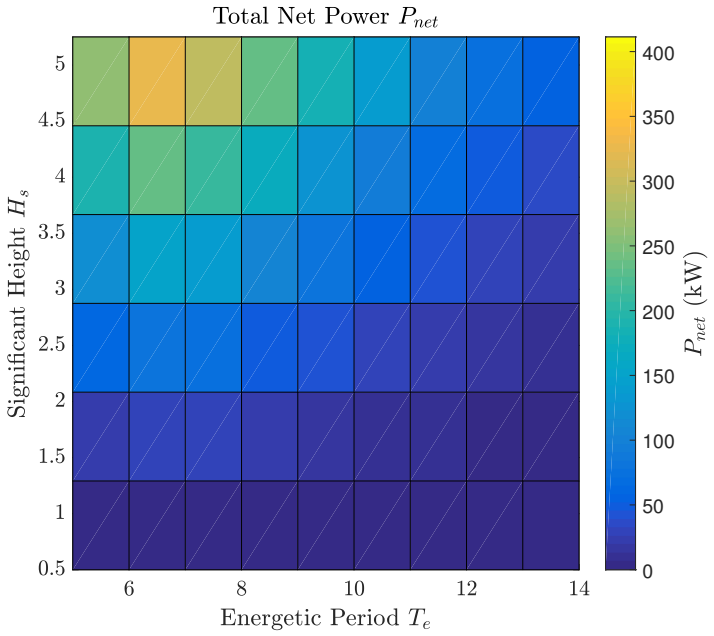

Figure 6.14 Total mean net mechanical power P_{net} plot grid. Optimal IOwec - Active Ut-Tank control case.

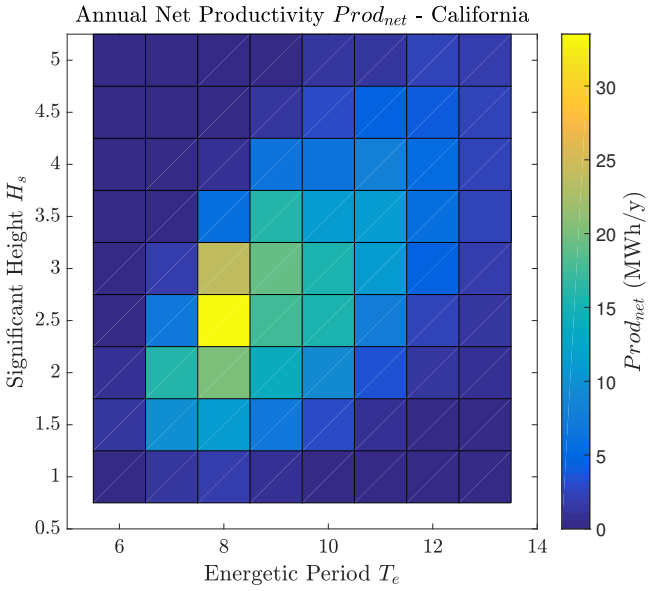

(a)

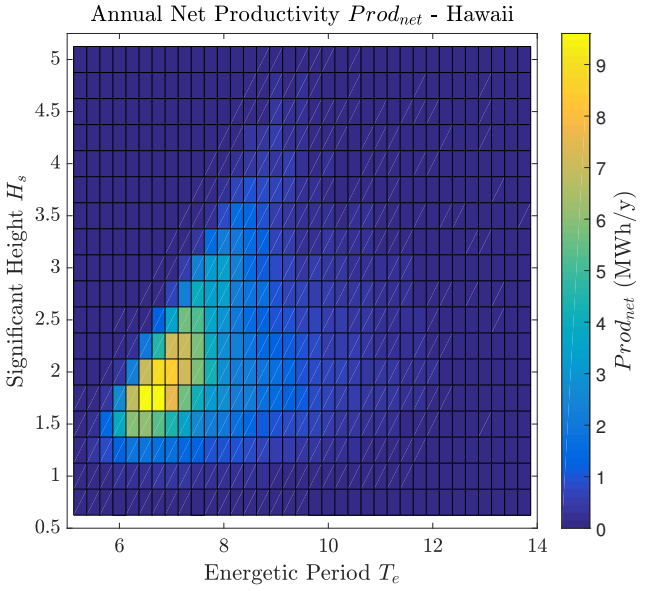

(b)

Figure 6.15 Productivity *Prod* interpolated plot grids. Optimal IOwec - Active Ut-Tank control case. Active U-Tank control case.(a) Humboldt Bay (California) (b) WETS (Hawaii).

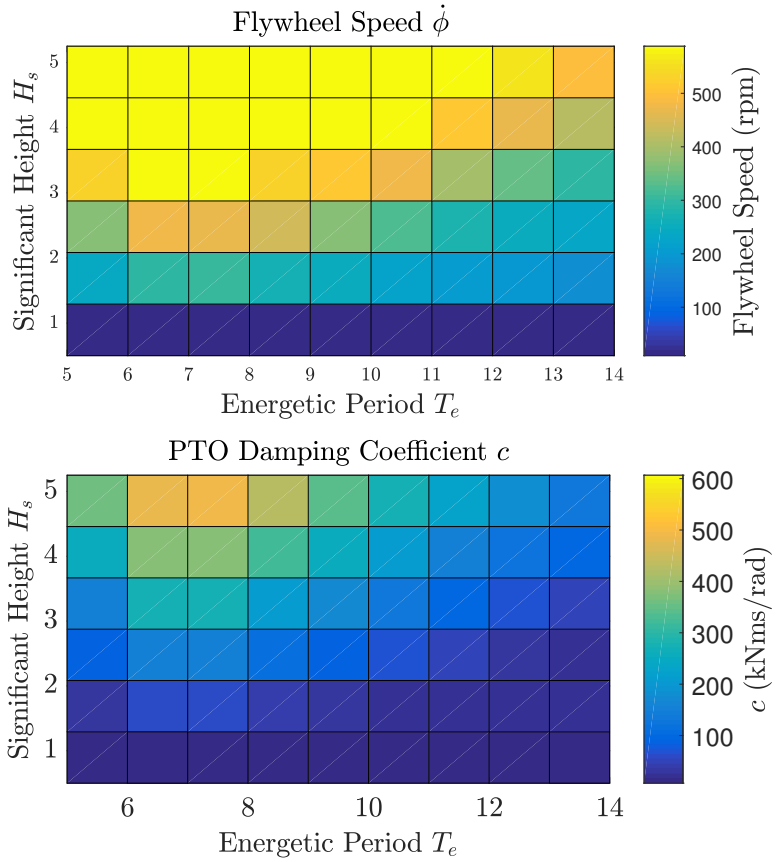

Figure 6.16 Optimal flywheel speed $\dot{\phi}$ and PTO damping coefficient c plot grids. Optimal IOwec - Active U-Tank control case.

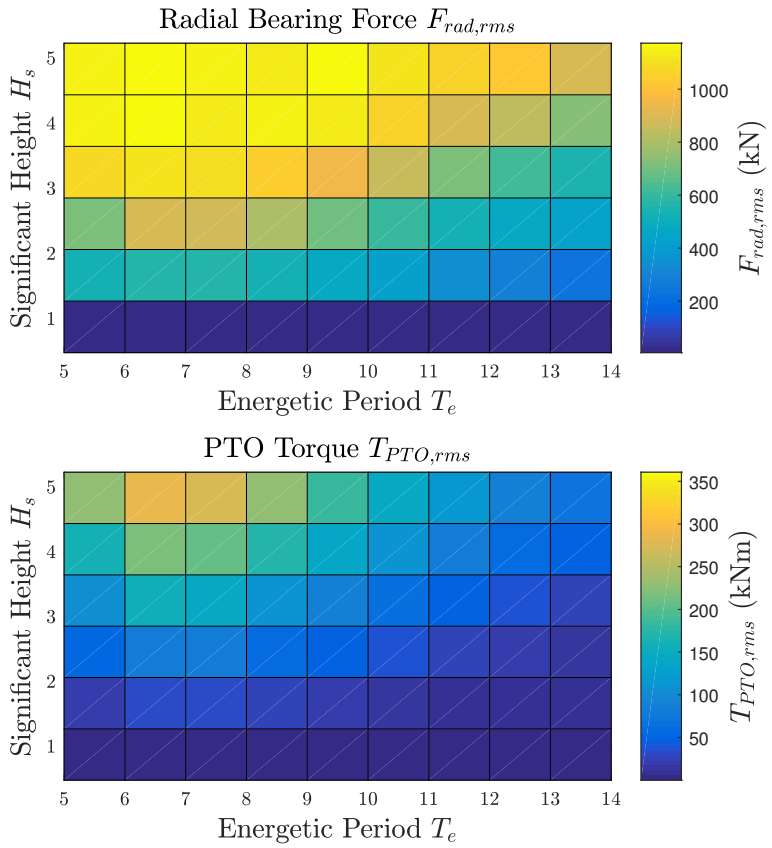

Figure 6.17 U-Tank stiffness ratio $c^*_{\tau\tau}/c_{\tau\tau}$ and U-Tank angle τ_{rms} plot grids. Optimal IOwec - Active U-Tank control case.

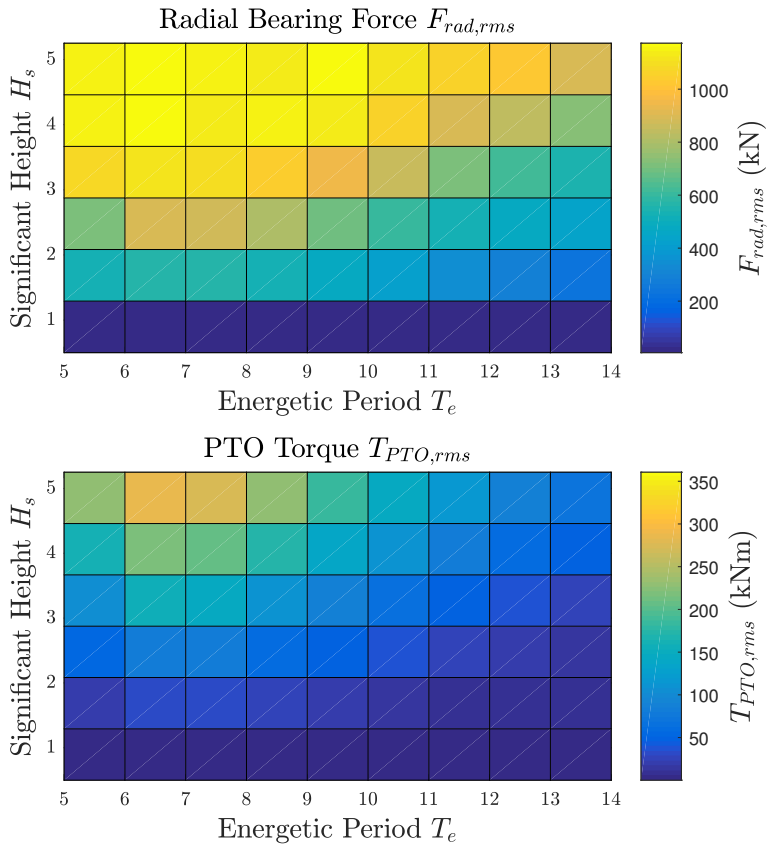

Figure 6.18 Radial bearing forces $F_{rad,rms}$ and PTO torque $T_{PTO,rms}$ grid plots. Optimal IOwec - Active U-Tank control case.

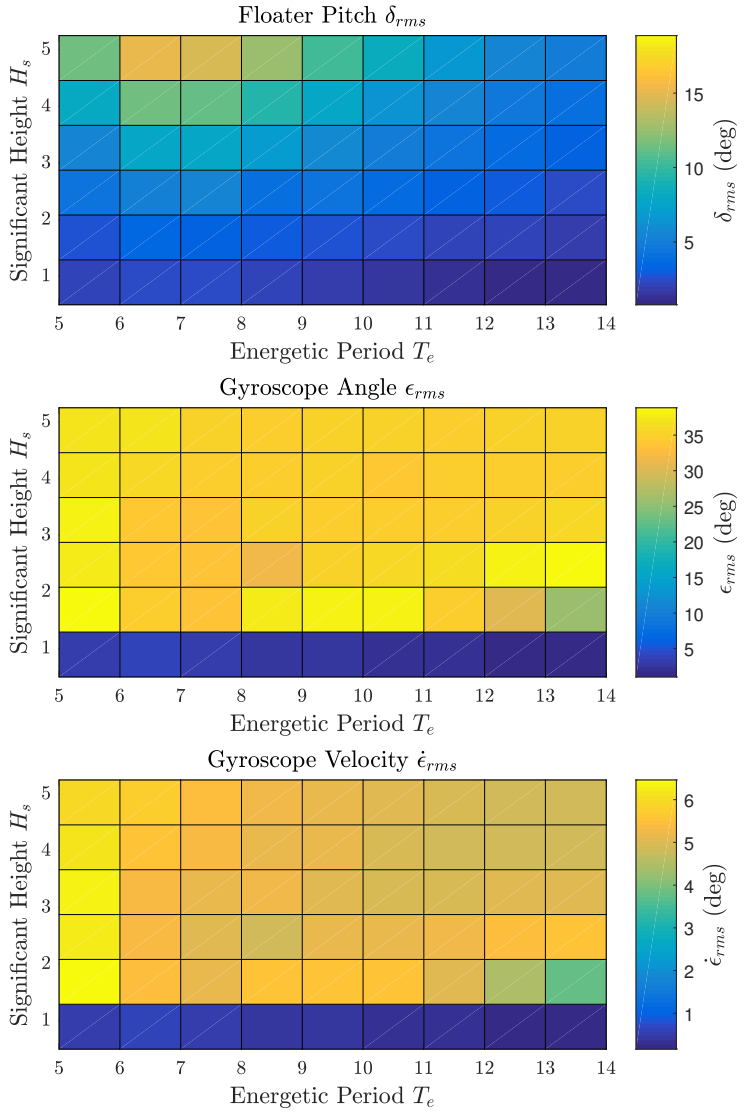

Figure 6.19 Floater pitch δ_{rms}, gyroscope angle ε_{rms} and velocity $\dot{\varepsilon}_{rms}$ grid plots. Optimal IOwec - Active U-Tank control case.

Chapter 7

Conclusions and further work

The objective of this thesis work is to integrate water ballast tanks (U-Tanks) into ISWEC device to vary its resonance period and enhance its conversion efficiency. The new device is called IOwec, Inertial Oscillating wave energy converter, and it has been developed with the purpose to be deployed in ocean environments and to be flexible and adaptable to different wave climates and thus site-independent. To prove the IOwec concept with integrated U-Tank technology, the following steps have been completed:

- **development of the IOwec numerical model**: a linear numerical model is developed to simulate the dynamics of the whole system, constitute of three systems, floater, gyroscope and U-Tank.
- **U-Tank model validation**: The floater hydrodynamics and gyroscope models have been validated in the past with experimental campaigns and a 1:8 hardware-in-the-loop test rig. In this thesis the validation of the U-Tank lumped parameter model is achieved with CFD and experimental results in model scale.
- **Development of the IOwec Design Tool**: a numerical tool entirely coded in Matlab environment has been developed for the preliminary design of the IOwec device. All the experience acquired during the design and realization full-scale and 1:2 device deployed in open sea, has been poured in the IOwec Design Tool: the device geometry and characteristics are given uniquely by the definition of a set of design parameters and assumption. With the

implementation of the IOwec numerical model is possible to simulate in time-domain the device and assess its performances.

A first draft of the IOwec technology has been developed and presented in chapter 5. This first version of IOwec has been designed taking into account the experienced and lessons learned during the design of the ISWEC device. Two possible installation sites have been chosen for the assessment and proof the the technological solution: Humboldt Bay in California (USA) and Wave Energy Test Site (WETS) in Hawaii islands (USA). Humboldt Bay has been chosen because suggested by the Department of Energy (DOE) of the United States as site of reference for the assessment of wave energy converter technologies, with providing the wave resource data. The Wave Energy Test Site is an interesting installation site because of the possibility to test a full-scale device and connect it the electrical grid. The provided data of the two sites have been elaborated in order to assess the wave resource characteristics: the power density and the occurrence diagrams are substantially different.
Therefore, the two sites are well suited to demonstrate the tunability and adaptability of the IOwec device in different wave-climates. A sea-state based control of the U-Tank is proposed and modeled. Through the discrete partialization of the volume of air in the two U-Tank chambers is possible to vary the dynamic response of the U-Tank and thus of the IOwec device. The result is the possibility to tune the pitch resonance period with the incoming sea-state to enhance the energy harvesting.

The dynamics and performance of the U-Tank active control have been numerical assessed in different wave conditions: regular waves, irregular waves described by standard analytical spectrum (Bretschneider) and by measured complex spectra. The results show consistent improvement of power extraction when activating the U-Tank control compared with the case of inactive U-Tank.
The promising results of the first version of IOwec encouraged the development of a more efficient device. Since the complexity of the dynamics and the presence of many design parameters, it is hard to carry out an optimization by manual iteration. To accomplish this task, a multi-objective optimization algorithm has been used. The performance index to be optimized is related to a techno-economic parameter: the device costs spread over the expected life of the device divided by the annual productivity calculated in both the installation sites of interest.
The optimization results did not show any Pareto-front and thus the the optimal solution is optimal for both sites. This result demonstrates the adaptability of the

device for different wave climates: only one device can be designed and realized for the deployment in various deployment sites, with enormous advantages in design, engineering and economic terms. Moreover, the huge amount of explored solutions (10800 evaluations) permits important techno-economic considerations and trends. The two gyroscope design solution is always advantageous when costs are considered and several optimal devices with different costs and productivity lead to the same performance index. Therefore, when designing a farm of devices, it is possible to choose the best solution in terms of cost of productivity that minimize the levelized cost of the energy (LCOE) associated to the farm.
A device has been chosen among the set of most optimal devices with techno-economical considerations. The performance index reduction compared with the initial first draft is about 22 % in both installation sites, and the annual productivity improvement due to the active U-Tank control is about 20 % compared with the inactive U-Tank case.

7.1 Further work

The results of this preliminary work demonstrate the capability of the IOwec novel technology to adapt to different wave climates with the tuning of the dynamics of the water sloshing tank. IOwec can be a valid solution for the ocean energy harvesting, also considered the experience matured with the ISWEC prototype developed for the Mediterranean sea. Further work will be done on the basis of these preliminary results:

- A higher-fidelity wave-to-PTO model will be develop to accurately assess the annual productivity of the device and test the control logics. The mooring system will be modelled in Matlab environment to investigate its influence during operational condition and to assess the survivability in extreme wave conditions. The PTO technological solution will be chosen and modelled on the basis of the resulting loads from this thesis work.
- Since the mechanical losses due to the flywheel bearing are relevant (15-25 %), research efforts will be carried out to reduce these losses. Magnetic

bearings are an interisting solution to decrease the losses and a feasibility and techno-economic analysis will be carried out.

- Medium-scale experimental tests in wave tank may be conducted to validate the IOwec technology and test different U-Tank control logics.
- The CFD model of the full coupled system will be modeled and validated through experimental data, in order to have a high-fidelity model in order to assess the dynamics of full-scale devices.
- The cost assessment of fixed and operational costs of the device will be evaluated more in detail in order to set a global optimization with the levelized cost of energy (LCOE) as fitness value to minimize.

Bibliography

[1] Gunn K. and Stock-Williams C. Quantifying the global wave power resource. *Renewable Energy*, 44, 2012.

[2] Lopez I., Andreau J., Ceballos S., Martinez de Alegria I., and Kortabarria I. Review of wave energy technologies and the necessary power-equipment. *Renewable and sustainable energy reviews*, 27, 2013.

[3] Ramirez D., Bartolome J.P., Martinez S., Herrero J.C., and Blanco M. Emulation of an OWC ocean energy plant with PMSG and irregular wave model. *IEEE transactions on sustainable energy*, 6, 2015.

[4] Dummett R.P. MVSearod Tamar modifications to improve ship motions. In *The Australian naval architect*, volume 2, 1998.

[5] Vasta J., Gidding A.J., Taplin A., and Stiwell J.J. Roll stabilization by means of passive tanks. In *Transactions of society of naval architects and marine engineers*, volume 69, 1961.

[6] Gawad A.F.A., Ragab S.A., Nayfeh A.H., and Mook D.T. Roll stabilization by anti-roll passive tanks. *Ocean Engineering*, 28:457–469, 2001.

[7] Ribeiro e Silva S., Gomes R.P.F., and Falcão A.F.O. Hydrodynamic Optimization of the UGEN: Wave Energy Converter with U-shaped Interior Oscillating Water Column. In *Proceedings of the 11th EWTEC*, Nantes, France, September 2015.

[8] Pisacane G., Sannino G., Carillo A., Struglia M.V., and Bastianoni S. Marine energy exploitation in the mediterranean region: Steps forward and challenges. *Frontiers in Energy Research*, 6:109, 2018.

[9] Passione B. *Hydrodynamic analysis and mooring design of a floating pitching Wave Energy Converter*. PhD thesis, Politecnico di Torino, 2018.

[10] Sirigu S.A., Bracco G., Bonfanti M., Dafnakis P., and Mattiazzo G. On-board sea state estimation method validation based on measured floater motion. In *11th IFAC Conference on Control Applications in Marine Systems, Robotics, and Vehicles CAMS 2018*, Opatija, Croatia, 2018.

[11] International Energy Agency. *World Energy Outlook 2018*. 2018. https://www.oecd-ilibrary.org/content/publication/weo-2018-en.

[12] Drew B., Plummer A.R., and Sahinkaya M.N. A review of wave energy converter technology. *Proceedings of the Institution of Mechanical Engineers, Part A: Journal of Power and Energy*, 223, 2009.

[13] Chozas J.F. *Technical and Non-Technical Issues towards the Commercialisation of Wave Energy Converters*. PhD thesis, Aalborg University, 2013.

[14] Ocean Energy Europe. Ocean Energy policies in Europe, 2018. https://www.oceanenergy-europe.eu/.

[15] Ocean Energy Systems. Ocean Energy policies in USA, 2017. https://report2017.ocean-energy-systems.org/international-activities/united-states-of-america/.

[16] Ross D. *Power from sea waves*. Oxford University Press, 1995.

[17] Thorpe T.W. A brief review of wave energy. Technical report, The UK Department of Trade and Industry, 1999.

[18] Clement A., McCullen P., Falcao A., and et Al. Wave energy in Europe: current status and perspectives. *Renewable and Sustainable Energy Reviews*, 6, 2002.

[19] Falcao A. The shoreline OWC wave power plant at the Azores. In *Proc. 4th European Wave Energy Conf*, Aalborg, Denmark, 2000.

[20] Ohneda H., Igarashi S., Shinbo O., Sekihara S., Suzuki K., Kubota H., and et Al. Construction procedure of a wave power extracting caisson breakwater. In *Proc. 3th symposium ocean energy utilization*, Tokyo, Japan, 1991.

[21] Ocean Power Technology. PowerBuoy OPT website. https://www.oceanpowertechnologies.com/.

[22] CETO Carnagie website. https://www.carnegiece.com/wave/.

[23] Kourakis I. Structural systems and tuned mass dampers of super-tall buildings: case study of taipei 101. Master's thesis, Massachusetts Institute of Technology. Dept. of Civil and Environmental Engineering, 2007.

[24] Cordonnier J., Gorintin F., De Cagny A., Clément A.H., and Babarit A. Searev: Case study of the development of a wave energy converter. *Renewable Energy*, 80:40–52, 2015.

[25] Pozzi N. *Numerical Modeling and Experimental Testing of a Pendulum Wave Energy Converter (PeWEC)*. PhD thesis, Politecnico di Torino, 2018.

[26] WITT Limited. WITT. https://www.witt-energy.com/.

[27] Crowley S., Porter R., Taunton D.J., and Wilson P.A. Modelling of the witt wave energy converter. *Renewable Energy*, 115:159–174, 2018.

[28] Wello. Penguin Wello Technology, 2019. https://wello.eu/.

[29] EMEC. Penguin Wello tested in EMEC test site, 2019. {http://www.emec.org.uk/about-us/wave-clients/wello-oy/}.

[30] McCabe A.P., Bradshaw A., Meadowcroft J.A.C., and Aggidis G. Developments in the design of the ps frog mk 5 wave energy converter. *Renewable Energy*, 31(2):141–151, 2006.

[31] Salcedo F., Ruiz Minguela P., Rodriguez A.R., Ricci P., and Santos-Mugica M. Oceantec: Sea trials of a quarter scale prototype. In *Proceedings of 8th European Wave Tidal Energy Conference*, Uppsala, Sweden, 2009.

[32] Ringwood J.V., Bacelli G., and Fusco F. Energy-maximizing control of wave-energy converters: The development of control system technology to optimize their operation. *IEEE Control Systems Magazine*, 34(5):30–55, 2014.

[33] Bharadwaj Nanda and Kishor Chandra Biswal. A review on applications of tuned liquid dampers in vibration control. In Mohanty C.R. and Panigrahi S.K., editors, *Advances in Civil Engineering*, chapter 14. 2004.

[34] Moaleji R. and Alistair R.G. On the development of ship anti-roll tanks. *Ocean Engineering*, 34(1):103–121, 2007.

[35] Watts P. On a method of reducing the rolling of ships at sea. In *Transactions of institution of naval archicture*, volume 24, 1883.

[36] Watts P. The use of water chambers for reducing the rolling of ships at sea. In *Transactions of institution of naval archicture*, volume 26, 1885.

[37] Froude W. On the rolling of ships. In *Transactions of institution of naval archicture*, volume 2, 1861.

[38] D.W. Bass. Roll stabilization for small fishing vessels using paravanes and anti-roll tanks. *Marine Technology*, 35:74–84, 04 1998.

[39] Birmingham R., Webster B., and Roskilly T. The application of artificial intelligence to roll stabilisation for a range of loading and operating conditions. *International Journal of Maritime Engineering*, 145, 01 2003.

[40] Herr H. Frahm. Results of trials of the anti-rolling tanks at sea. *Journal of the American Society for Naval Engineers*, 23(2):571–597, 1911.

[41] Goodrich G.J. Development and design of passive roll stabilisers. In *Transactions of royal institution of naval architects*, volume 111, 1969.

[42] Alujević N., Ćatipović I., Malenica Š., Senjanović I., and Vladimir N. Ship roll control and power absorption using a u-tube anti-roll tank. *Ocean Engineering*, 172:857–870, 2019.

[43] Wen-Chuan Tiao. Preliminary assessments of the anti-roll tank as a wave energy converter. *Ships and Offshore Structures*, 8(5):488–496, 2013.

[44] Fonseca N. and Pessoa J. Numerical modeling of a wave energy converter based on u-shaped interior oscillating water column. *Applied Ocean Research*, 40:60–73, 01 2013.

[45] Fonseca N., Pessoa J., Silva S., Le Boulluec M., and Omaha J. Model tests of a Wave Energy Converter based on water oscillating in a U-tank. In *12èmes Journées de l'hydrodynamique*, Nantes, France, 10 2010.

[46] Crowley S.H., Porter R., and Evans D.V. A submerged cylinder wave energy converter with internal sloshing power take off. *European Journal of Mechanics - B/Fluids*, 47:108–123, 2014.

[47] D.V. Evans and R. Porter. Wave energy extraction by coupled resonant absorbers. *Philosophical transactions. Series A, Mathematical, physical, and engineering sciences*, 370:315–44, 01 2012.

[48] Flocard F. and Finnigan T.D. Increasing power capture of a wave energy device by inertia adjustment. *Applied Ocean Research*, 34:126–134, 2012.

[49] G. Vissio. *ISWEC toward the sea: Development, Optimization and Testing of the Device Control Architecture*. PhD thesis, Politecnico di Torino, 2017.

[50] Bracco G. *ISWEC: A gyroscopic Wave Energy Converter*. PhD thesis, Politecnico di Torino, 2010.

[51] Bracco G., Cagninei A., Giorcelli E., Mattiazzo M., Poggi D., and Raffero M. Experimental validation of the iswec wave to PTO model. *Ocean Engineering*, 120:40–51, 2016.

[52] WaveforEnergy. Deployment of ISWEC full-scale in Pantelleria, 2015. http://www.waveforenergy.com/news/149-blue-energy-in-pantelleria-deployment-of-the-innovative\-iswec-inertial-sea-wave-energy-converter.

[53] Marine technology news. Deployment of ISWEC scaled-model in Adriatic sea, 2018. https://www.marinetechnologynews.com/news/pilots-energy-converter-587557.

[54] Marine technology news. Financial and industrial non-binding agreement for the industrialization of the ISWEC pilot project, 2019. https://marineenergy.biz/2019/04/19/eni-cdp-fincantieri-and-terna-enter-wave-power-pact/.

[55] Sirigu S.A., Brizzolara S., Bonfanti M., Dafnakis P., Bracco G., and Mattiazzo G. Pitch resonance tuning tanks: A novel technology for more efficient wave energy harvesting. In *OCEANS 2018 MTS/IEEE Charleston*, Charleston,(SC) USA.

[56] Folley M. *Numerical modelling of wave energy converters: state of- the-art techniques for single devices and arrays*. Academic Press, 1993.

[57] Faltinsen O. *Sea Loads on Ships and Offshore Structures*. Cambridge University Press, 1993.

[58] Garcia R.P., Costello R., Dias F., and Ringwood J. Hydrodynamic modelling competition: Overview and approaches. In *ASME 2015 34th International Conference on Ocean, Offshore and Arctic Engineering*, St. John's, Canada, 05 2015.

[59] Li Y. and Yu Y.H. A synthesis of numerical methods for modeling wave energy converter-point absorbers. *Renewable and Sustainable Energy Reviews*, 16:4352–4364, 2012.

[60] W. Sheng. Wave energy conversion and hydrodynamics modelling technologies: A review. *Renewable and Sustainable Energy Reviews*, 109, 04 2019.

[61] Yu Y.H., Lawson M., Ruehl K., and Michelén Ströfer C. Development and Demonstration of the WEC-Sim Wave Energy Converter Simulation Tool. In *2nd Marine Energy Technology Symposium*, Seattle, (WA) USA, 01 2014.

[62] Josset C., Babarit A., and Clément A. A wave-to-wire model of the SEAREV wave energy converter. *Proceedings of The Institution of Mechanical Engineers Part M-journal of Engineering for The Maritime Environment*, 221:81–93, 01 2007.

[63] S.K. Chakrabarti. *Hydrodynamics of Offshore Structures*. WIT Press / Computational Mechanics, 1987.

[64] G.B. Airy. *Tides and Waves*. J.J. Griffin, 1849.

[65] Babarit A. and Delhommeau G. Theoretical and numerical aspects of the open source BEM solver . In *Proceedings of the 11th European Wave and Tidal Energy Conference*, 2015.

[66] Cummins W.E. The impulse response function and ship motions. Technical Report 1661, Department of the Navy, David Taylor model basin, Washington DC, 1962.

[67] Ogilvie T.F. Recent progress toward the understanding and the prediction of ship motions. In *Proceedings of the 5th Symposium on Naval Hydrodynamics*, Bergen, Norway, 1964.

[68] Taghipour R., Perez T., and Moan T. Hybrid frequency time domain models for dynamic response analysis of marine structures. *Ocean Engineering*, 35:685–705, 2008.

[69] Unneland K. *Identification and order reduction of radiation force models of marine structures*. PhD thesis, NTNU, 2007.

[70] Roessling A. and Ringwood J. Finite order approximations to radiation forces for wave energy applications. *Proceedings 1st International Conference on Renewable Energies Offshore*, 2014.

[71] Perez T. and Fossen T. Time- vs. frequency-domain identification of parametric radiation force models for marine structures at zero speed. *Modeling, Identification and Control: A Norwegian Research Bulletin*, 29(1):1–19, 2008.

[72] Perez T. and Fossen T. Joint identification of infinite-frequency added mass and fluid-memory models of marine structures. *Modeling, Identification and Control: A Norwegian Research Bulletin*, 29(3):93–102, 2008.

[73] Mei C.C. *Theory And Applications Of Ocean Surface Waves*. World Scientific Pub Co Inc, 2005.

[74] Ochi M. *Ocean waves: the stochastic approach*. Cambridge University Press, 2005.

[75] Journèe J.M.J. and Massie W.W. *Offshore Hydromechanics*. Delft University of Technology, first edition, 2001.

[76] WMO. *Guide to wave analysis and forecasting (WMO)*. Secretariat of the World Meteorological Organization, 1998.

[77] Stansberg C.T., Contento G., Hong S.W., Irani M., Ishida S., Mercier R., Wang Y., and Wolfram J. The specialist committee on waves: Final report and recommendations to the 23rd ittc. In *23rd International Towing Tank Conference*, volume 2, pages 505–736, Venice, Italy, 2002.

[78] Hasselmann D. E., Barnett T., Bouws E., Carlson H., Cartwrith D., and et al. Measurements of wind-wave growth and swell decay during the joint north sea wave project jonswap. *Deutchen Hydrographischen Zeitschrift*, 8, 1973.

[79] Torsethaugen K. and Haver S. Simplified double peak spectral model for ocean waves. In *Proceedings of the 14th International Offshore and Polar Engineering Conference*, Toulon, France, 2004.

[80] Specialist Committee on Testing of Marine Renewable Devices of the 27th ITTC. Ittc – recommended guidelines - wave energy converter model test experiments. Technical Report 7.5-02-07-03.7, International Towing Tank Conference (ITTC), 2014.

[81] Chakrabarti S. *Handbook of offshore engineering Vol 1 and 2*. Elsevier Science, 2005.

[82] Raffero M. *Design of a Wave Energy Converter - a case of application: ISWEC*. PhD thesis, Politecnico di Torino, 2014.

[83] Bonfanti M., Sirigu S.A., Bracco G., Passione B., Vissio G., Pozzi N., and Mattiazzo G. Application of a passive control technique to the ISWEC. In *Proceedings of the 12th European Wave and Tidal Energy Conference*, Cork, Ireland, 2017.

[84] Chiccoli D., Bonfanti M., Bracco G., Dafnakis P., Sirigu S.A., and Mattiazzo G. Numerical analysis of two different hydraulic power take-off configurations for renewable energy applications. In *Proceedings of the 4th Asian Wave and Tidal Conference*, Taipei, Taiwan, 2018.

[85] Stigter C. The performance of u-tanks as a passive anti rolling device. *International Shipbuilding Progress*, 13(144):1249–275, 1966.

[86] LLoyd A.R.J.M. *Seakeeping: Ship behavior in rough weather*. Ellis Horwood Limited, 1989.

[87] Khaled S.Y., Saad A.R., Ali H.N., and Dean T.M. Design of passive anti-roll tanks for roll stabilization in the nonlinear range. *Ocean Engineering*, 29(2):177–192, 2002.

[88] Khaled S.Y., Dean T.M., Ali H.N., and Saad A.R. Roll stabilization by passive anti-roll tanks using an improved model of the tank-liquid motion. *Modal Analysis*, 9(7):839–862, 2003.

[89] Holden C., Perez T., and Fossen T. A lagrangian approach to nonlinear modeling of anti-roll tanks. *Ocean Engineering*, 38:341–359, 02 2011.

[90] Zhong Z., Falzarano J.M., and Fithen R.M. A numerical study of U-tube passive anti-roll tanks. In *Proceedings of the International Symposium of Offshore and Polar Engineering (ISOPE)*, volume 3, pages 504–512, Montreal, Canada, 1998.

[91] van Daalen E.F.G., Kleefsman K.M.T., Gerrits J., Luth H.R., and Veldman A.E.P. Anti-Roll tank simulations with a volume of fluid (VOF) based navier-stokes solver. In *Twenty-Third Symposium on Naval Hydrodynamics*, pages 457–472, Val de Reuil, France, 2000.

[92] Taskar B.U., Dasgupta D., Nagarajan V., Chakraborty S., Chatterjee A., and Sha O.P. CFD aided modelling of anti-rolling tanks towards more accurate ship dynamics. *Ocean Engineering*, 92, 2014.

[93] Kerkvliet M., Vaz G., Carette N., and Gunsing M. Analysis of U-Type Anti-Roll tank using URANS. Sensitivity and Validation. In *Proceedings of the International Conference on Offshore Mechanics and Arctic Engineering - OMAE*, volume 2, San Francisco, USA, 2014.

[94] Muzaferija S., Peric M., and Sames P. et al. A two-fluid Navier–Stokes solver to simulate water entry. In *Proceedings of the 22nd symposium on naval hydrodynamics*, pages 227–289, 1998.

[95] Siemens. *STAR-CCM+ User Guide*. Siemens PLM Software.

[96] Begovic E., Bertorello C., and Orsic J.P. Roll damping coefficients assessment and comparison for round bilge and hard chine hullforms. In *Volume 9: Odd M. Faltinsen Honoring Symposium on Marine Hydrodynamics*, Nantes, France, June 2013.

[97] SKF. *Rolling Bearings*, 2018. https://www.skf.com/binary/77-121486/SKF-rolling-bearings-catalogue.pdf.

[98] Penalba M., Kelly T., and Ringwood J. Using NEMOH for Modelling Wave Energy Converters: A Comparative Study with WAMIT. In *Proceedings of the 12th European Wave and Tidal Energy Conference*, 2017.

[99] ANSYS. *Aqwa Theory Manual*.

[100] Sirigu S.A.and Vissio G., Bracco G., Giorcelli E., Passione B., Raffero M., and Mattiazzo G. ISWEC Design Tool. *International Journal of Marine Energy*, 15:201–213, 2016.

[101] Lagarias J.C., Reeds J.A., Wright M.H., and Wright P.E. Convergence Properties of the Nelder-Mead Simplex Method in Low Dimensions. *SIAM Journal of Optimization*, 9:112–147, 1998.

[102] D'Errico J. fminsearchbnd, fminsearchcon - matlab central file exchang, 2012. https://it.mathworks.com/matlabcentral/fileexchange/8277-fminsearchbnd-fminsearchcon.

[103] MATLAB Optimization Toolbox. The MathWorks, Natick, MA, USA.

[104] Li N. and Cheung K.F. California Ocean Wave Energy Assessment. Technical report, California Energy Commission Public Interest Energy Research Program, 2007.

[105] La Bonte A., O'Connor P., Fitzpatrick C., Hallett K., and Li Y. Standardized cost and performance reporting for marine and hydrokynetic technologies. In *Proceedings of the 1st Marine Energy Technology Symposium METS13*, 2013.

[106] Hawaii Natural Energy Institute. Wave Energy Test Site (WETS), 2018. https://www.hnei.hawaii.edu/projects/wave-energy-test-site-wets.

[107] Li N. and Cheung K.F. Wave energy resource characterization. Technical report, Department of Ocean and Resources Engineering, University of Hawaii, 2014.

[108] Winden B. Anti Roll Tanks in Pure Car and Truck Carriers. Master's thesis, KTH Centre for naval architecture, 2009.

[109] A.R. Dallman and V.S. Neary. Characterization of U.S. Wave Energy Converter (WEC) Test Sites: A Catalogue of Met-Ocean Data. 2nd Edition. Technical report, Sandia National Laboratories, Albuquerque, New Mexico 87185 and Livermore, California 94550, 2015.

[110] Ochi M. and Hubble E. Six-parameter wave spectra. *Coastal Engineering Proceedings*, 1(15), 1976.

[111] Guedes Soares C. On the occurence of double peaked wave spectra. *Ocean Engineering*, 18(1):167–171, 1991.

[112] Lucas C. and Soares C.G. On the Modelling of Wave Spectra. *Ocean Engineering*, 108:749–759, 2015.

[113] Price A.A.E., Dent C., and Wallace A.R. On the capture width of wave energy converters. *Applied Ocean Research*, 31:251–259, 10 2009.

[114] J. Falnes and J. Todalshaug. Heaving buoys, point absorbers and arrays. *Philosophical transactions. Series A, Mathematical, physical, and engineering sciences*, 370:246–77, January 2012.

[115] Emmerich M.T.M. and Deutz A.H. A tutorial on multiobjective optimization: fundamentals and evolutionary methods. *Natural Computing*, 17, 2018.

[116] Ehrgott M. *Multicriteria Optimization*. Springer, 2005.

[117] Deb K. *Multi-Objective Optimization Using Evolutionary Algorithms*. Wiley, 2009.

[118] Back T., Hammel U., and Schwefel H.P. Evolutionary computation: Comments on the history and current state. *IEEE Transactions on Evolutionary Computation*, 1:3 – 17, 05 1997.

[119] Coello C.A., Coello D., Van Veldhuizen D.A., and Lamont G.B. *Algorithms for Solving Multi-Objective Problems*. Springer, 2002.

[120] M.K. Colby, E.M. Nasroullahi, and K. Tumer. Optimizing Ballast Design of Wave Energy Converters Using Evolutionary Algorithms. In *Proceedings of the 13th Annual Conference on Genetic and Evolutionary Computation*, pages 1739–1746, 2011.

[121] McCabe A.P. Constrained optimization of the shape of a wave energy collector by genetic algorithm. *Renewable Energy*, 51:274–284, 2013.

[122] Babarit A. and Clément A. Shape optimization of the SEAREV wave energy converter. In *Proceedings of 9th World Renewable Energy Congress*, Firenze, Italy, 2006.

[123] Miettinen K. *Nonlinear multiobjective optimization*. Springer, 2012.

[124] de Andres A.D., Maillet J., Todalshaug J., Möller P., Bould D., and Jeffrey H. Techno-economic related metrics for a wave energy converters feasibility assessment. *Sustainability*, 8:1109, 10 2016.

[125] Frederick R. Driscoll and et Al. Methodology to Calculate the ACE and HPQ Metrics Used in the Wave Energy Prize. Technical report, National Renewable Energy Lab. (NREL), Golden, CO (United States), 2015.

[126] Jenne D., Yu Y.H., and Neary V. Levelized Cost of Energy Analysis of Marine and Hydrokinetic Reference Models. In *3rd Marine Energy Technology Symposium*, Washington, (US) USA, 2015.

[127] Garcia-Rosa P.B., Bacelli G., and Ringwood J. Control-Informed Geometric Optimization of Wave Energy Converters: The Impact of Device Motion and Force Constraints. *Energies*, 8(12):13672–13687, 2015.

[128] Garcia-Rosa P.B. and Ringwood J. On the Sensitivity of Optimal Wave Energy Device Geometry to the Energy Maximizing Control System. *IEEE Transactions on Sustainable Energy*, 7(1):419–426, 2016.

[129] Kramer O. A Review of Constraint-Handling Techniques for Evolution Strategies. *Applied Computational Intelligence and Soft Computing*, 2010, 2010.

[130] Özgür Yeniay. Penalty function methods for constrained optimization with genetic algorithms. *Mathematical and Computational Applications*, 10, 2005.

[131] Zhang Y., Ogura H., Ma X., Kuroiwa J., and Odaka T. A Genetic Algorithm Using Infeasible Solutions for Constrained Optimization Problems. *The Open Cybernetics and Systemics Journal*, 8, 2014.

[132] U.S. Sandia National Labs. Dakota website. http://dakota.sandia.gov/.

[133] Adams B.M., Ebeida M.S., Eldred M.S., and Geraci G. *Dakota, A Multilevel Parallel Object-Oriented Framework for Design Optimization, Parametric Estimation, Uncertainty Quantification, and Sensitivity Analysis: Version 6.7 User's Manual*. U.S. Sandia National Labs, 6.7 edition.

Appendix A

Figures

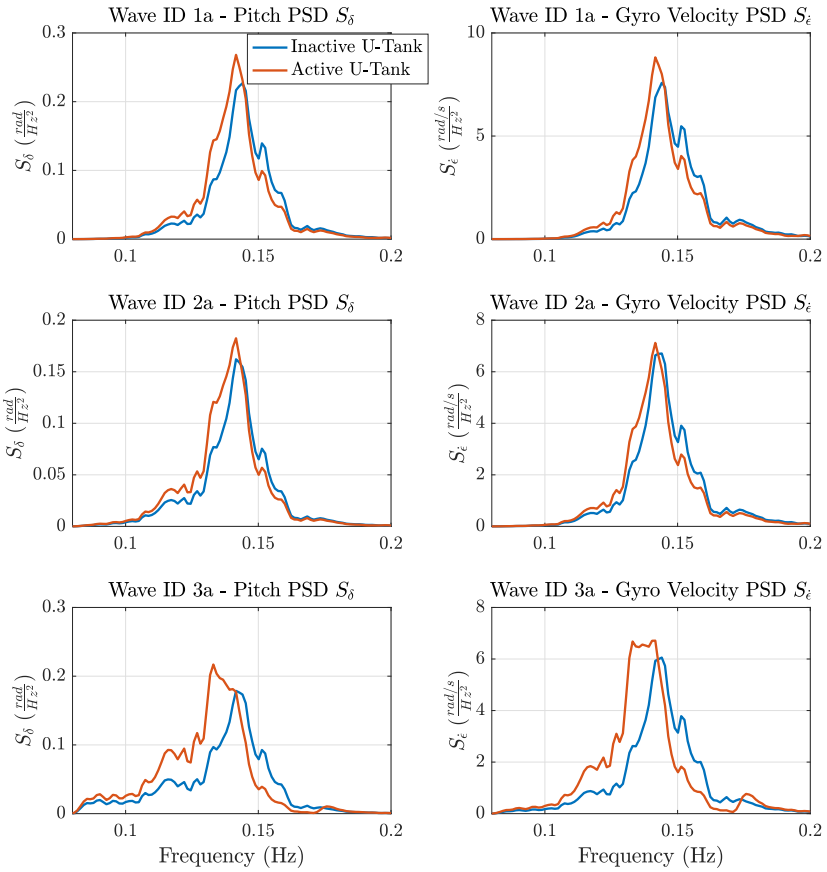

Figure A.1 Time domain results of the IOwec dynamics with active control of the U-Tank (2).

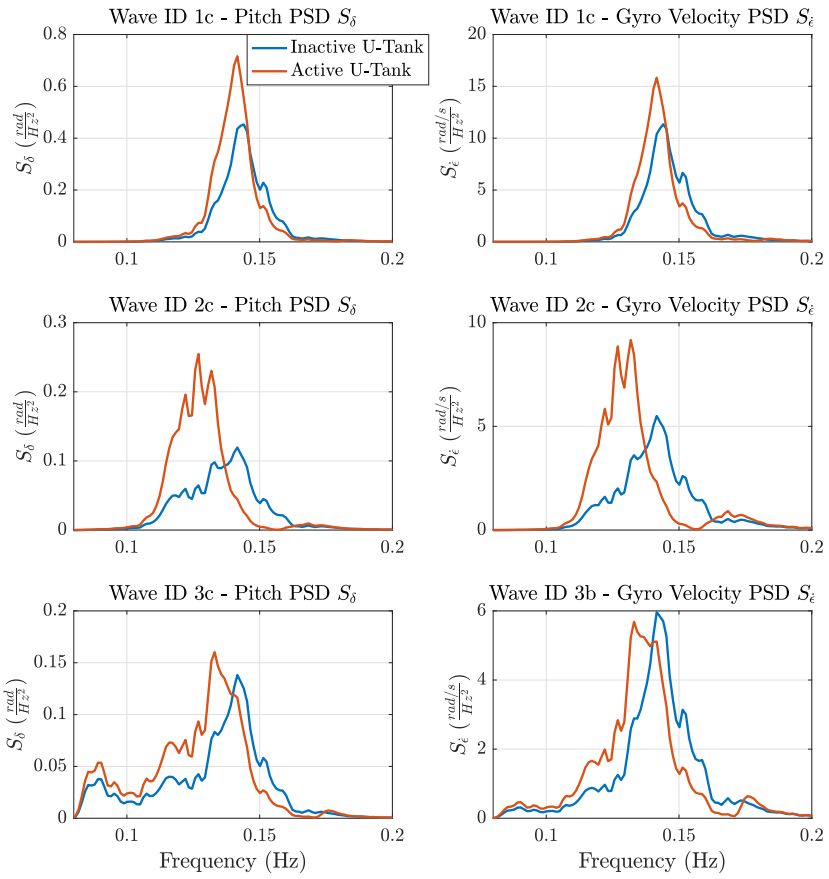

Figure A.2 Time domain results of the IOwec dynamics with active control of the U-Tank (2).

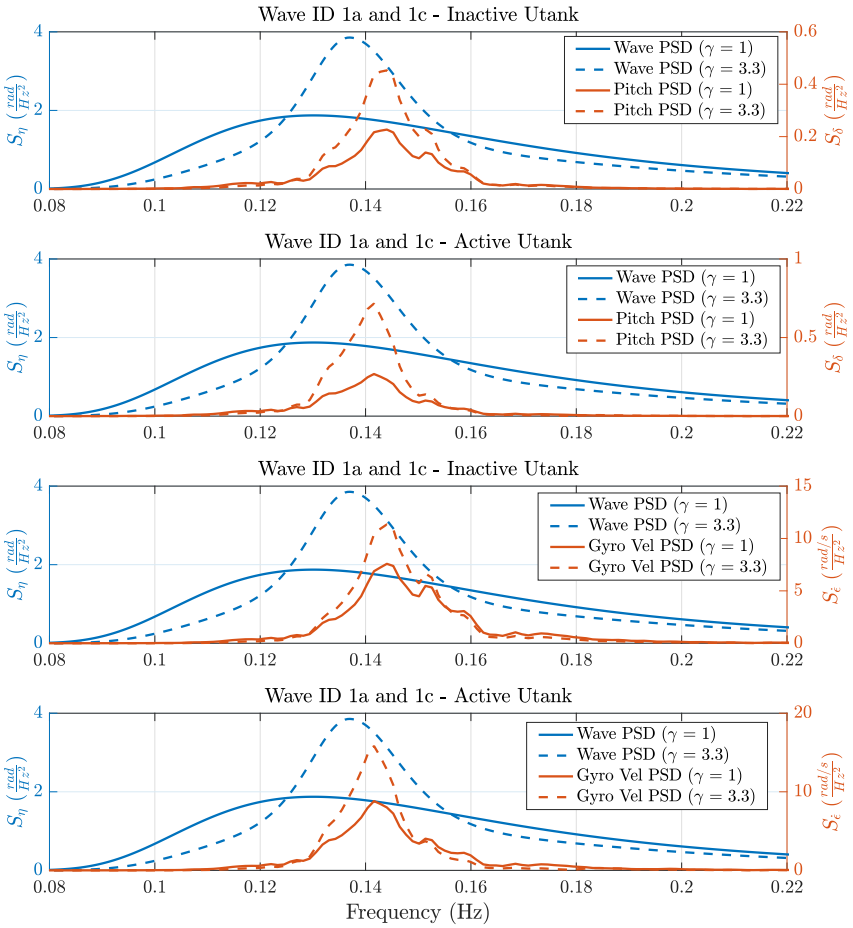

Figure A.3 Time domain results of the IOwec dynamics with active control of the U-Tank (2).

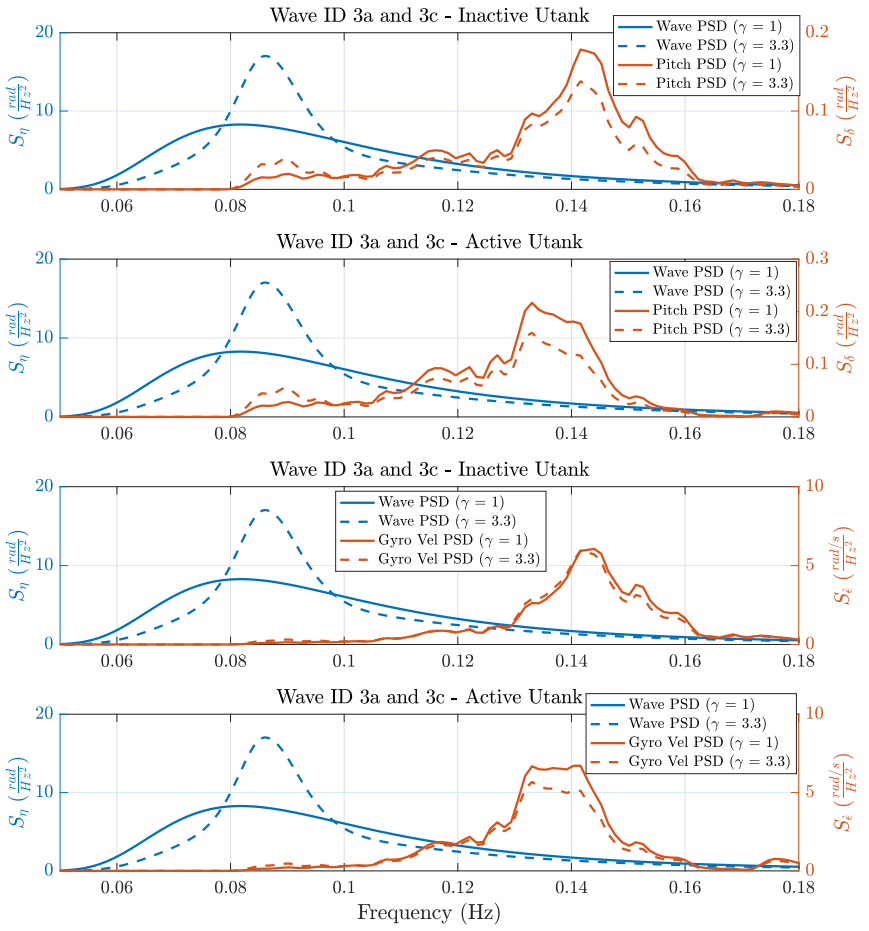

Figure A.4 Time domain results of the IOwec dynamics with active control of the U-Tank (2).

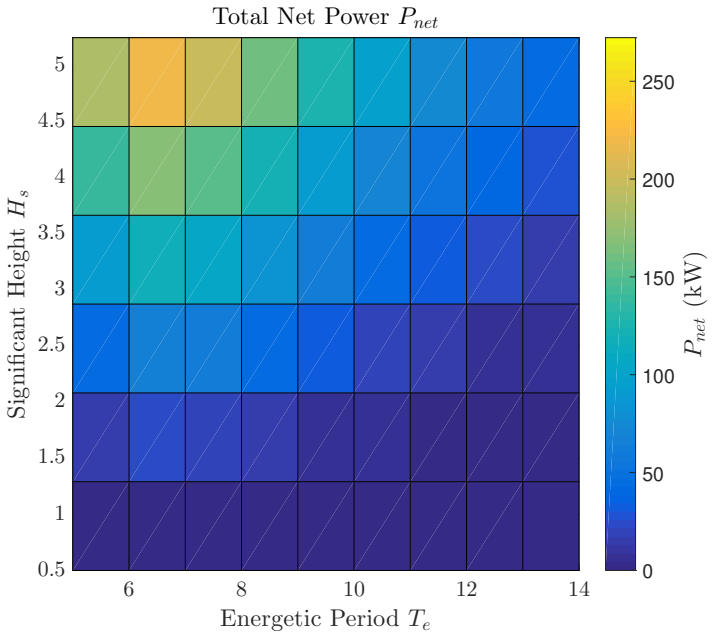

Figure A.5 Total mean net mechanical power P_{net} plot grid. First IOwec draft - Inactive U-Tank case.

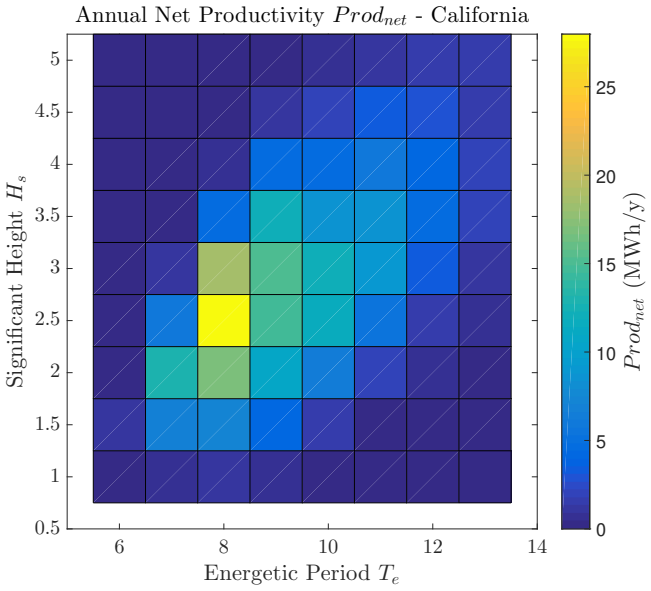

(a)

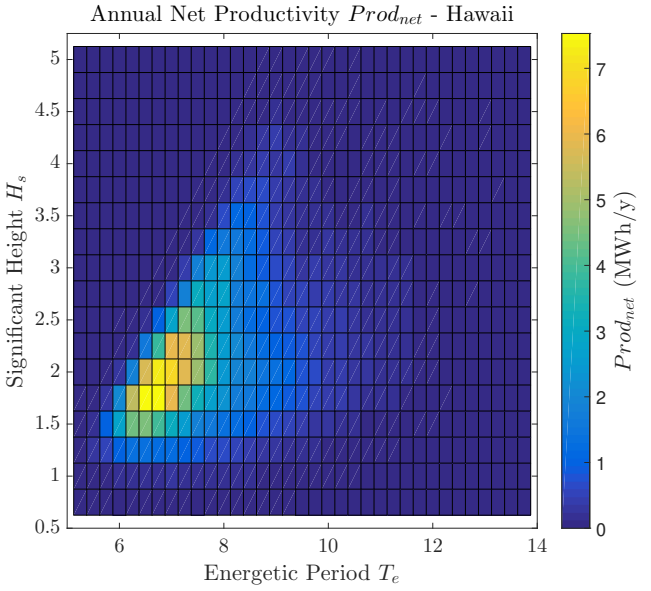

(b)

Figure A.6 Productivity *Prod* interpolated plot grids. First IOwec draft - Inactive U-Tank case.(a) Humboldt Bay (California) (b) WETS (Hawaii).

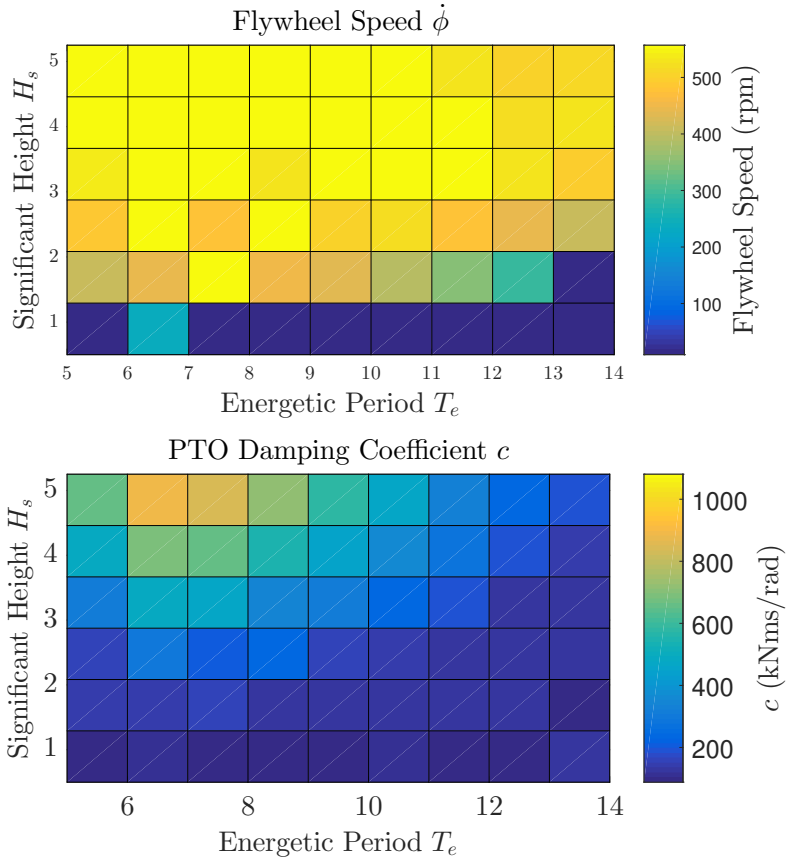

Figure A.7 Optimal flywheel speed $\dot{\phi}$ and PTO damping coefficient c plot grids. First IOwec draft - Inactive U-Tank case.

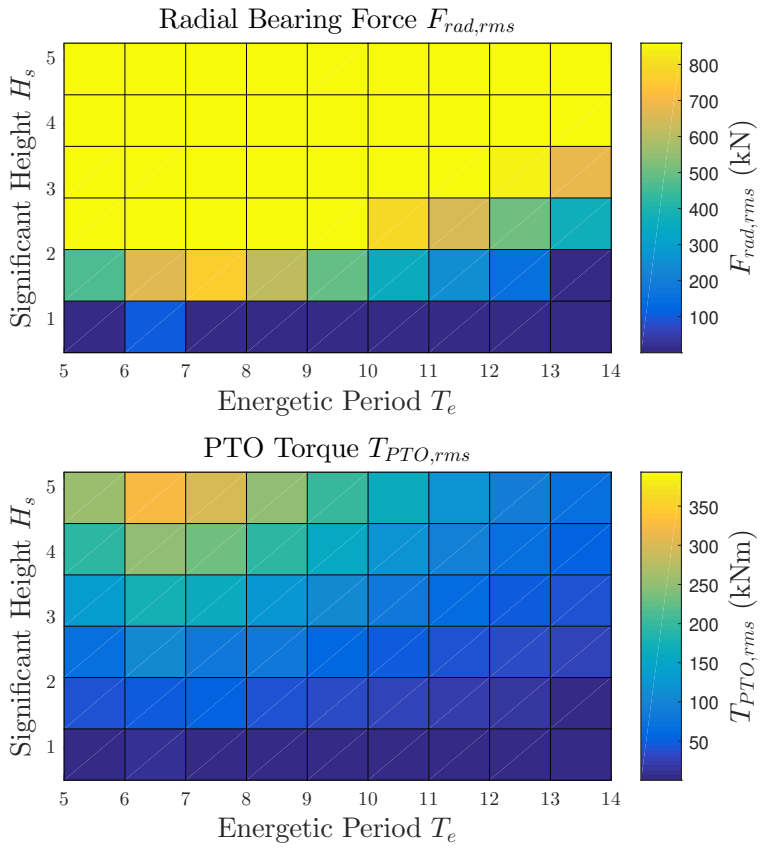

Figure A.8 Radial bearing forces $F_{rad,rms}$ and PTO torque $T_{PTO,rms}$ grid plots. First IOwec draft - Inactive U-Tank case.

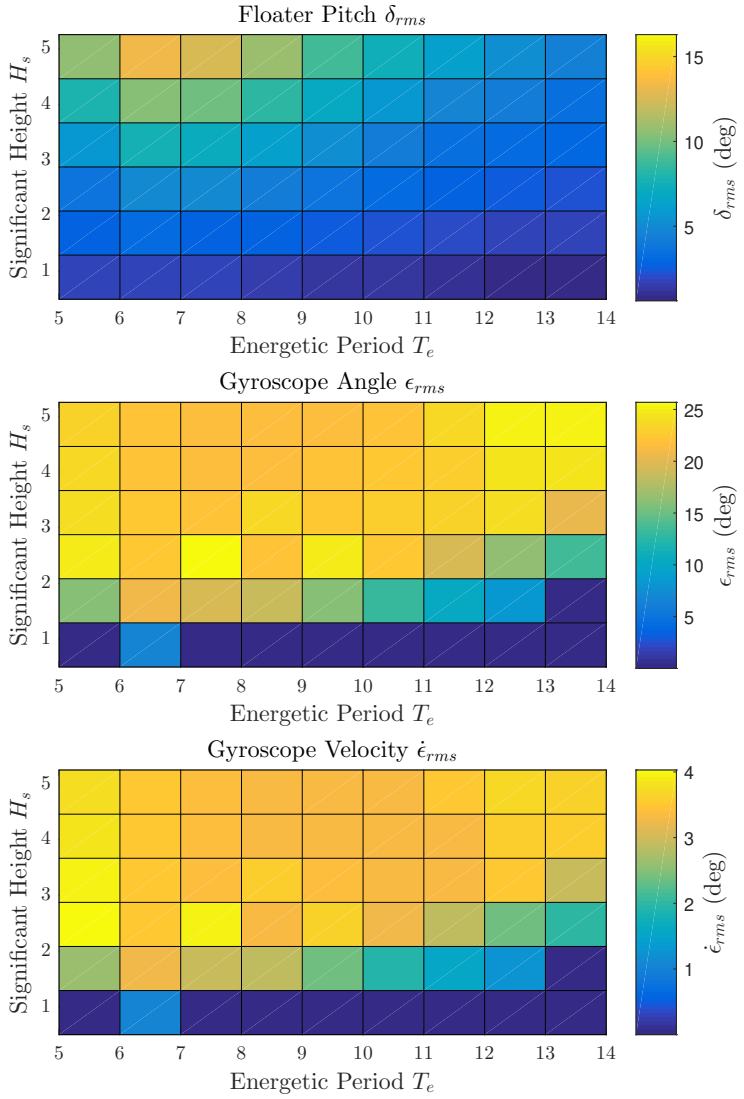

Figure A.9 Floater pitch δ_{rms}, gyroscope angle ε_{rms} and velocity $\dot{\varepsilon}_{rms}$ grid plots. First IOwec draft - Inactive U-Tank case.

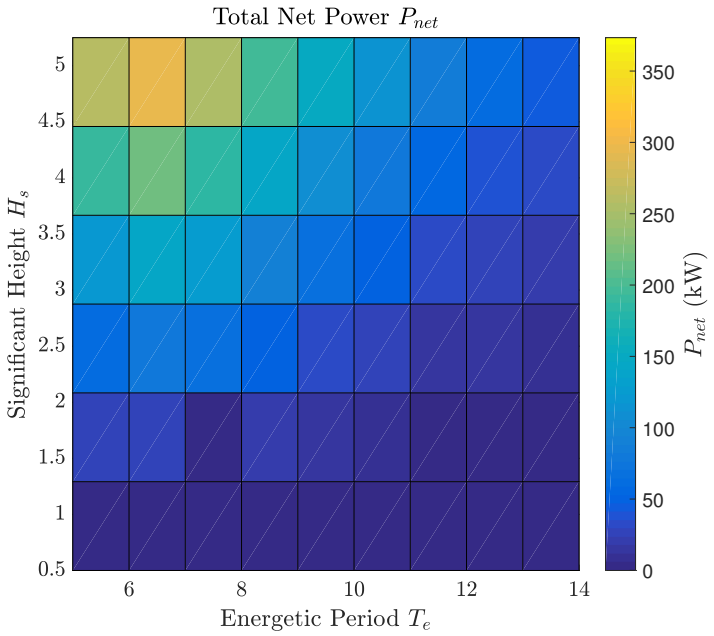

Figure A.10 Total mean net mechanical power P_{net} plot grid. Optimal IOwec - Inactive U-Tank case.

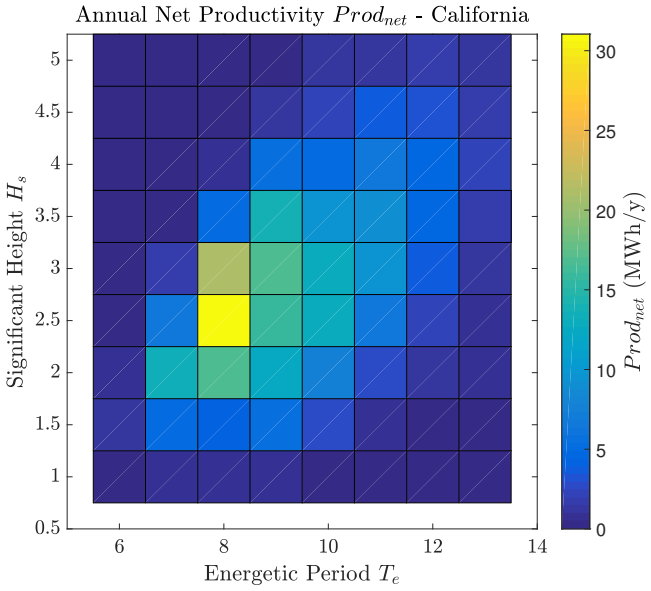

(a)

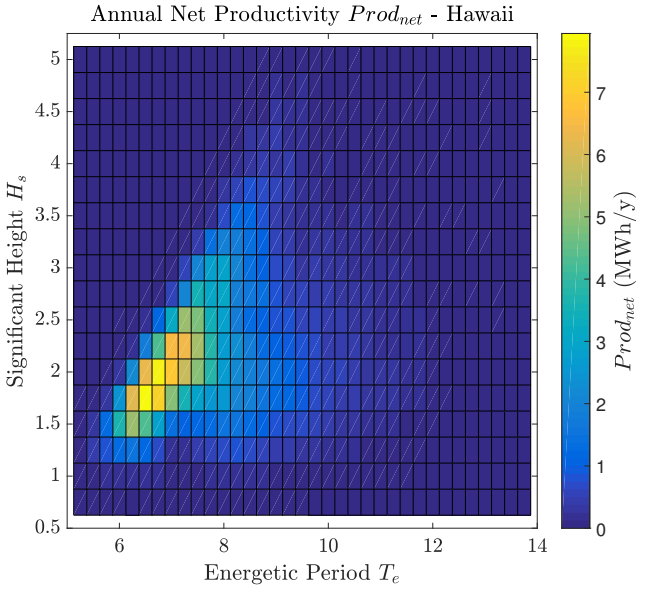

(b)

Figure A.11 Productivity *Prod* interpolated plot grids. Optimal IOwec - Inactive U-Tank case.(a) Humboldt Bay (California) (b) WETS (Hawaii).

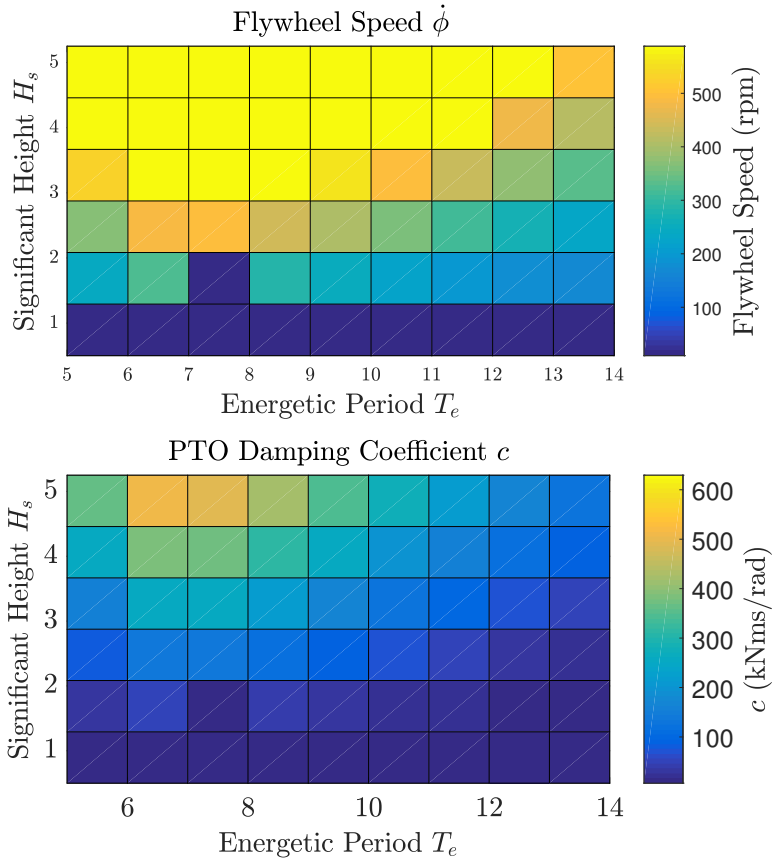

Figure A.12 Optimal flywheel speed $\dot{\phi}$ and PTO damping coefficient c plot grids. Optimal IOwec - Inactive U-Tank case.

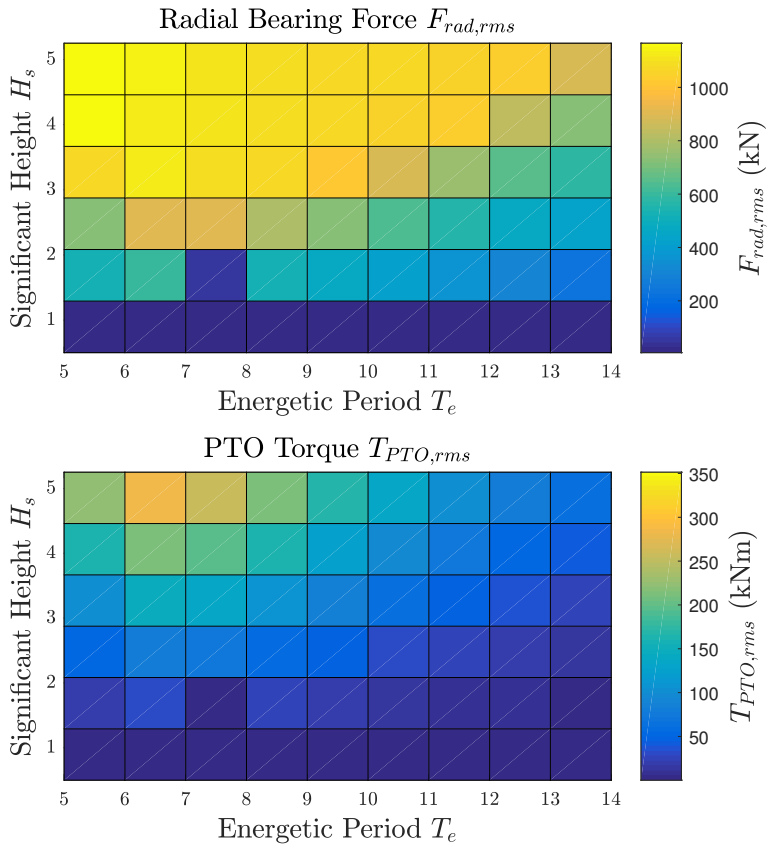

Figure A.13 Radial bearing forces $F_{rad,rms}$ and PTO torque $T_{PTO,rms}$ grid plots. Optimal IOwec - Inactive U-Tank case.

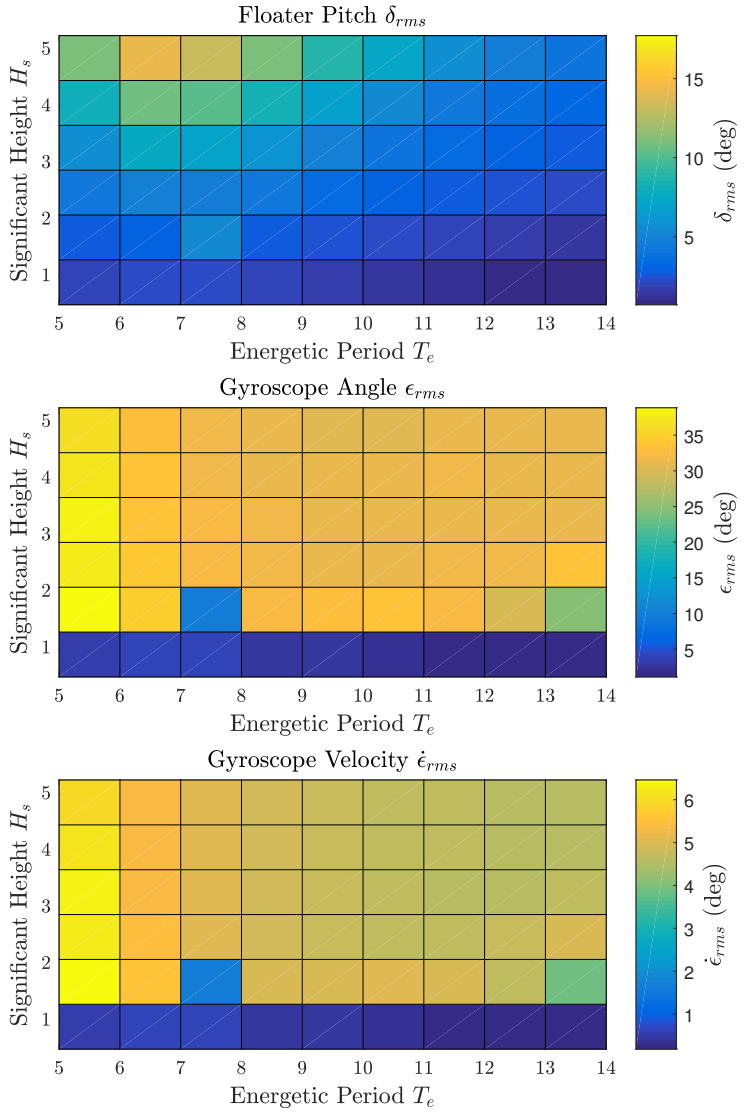

Figure A.14 Floater pitch δ_{rms}, gyroscope angle ϵ_{rms} and velocity $\dot{\epsilon}_{rms}$ grid plots. Optimal IOwec - Inactive U-Tank case.

Appendix B

Tables

Table B.1 Simulation results in irregular wave. Peakedness factor $\gamma = 1$.

		Inactive Utank			Active U-Tank		
		Wave ID			Wave ID		
Parameter	Unit	1a	2a	3a	1a	2a	3a
Tot. Net Power, P_{net}	kW	38.5	24.2	34.2	42.3	27.9	42.1
Tot. Gross Power, P_{gross}	kW	49.9	35.5	46.5	53.9	38.9	54.5
Flywheel Speed, $\dot{\phi}_{opt}$	rpm	471	483	508	474	477	520
PTO Damping Coeff., c_{opt}	kNms/rad	152	126	165	157	138	162
Utank Stiffness Ratio, $c^*_{\tau\tau}/c_{\tau\tau}$	-				4.9	4.9	3.8
Floater Pitch Angle rms, δ_{rms}	deg	3.92	3.31	3.88	4.10	4.53	4.34
U-Tank Angle rms, τ_{rms}	deg				1.18	0.98	2.22
Gyro. Angle rms, ε_{rms}	deg	25.1	23.7	24.3	26.3	24.2	28.2
Gyro. Velocity rms, $\dot{\varepsilon}_{rms}$	rpm	3.87	3.58	3.58	4.0	3.58	3.96
PTO Torque rms, T_{PTO}	kNm	61.6	47.3	62.0	65.0	51.2	67.1

Table B.2 Simulation results in irregular wave. Peakedness factor $\gamma = 3.3$.

		Inactive Utank			Active U-Tank		
		Wave ID			Wave ID		
Parameter	Unit	1b	2b	3b	1b	2b	3b
Tot. Net Power, P_{net}	kW	55	23	26	67	33	31
Tot. Gross Power, P_{gross}	kW	65	35	39	78	47	45
Flywheel Speed, $\dot{\phi}_{opt}$	rpm	436	527	527	431	527	543
PTO Damping Coeff., c_{opt}	kNms/rad	168	133	141	182	127	154
Utank Stiffness Ratio, $c^*_{\tau\tau}/c_{\tau\tau}$	-				4.2	3.2	3.8
Floater Pitch Angle rms, δ_{rms}	deg	5.0	3.2	3.5	5.6	4.0	3.9
U-Tank Angle rms, τ_{rms}	deg				2.4	2.8	1.9
Gyro. Angle rms, ε_{rms}	deg	27.6	23.7	24.3	29.7	30.0	26.5
Gyro. Velocity rms, $\dot{\varepsilon}_{rms}$	rpm	4.2	3.5	3.5	4.4	4.1	3.7
PTO Torque rms, T_{PTO}	kNm	74	49	52	84	54	59